SPECTRAL ANALYSIS FOR THE SPECIES CHARACTERIZATION OF MANGROVES OF BHITARKANIKA NATIONAL PARK, ODISHA, INDIA USING HYPERSPECTRAL REMOTE SENSING

A Thesis submitted

in partial fulfillment for the Degree of

Doctor of Philosophy

by

ARUN PRASAD K.

DEPARTMENT OF EARTH AND SPACE SCIENCES

INDIAN INSTITUTE OF SPACE SCIENCE AND TECHNOLOGY

THIRUVANANTHAPURAM – 695 547

OCTOBER, 2016

Dedicated

To my grandfather (Late) Mr. A. Thirumalai and my family

CERTIFICATE

This is to certify that the thesis entitled **Spectral Analysis for the Species Characterization of Mangroves of Bhitarkanika National Park, Odisha, India using Hyperspectral Remote Sensing**, submitted by **Mr. Arun Prasad K.,** to the Indian Institute of Space Science and Technology, Thiruvananthapuram, in partial fulfillment for the award of the degree of **Doctor of Philosophy**, is a *bona fide* record of research work done by him under my supervision. The contents of this thesis, in full or in parts, have not been submitted to any other Institute or University for the award of any degree or diploma.

Dr. L. Gnanappazham
Supervisor
Associate Professor
Department of Earth and Space Sciences

Thiruvananthapuram   Counter signature of HOD with seal
October 2016

DECLARATION

I declare that this thesis entitled **Spectral Analysis for the Species Characterization of Mangroves of Bhitarkanika National Park, Odisha, India using Hyperspectral Remote Sensing** submitted in partial fulfillment of the degree of **Doctor of Philosophy** is a record of original work carried out by me under the supervision of **Dr. L. Gnanappazham**, and has not formed the basis for the award of any other degree or diploma, in this or any other Institution or University. In keeping with the ethical practice in reporting scientific information, due acknowledgements have been made wherever the findings of others have been cited.

<div align="right">

Arun Prasad K.

SC11D003

</div>

Place: Thiruvananthapuram

October 2016

ACKNOWLEDGMENTS

ABSTRACT

Mangroves are salt tolerant woody halophytes usually thrives in the intertidal mudflats of tropical and subtropical coastlines. Globally mangroves are overexploited for the benefit of human needs such as conversion into aquaculture, agriculture, and logging for domestic and industrial purposes that resulted in a loss of 20% in the span of 1980 to 2005. Realizing its wide ecological and economic importance, as well as their ability to capture atmospheric carbon in the form of biomass and other associated organic matter, mangrove ecosystems are recognized as the critical habitat for protection, conservation, and management. Mapping and monitoring various dimensions of coastal zone are identified as preliminary steps for such conservation activities. For the past three decades, remote sensing technology has replaced the manual survey method and plays a major role in environmental resource monitoring and management activities from regional to micro-level. Recent advancement in remote sensing such as hyperspectral remote sensing becomes a reliable source of diversified information because of its high spectral resolution. High spectral resolution is the prerequisite for species level mapping as well as health monitoring of various natural ecosystems including mangroves.

Bhitarkanika National Park in Odisha is one of the major mangrove forests in India that covers nearly 145 sq. km and is recognized for its high species diversity. There are 76 mangrove species in which 30 are true species and 46 are associated species. This thesis aims at developing a methodological framework to spectrally characterize and map mangroves at the species level using hyperspectral remote sensing techniques.

Development of a spectral library is a prerequisite to map higher level vegetation classes using hyperspectral image analysis. Field survey is conducted in the study area to collect canopy level field spectra and leaf level laboratory spectra of 34 species (25 true and 9 associated mangroves) in the wavelength range of 400nm to 2500nm, using ASD Fieldspec® 3 spectroradiometer. Reflectance spectroscopy provides interoperable pure reflectance of feature of interest from its in-situ and laboratory measurements. The collected raw spectra are then undergone post-processing steps such as removal of water absorption bands, correction of thermal difference drifts, and smoothing of spectra for further utilization. The processed spectra are then compiled as a spectral library.

The main aim of developing such spectral database is to test their efficiency to uniquely identify the species in hyperspectral domain. Hence, the spectral data are analyzed using multiple statistical approaches followed by popular feature reduction methods such as Principal Component Analysis (PCA) and Stepwise Discriminant Analysis (SDA) to select optimal wavelengths for species discrimination. Initially, spectral signatures of eight mangrove species of *Rhizophoraceae* family are

analyzed using the proposed methodology since in earlier studies these species were reported as "less separable". First and second derivatives are derived for the reflectance spectra of eight species of *Rhizophoraceae* at first. Then spectral separability among species pairs are tested statistically using parametric and non-parametric statistical tests namely One-way Analysis of Variance along with Bonferroni post-hoc test and Kruskal Wallis test along with Mann-Whitney U test, respectively. Results show that non-parametric test provides better separability than parametric test especially in red edge (680nm to 720nm) and water absorption (around 1150nm and 1400nm) spectral regions.

To further explore the potential of hyperspectral region beyond 1400nm i.e., Short Wave Infra-Red (SWIR) region, spectral signatures in reflectance mode (RS) is transformed to (i) additive inverse of spectral reflectance (IS), (ii) continuum removal of reflectance spectra (CRRS), and (iii) continuum removal of inverse spectra (CRIS). When the four modes are analyzed using parametric and non-parametric tests, Continuum Removal of Inverse Spectra (CRIS) proposed in this study gives better result. CRIS utilizes the advantage of continuum removal in reflectance region beyond Near Infra-Red (NIR) which is often suppressed in Continuum Removal of Reflectance Spectra (CRRS). Later, PCA and SDA are performed on the transformed spectra to select optimal bands for spectral discrimination. Green (550nm), red edge (680nm to 720nm), and absorption region (1470nm and 1850nm) are found to be prominent wavelength region for species discrimination. Among *Rhizophoraceae* species, *Ceriops decandra* is found to be the most separable species.

The methodology is further extended to determine the spectral separability among all 34 species of the spectra developed in this study. To validate our results, the field and laboratory spectra of 34 species in CRRS and CRIS modes are classified using three supervised classification algorithms such as Maximum Likelihood Classification, Spectral Angle Mapper, and Support Vector Machines. Better classification accuracy is obtained using CRIS mode of field spectra and CRRS mode of laboratory spectra. This shows that CRIS has enhanced the separability in NIR and SWIR regions. Biophysical characteristics such as leaf area index, canopy structure, and leaf arrangement have potential contributions in these wavelengths when the spectra are collected in field condition rather than the simulated laboratory conditions. The same spectral transformation methodology is extended to classify the mangrove species using hyperspectral image of EO-1 Hyperion sensor.

To compare the potential of hyperspectral data, classification is also carried out using two widely used multispectral data namely Landsat-8 OLI and IRS-P6 LISS III. They are classified using ten base classifiers and their combination, the Multiple Classifier System (MCS). From the results, it is found that Support Vector Machine (SVM) algorithm gives maximum accuracy among base classifiers. Also, MCS increases the accuracy when compared to single best classifier in both

multispectral images. In case of hyperspectral data (EO-1 Hyperion), it is transformed into four spectral modes mentioned earlier. The transformed images in four spectral modes are compiled together as separate dataset to utilize the complementary spectral information provided by each of the spectral modes for mangrove species classification. The transformed hyperspectral images in all five spectral modes are dimensionally reduced using three dimensionality reduction (DR) methods: Principal Component Analysis (PCA), Minimum Noise Fraction (MNF), and Independent Component Analysis (ICA). They are classified individually using ten base classifiers. On analyzing the results, MNF-SVM is identified as the best DR-Classifier combination. The decisive function values from ten base classifiers are combined to classify 11 mangrove species classes using MCS for all 5 spectral modes. Results show that among MCS results, combined spectral mode gives better accuracy (82.82%) than other four individual spectral modes.

WorldView-2 data, though it is multispectral, combination of additional narrow bands such as Yellow and Red edge bands with high spatial resolution is recently explored for biomass estimation of various tropical forests. The potential of such high resolution data is investigated to estimate biomass of heterogeneous mangrove forest in the present study area by regressing image derived parameters with plot biomass. Plot biomass is calculated from 40 stratified sample plots using species specific and common allometric equations, and field measured biophysical parameters such as tree height, diameter at breast height (DBH), etc. After preprocessing, 8 spectral reflectance bands, 28 simple band ratios, 12 vegetation indices, and 8 textural parameters for each of the preceding parameters are derived from the image and their relation with the plot biomass are investigated using multiple regression analysis. From the results, it is found that the textural parameters improve biomass estimation in simple reflectance bands and band ratios whereas in case of vegetation indices, there is no such improvement observed. When the textural parameters of all three inputs are combined and regressed, it improves the R^2 value (0.46) and reduces the error (RMSE of 169.28 t/ha) as compared with other biomass models developed in this study using different input parameters.

The potential of hyperspectral data and high resolution data are analyzed in this study to understand the spectral behavior of mangrove species and its biomass using various statistical, image transformations, and processing techniques. Hope that outcome of the study will be a stepping stone in the studies of Indian mangroves using hyperspectral and other remote sensing techniques.

TABLE OF CONTENTS

LIST OF FIGURES

xxiii

LIST OF TABLES

xxvii

ABBREVIATIONS

ACE	Adaptive Coherence Estimation
ACEP	Atlantic Caribbean Eastern Pacific
AGB	Above Ground Biomass
AIRSAR	Airborne Synthetic Aperture Radar
AISA+	Airborne Imaging Spectrometer for Applications
ALOS	Advanced Land Observing Satellite
ANN	Artificial Neural Network
ANOVA	Analysis of Variance
AOI	Area of Interest
ASAR	Advanced Synthetic Aperture Radar
ASCII	American Standard Code for Information Interchange
ASD	Analytical Spectral Devices Inc.
ASI	Agenzia Spaziale Italiana
ASTER	Advanced Spaceborne Thermal Emission and Reflection Radiometer
ATSR	Along-Track Scanning Radiometer
AVHRR	Advanced Very High Resolution Radiometer
AVIRIS	Airborne Visible/Near Infra-red Imaging Spectrometer
AVNIR	Advanced Visible and Near Infra-red Radiometer
BI	Band Index
CASI	Compact Airborne Space Imager
CHRIS	Compact High Resolution Imaging Spectrometer
CRIS	Continuum Removed Inverse Spectra
CRRS	Continuum Removed Reflectance Spectra
CSDA	Canonical Stepwise Discriminant Analysis
DAIS	Digital Airborne Imaging Spectrometer
DBH	Diameter at Breast Height
DCM	Digital Canopy Model

DCS	Dynamic Linear Classification System
DEM	Digital Elevation Models
DN	Digital Number
DR	Dimensionality Reduction
DT	Decision Tree
DTM	Digital Terrain Model
DVI	Difference Vegetation Index
DWTDR	Discrete Wavelet Transform based Dimensionality Reduction
EMR	Electromagnetic Radiation
EnMAP	Environmental Mapping and Analysis Programme
ENVI	ENvironment for Visualizing Images software package
EO-1	Earth Observation-1 Satellite
ERS	European Remote Sensing Satellite
ERTS-1	Earth Resource Technology Satellite-1
ESA	European Space Agency
ETM+	Enhanced Thematic Mapper +
EVI	Enhanced Vegetation Index
FA	Factor Analysis
FAO	Food and Agricultural Organization
FLAASH	Fast Line-of-sight Atmospheric Analysis of the Spectral Hypercubes
FOTO	Fourier Based Textural Ordination
FOV	Field of View
FR	Feature Reduction
FSI	Forest Survey of India
FTIR	Fourier Transform Infra-red
FWHM	Full Width Half Maximum
GA	Genetic Algorithm
GEOBIA	Geographic Object-Based Image Analysis
GIS	Geographic Information System
GLAS	Geoscience Laser Altimeter System
GLCM	Grey Level Co-occurrence Matrix

GLS 2000	Global Land Survey 2000
GPS	Global Positioning System
GRFM	Global Rain Forest Mapping
GVI	Green Vegetation Index
HNN	Hidden Neural Network
HRVIR	High Resolution Visible Infra-red
HYDICE	Hyperspectral Digital Image Collection Experiment
HyMap	Hyperspectral Mapper
HySI	HyperSpectral Imager
HyspIRI	Hyperspectral Infra-red Imager
IASI	Infra-red Atmospheric Sounder Interferometer
ICA	Independent Component Analysis
ICESat	Ice, Clouds, and Land Elevation Satellite
IMS-1	Indian Miniature Satellite-1
InGaAs	Indium Gallium Arsenide
IRS	Indian Remote Sensing Satellite
IS	Inverse Spectra
ISME	International Society for Mangrove Ecosystems
ISODATA	Iterative Self-Organizing Data Analysis Technique
ISRO	Indian Space Research Organization
ITTO	International Tropical Timber Organization
IUCN	International Union for Conservation of Nature
IWP	Indo-West Pacific
JERS-1	Japan Earth Resource Satellite-1
JM	Jeffries-Matusita
JPL	Jet Propulsion Laboratory
k-NN	k-Nearest Neighborhood
LAI	Leaf Area Index
LDA	Linear Discriminant Analysis
LDC	Linear Discriminant Classifier
LIBSVM	A Library for Support Vector Machines

LiDAR	Light Detection and Ranging
LISS	Linear Imaging Self-Scanning Sensor
LR	Logistic Regression
LVIS	Land, Vegetation, and Ice Sensor
MCARI	Modified Chlorophyll Absorption Vegetation Index
MCDF	Multi-Classifier Decision Fusion
MCS	Multiple Classifier System
MD	Minimum Distance Classification
MF	Matched Filtering
MI	Mutual Information
MIR	Middle Infra-red
MLC	Maximum Likelihood Classification
MNF	Minimum Noise Fraction
MODIS	Moderate-resolution Imaging Spectroradiometer
MoEF	Ministry of Environment and Forests
mRe-SRI	modified Red edge Simple Ratio Index
MSAVI	Modified Soil Adjusted Vegetation Index
MSS	Multispectral Scanner
NASA	National Aeronautics and Space Administration
NBC	Naive Bayes Classifier
NDVI	Normalized Difference Vegetation Index
NED	Normalized Euclidean Distance
NIR	Near Infra-red
NIRNDVI	Near Infra-red Normalized Difference Vegetation Index
NOAA	National Oceanic and Atmospheric Administration
OA	Overall Accuracy
OBIA	Object Based Image Analysis
OBS	Optimal Band Selection
OLI	Operational Land Imager
OMIS II	Operational Modular Imaging Spectrometer II
OSAVI	Optimized Soil Adjusted Vegetation Index

OSP	Orthogonal Subspace Projection
PA	Producer Accuracy
PALSAR	Phased Array L-Band Synthetic Aperture Radar
PAN	Panchromatic
PCA	Principal Component Analysis
PLS	Partial Least Square selection
PRISMA	PRecursore IperSpettrale della Missione Applicativa
Proba	PRoject for OnBoard Autonomy
PVI	Perpendicular Vegetation Index
RDVI	Renormalized Difference Vegetation Index
REDD+	Reducing Emissions from Deforestation and Forest Degradation in Developing Countries
Re-NDVI	Red edge Normalized Difference Vegetation Index
Re-SRI	Red edge Simple Ratio Index
RF	Random Forest
RMSE	Root Mean Square Error
ROSIS	Reflective Optics System Imaging Spectrometer
RS	Reflectance Spectra
SADH	Sum and Difference Histogram
SAM	Spectral Angle Mapper
SAR	Synthetic Aperture Radar
SARVI	Soil and Atmospherically Resistant Vegetation Index
SAVI	Soil Adjusted Vegetation Index
SDA	Stepwise Discriminant Analysis
SFF	Spectral Feature Fitting
SFS	Sequential Forward Selection
SID	Spectral Information Divergence
SIR	Shuttle Imaging Radar
SPOT	System Pour l' Observation de la Terre
SR	Simple Ratio
SRTM	Shuttle Radar Topography Mission

SSM	Spectral Similarity Measure
SVM	Support Vector Machine
SVMW	Support Vector Machine Wrapper
SWIR	Short Wave Infra-red
TCIMF	Target Constrained Interference Minimized Filter
TIR	Thermal Infra-red
TIRS	Thermal Infra-red Sensor
TM	Thematic Mapper
TVI	Triangular Vegetation Index
UA	User Accuracy
UNEP	United Nations Environment Programme
UNESCO	United Nations Educational, Scientific and Cultural Organization
UNFCCC	United Nations Framework Convention on Climate Change
UNU–INWEH	United Nations University – Institute for Water, Environment and Health
USGS	United States Geological Survey
UV-B	Ultraviolet-B
VH	Vertical-Horizontal Polarization
VNIR	Visible Near Infra-red
VV	Vertical-Vertical Polarization
YNDVI	Yellow Normalized Difference Vegetation Index

NOTATIONS

°C	degree Celsius
$\Delta\lambda$	bandwidth
cm	centimeter
CO_2	carbon dioxide
m	meter
mm	millimeter
nm	nanometer
O_2	oxygen
ppt	parts per thousand
R^2	coefficient of determination
sq. km	square kilometer
t	tons
t/ha	tons per hectare
t/year	tons per year
US$	US Dollar currency
κ	kappa coefficient
λ	wavelength
ρ	wood density

CHAPTER 1

INTRODUCTION

1.1. Ecology of Mangroves

"Mangroves" is the term used to represent either a single plant or forest community which are salt tolerant woody halophytes generally thrive in the muddy and anaerobic substratum of intertidal regions in tropical and sub-tropical coastlines. It usually lives in the estuarine regions where mixing of fresh and saline water take place. Mangrove environment is characterized by extreme weather conditions such as high temperature, strong winds, turbulent inundation, and saline soil. In order to thrive in such extreme conditions and avoid mortality, it develops some physiological adaptations like specialized root cell membrane to avoid the entry of salts, prolonged tube like breathing structure called pneumatophores, and viviparous seedlings to germinate in parent tree. In earlier times mangroves were thought as unproductive transitional systems, however, now these are recognized as highly productive and viewed as ecologically important ecosystem. Accordingly, mangroves come under various conservation and restoration practices implemented by many government and research organizations.

Mangroves are found in diverse tropical coastal settings. Mangroves survive in the tropical and sub-tropical latitudes where the air temperature of the coldest month does not go below 16°C and the margins of incidence of ground frost, where water temperatures do not exceed 24°C (Gilman et al., 2008). Although mangroves can survive at an air temperature as low as 5°C, they are intolerant to frost. The optimal average sea surface temperature for mangroves growth is 24°C. Mangroves grow well in the tropical areas with an average annual rainfall in the range of 1500mm to 3000mm. High tidal range (12m in Sundarbans) and large amount of fresh water from upstream nourishes the mangrove growth. Though mangroves live in saline environment and adapted to

high salinity, the optimal salinity for survival of healthy mangroves is 28ppt to 34ppt (Aksornkoae, 1993; Duke et al., 1998).

Based on the location, mangroves are broadly classified into six functional types (Lugo and Snedaker, 1974; Woodroffe, 1992) as follows.

1. *Overwash mangroves* – Small mangrove islands formed by tidal washing.
2. *Fringing mangroves* – Formed along the borders of protected shorelines and are more exposed to turbulent waves and tides.
3. *Riverine mangroves* – Found along the creeks and rivers that are often inundated by tides.
4. *Basin mangroves* – Located along interior side of the swamps and drainage depressions.
5. *Hammock mangroves* – Similar to basin type except that they are evolved in more elevated site.
6. *Scrub mangroves* – Dwarf mangroves along flat coastal fringes.

The first three are primary functional types and the remaining are their modified forms (Figure 1.1).
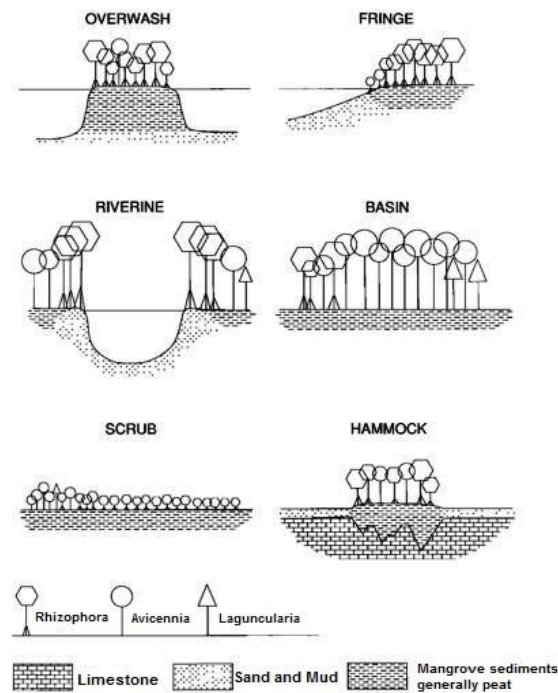
Figure 1.1 Six functional types of mangroves (*Source*: Woodroffe, 1992).

1.2. Distribution of Mangroves

Mangroves are found to be spread in 124 tropical and sub-tropical nations and spatial coverage of mangroves is estimated to be 157,050 sq. km (FAO, 2007). It is also found that about 75% of mangroves are distributed along the coastlines of just 15 nations and most importantly, in Southeast Asian nations. Maximum distribution of mangroves is found to be lying between 5°N and 5°S latitudes which can be categorized into two major realms: the Indo-West Pacific (IWP) realm and the Atlantic Caribbean Eastern Pacific (ACEP) realm (Spadling et al., 2010) where the extensive spatial coverage and rich species diversity are observed (Figure 1.2). Indo-West Pacific region, Australia, Southcentral America, Brazil, and Nigeria are some other important bio-geographical regions where the mangrove species distribution is clearly evident (Alongi, 2002). According to India State of Forest Report (2015) by Forest Survey of India (FSI), total forest cover in the country is 701,673 sq. km where the mangrove covered area is estimated to be 4,740 sq. km, 0.67% of country's total forest cover (FSI, 2015a). According to the habitat and physiological adaptations, mangroves are classified into two broad categories; they are 1) true or exclusive mangroves occur only in core intertidal region (mangal) or only rarely elsewhere, and 2) associate or non-exclusive mangroves typically occur in the landward margin of mangal and often in transition zone between mangrove and other niche such as rainforest, salt marsh, or lowland freshwater swamps. Many epiphytes also grow on mangrove trees; these include an assortment of creepers, orchids, ferns, and other plants, many of which cannot tolerate salt and, therefore, grow only in the mangrove canopy. Still confusion prevails in the exact number of species categorized as "true mangroves" which live in the core areas of mangrove ecosystem. According to different classifications, number of true mangrove species are reported differently in which such categorizations are completely author specific and the number ranges between 54 and 73. The list of mangrove species identified in the world categorized by (FAO, 2007) is given in Table 1.1.
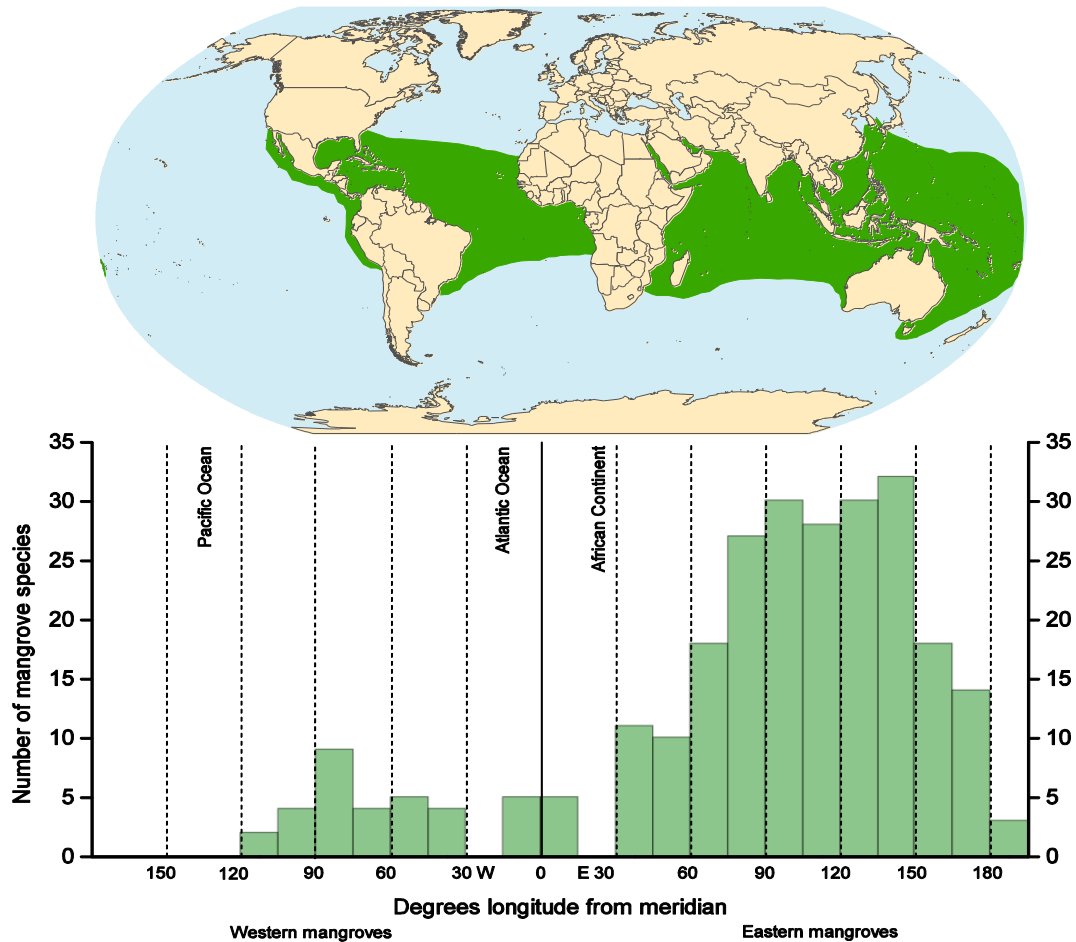
Figure 1.2 Global distribution and diversity of mangroves (*Source*: Tomlinson, 1994).

The abundance and occurrence of mangrove species over space is generally called as "species zonation" and is observed across environmental gradients in many types of ecosystems. There can be monospecific bands of vegetation mostly along the shoreline or along the banks of estuarine water bodies. Generally, gradual pattern of species distribution is seen from the brackish water environment through intertidal flats to the terrestrial environment for each ecosystem. For example, *Rhizophora mangle* occupies coastal/shoreline zone followed by *Avicennia germinans* and *Lumnitzera racemosa* towards landward in Florida mangroves. Contradicting to this, in Queensland and northeastern Australia, mangrove zonation is found to be not only complex but also the relative position of congeneric species is reversed from that of Florida, i.e., *Rhizophora* spp. in landward position and *Avicennia* spp. in the seaward side. In other parts of IWP realm, *Aegiceras*, *Avicennia,* and *Sonneratia* occupy

4

Table 1.1 List of True Mangrove Species as listed by FAO Forestry Report (2007)

Family	Species	Family	Species
Acanthaceae	Acanthus ebracteatus*	Rhizophoraceae	Bruguiera cylindrica*
	Acanthus ilicifolius*		Bruguiera exaristata
	Acanthus xiamenensis		Bruguiera gymnorrhiza*
Avicenniaceae	Avicennia alba*		Bruguiera hainesii
	Avicennia bicolor		Bruguiera parviflora*
	Avicennia eucalyptifolia		Bruguiera sexangula*
	Avicennia germinans		Ceriops australis
	Avicennia integra		Ceriops decandra*
	Avicennia lanata		Ceriops somalensis
	Avicennia marina*		Ceriops tagal*
	Avicennia officinalis*		Kandelia candel*
	Avicennia rumphiana		Kandelia obovata
	Avicennia schaueriana		Rhizophora x annamalayana*
Bombacaceae	Camptostemon philippinensis		Rhizophora apiculata*
	Camptostemon schultzii		Rhizophora harrisonii
Combretaceae	Conocarpus erectus		Rhizophora x lamarckii*
	Laguncularia racemosa		Rhizophora mangle
	Lumnitzera littorea*		Rhizophora mucronata*
	Lumnitzera racemosa*		Rhizophora racemosa
	Lumnitzera x rosea		Rhizophora samoensis
Caesalpiniaceae	Cynometra iripa*		Rhizophora x selala
	Cynometra ramiflora		Rhizophora stylosa*
Euphorbiaceae	Excoecaria agallocha*	Rubiaceae	Scyphiphora hydrophylacea*
	Excoecaria indica	Sonneratiaceae	Sonneratia alba*
Lythraceae	Pemphis acidula		Sonneratia apetala*
Meliaceae	Xylocarpus granatum*		Sonneratia caseolaris*
	Xylocarpus mekongensis*		Sonneratia griffithii*
	Xylocarpus rumphii		Sonneratia x gulngai
	Xylocarpus moluccensis*		
Myrsinaceae	Aegiceras corniculatum*		Sonneratia hainanensis
	Aegiceras floridum		Sonneratia ovate
Myrtaceae	Osbornia octodonta		Sonneratia x urama
Palmae	Nypa fruticans*	Sterculiaceae	Heritiera fomes*
Pellicieraceae	Pelliciera rhizophorae		Heritiera globosa
Plumbaginaceae	Aegialitis annulata		Heritiera kanikensis*
	Aegialitis rotundifolia*		Heritiera littoralis*
Pteridaceae	Acrostichum aureum*		
	Acrostichum speciosum*		

Species highlighted with symbol * are seen in Indian coast (Ravishankar et al., 2004a; Ravishankar et al., 2004b; Spadling et al., 2010; Barik and Chowdhury, 2014).

low intertidal region followed by *Bruguiera* and *Rhizophora* in mid-intertidal region, and *Heritiera*, *Xylocarpus*, and other species in high intertidal region (SmithIII, 1992).

1.3. Importance of Mangroves

Mangrove ecosystems are ecologically and economically important and have many benefits to the human society. Some of the commercial products we derive from mangroves are firewood, tannins, honey, livestock fodder, wood products, roofing, medicinal products, and variety of fishes and prawns. Some of the ecological services are coastal protection from fury of cyclones and tsunamis, screening solar UV-B radiation, minimizing atmospheric carbon and sequestration, prevention of coastal erosion by trapping the sediments by their extensive root system, biomass and litter production, trapping and recycling of nutrients which support the fish and marine wildlife population, maintaining the food web and energy fluxes within, and interaction with neighboring ecosystems. Wells (2006) estimated the summarized economic value of mangrove as US$ 2,000 to US$ 9,000 per hectare per year which shows the economic importance and value of mangroves.

In spite of its economic and ecological services, mangroves often face threats from natural calamities as well as anthropogenic threats. Natural calamities such as storm surges and tsunamis uproot mangrove trees whereas climate change induced sea level rise, increase in salinity, and sea surface temperature degrade mangroves and affect the ecosystem. Anthropogenic impacts include conversion of mangrove forest for agricultural land, housing, aquaculture ponds, over-harvesting of mangrove for timber and fuel, overfishing, soil and water pollution from neighboring human settlements, and alteration of freshwater flow to mangrove ecosystem due to the construction of dams and roads along its path ultimately cause hyper-salinization of mangrove environment.

According to FAO (2007), approximately 35,600 sq. km of mangroves were extinct between 1980 and 2005 which was estimated from the inputs of time-series remote sensing data. Assessing such changes in mangrove forest cover

6

with maximum accuracy becomes possible only with the application of remote sensing technology which is being practiced in the last four to five decades. Monitoring no-net-loss mangrove restoration activities also becomes possible through the analysis of temporal remote sensing data.

1.4. Remote Sensing

Remote sensing is defined as the science or art by which an object, area, or phenomenon can be inferred by a distant device which is not in direct contact with the object under study. It is extensively used in resource inventory and management using aerial surveyed photographs. Since the launch of Earth Resource Technology Satellite (ERTS-1) in 1972, followed by SPOT, IRS satellites, etc., remote sensing has become an important tool for repetitive observation of land and its dynamics (later it is renamed as Landsat Series). There are basic designing parameters for a remote sensor and they are called "sensor resolutions" such as spatial, spectral, radiometric, and temporal resolutions (Joseph, 2005).

Based on the utilized spectral regions, remote sensing strategies can be broadly categorized as follows.

a) *Multispectral remote sensing* analyzes the data acquired in 3 to 10 broad wavelength regions of EMR with a bandwidth approximately ranging between 10nm and 50nm (e.g. Landsat, SPOT, IRS satellites, etc.). Remote sensing data are also acquired in *Panchromatic* mode along with multispectral data with improved spatial resolution,

b) *Hyperspectral remote sensing* data is acquired in hundreds of narrow spectral wavelength regions with bandwidth ranging from 1nm to 15nm (e.g. Hyperion, CHRIS Proba, HyMAP, etc.),

c) *Infra-red remote sensing* processes the data recorded in the infra-red radiation emitted from earth's surface between 300nm and 1,500nm for image acquisition (e.g. NOAA-AVHRR, TERRA-MODIS, ERS-ATSR, etc.),

d) *Microwave remote sensing* analyzes the data acquired in the spectral range of 1mm to 1m. Both passive (microwave radiometers) and active (imaging radars) sensors are operational, however, active microwave sensors are often used due to its capability in the diversified field of applications, and

e) *LiDAR remote sensing* is similar to active microwave remote sensing where image is acquired by transmitting energy in narrow ranges of frequencies or pulses and also measures the backscattered energy to image the earth surface.

Satellite remote sensing has potential applications to extract information about different types of natural and man-made earth resources for its mapping, monitoring, and management. The present study focuses on the potential of hyperspectral remote sensing for mangrove related studies.

1.5. Remote sensing of mangrove ecosystem

Traditional field survey of any natural resources or ecosystem is laborious, time-consuming, and expensive. In addition to that, inhospitable environment in mangrove forest makes the field survey logistically difficult and consumes more money, manpower, and time than usual. Various remote sensing strategies such as aerial photography, optical, thermal, microwave, and LiDAR remote sensing are widely used in continuous, cost-effective monitoring, and surveying of such hostile mangrove environment for the past few decades. Kuenzer et al. (2011) have listed important potential applications areas of remote sensing in mangroves such as mapping and monitoring of area under mangroves, health monitoring, change detection, biomass modeling, nutrient intake modeling, identification of potential area for mangrove restoration, water quality assessment, disaster management, and ecosystem modeling. However, there are many management activities of mangroves such as micro-level vegetation mapping (species mapping), biomass estimation, biochemical, and biophysical characterization which are still highly dependent on manual and expensive field survey. To reduce such expensive and laborious activities, advanced techniques in remote sensing such as hyperspectral, microwave, and LiDAR can be explored.

1.5.1. Potential of Hyperspectral remote sensing

Hyperspectral sensors are actually "imaging spectrometers" which image the surface of the earth and acquire spatial distribution of reflected energy and/or transmitted energy in hundreds of contiguous spectral bands of very narrow bandwidth with a minimum of 4nm. Some of the important operating and upcoming hyperspectral sensors are listed in Table 1.2. The term "hyper" is derived from the Greek and it literally means "over", "above" or "exaggerated amount." Thus, the word "hyperspectral" symbolically represents "more colors." The collected data are often represented as three-dimensional "*hypercube*" where two dimensions represent the spatial dimension and the third represents the spectral bands in which the data are collected (Borengasser et al., 2008). Each pixel in the hypercube can be represented using a continuous spectrum, which is the characteristic of the materials present in that pixel location on the earth surface (Figure 1.3). Hyperspectral remote sensing has become an active area of research in past two decades because of its potential and applicability in the diverse areas such as the detection and discrimination of targets from similar objects (e.g. types of minerals, soil types, different types of vegetation species of a family, water quality, soil quality, etc.). A typical hyperspectral sensor records data between 400nm and 2,500nm and few sensors also record data up to thermal infra-red region (up to 15,000nm).

Higher dimension of spectral information is stored in the hyperspectral data, and compensates the lacuna in the broadband multispectral data when mangroves are concerned. Differences in spectral reflectance among different plant species provided by the contiguous bands can be used for (a) species level classification, (b) biochemical (chlorophyll and carotenoid content estimation), and (c) biophysical characterization (Leaf Area Index, Biomass, etc.). Though hyperspectral data has an enormous amount of spectral information, its analysis has some technical difficulties in deriving useful information out of such voluminous data.
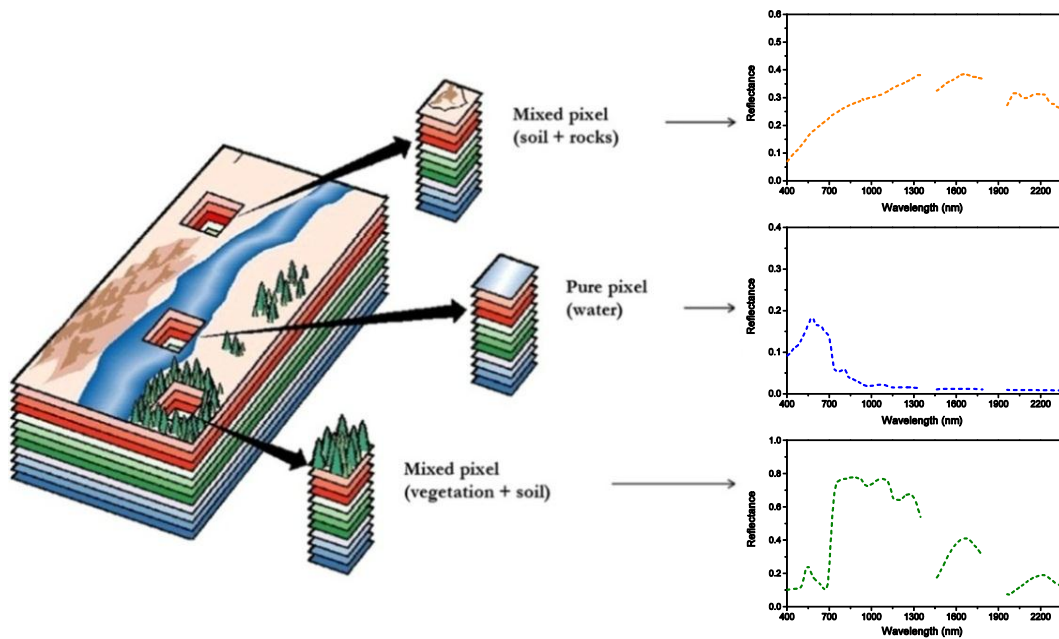
Figure 1.3 The concept of hypercube and spectra derived from various

components present in the scene

(Source: http://remotesensing.spiedigitallibrary.org/article.aspx?articleid=1352324).

1.5.2. Challenges in handling Hyperspectral Remote Sensing Data

As hyperspectral remote sensing data is collected in hundreds of spectral bands, it provides an immense amount of information and a large quantity of data. Extraction of useful information is required for the analysis which is a crucial part in the hyperspectral image analysis. Apart from this, hyperspectral data also possesses multi-collinearity problem due to the redundant information. This confuses a user regarding the selection of bands having the required information for a particular analysis. Some of the common issues in handling the hyperspectral data are as follows.

a. *Computation and Storage*: The handling of higher dimension hyperspectral data requires sophisticated storage and data processing hardware and software. Often data storage capacity may not be affordable for a user and the processing also becomes a problem due to its large size (Thenkabail et al., 2012).

b. *Data Dimensionality*: The dimensionality problem in hyperspectral data is often referred as "the curse of dimensionality." As the number of bands increases, the number of pixels to train the classifiers also increases to maintain classification accuracy. This is popularly known as "Hughes Phenomenon" (Richards and Jia, 2005). The increase in number of training samples, according to the number of bands, is often not possible due to the non-availability of pure pixels in the highly mixed forest environment. To handle this situation, proper dimensionality reduction method is needed to extract only useful information.

c. *Data Redundancy*: As mentioned earlier, information stored in neighboring bands of hyperspectral data is highly correlated. This leads to the multicollinearity problem and can be observed by non-diagonal covariance matrices and wide autocorrelation function (Bioucas-dias et al., 2013).

d. *Noise*: Unlike multispectral data, hyperspectral data is often affected by well-defined atmospheric absorption features because of its finer spectral resolution. Hence, it needs to be calibrated before the analysis (Richards and Jia, 2005)

The above mentioned limitations make the analysis of hyperspectral data more complex analytical procedure than conventional multispectral image analysis. Contemporary methods developed for hyperspectral data analysis address such limitations and effectively process data to derive useful information.

1.6. Research Gaps and Motivation

As mentioned in Section 1.5, there are many unexplored research areas in the context of conservation and management of mangroves that can very effectively be supported through the applications of advanced remote sensing techniques.

Table 1.2 List of some of the Operating and Upcoming Hyperspectral Sensors and their Specifications

Sensor	Agency	Platform	Altitude (km)	Spectral Range (nm)	Number of spectral bands	Spectral Resolution (nm)	Spatial Resolution (m)
AVIRIS (1986)	NASA – JPL	Airborne	20	400 – 2500	224	10	4 to 20
ROSIS (1992)	DLR	Airborne		430 - 860	115	4	< 1
DAIS 7915 (1995)	GER Corporation - DLR	Airborne		430 - 12300	79	15	3 to 20
Hyperion (2000)	NASA	EO - 1 Satellite	705	400 – 2500	220	10	30
CHRIS (2001)	ESA	Proba - 1 Satellite	556	415 – 1050	63	1.3 – 12	18 to 36
IASI (2006)	ESA	EUMETSAT MetOp-A Satellite	817	3620 - 15500 (645-2760 cm^{-1})	8461	0.5 cm^{-1}	V: 1-2 km H: 25 km
HyMap (2008)	HyVista Corp.	Airborne	2 to 5	450 - 2480	128	13 - 17	2 to 10
CASI 1500 (2012)	ITRES Research	Airborne	3	380 – 1050	288	2.2	20
EnMAP (2016)	DLR - ESA	Satellite (Upcoming)	653	420 - 2450	228	6.5-10	30
PRISMA (2018)	ASI	Satellite (Upcoming)	614	400 - 2505	238	10	5 to 30
HISUI (2018)	JAXA	Satellite (Upcoming)	618	400 - 2505	185	10-12.5	30
HypsIRI (2022)	NASA – JPL	Satellite (Upcoming)	626	380 – 2500; 7500 – 12000	217	4 – 12	60

Source: Varshney and Arora (2004), Forzieri et al., (2012), http://www.optoknowledge.com/airborne-pushbroom-vnir-system.html, https://hyspiri.jpl.nasa.gov/, http://www.gfz-potsdam.de/en/section/remote-sensing/topics/optical-remote-sensing/spectroscopy/hyperspectral-sensors/, http://messtec.dlr.de/en/technology/dlr-remote-sensing-technology-institute/hyperspectral-systems-airborne-rosis-hyspex/, https://directory.eoportal.org/web/eoportal/satellite-missions/i/ims-1.

1. Mangroves face threats such as reduction in areal extent and loss in species diversity. Hence, there is a need to regularly map and monitor its species distribution.

2. Mangroves are considered to be the major source of blue carbon sequestration and thus, loss of mangroves and their diversity have the adverse impact on the coastal ecosystems by creating an imbalance in local environment and regional climate. Hence, quantifying the leaf area index, biomass, and biochemical properties of mangrove forest are becoming crucial baseline information in studies related to the global warming and the climate change.

3. Though mapping and monitoring of mangroves in a periodic basis are applicable through multispectral remote sensing, micro-level mapping of mangrove species is still under research because of its inherent limitations. Hence, advanced remote sensing techniques such as hyperspectral and LiDAR remote sensing should be explored for their potential to support the requirements of mangrove management practices.

To address the above-mentioned requirements of mangrove management practices, research initiatives are triggered by the international organizations namely United Nations Educational, Scientific and Cultural Organization (UNESCO), Ramsar Convention on Wetlands, United Nations Environment Programme (UNEP), Food and Agricultural Organization (FAO), United Nations University – Institute for Water, Environment and Health (UNU–INWEH), International Tropical Timber Organization (ITTO), International Union for Conservation of Nature (IUCN), International Society for Mangrove Ecosystems (ISME), ministries and departments of national government, academic and research institutions, and non-government organizations where inventory and assessment through remote sensing are listed as one of the fundamental and crucial activities (MacKay et al., 2009).

In India, multispectral remote sensing data is used to map the national mangroves once in three years and the mangrove community once in ten years (Nayak and Bahuguna, 2001; Ajai et al., 2012). However, mapping the species of

mangroves is limited as far as Indian mangroves are concerned. To map the mangroves at species level, i.e., higher order classification, we need to think beyond the multispectral data. This can be possible by utilizing hyperspectral data with sufficient spectral information about the mangroves present in India, similar to the spectral library of minerals as developed by the United States Geological Survey (Clark et al., 2007). Moreover, we need to frame suitable analytical methods to spectrally discriminate the species identified from in-situ spectral data as well as satellite data (Schmidt and Skidmore, 2003; Manevski et al., 2011; Koedsin and Vaiphasa, 2013). This process is still under research as far as Indian mangroves are concerned.

1.7. Objectives of the Study

With the research gaps identified in Section 1.6, the present study aims at achieving the following objectives which can be a stepping stone in the field of hyperspectral remote sensing in the context of effective and efficient management of Indian mangroves. Our research objectives in this thesis are as follows.

1) Development of spectral library for true and associated mangrove species of India.
2) Investigation of spectral separability among species using multiple statistical approaches, spectral transformation, and different dimensionality reduction methods.
3) Classification of multispectral and hyperspectral satellite data for mapping mangroves at micro level, i.e., species level using single classifiers and Multiple Classifier System (MCS).
4) Biophysical characterization of mangroves using high spatial resolution multispectral satellite data.

1.8. Organization of the Thesis

Remaining of the thesis is organized as follows.

- **Chapter 2** presents a detailed literature review of applications of different types of remote sensing for mangrove monitoring and conservation in the global and Indian scenarios. It also discusses the research gaps in this field of research and highlights potential contributions of this thesis to fill the gaps.

- **Chapter 3** addresses the sampling, collection, and post-processing methodologies adopted for the development of the spectral signature library of 34 true and associated mangrove species present in Bhitarkanika National Park and Godavari Wildlife Sanctuary, east coast of India.

- **Chapter 4** investigates statistical significance in the context of separability of spectral signatures among the members of mangrove family *Rhizophoraceae* using multiple statistical procedures and dimensionality reduction methods. The methodology is then extended to 34 species to investigate the separability.

- **Chapter 5** shows the application of single classification algorithm and multiple classifier systems in analyzing the multispectral (IRS P6 LISS III and Landsat 8 OLI) and hyperspectral (EO-1 Hyperion) satellite data to enhance the accuracy of species-level classification of mangroves for Bhitarkanika National Park.

- **Chapter 6** explores the potential of high spatial resolution multispectral WorldView-2 data to model and estimate mangrove biomass in Bhitarkanika National Park by integrating biophysical data, collected from the field samples.

- **Chapter 7** summarizes the research contributions. It also gives future directions of research when application of remote sensing for the mangrove ecosystem is concerned.

CHAPTER 2

REVIEW OF LITERATURE

Mangroves are the evergreen forests which are distributed in the coastal region of tropical countries. Similar to other natural resources, coastal resources including mangroves, marsh, backwaters, coral reefs also experience threats such as mass clearance, degradation, pollution, creation of adverse environment from different directions due to the recent regional and global developmental activities. To overcome such threats various sustainable management measures are being devised which need primarily the assessment of coastal resources. Remote sensing technology is the cost effective method of resource assessment and monitoring with more accuracy than traditional field survey methods. Recent advancements in remote sensing technology enable us to extract more information about the various aspects of earth resources including mangroves in an efficient manner. This chapter reviews the status of global mangroves, their importance, threats, management measures, application of remote sensing for mangrove management in general. Later this chapter deals with the literature reviewed in the hyperspectral remote sensing for assessing the vegetation diversity and biophysical properties of mangrove forests along with Indian scenario which justifies the motivation and objectives of the study.

2.1. Global status on mangrove research

2.1.1. Mangrove Ecosystem and Plant Diversity – An Overview

"Mangroves" are salt-tolerant woody halophyte plants or trees generally live in a swampy environment of tropical and sub-tropical coastlines generally in regions with daily tidal inundations. Because of the extreme weather conditions prevailing in mangrove environment, mangroves develop several physiological and biological adaptations for its survival which make this ecosystem unique from other terrestrial and coastal ecosystems. Generally, mangrove environment serves as a suitable habitat for several flora and fauna associated with them which

attracts researchers all over the world to understand and study the mangroves (Tomlinson, 1994; Kathiresan and Bingham, 2001).

As per the framework of the Global forest cover assessment documented by Food and Agricultural Organization (FAO) in the year 2007, the spatial coverage of mangroves is 152,000 sq. km spread across 124 tropical and sub-tropical nations which is estimated by compiling the spatial coverage from different data sources (FAO, 2007). Giri et al. (2011) used GLS 2000 mosaics prepared from Landsat archive images acquired from the year 1997 to 2000 and prepared the global distribution map of mangroves at a resolution of 30m. They estimated that the spatial coverage of mangroves as 137,760 sq. km in 118 nations. It is also found that about 75% of the mangroves are distributed along the coastlines of just 15 countries and most importantly in Southeast Asian countries. Generally, the global distribution of mangroves is divided into two major regions: Indo-West Pacific (IWP) or "Old world" and Atlantic–Caribbean–East Pacific (ACEP) or "New world". Considering the genetic and species diversity, IWP is considered to be more diverse (23 genera and 58 species) when compared with that of ACEP (7 genera and 12 species). Only one species, *Acrostichum aureum*, a mangrove fern is common in both regions. Even though mangroves are generally confined to tropical latitudes, some species of *Avicennia* occurs in high latitudes in some temperate areas such as southern Australia and New Zealand. Two generas, *Avicennia* and *Rhizophora* occur in both regions and the mangrove palm *Nypa* is widely seen in IWP region and their fossil records could be found in ACEP region (Duke, 1992; Ricklefs and Latham, 1993; Hogarth, 2007).

As far as the geographic realms of mangrove distribution are concerned, the major proportion of global cover goes to South-East Asia (33.5%) followed by South America (15.7%), North and Central America (14.7%), West and Central Africa (13.2%), South Asia (6.8%), Australasia (6.7%), East and South Africa (5.2%), Pacific Ocean (3.8%), Middle East (0.4%), and East Asia (0.1%) (Spadling et al., 2010). According to Tomlinson (1994), 110 species are identified as mangroves in which only 54 species from 20 genera of 16 families are considered to be "true" mangrove species and remaining species are categorized

18

as "associated" species as they occur mostly in transition zone between marshy lands of true mangroves and terrestrial ecosystems. He categorized true mangroves into two components such as (i) Major component (34 species in 9 genera and 5 families) and (ii) Minor components (20 species in 11 genera in 11 families) based on their physiological adaptations and development of root system.

Table 2.1 The global distribution of mangrove genera and species in two major geographical regions as given by Ricklefs and Latham (1993)

Genera	ACEP	IWP
Avicennia	3 species	4 to 6 species
Rhizophora	2+1 hybrid	3+2 hybrid
Laguncularia / Lumnitzera	1 species	2 species
Nypa	Paleogene fossil	1 species
Wetherellia	Paleogene fossil	
Pelliciera	1 species	
IWP endemics		14 genera, 32 species
Total	4 genera	17 genera
	7 species	40 to 42 species

Mangroves are considered to be the most productive ecosystem in the world due to its complex survival capability through self-adaptation, habitat hosting, and diverse range of flora present in the community. The mangrove ecosystem acts as breeding and feeding ground for large varieties of fishes, mollusks, crustaceans, and other related fauna. Therefore, mangroves are credited for its autotrophic nature which helps to maintain coastal food chain (Alongi, 2002). Considering the ecological value of mangroves, they produce phenols and flavonoids which act as a screen against the solar UV-B radiation and produce UV-free under canopy environment (Moorthy and Kathiresan, 1997). Utilizing the advantage of having strong network of complex aerial root system, mangroves act as a potential natural shield for coastal community against the storm surges, tsunamis, and coastal erosion and improves sedimentation of silt and soil by trapping them from the water column along deltaic regions (Badola and Hussain,

2005; Danielsen et al., 2005; Alongi, 2008). Mangroves are often credited for its efficiency in the absorption of CO_2 from the atmosphere thereby reducing the Green House effect. It is been reported that the CO_2 fixation of mangroves per unit area exceeds what phytoplankton fix in tropical oceans. Even though mangroves occupy only 0.5% of the global coastal area, they store 10% to 15% of carbon (2.4×10^7 t/year) in coastal sediment (Kathiresan and Bingham, 2001; Alongi, 2014). According to Spadling et al. (2010), the total above ground biomass of global mangroves is estimated to be 3.7×10^9 tons (t) of carbon and annual sequestration of organic matter in mangrove sediments ranges between 1.4×10^7 t to 1.7×10^7 t of carbon. Therefore mangroves are regarded as great "Carbon Sinks" due to its ability to sequestrate carbon better than terrestrial ecosystems and has a huge impact on global carbon budget (Bouillon et al., 2008; Kristensen et al., 2008; Nellemann et al., 2009; Ellenbogen, 2012; Alongi et al., 2015). The carbon storage capacity of Indo-Pacific mangroves is estimated to be 1.023×10^3 t/ha (Donato et al., 2011; Murdiyarso et al., 2015). It is been reported that there was a net loss of about 38×10^7 t of carbon stored in mangrove biomass due to the loss of about 35% of mangroves in the world in past decades (Cebrian, 2002). Alongi (2014) estimated the loss of carbon storage due to mangrove deforestation as 9 to 97×10^7 t/year which is much higher than their annual carbon sequestration.

The mangroves are considered to be the most important coastal resource as they provide valuable commercial products such as fisheries, medicinal products, aquaculture seeds etc. Mangroves are such a productive ecosystem which provides US\$ 1.6 billion each year from its ecosystem services and coastal livelihood support in the global level. Because of that, anthropogenic disturbances are often experienced and mangroves are often cleared for activities such as coastal zone development, conversion to aquaculture and shrimp ponds, logging for timber, and fuel. The loss of mangroves leads to drastic consequences in the coastal environment such as coastal erosion, increase in soil salinity, the decline in fisheries etc. (Huitric et al., 2002; Danielsen et al., 2005). Due to its vulnerable location and its commercial value, mangroves are often exposed to deterioration. Valiela et al. (2001) stated that about 35% of mangrove forest was lost worldwide

in 1980's and 1990's. Since 1980, the annual loss of mangrove cover was about 3,000 sq. km which resulted in overall loss rate of about 2.1% per annum. According to FAO (2007), approximately 35,600 sq. km of mangrove cover was lost between 1980 and 2005. The annual rate of depletion of mangroves was estimated to be 0.66 % in 2005 and this loss is almost three to five times to the rate of loss of global forest cover. This rate of mangrove forest loss was so alarming that it exceeded the loss of other ecosystems like rain forest, coral reefs etc., which clearly states that the mangroves are "most threatened" ecosystem and depleting fast. Due to the continuous decline in mangrove areas, the species richness is also expected to decline (Duke et al., 2007). Threats to mangroves range from nature influenced climatic changes to anthropogenically influenced disturbances. Some of the climatic factors influencing the decline of mangroves are sea-level rise, storms, low precipitation, high temperature, adverse response from adjacent coastal ecosystems (such as coral reefs, seagrass, estuaries etc.), and changes in ocean current pattern (Gilman et al., 2008). Anthropogenically, the deforestation of mangroves for shrimp farming and aquaculture activities lead to the massive depletion of mangrove which eventually lead to 0.08 to 0.48 x 10^9 t CO_2 e yr^{-1} (carbon dioxide emission per year) or 10% of the total global emission from tropical deforestation (Murdiyarso et al., 2015).

So to conserve the mangroves from such natural and anthropogenic threats, many studies and steps were taken up by researchers and ecological experts. The restoration of mangrove areas in past decades has been successful to a certain extent. One of the important steps taken towards the wetland ecosystem restoration activities was "Ramsar Convention of Wetlands" (http://www.ramsar.org/), an intergovernmental treaty by which the sustainable conservation of global wetlands and their resources would be conserved by imposing laws and seeking International cooperation. Most of the wetlands have been included under this treaty and their conservation activities are under international attention (Kuenzer et al., 2011). However, it is recommended that no-net-loss mangrove restoration in global level requires mass restoration through the involvement of government and local community using common ecological and engineering approaches such as site selection, species selection, artificial

regeneration etc. (Kairo et al., 2001; Bosire et al., 2008). This required continuous mapping and monitoring of restored mangroves which demands periodic cost-effective and less laborious survey of mangroves. In such scenario, remote sensing plays a major role in mangrove assessment which has become inevitable in current management practices.

2.1.2. Remote Sensing of Mangroves

Since early 1980's, remote sensing has become popular by its broad application in various fields of research including environmental monitoring and conservation management eventually replaced traditional field surveys which were laborious, inhospitable, logistically difficult, time-consuming, and expensive and become popular since the early 1980's. Temporal monitoring of inhospitable mangrove environment using multi-platform remote sensing data such as aerial photographs, multispectral, hyperspectral, microwave, and LiDAR (Light Detection And Ranging) were found to be successful, cost-effective, and efficient in the different levels of management of mangrove ecosystem in the last four decades. Using these datasets, various aspects of mangroves were extracted using number of analytical approaches primarily for mapping the distribution, change detection, time series analysis, health status monitoring, field survey planning, biomass estimation, tree crown delineation, invasive species identification, anthropogenic impact assessment, ecosystem evaluation, planning, monitoring and management of conservation, and restoration practices. The following sections give a detailed description of *global scenario* of studies dealt with applications of various remote sensing techniques in different areas of mangrove ecosystem management.

2.1.3. Mapping and monitoring of mangrove ecosystem using Remote Sensing techniques

Mapping mangroves at different floristic hierarchical level are possible using diverse remote sensing methods available. Kuenzer (2011) has pointed out some prevailing challenges in mapping the mangroves. They are,

- As the mangroves live in the intertidal region, the image scene is highly influenced by seasonal and diurnal tides and it causes the radiometric correction a difficult task. Moreover, the spectral reflectance obtained from the image pixel would be a combination of vegetation, soil and water in fringing and open mangroves.
- The mangroves generally occur mixed in many parts of the ecosystem which make the analyst a difficult job to identify pure pixel for unique species / community.

Green et al. (1996) reviewed the application of remote sensing in tropical coastal resource management. He opined that there are certain factors such as cloud cover, sensor specifications, the difference in mapping scale, lack of real-time data, and confusion in selecting appropriate datasets also has a major influence in mangrove mapping. Although over a period of time many of the limitations he pointed out in his review were solved, certain practical and user management related problems are still prevailing and need special attention.

2.1.3.1. Aerial Photography

Aerial photography has been a prominent source of the remote sensing image for mapping individual patches of coastal vegetation but comparatively less number of such studies were made as far as mangroves are concerned. This is primarily due to the wide usage of spaceborne sensors for mapping purposes. Still there are some prominent studies which need to be pointed out.

The damage caused to black mangroves (*Avicennia germinans*) in lower Texas Gulf coast due to hard freeze in the years 1983 and 1989 were mapped using Colour Infra-Red (CIR) aerial photography and video imagery along with

spatial information recorded. Results of these studies concluded that the damaged black mangroves were able to be distinguished by these imageries (Everitt and Judd, 1989; Everitt et al., 1991; Everitt et al., 1996). Manson et al. (2001) estimated the extent of mangroves using multiple sources such as topographic maps, aerial photographs, and Landsat images in two regions, the Joseph Bonaparte Gulf and the Embley River on Cape York Peninsula in northern Australia. Aerial panchromatic photographs, Geographic Information System (GIS), and ground truth data were used to assess the status of mangroves in Kiuga Marine Protected Area, Kenya including their standing volume of productive and non-productive mangroves and infer that the information derived would be used for potential exploitation for sustainable development (Kairo et al., 2002). In Sri Lanka, three mangrove forests were mapped at genus level using aerial photographs with the help of visual interpretation method. Though the methodology adopted could successfully map mangroves, it lacks applicability to other mangrove ecosystems with different species combination (Verheyden et al., 2002).

Sulong et al. (2002) used the combination of 160 aerial photos taken at a scale of 1:5,000 and Landsat TM imagery (30m) to map mangroves in Kemaman district, Malaysia. He analyzed aerial photographs using visual interpretation keys with the help of field data and Landsat image using digital image processing method. They could identify 14 mangrove forest types in aerial photos with an accuracy of 92.7% whereas only 5 mangrove forest types were identified in Landsat image with an accuracy of 87.8%. Time series analysis to map the extent and height of mangroves along West Alligator River in Northern Australia was studied using stereo aerial photographs and Digital Elevation Models (DEM). They found that in 41 years there was a landward extension of saline condition primarily due to sea level rise (Lucas et al., 2002). Dahdouh-Guebas et al. (2002) investigated the change in extent of mangroves and shrimp ponds in Pambala-Chilan Lagoon complex, Sri Lanka using aerial photographs (1:20,000 scale) and periodical field surveys to produce land use change map for the time period of 1994 to 1999 in GIS environment and found that over this period of time, 0.11 sq. km of mangroves were removed for shrimp farming. Spatio-temporal variation of

mangrove cover in Moreton Bay, Australia between the time period of 1973 and 1997 was analyzed using aerial photographs of 1:25,000 scale and classified mangroves into six broad classes (Manson et al., 2003). The coastline change and mangrove forest dynamics in Sinnamary Estuary of French Guiana was investigated by Fromard et al. (2004) using aerial photographs, SPOT (System Pour l'Observation de la Terre) images, and field surveys for the time period of 1951 to 1999 and proposed a global scenario of mangrove forest dynamics including a model of forest development, forest gap processes, and sedimentological dynamics. Benfield et al. (2005) mapped the change in the extent of fringing mangrove species (*Laguncularia racemosa*) due to the construction development in Punta Mala Bay in Panama using aerial photographs of scale 1:25,000 acquired for the years 1980, 1992, 1997, and 2002 by visual interpretation. Nowadays aerial photographs are used to validate the mapping carried out using satellite images. True colour aerial photographs of Moreton Bay, Australia were used to validate the accuracy of mangrove maps produced from the classification of different datasets such as Landsat TM (Thematic Mapper), ALOS AVNIR-2 (Advanced Land Observing Satellite - Advanced Visible and Near Infrared Radiometer - 2), WorldView-2, and LiDAR data (Kamal et al., 2015).

Aerial photographs have been widely used to map the extent of mangroves and associated land cover features. Though they have high resolution, as satellite data became available, usage of aerial photographs is now reduced. Rather they are used for validation and enhancement of classification accuracy. The visual interpretation method was mostly used to analyze the data which requires local knowledge and used for location-specific mapping, monitoring, and management of mangrove ecosystem at the micro level.

2.1.3.2. Multispectral Remote Sensing

The advancement in space technology and frequent availability of medium resolution data from satellites like Landsat, SPOT, IRS (Indian Remote Sensing Satellites), ASTER (Advanced Spaceborne Thermal Emission and Reflection Radiometer) have made the regional mapping of mangroves an easy job and helped in monitoring the resources and regular management activities for the

sustainable development in the last three decades. Most of the medium resolution multispectral data were used for delineation of mangroves from other land use/ land cover types and change detection analysis.

Jensen et al. (1991) correlated the vegetation indices such as Simple ratio (SR), Normalized Difference Vegetation Index (NDVI), Green Vegetation Index (GVI) and Perpendicular Vegetation Index (PVI) derived from SPOT-XS multispectral data of Marco Island in Southwest Florida with the mangrove canopy cover and found that of all vegetation indices derived, NDVI has higher correlation with plant canopy closure with correlation coefficient of 0.91. Mangrove cover in wetlands of Southern Gulf of Carpentaria in Australia was identified using Landsat TM image and their spatial extent was calculated to be 66.25 sq. km (Long and Skewes, 1996). Gao (1998) used pixel-based classification algorithms such as Minimum Distance (MD) and Maximum Likelihood Classification (MLC) to distinguish dense and sparse mangroves along with seven other land cover classes in Waitemata Harbour of Auckland in New Zealand using SPOT multispectral data with overall accuracy of 72.5% and 63.3% for tall and sparse mangroves. Landsat MSS and TM data were effectively used to identify the temporal changes in the land cover associated with the mangroves using unsupervised classification method such as ISODATA (Kovacs et al., 2001), supervised classification (Muttitanon and Tripathi, 2005; Long et al., 2014) and object-based classification methods (Ruiz-Luna and Berlanga-Robles, 1999). Giri and Muhlhausen (2008) also classified Landsat (MSS, TM, ETM+) and ASTER data to detect mangrove cover change for the time period of 1975 to 2005 in three wetlands of Madagascar and found that there was a loss of 7% of mangrove cover over the period of time mainly due to conversion to agriculture, logging, aquaculture and urban development and the spatial coverage in 2005 was estimated to be 2,797 sq. km. Mangroves in United Arab Emirates (UAE) between Dubai and Abu Dhabi was classified using SPOT-4 HRVIR (High-Resolution Visible Infra-Red) and TERRA ASTER data using Minimum Distance, Maximum Likelihood, and Mahalanobis classification methods and concluded that SPOT-4 HRVIR data (20m) proves at least as efficient as TERRA ASTER data (15m), in spite of a slightly finer ground resolution and the great

number of channels of ASTER (Saito et al., 2003). The mangrove forest and associated land cover changes between 1968 and 2003 in Cai Nuoc district, Vietnam was investigated using topographic maps, aerial photos from 1968 and 1992, SPOT-4 images for the year 1997/98, and Landsat ETM+ image for the year 2003 and identified 15 land use / land cover types including 5 mangrove forest types under 6 major land cover categories and estimated that 75% of mangrove area was lost during the time period of 1968 to 2005 mainly due to conversion into agricultural land and shrimp ponds (Binh et al., 2005).

The recent advances like fine resolution multispectral data such as IKONOS, QuickBird and Worldview and recent classification algorithms such as Object Based Image Analysis have refined the classification accuracy of mangroves further.

Mangroves of Danshui estuary, Taiwan was found increased about 0.55 sq. km during the time period of 1995 to 2004 when SPOT, Landsat, and QuickBird satellite images of the study area were classified using Maximum Likelihood Classification (MLC) (Lee and Yeh, 2009). Global Land Survey (GLS) 2000 mosaic data and 1000 archived Landsat scenes of the time period 1997 to 2000 were used to estimate total area of mangrove cover in the year 2000 as 137,760 sq. km in 118 countries (Giri et al., 2011). Vo et al. (2013) has detected the clearing of mangroves for shrimp farming activities in Mekong Delta, Vietnam by implementing a new method called multi-resolution segmentation and classification using a decision tree approach to analyze SPOT 5 image. They successfully detected mixed aquaculture-mangrove land cover in mono-cultivation areas with higher accuracy (more than 75%). Multi-temporal Landsat (TM, ETM+ and OLI) data for the time period of 1989 to 2015 were classified using MLC and SVM (Support Vector Machines) to find the changes in mangrove cover of Iskandar Malaysia (IM), Southern Johor, Malaysia and found that MLC outperformed SVM in delineating mangroves and it is found that 67.4 sq. km of mangrove were lost from 1989 to 2014 (Kanniah et al., 2015).

2.1.3.3. Hyperspectral Remote Sensing

Hyperspectral Remote Sensing is otherwise called as imaging spectrometry as it combines two sensing modalities, imaging and spectrometry. Normally the spectral wavelength range of 400 to 2500nm is used in imaging spectrometry technique which typically acquires images in more spectral bands in a narrow bandwidth approximately ranging from 0.5 to 25nm. The fundamental property that we derive from hyperspectral remote sensing is spectral reflectance or spectral signatures. These signatures are unique like fingerprints of human and it varies for each material on earth's surface. This difference in reflectance properties among materials has made the hyperspectral remote sensing, a potential technique for identifying the intricacies in micro-level in earth observation. Contrary to multispectral remote sensing, hyperspectral remote sensing provides data in contiguous bands but in nominal spatial resolution.

Applications of Hyperspectral Remote Sensing Data

Because of its diverse application potentiality, hyperspectral remote sensing data has become an active area of research in past two decades and the number of scientific work published using hyperspectral data increases exponentially (Bioucas-dias et al., 2013). Some of the important areas of hyperspectral remote sensing applications are summarized below.

a. Archaeology and Forensic Sciences: Hyperspectral imaging has become an important area in retrieval of hidden and/or weathered information from archaeological sites, rock and metal imprints, palimpsest etc. (Rapantzikos and Balas, 2005; Salerno et al., 2007; Joo Kim et al., 2011; Liang, 2012) and also useful in analyzing the crime scene in a non-destructive and non-contact way (Edelman et al., 2012).

b. Atmospheric calibration: Here, the hyperspectral data are primarily used for the retrieval of atmospheric characteristics such as estimation of columnar water, aerosol concentration, CO_2 and O_2 concentration etc. for sensor calibration (Gao and Goetz, 1991; Curran, 1994).

c. Environmental Monitoring: Hyperspectral imaging is actively used in monitoring of environmental pollution caused due to mining, its impact on local vegetation, introduction of invasive plant species (Ferrier, 1999; Underwood, 2003; Borengasser et al., 2008; Choe et al., 2008; Zhang et al., 2012).

d. Food Safety and Pharmaceutical Industry: Hyperspectral Imaging is used in food processing industry and pharmaceutical industry for quality assessment and management (Hamilton and Lodder, 2002; Gowen et al., 2007; Díaz et al., 2011).

e. Geological Applications: The recent advances in sensor technologies have led the hyperspectral remote sensing a handful of applications in the study of minerals, rocks and soils. Hyperspectral imaging helps in identifying minerals in the rocks from lunar and martian analog sites which eventually helps to study the planetary mineral composition and their evolution (Brown et al., 2005; Ting-ting, 2012; van der Meer et al., 2012).

f. Hazards and Disaster Management: Hyperspectral remote sensing is used for monitoring the naturally as well as anthropogenic induced calamities such as forest fires, deforestation, water pollution, chemical plumes in atmosphere, soil salinity etc. (Gurram and Kwon, 2010; Hirsch and Agassi, 2010; Manolakis et al., 2014).

g. Military and Defense: Hyperspectral remote sensing particularly operating in thermal IR region helps to identify camouflaged military drones and vehicles and helps in surveillance of buffer zones between nations (Bongiovi et al., 1996; Hackwell et al., 1996; Manolakis et al., 2003).

h. Vegetation Mapping and biodiversity monitoring: Species level mapping, biomass characterization, health status monitoring, precision agriculture, biochemical and biophysical characterization of vegetation are some of the application areas of hyperspectral remote sensing in vegetation (Thenkabail et al., 2000; Gupta et al., 2006; Govender et al., 2007; Rao et al., 2007; Stagakis et al., 2010; Nidamanuri and Zbell, 2011; Thenkabail et al., 2012; Thenkabail et al., 2013).

Unlike multispectral data, in hyperspectral systems, the reflectance acquired in narrow contiguous bands provide the analyst with very peculiar information in relation with the leaf biochemical and biophysical characters which could be utilized to characterize the wetland ecosystem such as species discrimination, plant health monitoring, nutrient intake characterization, invasive species monitoring etc. Conventional image processing techniques were not sufficient to handle such voluminous heterogeneous hyperspectral data. So new image processing algorithms were developed to derive useful information in an efficient manner.

Clark et al. (1997) first tested the mapping of the tropical coastal environment using the then new hyperspectral sensor, Compact Airborne Spectrographic Imager (CASI) to quantify habitat extent and composition, water depth, seagrass biomass, mangrove canopy cover etc. of Cockburn Harbour, South Caicos Island of British West Indies. Images from three sensors (Landsat TM, SPOT XS and CASI) were used for distinguishing mangroves of Turks and Caicos Islands at species level using different processing methods (NDVI, band ratio and PCA) followed by supervised and unsupervised classification methods. Results showed that though CASI outperformed other two multispectral sensors and distinguished mangroves and non-mangroves (96% overall accuracy) and nine mangrove habitats (85% overall accuracy) in single stands, it was unable to distinguish among mangrove species in mixed stands (Green et al., 1998). Temporal monitoring of mangroves of Port Hedland, Australia using in-situ spectral signature collected and airborne HyMap data was carried out to quantify and map iron oxide dust sediment on mangrove leaves (Ong et al., 2001). EO-1 Hyperion data (242 bands; 400 to 2500nm; 30m resolution) was classified using SAM to discriminate mangroves from casuarina forest. Prior to that, noisy bands were removed using Minimum Noise Fraction (MNF) followed by endmembers collection using Mixed Tuned Matched Filtering (MTMF) from mixed pixels to overcome coarse resolution of Hyperion (Demuro and Chisholm, 2003). Hyperspectral data have been used in micro-ecological studies of mangroves as well such as Airborne DEDALUS image scanned in the thermal band (8500 to 13000nm) was used for a large-scale survey of potential mosquito breeding sites

covered by a canopy of mangrove and salt marsh in Lake Coombabah, Australia (Dale et al., 2005).

Empirical Line method was used to calibrate airborne AISA+ data (244 bands; 400 to 970nm) acquired over South Padre Island, Texas, USA, by converting that into percentage reflectance and classifying four different land cover types. They suggested that calibrated data may be appropriate to discriminate coastal mangrove vegetation from other land use / land cover types (Jensen et al., 2007). Yang et al. (2009) analyzed AISA+ imagery acquired over two sites of South Texas Gulf Coast, USA to map black mangroves and concluded that airborne hyperspectral data combined with image transformation and classification techniques is efficient to monitor and map mangrove distribution in coastal environments. Literatures related to the application of hyperspectral data for species level classification for mapping and monitoring of mangroves is reviewed in detail and given in Chapter 5.

2.1.3.4. Field spectrometry for mangrove species discrimination

Ground truth data is the vital information for any type of satellite remote sensing for its accuracy. While categorical and qualitative ground truth data is used for multispectral data analysis, the accuracy levels of hyperspectral image analysis are increased by in-situ spectral data collected using spectroradiometer for the discrimination of features having a similar response to the light energy (spectral characteristics) such as minerals, vegetation types, soil and water quality parameters.

Field spectrometry is the technique which is used to quantify the radiance, irradiance, transmission/reflectance from various earth surface features in field condition (Jackson et al., 1980; ASD, 2001). It is being actively used in last two decades in forestry and vegetation sciences for species identification, classification, health status monitoring, nutrient intake estimation, invasive species monitoring etc. Several site-specific spectral libraries were collected so far for various species including, non-native species (Underwood, 2003), wetland species (Zomer et al., 2009), Mediterranean species (Manakos et al., 2010),

shrubland species (Jiménez and Díaz-Delgado, 2015), coral reefs (Kutser et al., 2006), and agricultural crops (Datt et al., 2003; Rao et al., 2007; Nidamanuri and Zbell, 2012). Even though old studies had reported that there was no unique spectral signature for certain crops (Price, 1994; Cochrane, 2000), recent studies revealed that for certain agricultural species, unique spectral reflectance existed during phenological stage which had more control over the resultant spectra rather than inter-seasonal variation (Dehaan and Taylor, 2003; Andrew and Ustin, 2006; Nidamanuri and Zbell, 2011). Considering mangroves, the studies related to spectral library development are limited (Vaiphasa et al., 2005; Kamaruzaman and Kasawani, 2007b; Wang and Sousa, 2009; Manjunath et al., 2013; Zhang et al., 2014).

Vaiphasa et al. (2005) have collected laboratory spectral signatures of 16 tropical mangrove species in AoSawi, Chumporn Province of Thailand in the wavelength range of 350 to 2500nm and investigated the spectral discrimination properties. Similar study was carried out by Kamaruzaman and Kasawani (2007a) for five mangroves species in Tok Bali, Kelantan and Setiu, Terengganu in Malaysia using their field spectral data collected in the wavelength range of 350 to 1050nm by implementing canonical stepwise discriminant analysis and Student's T test to identify statistically significant bands for mangrove species discrimination. The spectral separability of three mangrove species of Punte Galeta, Panama was derived using their laboratory spectral signatures by applying one-way ANOVA test followed by Linear Discriminant Analysis (LDA) for classification of mangrove species (Wang and Sousa, 2009). A different type of analysis was performed by Zhang et al. (2014). He collected laboratory spectral signatures from the leaves of three mangrove species under degraded and healthy conditions in the coastal lagoon of Mazatlán in the Mexican State of Sinaloa and used squared correlation coefficient (R^2 plot), principal components analysis (PCA), and stepwise discriminant analysis (SDA) to identify optimal wavebands for the mangrove classification. In all these studies, spectra were investigated using parametric statistical analysis for the identification of significant wavelengths for spectral discrimination and then followed by feature reduction algorithms to identify optimal bands for classification.

2.1.3.5. Microwave Remote Sensing

Analysis of microwave remote sensing data for mangrove studies are very few and they are often combined with multispectral and hyperspectral data for mangrove mapping. The most important property of microwave data is that it is not prone to cloud cover, haze, and other atmospheric disturbances and this property makes it suitable for mapping mangroves as they locate in tropical and sub-tropical areas. Microwave data were used for mangrove cover mapping, biophysical parameters retrieval, health status monitoring, and biomass estimation. Mostly microwave backscattering data were used for retrieval of biomass characteristics (discussed later in the section 2.1.4 in this chapter) rather than mapping mangroves at the species level.

Wang and Imhoff (1993) applied Santa Barbara canopy backscatter model to model radar backscatter from Shuttle Imaging Radar (SIR-B) from mangrove forest stands of Ganges delta of southern Bangladesh and delineated the flooding boundaries within the stands using radar data with small incidence angles. SIR-C SAR data of Mahajamba Bay, Madagascar was classified using both the L-band associated with two polarizations and the C-band associated with crossed polarization, namely L-VH, L-VV, and C-VH to identify mangrove density and found that the discrimination between wetland is easier when the frequency used is low and the polarization is crossed (Pasqualini et al., 1999). Simard et al. (2002) used JERS-1 Global Rain Forest Mapping (GRFM) and ERS-1 Central Africa Mosaic Project (CAMP) datasets of Gabon Coast and applied Decision Tree classifier and texture mapping to map two mangrove species. In his study, the combination approach improved accuracy to about 18% when compared with single band derived approach. Rocha et al. (2012) used incoherent attributes of multi-polarized Phased Array L-Band Synthetic Aperture Radar (PALSAR) for frequency-based contextual classification to highlight the mangrove areas. The overall classification accuracy were obtained with the use of all the incoherent attributes and the SAR vegetation indices were 80.73% and 80.36% respectively which shows that the use of L-Band SAR data was effective in mapping mangrove areas.

Six mangrove species in Phangnga Bay, Thailand was mapped by classifying combined SPOT optical and JERS-1 radar data using Maximum Likelihood Classification algorithm (Giri and Delsol, 1993). Later Aschbacher et al. (1995) tried to overlay SPOT XS optical data and ERS-1 SAR radar data to exploit advantages of both optical and microwave data for classifying heterogeneous mangrove environment of the same area and concluded that ERS-1 SAR data alone could not discriminate mangroves and non-mangroves. But the combination of ERS-1 SAR and SPOT could identify trees of varying heights and types.

Airborne polarimetric radar AIRSAR data (L and P-band polarimetry; C-band interferometry; 10m resolution) was integrated with airborne hyperspectral CASI data (14 bands; 400 to 1000nm; 2.5m) to classify using Maximum Likelihood Classification (MLC) and Hierarchical Neural Network (HNN) methods to map mangroves and achieved 75% to 80% overall accuracy (Held et al., 2003). The combination of spaceborne hyperspectral Hyperion data and multi-temporal ASAR radar data were used for classification using Maximum Likelihood (MLC), Decision Tree (DT), Artificial Neural Network (ANN) and Support Vector Machines (SVM) classification methods. It is found that the integration of optical hyperspectral and radar data has improved the classification accuracy and among classifiers, ANN gave more accurate and robust estimation (Wong and Fung, 2014).

2.1.3.6. Light Detection and Ranging (LiDAR) Remote Sensing

Since the advent of LiDAR technologies in recent times, only very few studies were conducted in characterizing mangroves when compared to terrestrial forests. Lucas et al. (2008) reviewed the opportunities of integrating high resolution multispectral/ hyperspectral data with LiDAR and derived products to interpret and derive information from SAR and optical data. Further, it helps to parameterize models that simulate and assist understanding of the interaction of electromagnetic energy with forest components. Knight et al. (2009) experimented the use of LiDAR data to map the micro-topography of the intertidal wetland in southeast Queensland, Australia for mosquito management

by identifying potential zones for tidal water stagnation. He derived a high-resolution digital elevation model (DEM) with a vertical resolution of 0.05m from LiDAR data. He concluded that LiDAR data has huge application for understanding and mapping the structure of mangrove wetlands. The distribution of mangroves and other tropical and subtropical vegetation in the Greater Everglades Ecosystem were mapped by integrating the digital terrain model (DTM) derived from LiDAR data and IKONOS multispectral imagery and classified using maximum likelihood classification algorithm and found that the combined data gave 7.1% increase in overall accuracy when compared with that of IKONOS data alone (Chadwick, 2011). Giri et al. (2011) proposed an operational framework based on remote sensing data such as Landsat, Advanced Spaceborne Thermal Emission and Reflection Radiometer (ASTER), hyperspectral, LiDAR, aerial photographs along with field data to monitor the existing, emerging mangrove areas, their disturbance and the regrowth patterns in oil spill-affected areas in Gulf of Mexico. Similar framework was designed to integrate aerial photographs, hyperspectral imagery (EO-1 Hyperion) and LiDAR data to map wetland vegetation of Florida Everglades. The fused data were then classified using an ensemble of three different classifiers (k- Nearest Neighborhood, SVM, and Random Forest) to achieve the most accurate classification map having 11 land use/land cover level vegetation types with an overall accuracy of 91.1% (Zhang et al., 2015).

2.1.4. Retrieval of Biophysical properties of mangroves using Remote Sensing techniques

Remote sensing tools are not only used to map the mangrove cover and their diversity in two dimensions but also used to derive structural properties of the forest cover in vertical profile as well as the leaf properties at micro-level. Different remote sensing techniques were used for the retrieval of biophysical properties such as biomass and Leaf Area Index (LAI), biochemical characteristics of mangroves and other wetland vegetation. Biomass is one of the structural properties of the vegetation and its estimation is one of the essential baseline information needed for climate change mitigation program. Reduction in

biomass is an indicator of vegetation stress induced by natural and anthropogenic causes.

In remote sensing perspective, the retrieval of biomass from satellite data using average stand biomass values and optical data such as aerial photography or satellite images (Landsat, MODIS, IKONOS, QuickBird, WorldView-2 etc.) are widely being done (Kovacs et al., 2004; Proisy et al., 2007; Ji et al., 2010; Zhu et al., 2015; Wicaksono et al., 2016). Later, microwave radar data such as JERS, SIR-C, SRTM etc. have been used to derive forest biomass values (Mougin et al., 1999; Proisy et al., 2002; Kovacs et al., 2006; Li et al., 2007; Englhart et al., 2011; Hamdan et al., 2014). Recent developments in LiDAR remote sensing (ICESat/GLAS, LVIS) is found to be useful in retrieving more accurate measurements of forest biomass (Fatoyinbo and Armstrong, 2010; Chadwick, 2011). Koch (2010) has reviewed the latest developments in different fields of remote sensing for forest biomass mapping with a primary focus on full wave airborne laser scanning, hyperspectral, and polarimetric synthetic aperture radar interferometry. The application of remote sensing data for biomass and productivity estimation in different ecosystems was reviewed and suggested that the unique characteristic of plants is displayed by its reflectance in the red and infrared region of electromagnetic radiation and have a strong relationship with the biophysical parameters of plants (Kale et al., 2002; Klemas, 2013). Literatures related to this topic are reviewed in detail in Chapter 6.

2.2. Remote Sensing of Mangroves – Indian Scenario

Since the launch of India's first remote sensing satellite IRS-1A in 1988 and the advent of high-resolution sensor technologies, the application of remote sensing has spread across various fields of application especially in natural resource management. India has now a handful of operational high resolution optical multispectral and microwave satellites which are being used in environmental monitoring, change detection analysis and biodiversity conservation activities. As far as mangroves are concerned, India harbors 4,740 sq. km of mangroves along its coast which accounts 0.67% of its total forest cover of 701,673 sq. km. Of

these, 1,475 sq. km area is covered by dense mangroves, 1,391 sq. km area by moderately dense mangroves and 1,877 sq. km area by open mangroves (FSI, 2015b). In this section, we discuss the application of different types of remote sensing data for mapping and characterization of mangroves in India.

The impact of restoration activities of degraded mangroves in Pichavaram, Tamil Nadu was studied by comparing the classified images of Landsat 5 TM data (1986) and IRS 1D LISS III data (2002) and found that the area of the mangrove forest cover has increased by about 90% due to restoration activities (Selvam et al., 2003). Change in the spatial extent of mangrove cover in estuaries of Goa for the time period 1994 to 2001 was interpreted using LISS II and LISS III data from IRS 1B and IRS 1D satellites and found that there was an increase of 44.90% of mangrove covered area (Singh et al., 2004). Temporal satellite images from Landsat 5 TM and LISS III data from IRS 1C and IRS 1D satellites were used to interpret the effect of aquaculture development over mangrove forest of Godavari estuary, Andhra Pradesh for the time period 1986 to 2001(Ramasubramanian et al., 2006). Similar kind of study was done for determining the change in mangrove and other land cover for the time period of 1973 to 2004 in Bhitarkanika mangroves, Odisha (Reddy et al., 2007). Multi-temporal GeoCover data set (a collection of Landsat dataset) were used to detect change in forest cover of Sundarbans mangroves over the time period of 1973 to 2000 (Giri et al., 2007). Chaves and Lakshumanan (2008) analyzed the change in wetland cover over the period of 35 years in Ennore Creek, Chennai using Survey of India Topographic map (1972) as the base map along with multispectral data from Landsat TM (1991), IRS-P6 LISS-III data (2004), and IKONOS data (2004).

Visual interpretation of temporal multispectral images taken in years 1976, 1999 and 2005 was done to analyze the impact of tsunami and anthropogenic activities on the mangrove forest of North Andaman Islands and estimated that there is decline of 116.7 sq. km of forest cover from 1976 to 2005 with a deforestation rate of 3.89 sq. km per year. He stated that anthropogenic activities such as conversion of natural vegetation to agriculture, settlement, sand and water as well as tsunami were major causes for the destruction which was validated by

post-tsunami field survey in January 2005 (Prasad et al., 2009). Ajai et al. (2012) used Resourcesat-1 LISS III and LISS IV data of the time period 2005 to 2007 for community-level mapping of mangroves at 1:25,000 scale for the entire country and estimated that the total area of mangrove forest in the country as 4,956.2 sq. km. The area is found to be increased by 515.10 sq. km from the previous estimate of 4,441.10 sq. km for the year 1990–1993 using IRS 1B LISS II data (Nayak and Bahuguna, 2001). Ambastha et al. (2010) interpreted the spatial characteristics and extent of anthropogenic disturbances affecting the mangrove forests of Bhitarkanika, Odisha using IRS P6 LISS III data acquired in 2006. He developed disturbance index to model disturbance process by compiling forest type map derived from the satellite data along with other socio-economic factors to showcase the zones of conservation prioritization. The dynamics in the spatial distribution of mangroves in Pichavaram, Tamil Nadu was analyzed using time series multispectral data of Landsat and IRS series from 1997 to 2011 and found that area under mangrove forest was declined about 4.71 sq. km from 1970 to 1991 due to natural and anthropogenic factors and later a gain of 5.31 sq. km was observed in 2011 mainly due to restoration activities (Gnanappazham and Selvam, 2011).

Diversity of mangroves are studied using field based and space borne hyperspectral data. Panigrahy et al. (2012) have collected spectral signatures from dorsal and ventral sides of leaves collected from 4 Indian mangroves and investigated their discrimination properties using the parametric statistical method and data reduction methods and determined optimal bands for species discrimination. Similarly Manjunath et al. (2013) identified 960, 970, 1000, 1070, 1120, 1160, 2070, 2080, 2150, 2200, 2240 and 2340nm as optimal bands using One-way ANOVA and Optimal Wilk's Lambda test by analyzing the field spectral signatures collected from 17 species belonging to 9 families of Indian Sundarbans mangroves.

Kumar et al. (2013) used EO-1 Hyperion data to classify mangrove species in Bhitarkanika National Park in Odisha by implementing three supervised classification algorithms: Minimum distance (MD), Spectral Angle Mapper

(SAM), and Support Vector Machine (SVM) on 56 uncorrelated bands obtained from principal Component Analysis (PCA). From the results, SVM (kappa coefficient – 0.96) gave better results when compared with MD (kappa coefficient – 0.66) and SAM (kappa coefficient – 0.64) while classifying five mangrove classes. Same dataset was analyzed by Ashokkumar and Shanmugam (2014) by using three different band selection methods: Factor analysis (FA), Band Index (BI), and Mutual Information (MI) and classified using SVM algorithm to study the impact of band selection method in classification accuracy of ten land cover types including three mangrove types. The results show that FA band selection method gave better accuracy (92.73%) than BI (90.91%) and MI (91.82%) methods. Padma and Sanjeevi (2014) proposed a hyperspectral matching technique by combining Jeffries-Matusita (JM) measure and Spectral Angle Mapper (SAM) algorithm using tangent and sine functions and tested its potential to classify land cover types by implementing in two hyperspectral datasets: CHRIS PROBA and EO-1 Hyperion acquired over Lake Argyle region, Australia and Pichavaram mangroves, Tamil Nadu, India respectively. For both datasets, the proposed JM-SAM algorithms gave better accuracy when compared with Minimum Distance, SAM, and JM. Chakravortty and Sinha (2015) analyzed the multiple scattering of radiation among end members of mixed pixels collected from EO-1Hyperion data of Sundarban mangroves using Linear Unmixing Model and non-linear scattering model developed by Nascimento and Bioucas-Dias (2009). Non-linear model was able to successfully identify areas of interaction of mangrove mixtures such as *Ceriops - Excoecaria - Phoenix, Excoecaria - Avicennia alba - Avicennia officinalis* etc. in the study area.

Integration of IRS multispectral data and SAR microwave data have been attempted to derive more information and enhance the classification accuracy of mangroves to evaluate the temporal behavior of its spatial distribution (Dwivedi et al., 1999; Rao et al., 1999). Shanmugam et al. (2005) used four sensor fusion methods: two algebraic models (Multiplicative and Brovey Transforms) and two spectral domain models (Principal Components Transform and Intensity-Hue-Saturation) to fuse multispectral IRS-1D LISS-III and Panchromatic (PAN) images as well as the microwave ERS-2 SAR image to facilitate the classification

of different mangrove types present in Pichavaram coastal wetland. Among the fusion methods, Brovey transform provided higher spatial and spectral details from both LISS-III and SAR images to distinguish mangroves. Kumar and Patnaik (2013) used C-band dual-polarization (HH, HV) SAR data from RADARSAT - 2 satellite to discriminate and characterize mangrove forests of the Sundarbans. They were able to characterize the mangrove forest by a decision rule classifier of having the components of textural characteristics with multi-temporal HH backscatter and single-date cross-polarization ratio.

As the literatures related to remote sensing on Indian mangroves are reviewed, studies utilizing the hyperspectral data analysis of Indian mangroves are very limited. This includes (a) lack of baseline information on spectral signatures of Indian mangroves and (b) tools and techniques for the separability analysis to spectrally discriminate more number of mangrove species. Other than that applying efficient classification algorithms to map Indian mangroves at species level are not much researched. A detailed study on hyperspectral remote sensing was found to have great scope in bringing out the potential of hyperspectral data. This motivated the present study of taking up hyperspectral analysis for one of the Indian mangroves, Bhitarkanika.

CHAPTER 3

DEVELOPING SPECTRAL LIBRARY OF MANGROVE SPECIES OF INDIAN EAST COAST

This chapter presents the sampling methodology, field and laboratory spectral signature collection protocols, and post-processing techniques involved to develop a spectral library of mangroves in Indian east coast. The development of the spectral library is a prerequisite for the higher order classification of satellite data and hyperspectral image analysis to map mangrove ecosystem. Canopy level field spectra and leaf level laboratory spectra of 34 species (25 true and 9 associated mangroves) from two different mangrove ecosystems of the Indian east coast were collected using ASD Fieldspec 3 spectroradiometer. The raw spectra collected were then undergone post-processing steps such as removal of water absorption bands, correction of thermal difference drifts and smoothing of spectra for further utilization. The processed spectra were then compiled as a spectral library.

3.1. Introduction

Field spectroscopy provides ground truth information and is regarded as the precursor of hyperspectral image analysis in most of the applications to get the detailed knowledge about the relationship between the characteristic feature of the material and the spectral reflectance in the Electromagnetic radiation (EMR) domain. In the field of vegetation science, forestry, agriculture, environmental monitoring, and management field spectroscopy is often integrated with hyperspectral remote sensing for its application. It provides intricacies of detailed spectral characteristics of plant species which help to map vegetation at the species level. Field spectrometry is the technique which is used to quantify the radiance, irradiance, transmission/reflectance from various earth surface features in field condition (Jackson et al., 1980; ASD, 2001). Spectral library of earth features will be the ideal complementary information to the ground truth data in training the classification algorithm. This has an added advantage of identifying the presence of a particular feature in the hyperspectral satellite image of the unknown region. Jet Propulsion Laboratory, Johns Hopkins University and United

States Geological Survey (USGS) together developed the Advanced Space-borne Thermal Emission Reflection Radiometer (ASTER) spectral library for vegetation, soil, man-made materials, terrestrial soils, lunar soils, rocks, minerals, snow, and ice in visible to thermal infrared region (400nm to 15400nm) with more than 2000 spectra in the database (Baldridge et al., 2009). "*Splib06a*", the USGS digital spectral library was developed for different types of materials in the wavelength range of 200nm to 15000nm including X-Ray Diffraction data (Clark et al., 2007). Christensen et al. (2000) developed a spectral library of silicate, carbonate, sulfate, phosphate, halide, and oxide minerals from different rocks for comparison to spectra obtained from planetary and earth-orbiting spacecraft, airborne instruments, and laboratory measurement. Herold et al. (2004) analyzed more than 4500 in-situ spectra from various urban features to develop a spectral library for the urban environment and investigated its separability using Bhattacharya distance to quantify the spectral discrimination among the urban features. Shepherd and Walsh (2002) developed spectral library for over 1000 top-soils from eastern and southern Africa for non-destructive estimation of soil properties such as soil pH, exchangeable Calcium (eCa), exchangeable Magnesium (eMg), exchangeable Potassium (eK), extractable Phosphorous (eP), potential Nitrogen mineralization (PNM), organic Carbon (OC), effective cation exchange capacity (ECEC), clay content, and sand content. Viscarra Rossel et al. (2008) also developed spectral library in mid infra-red (MIR) for the soils of cotton-growing regions of eastern Australia from 1878 legacy soil samples from different layers to predict their properties such as OC, ECEC, clay content, eCa, total Nitrogen (TN), total Carbon (TC), gravimetric moisture content (θg), total sand, and eMg.

Even though old studies had reported that there was no unique spectral signature for certain crops (Price, 1994; Cochrane, 2000), recent studies revealed that for certain agricultural species, unique spectral reflectance existed during phenological stage which had more control over the resultant spectra rather than inter-seasonal variation (Dehaan and Taylor, 2003; Andrew and Ustin, 2006; Nidamanuri and Zbell, 2011). In case of vegetation science, several site-specific spectral libraries were developed and archived. Field spectrometry is being

actively used for last two decades in forestry and vegetation sciences for species identification, classification, health status monitoring, nutrient intake estimation, invasive species monitoring, etc. Normally the spectral libraries collected are in the wavelength region of 400nm to 2500nm. This includes diverse groups of vegetation such as non-native species (Underwood, 2003), Mediterranean species (Manevski et al., 2011), wetland species (Schmid et al., 2004; Zomer et al., 2009), macroalgal species (Casal et al., 2013), shrubland species (Jiménez and Díaz-Delgado, 2015), rangeland grasses (Schmidt and Skidmore, 2001), and agricultural crops (Datt et al., 2003; Rao et al., 2007; Nidamanuri and Zbell, 2012). Pandya et al. (2013) recorded the plant emissivity in Thermal Infra-Red (TIR) region for eight plant species in the field conditions using FTIR (Fourier Transform Infra-Red) field spectroradiometer working in 4000 to 14000 nm.

As far as mangroves are concerned, only a few studies have been conducted in collection and analysis of the spectral information in laboratory and field conditions. Vaiphasa et al. (2005) have collected laboratory spectral signatures in the wavelength domain of 350nm to 2500nm for 16 tropical mangrove species in AoSawi, Chumporn Province of Thailand and found that the spectral discrimination among mangrove species is possible using their laboratory spectra. Field spectral data in the wavelength range of 350nm to 1050nm were collected from five mangroves species in Tok Bali, Kelantan and Setiu, Terengganu in Malaysia (Kamaruzaman and Kasawani, 2007a). Laboratory spectral signatures were collected for three mangrove species of Punte Galeta, Caribbean coast of Panama (Wang and Sousa, 2009) and mangrove species in degraded and healthy conditions in the coastal lagoon south of the city of Mazatlán in the Mexican State of Sinaloa (Zhang et al., 2014).

In Indian context, Panigrahy et al. (2012) had collected spectral signatures from dorsal and ventral sides of leaves collected from 4 Indian mangroves to investigate their separability using different statistical methods and concluded that unique spectral signature exists for four species and it is the function of biochemical content present and cellular structure of the leaves. From Indian Sundarbans, field spectral signatures were collected from 17 mangrove

species belonging to 9 families and their associated mudflat regions and creek waters (Manjunath et al., 2013) to statistically analyze and find optimal bands for species discrimination. Spectral data recorded in the field and in the laboratory provide the base information for the classification of hyperspectral satellite image to map the spatial distribution of species. Apparently, assessment and mapping of species diversity is one of the major objectives of Biodiversity Act of the Ministry of Environment, Forests and Climate (formerly MoEF), Government of India (MoEF, 2002). This study of acquiring and developing the spectral data is motivated by the lack of complete spectral signatures of floristically rich Indian mangroves. In this chapter, we discuss various techniques and procedures adopted to generate an exclusive spectral library of 34 mangrove species (25 true and 9 associated) from 23 families found in Bhitarkanika National Park, Odisha and Coringa Wildlife Sanctuary, Andhra Pradesh of the east coast of India. Most of the species considered for the study also present in other mangrove ecosystems in India including Sundarbans.

3.2. Materials and Methodology

3.2.1. Study area description

The first site, *Bhitarkanika National Park* is situated in the north-eastern part of Kendrapara district, Odisha. It is the fourth largest contiguous mangrove ecosystem in mainland India next to Sundarbans, Gujarat and Andhra Pradesh and is located in the area of combined deltaic region of rivers Brahmani, Baitrani, Maipura, and Dhamra (Figure 3.1). Geographically, the study area extends in the latitudinal range of 20° 38′ 19″ N to 20° 47′ 27″ N and the longitudinal range of 86° 49′ 26″ E to 87° 05′ 48″ E. The rich alluvial deposits and gently sloping topography of Bhitarkanika support rich flora and fauna and is well known for its ecological and biological diversity. The total area of Bhitarkanika Wildlife Sanctuary is 672 sq. km., in which the core area of 145 sq. km. is covered by mangroves. This core area was declared as a National Park in the year 1998. Later in 2002, Bhitarkanika was declared as the 'Ramsar site' (Wetland of International Importance) considering its rich biodiversity and its ecological importance. There

are 76 mangrove species present in Bhitarkanika in which 30 are true species and 46 are associated species. The major species found here are *Avicennia marina, Avicennia officinalis, Ceriops decandra, Excoecaria agallocha, Heritiera fomes, Kandelia candel, Sonneratia apetala, Sonneratia caseolaris, Xylocarpus granatum,* and *Xylocarpus moluccensis*. *Heritiera kanikensis* is the only endemic species seen in the sanctuary. *Sonneratia griffithii* and *Merope angulata* are some of the endangered species found in the study area (Patnaik et al., 2000; Upadhyay and Mishra, 2008; Kar and Satapathy, 2012). The area experiences semi-diurnal tides with high and low tides twice a day. The tidal amplitude varies between 2 and 3.5 m in the upstream region and between 3.5 and 6 m near to the river mouths (Ravishankar et al., 2004b).

The second site, *Coringa Wildlife Sanctuary* is located in the deltaic region of the Gautami – Godavari River. The Coringa and Gaderu creeks are the major distributaries of River Godavari providing tidal water to the sanctuary (Figure 3.1). The geographical extension is between 16° 44′ 01″ N and 16° 56′ 16″ N along latitudes and between 82° 14′ 16″ E and 82° 21′ 29″ E along longitudes. The sanctuary covers an area of about 235.7 sq. km and has 15 true mangrove species and 18 associated mangrove species. *Avicennia marina, Excoecaria agallocha* and *Sonneratia apetala* are some of the dominant species present in this area. Sparsely occurring species are *Acanthus ilicifolius, Aegiceras corniculatum, Avicennia officinalis, Lumnitzera racemosa*, *Rhizophora apiculata, Xylocarpus moluccensis, Bruguiera cylindrica, Ceriops decandra,* and *Bruguiera gymnorrhiza. Suaeda maritima* and *Suaeda nudiflora* are commonly seen in hypersaline clayey mud soil of the study area (Azariah et al., 1992; Ravishankar et al., 2004a)
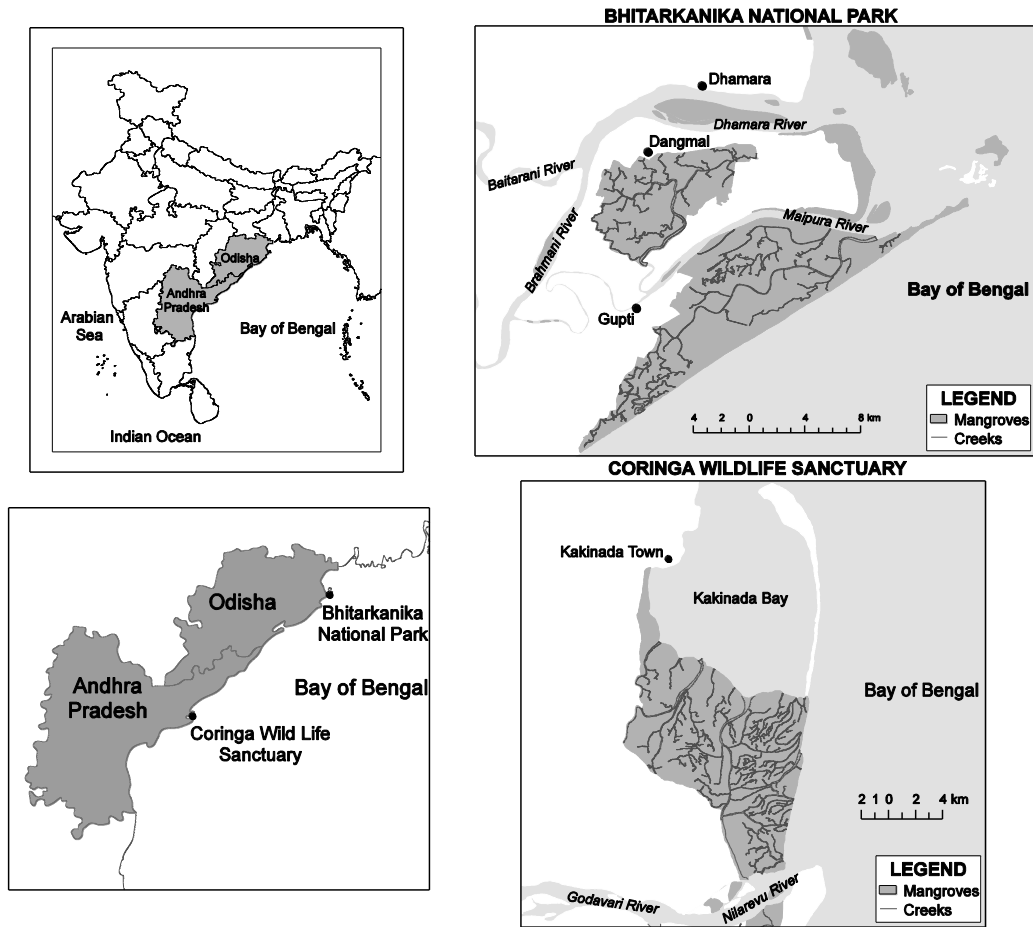
Figure 3.1 Location Map of Bhitarkanika National Park, Odisha and Coringa Wildlife Sanctuary, Andhra Pradesh.

3.2.2. Spectral data collection

For collecting spectral reflectance data, ASD Fieldspec 3[®] spectroradiometer was used which records reflectance in the wavelength range of 350nm to 2500nm at a spectral resolution of 3nm and 10nm with the sampling interval of 1.4nm and 2nm in Visible Near Infra-Red (VNIR: 350nm to 1000nm) and Short Wave Infra-Red (SWIR: 1001nm to 2500nm) wavelength regions respectively. The ASD Fieldspec 3[®] spectroradiometer has three detectors: one 512 channel silicon photodiode array for VNIR region (350nm to 1000nm) and two Indium Gallium Arsenide (InGaAs) detectors which are thermo-electrically cooled to record radiance from two SWIR regions (SWIR 1: 1001nm to 1830nm and SWIR 2: 1831nm to

2500nm). The list of 34 mangrove (25 true and 9 associated) species for which the spectral data collected are listed in Table 3.1 (Photographs of the species are given in Appendix 1). The remaining five true mangrove species present in Bhitarkanika such as *Acanthus volubilis, Cyanometra ramiflora, Heritiera kanikensis, Rhizophora stylosa* and *Sonneratia griffithii* were very rare and extremely difficult to find during our field expeditions because of its remote location (Nayak, 2004). So, spectral signatures were collected for 25 out of 30 true mangrove species present in Bhitarkanika.

Table 3.1 List of mangrove species (first 25 are true mangroves and the remaining 9 are associated mangrove species) selected for spectral data collection

Sl. No	Species Name	Sl. No	Species Name
1	*Acanthus ilicifolius*	18	*Lumnitzera racemosa*
2	*Aegialitis rotundifolia*	19	*Rhizophora apiculata*
3	*Aegiceras corniculatum*	20	*Rhizophora mucronata*
4	*Amoora cucullata*	21	*Sonneratia apetala*
5	*Avicennia alba*	22	*Sonneratia caseolaris*
6	*Avicennia marina*	23	*Xylocarpus granatum*
7	*Avicennia officinalis*	24	*Xylocarpus mekongensis*
8	*Bruguiera gymnorrhiza*	25	*Xylocarpus moluccensis*
9	*Bruguiera parviflora*	26	*Acrostichum aureum*
10	*Bruguiera sexangula*	27	*Brownlowia tersa*
11	*Ceriops decandra*	28	*Cerbera odollam*
12	*Ceriops tagal*	29	*Intsia bijuga*
13	*Cynometra iripa*	30	*Merope angulata*
14	*Excoecaria agallocha*	31	*Phoenix paludosa*
15	*Heritiera fomes*	32	*Salvadora persica*
16	*Heritiera littoralis*	33	*Suaeda maritime*
17	*Kandelia candel*	34	*Tamarix troupii*

3.2.2.1. Field spectral data

The ASD Fieldspec 3® spectroradiometer sensor was positioned at an average height of 60cm above the target in nadir position using 25° angular field of view (FOV) (i.e., bare fiber optic) to measure bidirectional diffuse spectral reflectance

values at the canopy level in field condition. The selection of height and angular FOV of fiber optic sensor is crucial as they determine the size or diameter of the target being sensed. The standard white reference panel Spectralon®, the calibrated barium sulphate plate was used to measure white reference spectra in each set of measurements. The coordinates of each sample plots were precisely recorded using Global Positioning System. All readings were taken on sunny days with clear sky between 10:00 am and 02:00 pm so that the sun zenith angle would be near nadir (Figure 3.2a). Parameters such as sun zenith angle and sky condition have a major impact on overall intensity and illumination geometry. Diffuse incoming radiation from the sun at off-nadir position can affect the spectral characteristics of the material under observation. In the forest environment, if the target is shadowed, direct solar illumination is not the only source of illumination but it is accompanied with diffused and scattered illumination from the surrounding environment (Curtiss and Goetz, 2012). The general sampling rules and precautions to be adopted during field spectral data collection were followed during our field spectral data collection (Zomer and Ustin, 1999). In field condition, the number of spectra collected depends on several factors such as present sun illumination, cloud cover and presence of a species in sample plots. A minimum of 100 sample spectra were collected for each of the species.

3.2.2.2. Laboratory spectral data

Fresh mature leaves from upper and lower part of canopies of mangrove species were collected since leaves at different positions in the canopy might exhibit distinct spectral characteristics because of their differences in photosynthetic properties or water content (Wang and Sousa, 2009). Collected leaves were packed in air-tight covers to preserve the freshness and transported carefully to the laboratory to measure leaf-level laboratory spectral measurement. The fiber optic sensor cable was mounted using a pistol grip and tripod at a height of 60cm and kept in 90° angle to the leaf sample. A tungsten filament halogen lamp was used for artificial light source and mounted at the same position as the sensor which gave constant electromagnetic radiation energy in the wavelength range of 400nm to 2500nm. A black cloth was spread on the surface and complete measurement

was made in a dark room set up in the laboratory to avoid noise from adjacent objects. The collected leaves were segregated into 20 piles of the same amount and spectral measurements were made. Enough care was taken to make sure that each pile was thick enough to cover the field of view of the sensor and leaves facing upwards (Figure 3.2b). About 150 spectra were collected for each species. All these steps of laboratory measurements were made within four hours to avoid degradation of cells which eventually affects the optical properties of leaves and show anomalies in their spectral reflectance (Vaiphasa et al., 2005).
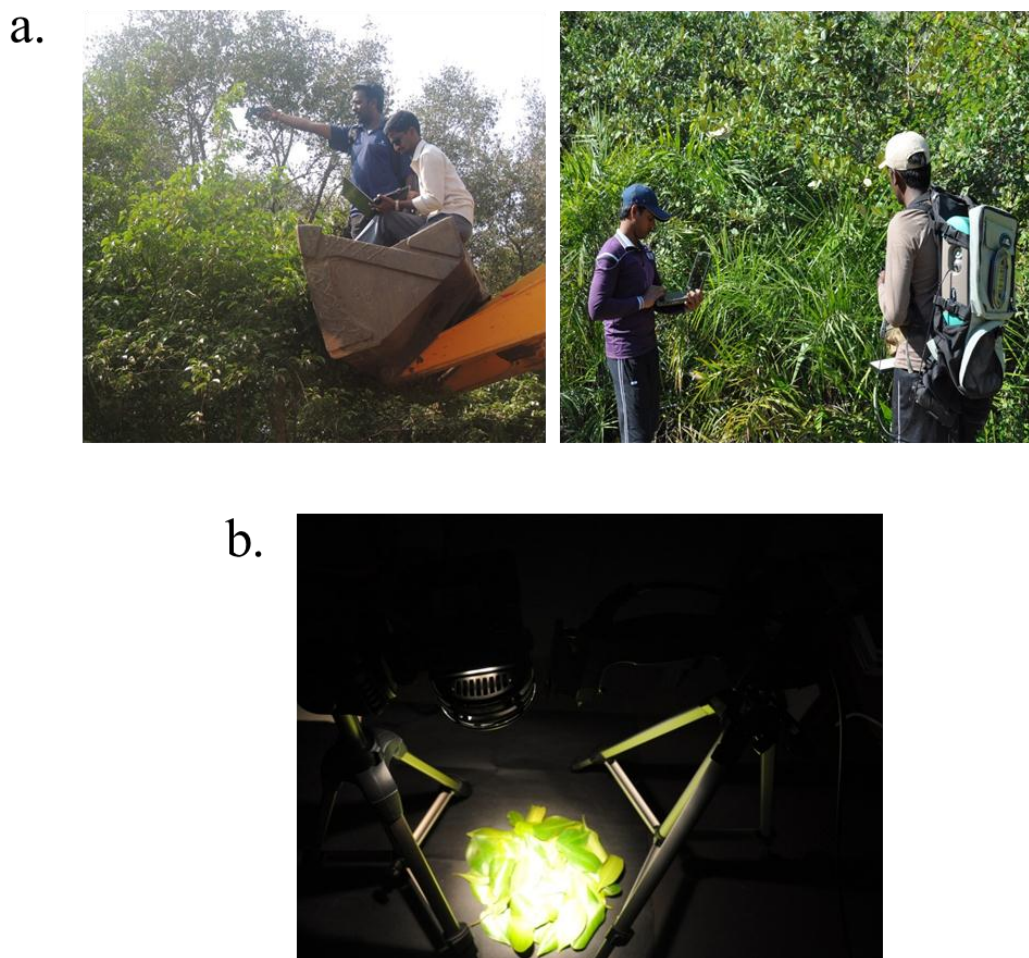
Figure 3.2 Collection of spectral signatures in (a) field and (b) laboratory conditions.

3.2.3. Spectral data post-processing

The spectral data collected in field and laboratory conditions are needed to be processed prior to spectral library building as they could be used as the reference for spectral matching technique and species level discrimination. Prior to post-processing of spectra, all field spectra were visually interpreted to remove spectral samples which are highly affected due to poor light conditions and saturation problem during field data collection. The flow of post-processing techniques is schematically represented in Figure 3.3.
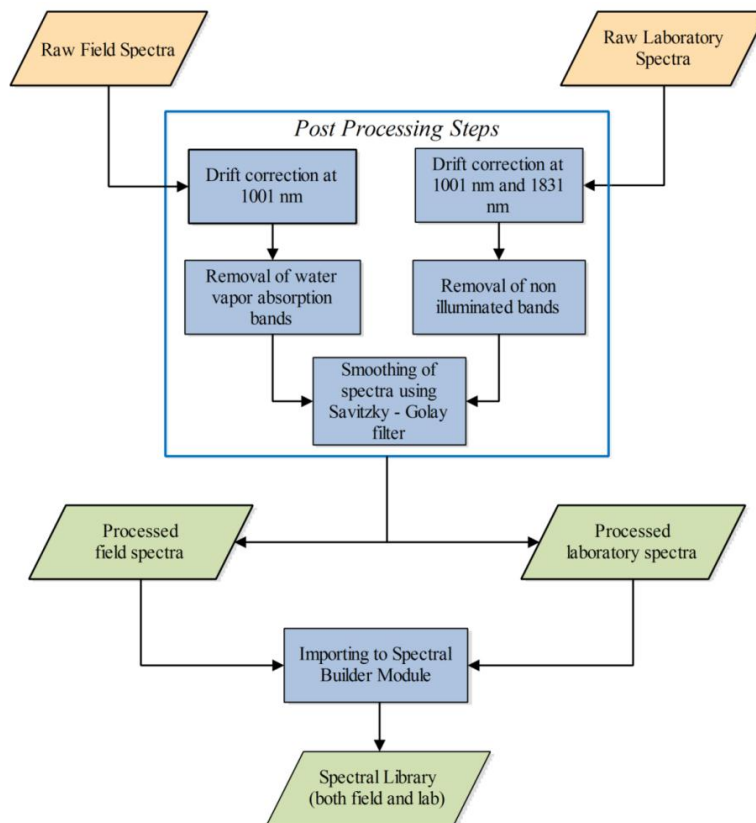
Figure 3.3 Methodology flowchart showing steps involved in post processing of raw spectra to build spectral library.

3.2.3.1. Correction of temperature difference drifts

Generally, the spectroradiometer is preferably needed to be switched on for 75 to 90 minutes prior to spectral data acquisition to "warm-up" for radiometric

calibration. But practically it is not possible all the times during the survey in dense forest and hostile areas due to logistic and battery power issues. Thus, the inherent variation in temperature conditions among the sensors in the radiometer causes spectral drifts at the wavelength located in the juncture of the three sensors. The sensors dedicated to data collection in VNIR and SWIR 1 spectral regions meet at 1000nm whereas the SWIR 1 and SWIR 2 sensors meet at 1830nm (Beal and Eamon, 1996). The temperature difference influenced drifts are corrected at 1001nm and 1831nm by applying "splice correction" function of ASD Viewspec Pro[TM] software. The correction was made by assuming the average of tangents at either side of breakpoints to determine the new point through which the line passes without drift (Figure 3.4).

3.2.3.2. Removal of water absorption and non-illuminated bands

The water vapor present in the atmosphere strongly affects the incoming electromagnetic radiation to the sensor in wavelength regions such as 1350nm to 1460nm, 1790nm to 1960nm, and 2350nm to 2500nm during field data acquisition. The signals in these regions are highly attenuated and so need to be removed from field spectra for further analysis. As far as laboratory spectra are concerned, the artificial light source does not illuminate in the wavelength range of 350nm to 400nm. So the attenuated reflectance in this wavelength region was also removed from laboratory spectra (Figure 3.5).

3.2.3.3. Smoothing of spectra

In general, spectral data collected have to be smoothed to remove the self-generated noise inherent to the sensor which arises due to the little energy detected in the narrow bandwidth of the hyperspectral sensor. In this study, smoothing filters which are commonly used such as Moving Average filter and Savitzky - Golay filter were used to smooth the frequency data. Moving Average filter smooths the data by replacing each data point with the mean of neighboring data values within the specified filter size. Even though this method is effective in eliminating the noise in the data, it is found unsuccessful in smoothing high frequency, as they are eliminated as noise. It could preserve only the lower

moments of a peak such as the centroid. Moreover, the endpoints are not smoothed because a span (filter) cannot be defined for them. In the present study, Moving Average filter of different filter sizes ranging from 5 to 41 (5, 7, 9, ……, 39, 41) were implemented to the spectra and results were compared. On the other hand, Savitzky-Golay smoothing algorithm works on simple polynomial least square calculations which deduce the filter coefficients by performing unweighted linear least squares fit using a polynomial of a given degree. This method is suitable for spectroscopic data as it preserves higher frequency components in the data. Contrary to Moving Average method, this method does not ignore start and end points while smoothing the data. To compute the new value for start and end point, this method uses a methodology of artificially extending the data by adding in reverse order according to the filter size. For example, if filter size is defined as $m = 5$, $(m - 1)/2$ points at the start and end of the series could be calculated by artificially extending the data points by adding, in reverse order (two points are added at the start and end of the data as y_3, y_2, y_1, y_2, y_3, ..., y_{n-2}, y_{n-1}, y_n, y_{n-1}, y_{n-2}). While applying Savitzky-Golay filtering algorithm, the selection of the filter size and polynomial order become crucial to preserve the originality and the shape characteristics of spectra because improper filter and order size may lead to too much smoothing and loss of the spectral shape characteristics (Figure 3.6). Moreover, it will also affect the statistical characteristics of the spectra (Savitzky and Golay, 1964; Vaiphasa, 2006).

In our study, we smoothed the data with these two filters and a comparative analysis was done to choose the optimal filter for the development of the spectral library. The field spectra were smoothed for each segment separately with their corresponding start and end points (400nm to 1349nm; 1461nm to 1789nm; 1961nm to 2349nm) as water absorption bands were removed prior to smoothing. In the case of laboratory spectra, smoothing was done as a single segment (400nm to 2500nm) instead of multiple parts. After smoothing, mean spectrum of each species was calculated to build spectral library.

3.2.3.4. Spectral Library Building Module

The mean spectra calculated were then imported to ENVI (image processing software package) spectral library module in ASCII format with corresponding wavelength and full-width half maximum (FWHM) as input. Then the corresponding metadata regarding the species information, location information and other secondary details (Nayak, 2004) were appended and finally the spectral library was built for 34 mangrove species in the specified format (Research Systems Inc., 2004).

3.3. Results and Discussion

3.3.1. Drift correction

Due to the inherent variations in the detector's sensitivity to thermal cooling difference, detectors at VNIR (350nm – 1000nm) and SWIR 2 regions (1831nm – 2500nm) record radiance with higher level of variations than the actual radiance values in a parabolic manner from 1000nm down the wavelengths and 1800nm onwards (ASD, 2008). Correcting such errors away from these splice points was carried out by making use of (i) the recorded values at the end points of SWIR 1 region detector (as it is a stable detector and not adversely affected by the warm up period) and (ii) the slope calculated from the spectrum in wavelength regions of error. Hence, the raw spectra of samples were subjected to drift correction at two splice points for laboratory spectra i.e., at 1001nm and 1831nm and only at 1001nm for field spectra using splice correction of Viewspec Pro^{TM}. Correction at 1001nm of field spectra fetched a good result in the wavelength region up to 1830nm. However, the original shape of the spectra was completely modified in the wavelength range beyond 1830nm as the second splice point which was at 1831nm falling within the water absorption bands between 1790nm and 1960nm (Figure 3.4a). So the spectra gave erroneous reflectance in the SWIR 2 wavelength region between 1831nm and 2350nm. In order to overcome that, the original reflectance values of SWIR 2 bands were updated from 1831nm to 2500nm and the parabolic error occurring from 1830nm was not corrected for all field spectra. First drift correction of both field and laboratory spectra at 1001nm

resulted in a significant difference in their reflectance value from their original spectra varying from -0.004 at 350nm and the maximum difference of -0.04 at 1000nm. In the case of laboratory spectrum, the drift correction in 1831nm resulted in a difference in reflectance value of +0.014 from those of original spectra at a wavelength of 1831nm and gradually reduced to +0.008 at 2200nm and finally reached the value of 0.003 at 2500nm (Figure 3.4b). In both the cases discussed above, the wavelength region between 1001nm and 1830nm remain unchanged as that region was taken as reference for splice correction. However, those variations were specific to the species chosen to discuss the result i.e., *Rhizophora apiculata* and the corrections varied either positively or negatively or even without variation for other species. After the drift correction, the signatures would be continuous and ready for further processing.
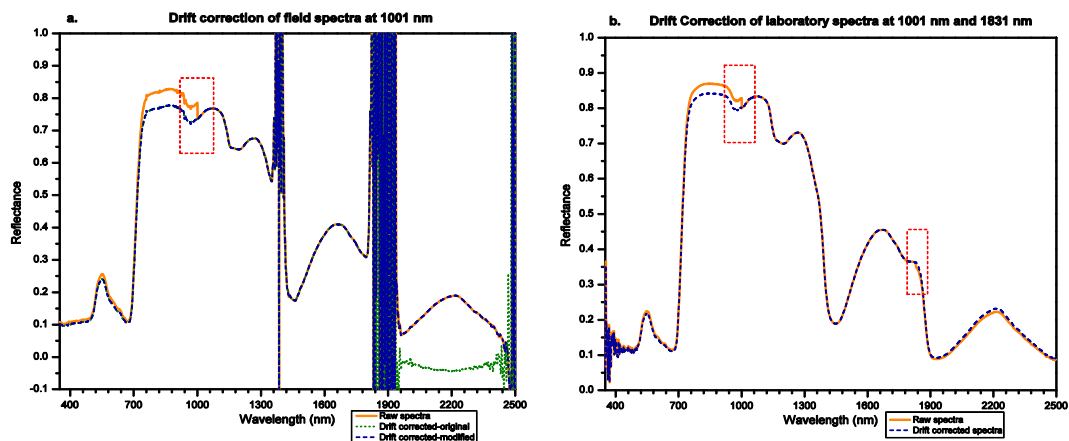
Figure 3.4 (a) Correction of temperature difference drift for raw field spectrum at 1001nm. The dotted line represents the original splice corrected data; (b) Drift correction of laboratory spectrum at 1001nm and 1831nm of *Rhizophora apiculata*. The dotted boxes indicate the places of correction.

3.3.2. Water Absorption and Unilluminated bands removal

Water vapor in the atmosphere absorbs certain wavelength range of electromagnetic radiation traveling through it which results in adverse noise in the reflectance from the target in these wavelength regions. So these bands were removed from raw spectra of all species collected in field condition. Drift

corrected original field spectra of *Rhizophora apiculata* is shown in Figure 3.5a using solid line within the range of absorption bands indicated using dotted bounds. The reflectance spectrum of the sample species had a discontinuity in reflectance value with very high peaks and falls ranging from 5.23 to -12.63 in the wavelength regions between 1350nm to 1460nm, 1790nm to 1960nm, and 2350nm to 2500nm. So these bands had been removed to reduce the level of noise and to maintain the reflectance value between 0 and 1. Spectral data less than 400nm is often affected by haze; therefore, most airborne and satellite-borne systems are not sensitive to wavelengths less than 400nm. So in field spectra, spectra between 350nm and 400nm were removed. In the case of laboratory spectra (Figure 3.5 b), far-UV region (350nm to 400nm) resulted in noisy data fluctuating from 0.42 to -0.05. So those bands were removed.
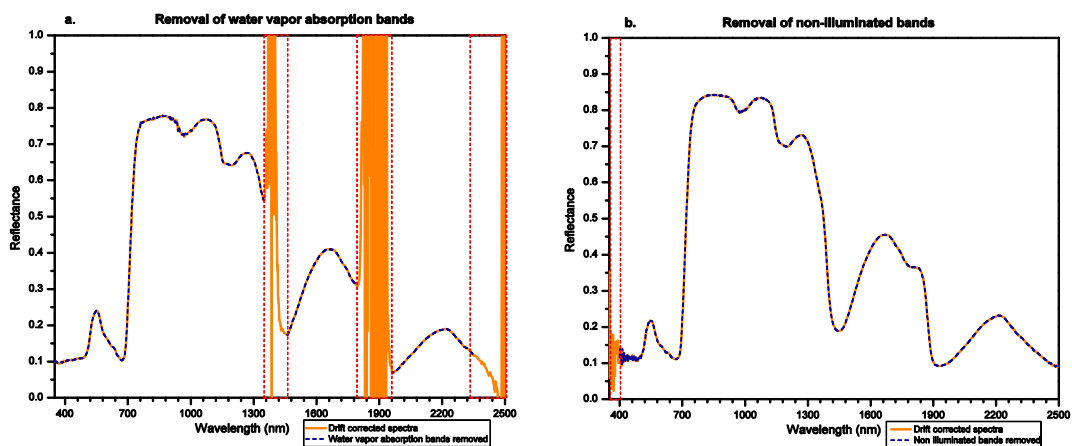
Figure 3.5 (a) Removal of water vapour absorption bands from drift corrected field spectrum; (b) Removal of non-illuminated bands from drift corrected laboratory spectrum of *Rhizophora apiculata*. Removed bands are highlighted in dotted boxes.

These two corrections in field and laboratory spectra became essential mainly for two reasons. The first one was that the light source used for artificial illumination. The tungsten-halogen lamp used to artificially illuminate the samples emits very weak radiation in the far-UV region which eventually results in too many fluctuations in spectra particularly in this region and needs to be removed. The second reason was the spectral library of any object could not be used with huge fluctuations in water absorption bands when used as reference

spectra in classifying the hyperspectral satellite image comprising these bands. After the removal of bands in water absorption region and far UV region, bands in the wavelength range of 400nm to 1349nm, 1461nm to 1789nm, and 1961nm to 2350nm were retained for field spectra and 401nm to 2500nm were retained for laboratory spectra for all species.

3.3.3. Smoothing of spectra

Smoothing of spectra is an important step in order to remove any ambiguities in the representative spectra before it is included in the spectral library. Moving Average algorithm (filter sizes ranging between 5 and 41) and Savitzky-Golay filtering techniques (with 2 and 3 polynomial order and filter size from 5 to 41) were implemented. Among these methods, the Savitzky-Golay method gave satisfactory results which not only removed noise but also smoothed data without much attenuation. Moving Average method showed a trend of higher the filter size higher the deviation from the original spectra which could be noticed in peaks (Figure 3.6). In the case of the Savitzky-Golay filtering method, it performed the smoothing piece by piece by linear polynomial fit with specified order and filter size. Several degrees of polynomial order and filter sizes were tried for Savitzky-Golay filter. Of those implemented, the optimal degree of polynomial order and filter size were identified as 2 and 15 respectively based on their fitness to preserve the actual slope and orientation of the spectra without much deviation. For a better understanding of the selection of optimal smoothing filter, smoothing of the spectrum of *Avicennia alba* using Moving Average method and Savitzky - Golay filtering method with different polynomial orders and filter sizes and their effect in the spectrum, is illustrated in Figure 3.6. In the case of field spectra of many species, smoothing was required in the shoulder of the reflectance curve in NIR region (between 700nm and 1000nm) and in SWIR-2 region (between 1900nm and 2350nm) (Figure 3.7a). On the other hand, the Savitzky - Golay smoothing technique had eliminated noise in blue region (400nm to 500nm) for laboratory spectra, because the light source that we used emits weak in this region. Other notable regions of the curve where smoothing was evident were NIR region (800nm to 1000nm) and towards the end of the spectra i.e., in SWIR 2

region (2300nm to 2500nm) (Figure 3.7b). This does not mean that other regions were not smoothed or completely noise-free. But in these areas the smoothing technique had helped to remove adverse noise effects and made the curve look smooth which is a prerequisite for the selection of spectra to be compiled in the spectral library.
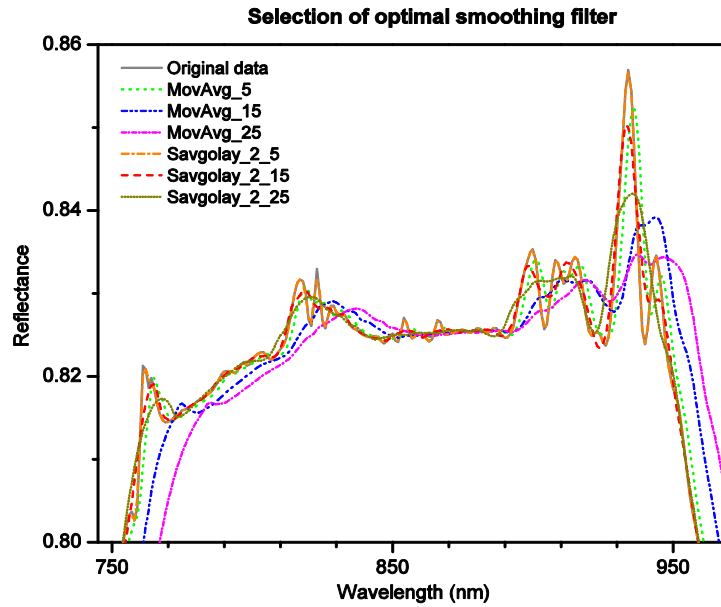
Figure 3.6 Smoothing of field spectra of *Avicennia alba* using Moving Average filter and Savitzky-Golay filter (polynomial order of 2) with different filter sizes 5, 15 and 25.
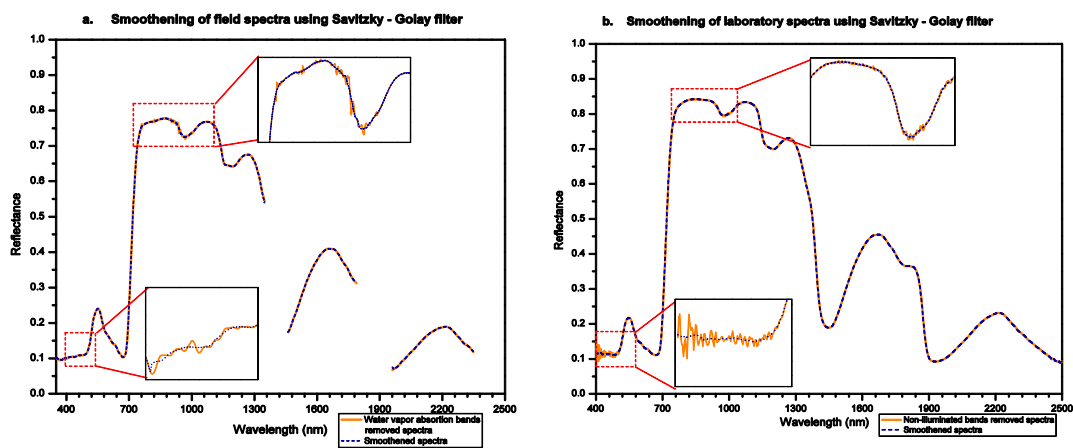
Figure 3.7 Smoothed spectra of *Rhizophora apiculata*, (a) field spectrum and (b) laboratory using Savitzky-Golay filter method (second order polynomial and filter size of 15). Inset plot represents the enlarged view of spectra wherein smoothing is essential.

3.3.4. Spectral library building

The whole post processing procedures were followed for both field and laboratory spectral signatures of selected 34 species. The processed spectra were later compiled and the spectral library was built separately for field and laboratory conditions. The spectral libraries which were developed for 34 mangrove species using field and laboratory spectra are given in Figure 3.8 and Figure 3.9 respectively.
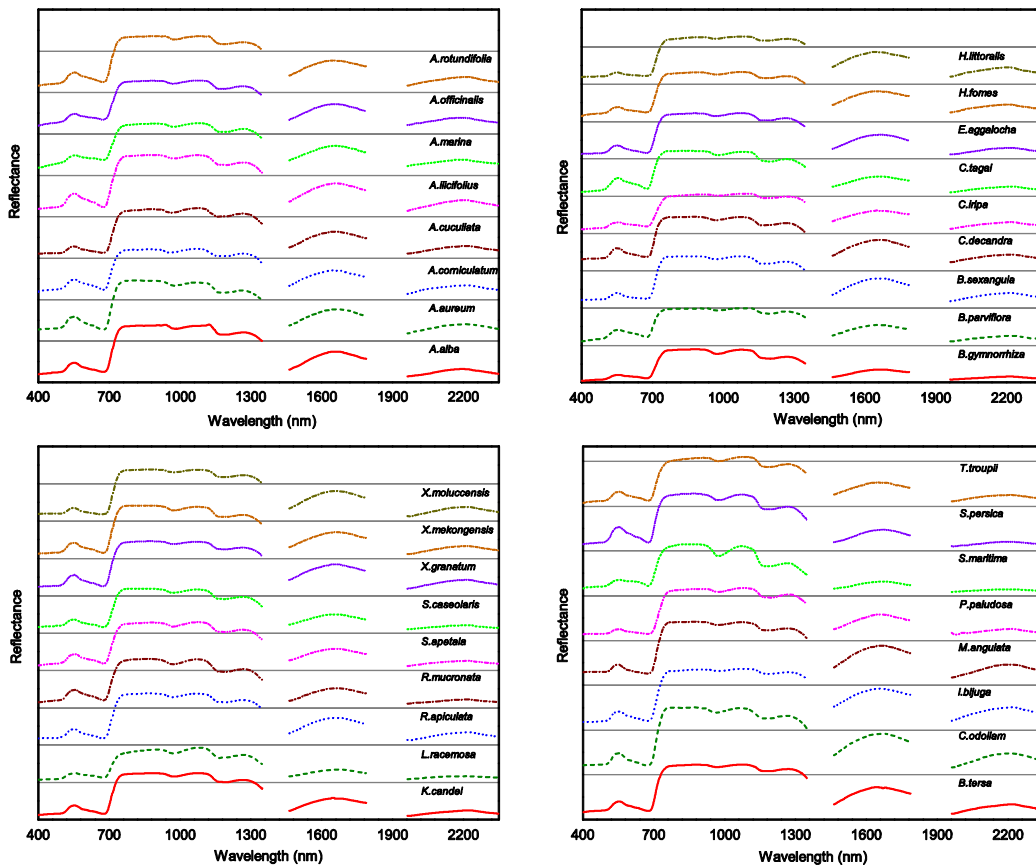
Figure 3.8 Field spectral reflectance plots of 34 mangrove species. The reflectance values of all species are reduced to half and are offset by 30% progressively for each species given along the Y- axis in each box to increase the visibility.

In the figure, mean spectra of all species are represented. The reflectance values for each species at each band were first divided by 0.5 (to normalize the reflectance value to 50% of its original) and then they were offset by 30% in order to enhance the visibility among the spectra of all species. Though the representation of spectra in the figure shows visual separability among the mangrove species in most of the wavelengths in the visible, NIR and SWIR regions, the statistical and geometrical properties of the spectra has to be analyzed effectively to differentiate the species quantitatively. The webpage developed for the spectral library is given in Appendix 2.
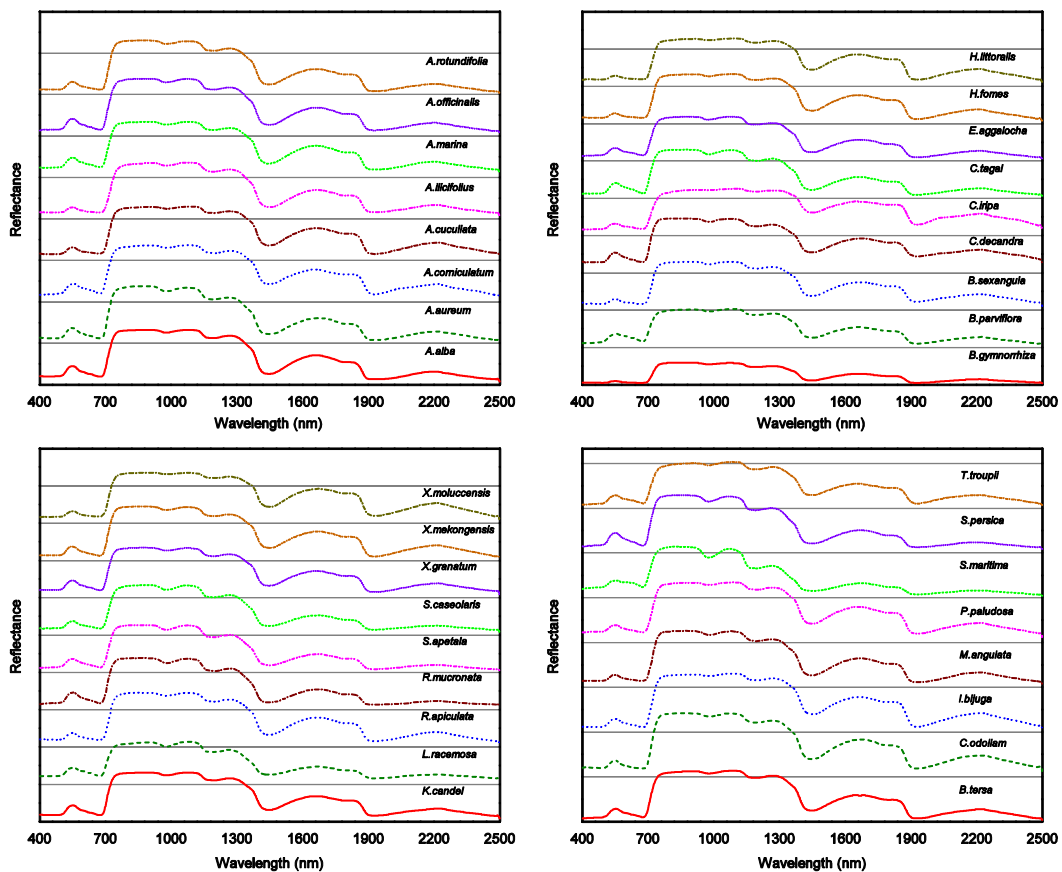
Figure 3.9 Laboratory spectral reflectance plots of 34 mangrove species. The reflectance values of all species are reduced to half and are offset by 30% progressively for each species given along the Y- axis in each box to increase the visibility.

3.4. Conclusion

In this chapter, the post-processing processes carried out for the development of a spectral library for the mangroves are discussed. The ambiguities in the spectra had to be rectified, as the errors are specific to (a) limitations and specifications of the instrument used to collect spectral data, (b) nature of spectral data i.e., either field or laboratory, and (c) prevailing environmental conditions during data collection. There is a little difference in spectral reflectance of the same species taken in field and laboratory condition observed for some species. This difference is due to the difference in leaf arrangement in natural and laboratory conditions. This spectral library is first of its kind in Indian mangroves and covers most of the important species found in India. Earlier studies had proven that the temporal and spatial transfer of spectral signatures of many agricultural crops as successful. However, the inequality of canopy structure in forest cover will be the major limiting factor in replicating the same especially in the mangroves where the canopy structure and zonation are very much dependent on many natural parameters including soil type, tidal inundation, and salinity. The spectral library generated could be upgraded by appending signatures of remaining mangrove species in these sites such as *Acanthus volubilis, Cynometra ramiflora, Dalichondrone spathaceae, Excoecaria indica, Heritiera kanikensis, Rhizophora stylosa, Scyphiphora hydrophyllaceae,* and *Sonneratia griffithii* along with other mangrove associate species to have a complete collection of spectral signatures of Indian mangroves.

CHAPTER 4

SPECTRAL SEPARABILITY ANALYSIS FOR MANGROVE SPECIES DISCRIMINATION

This study aims at discriminating 34 true and associated mangrove species of Indian east coast using field and laboratory spectra in the spectral range of 350nm to 2500nm. First, the spectral signatures of eight mangrove species of "Rhizophoraceae" family were taken for the analysis. Initially, derivative spectral analysis was tested for spectral separability using laboratory signatures of eight species of Rhizophoraceae by taking first and second derivative of reflectance spectra and tested using parametric and non-parametric statistical analysis. Results shows that non-parametric test gave better separability than parametric test and spectral regions such as red edge (680nm to 720nm) and absorption region (around 1150nm and 1400nm) are found to be optimal in discriminating species in reflectance spectra as well as in its first and second derivative spectra. Since our objective was to improve separability in Short Wave Infra-red (SWIR) region, spectral signatures were undergone different transformation techniques such as (i) Additive inverse of spectral signatures, and (ii) Continuum removal of reflectance and its inverse spectra. Parametric and non-parametric analyses were applied on these spectrally transformed spectra to determine significant spectral bands for species discrimination. In this case also, non-parametric test gave better separability than parametric test. The continuum removal of inverse spectra (CRIS) introduced in this study utilizes the advantage of continuum removal in reflectance region beyond Near Infra-red (NIR) region which is often suppressed in continuum removal of reflectance spectra (CRRS). Principal component analysis and stepwise discriminant analysis were applied for feature reduction and to identify optimal wavelengths for species discrimination. To quantify the separability, Jeffries–Matusita distance measure was derived. Green (550nm), red edge (680nm to 720nm) and absorption region (1470nm and 1850nm) were found to be prominent wavelength region for species discrimination. The continuum removal of additive inverse spectra gave better separability than the continuum removed reflectance spectra. Later the methodology was extended to determine the spectral separability among 34 species under consideration. To validate the advantage of the proposed methodology, the field and laboratory spectra of 34 species in CRRS and CRIS spectral modes were classified using three supervised classification algorithms: Maximum Likelihood Classification, Spectral Angle Mapper and Support Vector Machines. Results show that, for field spectra, CRIS gave better classification accuracy and for laboratory spectra, CRRS gave better accuracy than CRIS. CRIS has enhanced the separability in NIR and SWIR regions which is the function of biophysical characteristics like Leaf Area Index (LAI), canopy structure and leaf arrangement which are usually well evident in field condition rather than simulated conditions in laboratory. Furthermore, the selection of wavelengths from SWIR regions helps in enhancing the classification accuracy.

4.1. Introduction

Reflectance spectrometry provides interoperable pure reflectance of feature of interest from its in-situ and laboratory measurements. Earlier it was reported that the field and laboratory signatures are not unique for plant species and suggested that several species may have quantitatively similar spectra (Price, 1994; Cochrane, 2000). But recent studies revealed that for certain agricultural species, unique spectral reflectance existed during phenological stage which had more control over the resultant spectra rather than inter-seasonal variation (Dehaan and Taylor, 2003; Andrew and Ustin, 2006; Nidamanuri and Zbell, 2011). The difference in spectra is due to the intra-species variation causing spectral distribution among the species. However, the biophysical and biochemical nature of species could be characterized and monitored effectively using hyperspectral data (Curran, 1989; Asner, 1998). Spectral data recorded by hyperspectral sensors provide contiguous data in more number of bands with minimal band width and has the potential to discriminate micro-level physiological changes among the species. Therefore hyperspectral remote sensing had become an important tool in several ecological and environmental applications (Schlerf et al., 2005; Stagakis et al., 2010; Thenkabail et al., 2013).

In past two decades several environmental related studies had been carried out by utilizing air-borne and satellite hyperspectral remote sensing data particularly in species level discrimination of many vegetation types including mangroves (Clark et al., 1997; Yang et al., 2009; Kamal and Phinn, 2011; Koedsin and Vaiphasa, 2013; Kumar et al., 2013). Recent studies on hyperspectral signatures acquired using spectroradiometer in field and laboratory conditions were used for species level discrimination of agricultural crops (Song et al., 2011), other cash crops (Daughtry and Walthall, 1998), tropical trees (Clark et al., 2005; Zhang et al., 2006; Pu, 2009), coniferous species (Kokaly et al., 2003), savanna tree species (Cho et al., 2010), Mediterranean species (Manevski et al., 2011), marshland vegetation (Rosso et al., 2005; Belluco et al., 2006), and wetland species (Schmidt and Skidmore, 2003; Sun et al., 2008; Adam and Mutanga, 2009; Ullah et al., 2012). Similarly field and laboratory spectral

signatures were analyzed to discriminate mangrove species of tropical coastal forests as well (Vaiphasa et al., 2005; Kamaruzaman and Kasawani, 2007b; Wang and Sousa, 2009; Panigrahy et al., 2012; Manjunath et al., 2013; Zhang et al., 2014).

Gong et al. (1997) conducted the derivative spectral analysis of in-situ reflectance data in the spectral range of 350nm to 1050nm for the spectral classification of six conifer species using Artificial Neural Network (ANN) and Linear Discriminant Analysis (LDA) algorithms and concluded that while first derivative spectra was classified, ANN gave better accuracy (79%) than LDA (69%). Optimal band selection for the identification of wetland species of Prentiss Bay and Horseshoe Bay, Lake Huron, USA was done using its second derivative spectra and eight bands (514.9nm, 560.1nm, 685.5nm, 731.5nm, 812.3nm, 823.9nm, 835.5nm, and 939.9nm) were identified as optimal bands (Becker et al., 2005). Smith et al. (2004) identified the plant stress caused due to gas leaks using derivative spectral ratios and found that the ratio of the magnitude of the derivative at 725nm to that at 702nm were less in plants present in the areas of gas leakage. Canopy level field spectra and Leaf level laboratory spectra of two closely associated grapevine species were tested using first and second derivative spectra and analyzed with parametric one way ANOVA and pair wise Bonferroni adjusted t-test. It was concluded that first and second derivative spectra were important in species discrimination mainly in visible region (Maimaitiyiming et al., 2016).

Vaiphasa et al. (2005) collected laboratory spectral signatures from 16 tropical mangrove species of Thailand and statistically analyzed using parametric one way ANOVA to identify the wavelengths for species discrimination. He used wrapper feature selection (combination of feature selection method and classifier) to reduce number of bands and identified 720nm, 1277nm, 1415nm, and 1644nm as optimal bands. Similarly laboratory signatures of three mangrove species of Caribbean coast of Panama were analyzed using one way ANOVA and Linear Discriminant Analysis (LDA) and wavelengths such as 780nm, 790nm, 800nm, 1480nm, 1530nm, and 1550nm were identified as useful bands for mangrove

species classification (Wang and Sousa, 2009). Kamaruzaman and Kasawani (2007b) used canonical stepwise discriminant analysis (CSDA) for classifying field spectra (350nm to 1050nm) of five mangrove species from two locations: Tok Bali and Kelantan Seitu in Malaysia. 29 bands between the spectral range of 420nm and 790nm were identified for the discrimination of mangroves in two sites using CSDA. Field spectral signatures collected from random leaves, dorsal and ventral sides of leaves collected from four mangrove species of Indian Sundarbans and investigated their spectral discrimination using one way ANOVA combined with factor analysis to identify wavelengths for classification (Panigrahy et al., 2012). Similar kind of study was done to analyze the spectral seperability among 17 mangrove species of Indian Sundarbans using the canopy spectral signatures collected in field. From discriminant analysis, optimal bands were identified and they were 960nm, 970nm, 1000nm, 1070nm, 1120nm, 1160nm, 2070nm, 2080nm, 2150nm, 2200nm, 2240nm, and 2340nm (Manjunath et al., 2013). Zhang (2014) aimed to identify potential wavelengths to discriminate healthy and degraded stands of three mangrove species (*Rhizophora mangle, Avicennia germinans,* and *Laguncularia racemosa*) in coastal lagoons of Mazatlán, Mexico using their laboratory spectral reflectance measurements. He used R^2 plot, principal components analysis, and stepwise discriminant analysis and identified 520nm, 560nm, 650nm, 710nm, 760nm, 2100nm, and 2230nm as optimal bands.

Even though, Adam and Mutanga (2009) stated that unique statistical technique does not exist for the species discrimination analysis, many studies have been carried out for agricultural crops and forest species by using single statistical approach. *Further to work on that, this chapter of the thesis aims at framing a methodology by incorporating multiple statistical and dimensionality reduction approaches on reflectance spectra and different transformations of reflectance spectra to find out wavelengths which are potential for species discrimination which is then followed by spectral distance measurement to quantify the separability.* The methodology tries to find a solution to improve the discrimination in spectral region beyond NIR region. For that, we initially chose eight mangrove species of *Rhizophoraceae* family which are closely related and

reported "less separable" in earlier studies (Vaiphasa et al., 2005; Manjunath et al., 2013). Moreover, the members of *Rhizophoraceae* family are most important and abundant true mangrove species distributed in eastern world and it includes four genera namely *Bruguiera, Ceriops, Kandelia,* and *Rhizophora* comprising of 18 species (Tomlinson, 1994).

4.2. Frame work for Spectral Separability Analysis of *Rhizophoraceae*

Initially, as a pilot study, the derivative analysis was experimented for laboratory spectra of eight species of *Rhizophoraceae* and statistically analyzed by parametric and non-parametric tests to evaluate the potential of derivative spectra for species discrimination. After that, the field and laboratory spectral data were undergone different transformation method to transform data into four spectral modes: a) Reflectance Spectral mode (RS), b) Continuum Removed Reflectance Spectral mode (CRRS), c) Inverse Reflectance Spectral mode (IS), and d) Continuum Removed Inverse Spectral mode (CRIS). Then the transformed spectra in four spectral modes were subjected to both parametric and non-parametric statistical tests for the discriminant analysis. Feature reduction methods such as Principal Component Analysis (PCA) and Stepwise Discriminant Analysis (SDA) were implemented to identify potential uncorrelated wavelengths (bands) for species discrimination in each spectral mode. Then quantitative measurement of the separability had been measured using the Jeffries-Matusita (JM) distance to determine "how much separable" the species were. Later this methodology was adopted to quantify the seperability among 34 true and associated mangrove species.

4.2.1. Data acquisition and pre-processing

Field and laboratory spectral data were collected from eight mangrove species (Table 4.1) of *Rhizophoraceae* family from random sample plots in the mangrove forest of Bhitarkanika National Park, Odisha, India (Chapter 3.2.1, Figure 3.1) using Analytical Spectral Device (ASD) Fieldspec $3^{®}$ spectroradiometer. All

reflectance spectra collected were pre-processed and prepared for further statistical analysis. The mean field and laboratory spectra of eight species of *Rhizophoracaea* are schematically represented in Figure 4.1. Statistical analysis and feature reduction analysis were done in Matlab R2013a and ENVI 5.1v.
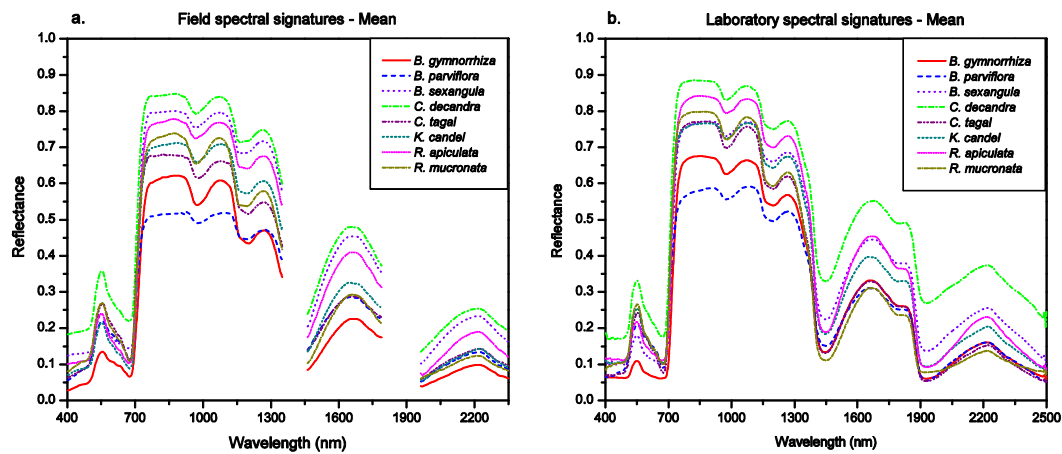
Figure 4.1 Average spectral reflectance of eight species of *Rhizophoraceae* collected in field condition (a) and laboratory condition (b).

Table 4.1 List of mangrove species belonging to *Rhizophoraceae* family considered and number of spectral observations acquired from them at canopy and leaf levels in field and laboratory conditions respectively

Sl. no	Species name	Species code	Number of field spectral observations	Number of laboratory spectral observations
1	*Bruguiera gymnorrhiza* (L.) Lamk	BG	89	150
2	*Bruguiera parviflora* Wight and Arnold ex Griffith	BP	151	150
3	*Bruguiera sexangula* (Lour.) Poir.	BS	110	150
4	*Ceriops decandra* (Griff.) Ding Hou	CD	106	150
5	*Ceriops tagal* (Perr.) C. B. Robinson	CT	78	150
6	*Kandelia candel* (L.) Druce	KC	120	150
7	*Rhizophora apiculata* BL.	RA	110	150
8	*Rhizophora mucronata* Lamk.	RM	136	150

4.2.2. Spectral transformation for separability analysis

Initially, as a pilot study, to evaluate the potential of derivative analysis for the discrimination of species, laboratory signatures of *Rhizophoraceae* were taken and tested using parametric and non-parametric statistical analysis. Then different transformation techniques such as additive inverse and continuum removal were implemented on field and laboratory spectra to identify optimal wavelengths for species discrimination.

4.2.2.1. Species discrimination analysis using derivative spectra – A pilot study using laboratory spectral signatures

Laboratory signatures of eight mangrove species of *Rhizophoraceae* were considered for this study and spectral derivative analysis was done by dividing the difference between successive spectral values by its wavelength interval (bandwidth). Finite approximation method could be used to estimate derivatives based on the spectral resolution of the data (i.e., bandwidth) $\Delta\lambda$ (Tsai and Philpot, 1998). The first derivative of the spectra is calculated using the formula,

$$\frac{ds}{d\lambda}\bigg|_i \approx \frac{s(\lambda_i) - s(\lambda_j)}{\Delta\lambda}$$

where, $\Delta\lambda$ is the band width which is given as $\Delta\lambda = \lambda_j - \lambda_i$ and also $\lambda_j > \lambda_i$. Here $\Delta\lambda$ (1nm) is constant throughout the spectrum. The second derivative was calculated from the first derivative and it could be expressed as,

$$\frac{d^2s}{d\lambda^2}\bigg|_j = \frac{d}{d\lambda}\left(\frac{ds}{d\lambda}\right)\bigg|_j \approx \frac{s(\lambda_i) - 2s(\lambda_j) + s(\lambda_k)}{(\Delta\lambda)^2}$$

where, $\Delta\lambda = \lambda_k - \lambda_j = \lambda_j - \lambda_i$ and $\lambda_k > \lambda_j > \lambda_i$.

The reflectance, first and second derivative spectra (illustrated in Figure 4.2 as sample spectra) were subjected to parametric and non-parametric analysis (Section 4.2.3) for species discrimination (Figure 4.3).
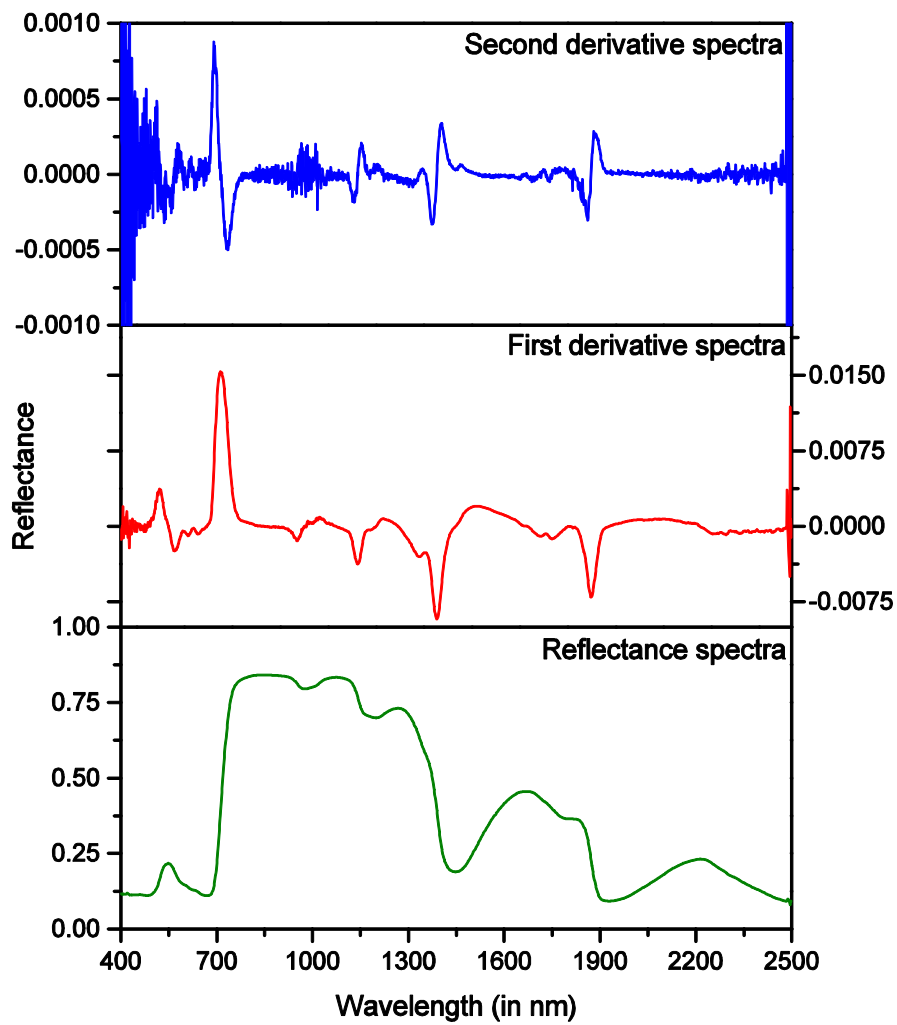
Figure 4.2 Reflectance and its corresponding first and second derivative spectra of mangrove species *Rhizophora mucronata*.
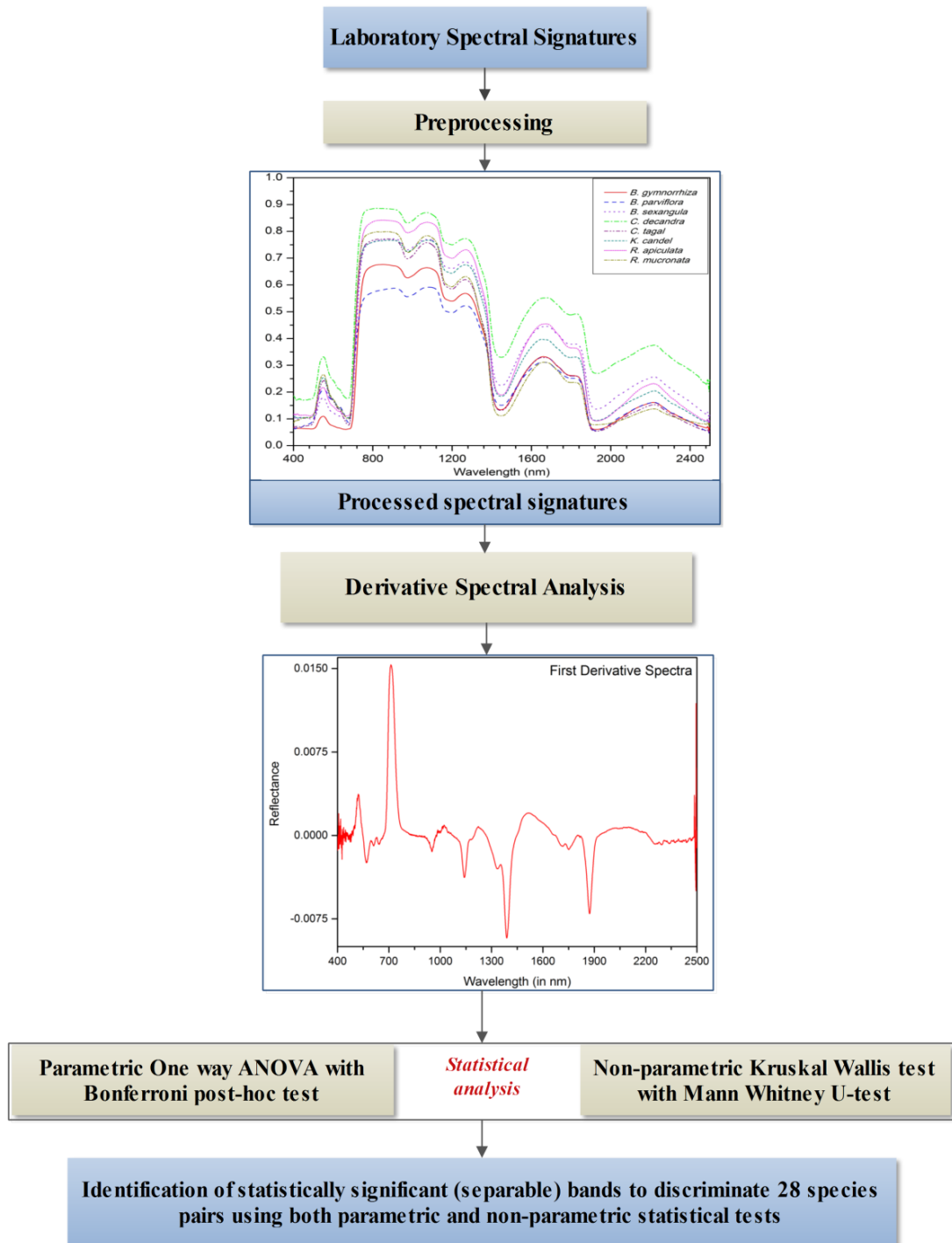
Figure 4.3 Methodology flowchart for spectral separability analysis using derivative spectral transformation method.

The primary objective of framing the methodology is to improve the spectral separability in NIR and shortwave infra-red (SWIR) region. However, derivative spectral analysis alone may not be sufficient as they are primarily helpful in identification of wavelengths for species discrimination mainly in visible region (Maimaitiyiming et al., 2016). So we utilized different spectral transformation methods such as continuum removal and additive inverse of spectra and conceptualized the new transformation called continuum removal of additive inverse spectra to utilize the spectral difference in SWIR part of spectrum for species classification. The methodology flowchart framed for the analysis is schematically represented in Figure 4.4.

4.2.2.2. Continuum removal of reflectance spectra

Continuum removal method is commonly used to enhance the absorption region of spectra which has broad applications in the field of geology to identify mineral composition. Later, it is also being applied in vegetation related studies such as species discrimination and to correlate pigment content with spectra (Schmidt and Skidmore, 2003; Shi, 2006; Mutanga and Skidmore, 2007; Sun et al., 2008). It is a normalization technique with values ranging between 0 and 1 with absorption features more emphasized and variability in absolute reflectance being eliminated. In our study, the "convex hull method" of continuum removal was applied, which connects the local maxima of the spectrum as the rubber band is stretched and connected in maximum reflectance points. The continuum line is drawn in such a way that it does not cross the spectrum but by connecting the consecutive local maxima. Then it transforms the selected local maxima to the maximum reflectance value of 1 and thereby the absorption features are enhanced (Mutanga et al., 2004). The contact points of convex hull vary from species to species as the wavelength position of local maxima for each species spectra varies in transforming the reflectance spectra (RS) to continuum removed reflectance spectra (CRRS).

4.2.2.3. Additive Inverse of reflectance spectra and their continuum removal

While enhancing the absorption features in spectral data, continuum removal technique generally inhibits the reflectance features (i.e., local maxima of the spectra). Vegetation species have significantly varying reflectance maxima in Near Infra-red (N), Short wave Infra-red (S1 and S2) regions because of their varying cell and canopy structure. But it was actually suppressed while continuum removal was done. An attempt was made to make use of the advantage of continuum removal method on reflectance feature by deriving additive inverse of reflectance spectra (which would be the pseudo-absorption phenomena). Hence the reflectance peaks (local maxima) in reflectance spectra became absorption troughs in inverse spectra which got enhanced when continuum removal was applied. Then, continuum removal using convex hull method was applied to reflectance and the additive inverse of reflectance spectra (1 − reflectance) of all species prior to the statistical analysis. The spectral reflectance of *Rhizophora mucronata* in all four spectral modes in laboratory condition is given in Figure 4.5 for example.

The reflectance spectra of eight species in four spectral modes are looking similar in many wavelength regions and overlaps exist. Identifying separable bands for species discrimination is very much ambiguous unlike one could discriminate various land cover features by simple visual interpretation of their spectra. To overcome this situation, statistical interpretation is adopted for spectral discrimination as it provides inherent quantitative variations among species spectra. In this study, both parametric and non-parametric statistical tests were carried out for species discrimination of all eight species considered using their field and laboratory spectral data in four spectral modes: Reflectance Spectra (RS), Continuum Removed Reflectance Spectra (CRRS), Inverse Spectra (IS), and Continuum Removed Inverse Spectra (CRIS).
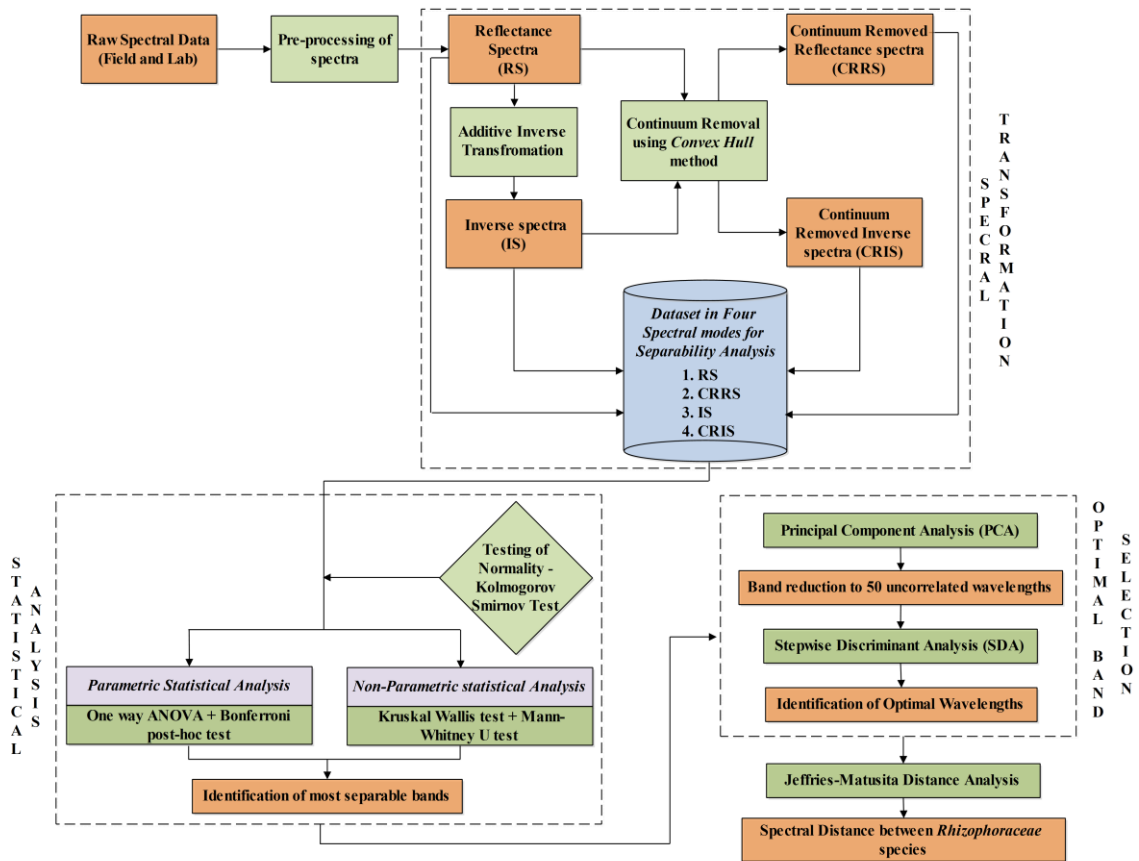
Figure 4.4 Methodology framework designed for spectral separability analysis.
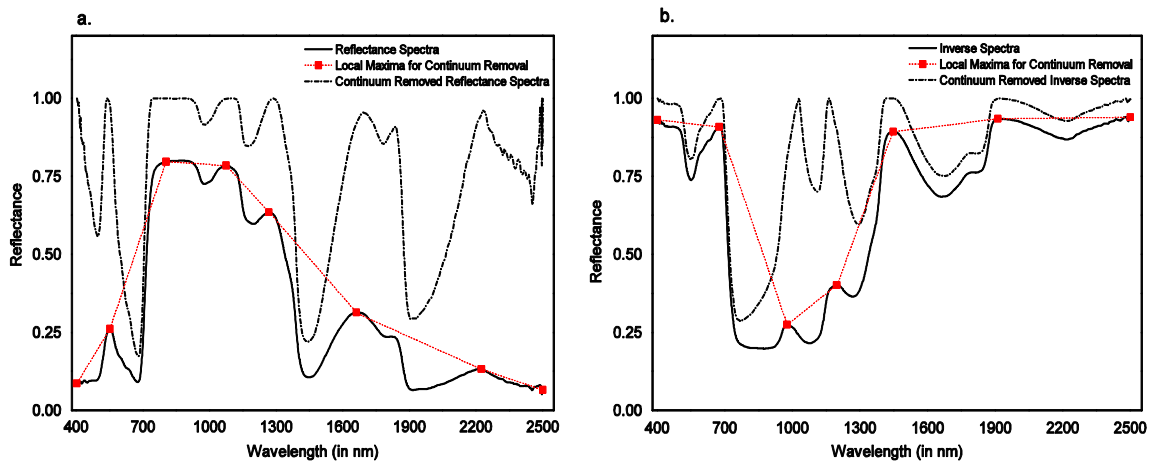
Figure 4.5 Four spectral modes of *Rhizophora mucronata*: (a) Reflectance Spectra (RS) and Continuum Removed Reflectance Spectra (CRRS), and (b) Inverse Spectra and Continuum Removed Inverse Spectra (CRIS).

4.2.3. Statistical Analysis

4.2.3.1. Testing of Normality

Kolmogorov Smirnov (K-S) test of normality (Sheskin, 2004) was implemented on spectral data of each species for four spectral modes to analyze whether at particular wavelength all samples of a species follow normal distribution by giving all sample spectra collected for each species separately as input. The normality was tested to ascertain that the parametric tests can be carried out based on general assumption of normality. Though the intra-seasonal spectral variation exists within a species, it is out of scope of this study as spectra collected in one season (April) are only considered for the current analysis. It was assumed that spectral reflectance of these species were normally distributed to perform parametric statistical analysis and not normally distributed to perform non-parametric statistical analysis (Manevski et al., 2011).

4.2.3.2. Parametric Statistical Analysis

The parametric statistical analysis was done using one way ANOVA test to identify significant wavelengths for species discrimination when mean spectra of eight species for four spectral modes were used. As the number of observations (spectral samples) for each species is more than 30 (our observations are more than 75 in each case), it is assumed that at each wavelength the spectra follows normal distribution under the assumption of Central Limit Theory. The null hypothesis was assumed that the mean reflectance spectra of eight mangrove species of *Rhizophoraceae* family were equal at a given wavelength

$$H_o: \mu_1 = \mu_2 = \ldots\ldots = \mu_8$$

against the alternative hypothesis which assumes that the mean reflectance of eight species at a given wavelength was not equal

$$H_a: \mu_1 \neq \mu_2 \neq \ldots\ldots \neq \mu_8$$

where μ_i represents the mean reflectance spectra of plant species taken for the test in each case. This test was performed at each wavelength at 95% and 99% confidence level. The homogeneity of variance was also tested as a prerequisite to perform one way ANOVA test as the number of spectral observations made in field condition were not equal among species (Table 4.1). To verify the uncertainty in the assumption of equality in variance, a thumb rule followed by Manevski et al., (2011) was adopted. Standard deviation (SD) was estimated for *Bruguiera parviflora* (for which maximum number of observations were made) and *Ceriops tagal* (for which minimum number of observations were made). The result had shown that SD of *Bruguiera parviflora* is not more than twice that of *Ceriops tagal* confirming that the assumption made was meaningful.

However, the outcome of one-way ANOVA test identifies the wavelength where at least one pair of mangrove species was statistically different. In order to minimize the Type I error resulting from the one way ANOVA test and to find out which pairs of mangroves that were separable at each wavelength location, an add-on test was mandatory. Hence the multiple comparison test, Bonferroni post-hoc test was chosen to minimize the possibility of Type I error by its bounds on alpha inflation (Abdi, 2007) and also make pair wise comparison. Bonferroni post-hoc test was implemented on 28 possible species pairs in all four modes of spectra at 95% and 99% confidence interval. Bonferroni test estimates new pairwise alpha to keep the alpha value corresponding to the confidence interval (0.05 or 0.01). The Bonferroni equation for the adjustment of alpha level is,

$$\alpha_{new} = 1 - (1 - \alpha_{fixed})^{1/c}$$

where α_{fixed} represents the input alpha (0.05 or 0.01) and the c represents the number of tests.

4.2.3.3. Non-parametric Statistical Analysis

Non-parametric statistical analysis was performed by assuming that spectral reflectance of eight mangrove species of *Rhizophoraceae* did not follow normal

distribution to test whether the variance of reflectance between groups was greater than the variance within the group. Kruskal–Wallis test, a non-parametric analysis which is similar to one way ANOVA test but performed on ordinal (ranked) data was implemented by assuming the null hypothesis that median spectra of species considered were equal in every wavelength location

$$H_0: \eta_1 = \eta_2 = \ldots = \eta_8$$

against the alternative hypothesis that the median spectra of eight species were not equal

$$H_a: \eta_1 \neq \eta_2 \neq \ldots \neq \eta_8$$

at every wavelength location at 95% and 99% confidence level. Here η represents the median spectral reflectance of species considered. Following that, median spectra of 28 species pairs in four spectral modes were analyzed by Mann-Whitney U test at 95% and 99% confidence interval. It compared median spectra of each species pair to find out the wavelengths where the spectral differences between them were evident (Sheskin, 2004).

Mann-Whitney U test does not assume normal distribution with null hypothesis $H_0: \eta_1 = \eta_2$, against the alternate hypothesis, $H_a: \eta_1 \neq \eta_2$. The data were ranked (in ascending order) and it follows Z table as the sample size is above 20. The test statistic used for the calculation was,

$$Z_a = \frac{U - \frac{\eta_1 \eta_2}{2}}{\sqrt{\frac{\eta_1 \eta_2}{N(N-1)} \left(\frac{N^3 - N}{12} - \sum T_i \right)}}$$

where U represents the U statistic and it is calculated using the formula

$$U = n_1 n_2 + \frac{n_1(n_1 + 1)}{2} - S$$

where S is the sum of ranks of a particular group whereas n_1 and n_2 represents the number of observations in each group and N is the total number of observations.

Here T_i represents the sum of ranks for tied observations and it is calculated by

$$T_i = \frac{t_i{}^3 - t_i}{12}$$

in which t represents the number of observations tied for rank i.

Though all the statistical tests were conducted in both 95% and 99% confidence intervals, results are given only for 99% confidence interval as they are more sensitive. Bands between 350nm and 400nm in field spectra were used for analysis, however, they were not included in the results because of following two reasons.

a. This part of the wavelength range is not considered in satellite data analysis as it is affected by atmospheric haze, and
b. To maintain the uniformity in spectral range with laboratory spectra.

This makes a total of 1667 bands accounted in field spectra while discussing the results. In laboratory condition, such elimination was not done and a total of 2100 bands are discussed.

4.2.4. Feature Reduction Analysis for optimal wavelength identification

4.2.4.1. Principal Component Analysis (PCA)

PCA (also known as Karhunen–Loeve or Hotelling Transform) is one of the dimensionality reduction methods which is used to reduce the large set of correlated variables to smaller sets of uncorrelated variables that retain the information from original data-set called 'principal components' (Campbell and Atchley, 1981). In this method, the original data is projected to the uncorrelated coordinate system or vector space so that first axis contains data having most variance followed by second mutually orthogonal axis with data having lesser variance and so on. In general, higher order principal components contribute very less to the separability and therefore ignored. In the present analysis, PCA was implemented using covariance matrix with input bands selected from non-

parametric Mann-Whitney U test and first five components were selected as they together contribute about more than 99% of total variance. Based on the factor loadings, 10 most distinct and uncorrelated bands were selected from each of the five components. So a total of 50 bands were extracted out for further analysis of both field and laboratory spectra.

4.2.4.2. Stepwise Discriminant Analysis (SDA)

SDA was used to further reduce the number of bands selected from PCA and to select most uncorrelated bands. SDA is one of the most important and efficient statistical techniques used to discriminate between groups. In this analysis, forward SDA was implemented in which the discrimination model is built in such a way that at each step all variables are included for the analysis and those variable which contribute much to the discrimination between the groups are picked based on the F value and Wilks' Lambda (L) value (Lewicki and Hill, 2005). The L value ranges between 0 and 1. Lower the L value higher the discrimination and vice versa. The forward SDA model was implemented by including the band which shows maximum F value and low L value at each step. This model stops when there is no further decrease in the L value (Panigrahy et al., 2012). This method was used to find out optimal bands which are most uncorrelated and are used for the measurement of spectral distance between species pairs using Jeffries-Matusita distance analysis.

4.2.5. Quantitative measurement of the spectral separability using Jeffries-Matusita Distance

Jeffries-Matusita (JM) distance analysis is a commonly used separability measurement which quantitatively measure the distance between the spectral classes in the field of remote sensing. The formula used for the squared JM distance is

$$JM_{ij}^2 = 2(1 - e^{-b})$$

where b represents Bhattacharya distance and is defined as

$$b = \frac{1}{8} \left(m_i - m_j\right)^t \left\{\frac{\Sigma_i + \Sigma_j}{2}\right\}^{-1} \left(m_i - m_j\right) + \frac{1}{2}\ln\left\{\frac{|(\Sigma_i + \Sigma_j)/2|}{|\Sigma_i|^{1/2}|\Sigma_j|^{1/2}}\right\}$$

where m_i and m_j represent the means of i and j classes. Σ_i and Σ_j represents the covariance of i and j classes. The squared JM distance ranges between 0 and 2 where the maximum value 2 represents the maximum separability (Richards and Jia, 2005). Thomas et al. (2002) suggested a threshold value of 1.90 which can be set to decide the spectral separability among classes.

4.3. Results of spectral separability of *Rhizophoraceae*

This section discusses the results obtained from parametric and non-parametric statistical analysis of field and laboratory spectra transformed using different transformation techniques for the separability analysis of *Rhizophoraceae* mangroves. The entire wavelength region (400nm to 2500nm) has been divided into four major spectral regions (V- Visible: 400nm to 700nm; N- Near Infra-red: 701nm to 1000nm; S1-Short Wave Infra-red 1: 1001nm to 1830nm; S2- Short Wave Infra-red 2: 1831nm to 2500 nm) for the ease of interpreting the results.

4.3.1. Statistical methods for separability analysis using derivative spectra

In the case of *parametric analysis*, in reflectance spectra, there are 8 species pairs which are separable in every wavelength (Table 4.2: lower left half) and they are BG vs BS, BG vs CD, BP vs CD, BS vs CD, CD vs CT, CD vs KC, CD vs RA, and CD vs RM (species code may be referred from Table 4.1). Thus in reflectance mode the species *Ceriops decandra* was found to be consistently separable from all the other species. Apart from that, seven other species pairs which are separable in more than 2000 bands (BG vs KC, BG vs RA, BP vs BS, BP vs RA, BS vs CT, CT vs KC and RA vs RM). The species pair with least separability was identified as BG vs BP which was separable only in 903 bands. In first derivative spectra, species pairs such as BP vs RM, BS vs RM, and RA vs RM were

Table 4.2 Number of spectrally separable wavelengths derived from parametric and non-parametric statistical analysis for each species pair at 99% confidence level while laboratory spectral reflectance and its corresponding derivative spectra were used. The results of parametric one way ANOVA is given in lower left half and non-parametric Mann-Whitney U test (shaded in grey colour) is given in upper right half of the table

Reflectance Spectra								
	BG	BP	BS	CD	CT	KC	RA	RM
BG		1191	2100	2100	2045	2021	2095	1648
BP	903		2089	2100	1938	1960	2074	1807
BS	2100	2058		2100	2084	1415	1937	1704
CD	2100	2100	2100		2100	2100	2100	2100
CT	1383	1262	2048	2100		2050	2081	1771
KC	2015	1987	1360	2100	2038		1477	1423
RA	2056	2028	1695	2100	1994	1509		2040
RM	1782	1471	1724	2100	1164	1562	2003	
First Derivative Spectra								
	BG	BP	BS	CD	CT	KC	RA	RM
BG		1297	1016	1196	1305	1143	805	1004
BP	1029		1020	1104	961	1335	1111	1179
BS	906	925		1194	1151	1311	1242	1328
CD	999	1172	825		1327	732	1051	1091
CT	707	1040	1050	1053		1160	863	1132
KC	731	942	697	871	816		1077	1199
RA	893	1191	1107	1146	1123	967		1495
RM	1074	1210	1256	1089	812	1013	1371	
Second Derivative Spectra								
	BG	BP	BS	CD	CT	KC	RA	RM
BG		414	339	433	410	386	294	342
BP	170		400	418	354	418	275	352
BS	202	278		383	413	414	368	428
CD	342	395	414		420	292	353	325
CT	111	167	241	299		362	271	313
KC	165	194	233	263	123		357	339
RA	167	260	269	407	183	190		379
RM	220	247	330	384	122	176	293	

identified as most separable species pairs with more than 1200 significant bands each. *Rhizophora mucronata* was found to be spectrally separable from other species while the first derivative spectra were used. BG vs CT, BG vs KC, and BS vs KC were identified as least separable species pairs. While second derivative spectra was used, BP vs CD, BS vs CD, and CD vs RA were found to be more separable species pairs with almost 400 significant bands each. *Ceriops decandra* was spectrally separable when second derivative spectra were used. Least separable species pairs were BG vs CT, CT vs KC, and CT vs RM making *Ceriops tagal*, the least separable species while second derivative spectra were used (Table 4.2: lower left half). Regarding the location of spectrally significant bands (wavelengths) in the spectral domain of 401nm to 2500nm (Figure 4.6), most of the species pairs were separable in green reflectance (~550nm) and red edge region (720nm to 730nm). In first derivative spectra, most of the species were separable in V (~580nm) and S1 (~740nm and ~1145nm) wavelength regions but not in S2 region. While considering the second derivative spectra case, higher separability was observed only in red edge region (680nm to 720nm) and also near absorption region around 1390nm.

The results reveal that spectral separability among species of *Rhizophoraceae* is found to be in higher order while analyzed using *non-parametric tests* than parametric tests considered for this study (Table 4.2: upper right half). In reflectance spectra, eight species pairs (BG vs BS, BG vs CD, BP vs CD, BS vs CD, CD vs CT, CD vs KC, CD vs RA, and CD vs RM) were completely discriminable at all wavelengths in non-parametric test also. Apart from them, nine other pairs (7 species pairs similar to parametric test result plus two additional pairs which are BG vs CT and CT vs RA) were discriminable in most of the bands (>2000 bands). *Ceriops decandra* and *Rhizophora apiculata* were identified as most discriminable species while reflectance spectra were used. Species pair with minimum separability was BP vs BG which was also similar to that of parametric test results. In first derivative spectra, most separability was obtained for CD vs CT, KC vs BP, KC vs BS, BS vs RM, and RA vs RM. *Bruguiera sexangula* was found to be consistently separable from other species in

first derivative spectra case. Minimum separability was observed in pairs such as BG vs RA, CD vs KC, and CT vs RA.
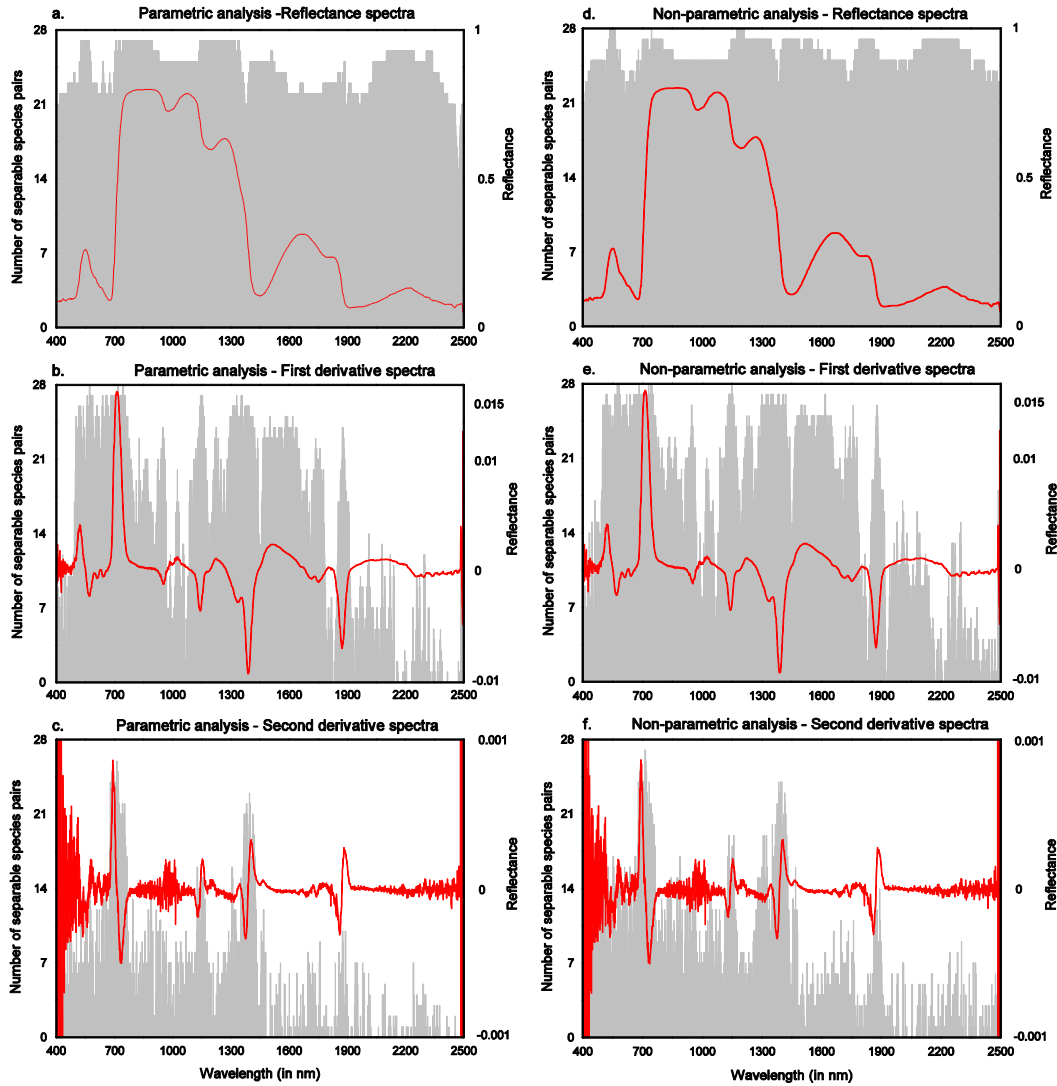
Figure 4.6 Frequency plots depicting the number of spectrally separable species pairs out of 28 pairs at each wavelength obtained from parametric (a, b, c) and non-parametric (d, e, f) statistical analysis in three modes respectively (Row wise - top to bottom: Reflectance spectra, First Derivative spectra and Second Derivative spectra) at 99% confidence interval. The average spectrum of *Rhizophora mucronata* species in each case is plotted in their respective frequency plot for easy interpretation.

81

While in second derivative spectra, maximum separability was observed in species pairs such as BG vs CD, BP vs CD, BP vs KC, and BS vs RM while minimum separability was observed in KC vs CD, BP vs RA, and CT vs RA. While interpreting Figure 4.6, it is evident that more number of spectrally separable species pairs has resulted from non-parametric analysis when compared to that of parametric analysis. In reflectance spectra case, the frequency has increased in green reflectance (~550nm), red edge (680nm to 720nm), absorption band at 1150nm, SWIR bands (1450nm to 2000nm) and in SWIR 2 region (beyond 2350nm). In first derivative spectra case, much improvement was evident in region around 1000nm and bands beyond 1900nm. While in second derivative spectra, more number of species pairs became separable beyond 1460nm.

4.3.2. Statistical methods for separability analysis using transformed spectra

The results represented in Figure 4.7 show the number of species pairs which have more than 90% of separable bands in each of the wavelength region (V, N, S1, and S2) for field and laboratory spectra. Figure 4.8 and Figure 4.9 are frequency plots showing the number of species pairs separable in each wavelength obtained from parametric and non-parametric statistical analysis respectively in four spectral modes for field and laboratory spectra. A threshold value of t=25 is fixed (90% of the total number of species pairs - 28) and those bands which have the value more than 25 are plotted in red colour.
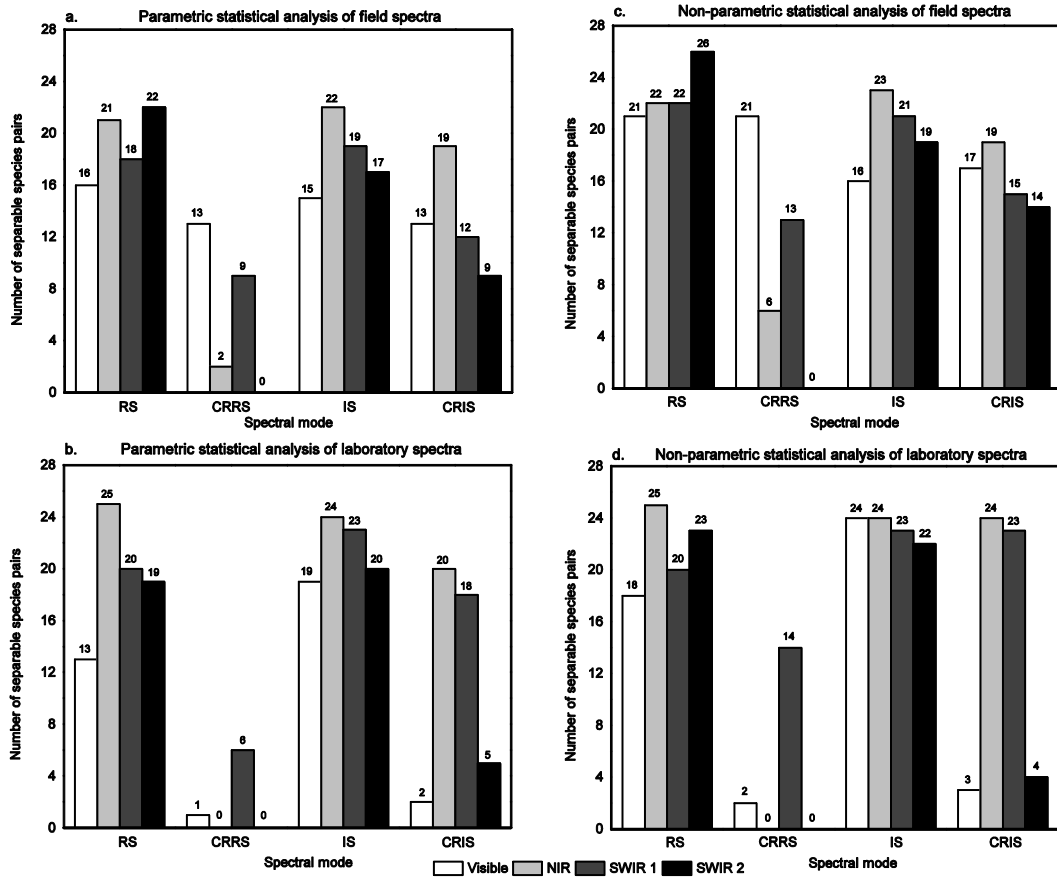
Figure 4.7 Number of species pairs with more than 90% of separable bands in each spectral region obtained from Parametric and Non-parametric statistical analysis using field (a and b respectively) and laboratory spectra (c and d respectively).

4.3.2.1. Spectral separability using parametric statistical analysis

In *field spectra*, we could observe that in CRRS, the continuum removal has reduced the separability in N, S1, and S2 regions (Figure 4.7 a). But CRIS has overcome this effect and enhanced the separability in those regions. 18 out of 28 species pairs have shown better separability in CRIS mode rather than CRRS. While interpreting Figure 4.8, one could infer that in CRRS mode (Figure 4.8 b) though more number of species pairs are separable in visible region particularly in red edge region (688nm to 748nm) and near absorption regions (around 990nm; 1150nm to 1250nm; 1460nm to 1510nm), it is less in NIR plateau (750nm to 950nm; 1060nm to 1100nm), S1 region (1290nm to 1349nm; 1691nm to 1789nm)

and S2 region (bands beyond 2200nm) when compared with RS (Figure 4.8 a). When IS and CRIS are compared (Figure 4.8 c and d), separability could be noticed in visible region (425nm to 525nm; 560nm to 600nm), red edge region (680nm to 720nm) and NIR region around 1050nm in CRIS.

Similar to field spectra, *laboratory spectra* also has shown significant improvement from CRRS to CRIS mode mostly in N, S1, and S2 regions which could be noticed from Figure 4.7 b. From the frequency plot (Figure 4.8), we can observe that IS (Figure 4.8 g) has increased separability when compared with RS (Figure 4.8 e). When RS and CRRS are compared (Figure 4.8 e and f), increase in separability is observed in red edge region (~700nm) and near absorption region in S1 (around 1220nm and 1440nm). Other spectral regions have resulted in decrease in frequency of separability. When CRRS and CRIS (Figure 4.8 f and h) are compared, CRIS has given better separability especially in regions such as 750nm to 1100nm, 1600nm to 1900nm and 2200nm to 2450nm.

4.3.2.2. Spectral separability using non-parametric statistical analysis

From Figure 4.7 c, for *field spectra*, other than RS mode, we could infer that CRRS has better separability in V region whereas CRIS has shown better separability in N and S2 regions. While comparing the RS and CRRS modes in the frequency plot (Figure 4.9 a and b), frequency increased in CRRS in wavelength locations such as visible green (500nm to 550nm), red edge region (690nm to 720nm) and water absorption regions (around 1000nm, 1215nm, and 1490nm). While CRIS and IS are compared (Figure 4.9 c and d), CRIS has increased the number of species pairs in visible green, red edge, N (1050nm to 1100nm) and S1 (1680nm to 1780nm). While CRRS and CRIS are compared (Figure 4.9 b and d), CRIS give better results in regions such as N plateau (750nm to 950nm; 1060nm to 1100nm) and S2 region (beyond 2200nm).

For *laboratory spectra*, it is observed that in all spectral regions, CRIS has improved separability than CRRS, especially in N region it has increased from 0 to 24 (Figure 4.7 d). In the frequency plot, when RS and CRRS are compared (Figure 4.9 e and f), the number of separable species pairs has increased from 26

to 28 in red edge region (690nm to 725nm) and water absorption band (~1220nm) whereas other bands show decrease in separability. But when IS and CRIS are compared (Figure 4.9 g and h), CRIS show separability for all species pairs in regions such as visible green and red regions (500nm to 700nm), red edge region (690nm to 720nm), S1 region (1460nm to 1900nm) and decrease in visible blue (400nm to 500nm) and S2 region particularly beyond 2450nm. When CRRS and CRIS are compared (Figure 4.9 f and h), a considerable increase in number of separable species pairs is seen in CRIS in visible (500nm to 650nm), red edge region (680nm to 720nm), N region (740nm to 1100nm) and S1 (1310nm to 1380nm; 1460nm to 1900nm) and in S2 region (beyond 2200nm).

From the results of both parametric and non-parametric statistical analysis of field and laboratory spectra in different modes, separability was found to be higher through the non-parametric analysis. Hence, further analysis to identify the optimal bands were chosen from the resultant bands of non-parametric analysis which are having more than 25 species pairs in four spectral modes of field and laboratory spectra (Table 4.3).

Table 4.3 Number of wavelengths in each spectral mode of field and laboratory spectra having more than 25 separable species pairs while tested using Mann-Whitney U test

Spectral mode	Field	Laboratory
RS	1144	1051
CRRS	722	308
IS	271	1346
CRIS	409	1087
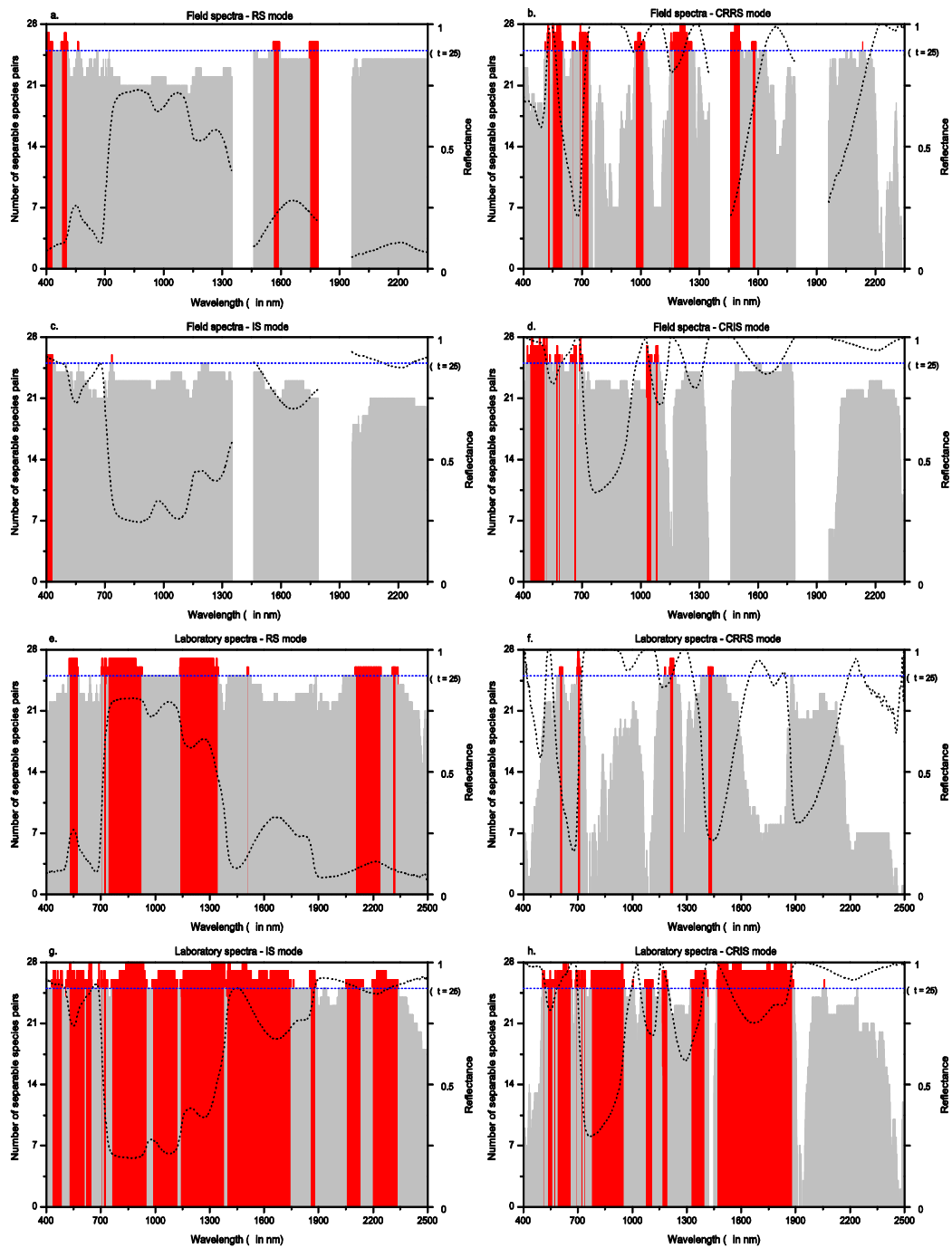
Figure 4.8 *Parametric Analysis*: Frequency plot showing the number of statistically significant pairs at each wavelength location in four spectral modes at 99% confidence interval in field and laboratory spectra. Bands in red colour show the separability above the threshold value (t=25). The average spectrum of *Rhizophora mucronata* species of each mode is plotted in their respective plot for easy interpretation.

86
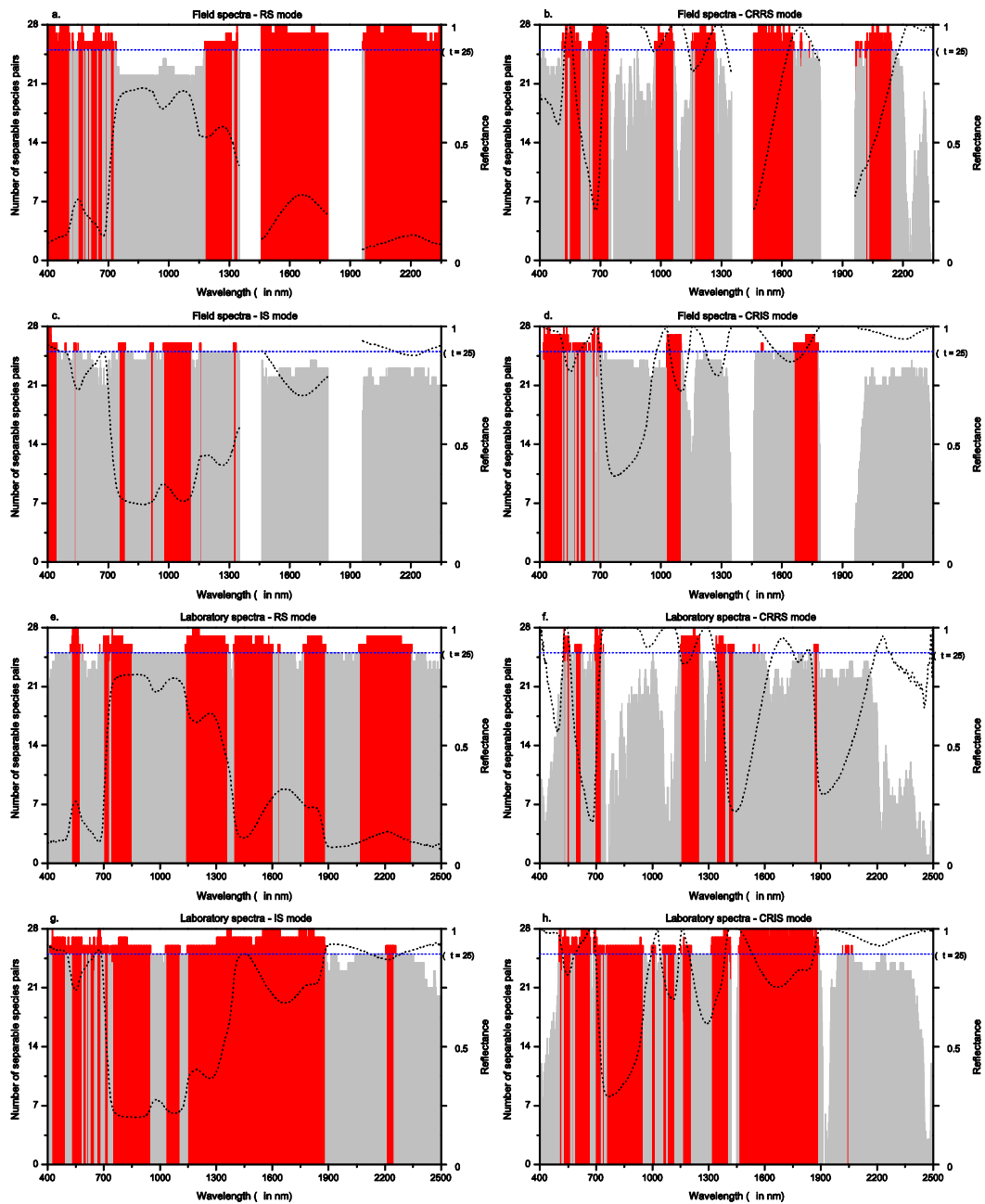
Figure 4.9 *Non-parametric Analysis*: Frequency plot showing the number of statistically significant pairs at each wavelength location in four spectral modes at 99% confidence interval in field and laboratory spectra. Bands in red colour show the separability above the threshold value (t=25). The average spectrum of *Rhizophora mucronata* species of each mode is plotted in their respective plot for easy interpretation.

4.3.3. Feature Reduction Analysis for optimal band selection

The bands selected from non-parametric statistical analysis were taken for further feature reduction and optimal band selection analysis using two feature selection methods: PCA and SDA.

4.3.3.1. Identification of uncorrelated bands using PCA

PCA was used for band reduction analysis to select most uncorrelated bands from the input bands using the covariance matrix. PCA was performed by giving wavelength set chosen from non-parametric analysis as an input. Based on their Eigen values, first five components which show maximum cumulative percentage of variance were selected. From each component, top 10 bands were selected based on their coefficient value. So totally, 50 bands were determined in each spectral mode. In some spectral mode, some of the bands (wavelengths) are redundant within the first five components. Such repetitions were ignored and so the total 50 bands were not achieved in such cases. Such reduced bands selected using PCA in four spectral modes of field and laboratory spectra are tabulated in Table 4.4. The location of wavelengths selected using PCA varies in each case and they are represented using blue colored star symbols (Figure 4.10).

Except in the case of "Laboratory spectra – CRIS mode" (Figure 4.10 h), green reflectance region is selected in all other modes. Similarly red edge region was also selected in all the spectral modes except field CRRS mode (Figure 4.10 b) while reduced using PCA method. Other than that, absorption regions such as 1470nm and 1850nm in S1 and S2 regions also have some significance in species discrimination.

4.3.3.2. Optimal band selection using SDA

To select the most optimal bands for quantitative analysis of spectral separability, bands selected from PCA was further reduced using SDA and results were obtained in four spectral modes for field and laboratory spectra. The selection of optimal bands depends on input data and on the maximum F value and minimum

L value involved in each step of the forward SDA methodology involved. Approximately seven bands got selected in this method, however it varies for each spectral mode based on the number of steps involved in the method. Such optimal bands selected using SDA method in four spectral modes of field and laboratory spectra are represented in Figure 4.10 using red lines and list of selected wavelengths are given in Table 4.5. Overall, uncorrelated bands could be identified in CRIS mode than any other modes in S2 region which is found in 1889nm and 2015nm. Then JM distance metric was used to quantify the separability among species using the wavelengths selected from SDA.

Table 4.4 Wavelengths selected from Principal Component Analysis (PCA) in four spectral modes of eight mangrove species of *Rhizophoraceae* for field and laboratory spectra

Sl. no	Spectral Mode	Selected Wavelengths (in nm)		Cumulative Percentage of variance	
		Field	Lab	Field	Lab
1	RS	421-429, 431, 566-568, 570-572, 701-704, 1285-1294, 1474, 1476-1484 (*40 bands*)	557-563, 699, 701, 704, 709-711, 718-724, 743-752, 768-777, 1818-1827 (*50 bands*)	99.81	99.95
2	CRRS	591-598, 601-602, 1054-1063, 1153-1158, 1557-1566, 1647-1648, 1656-1658, 1692-1698, 1736 (*49 bands*)	537, 543-556, 711-720, 1363-1372, 1874-1883 (*45 bands*)	97.7	99.67
3	IS	401-410, 429-438, 555-564, 762-771, 1337-1344, 1346-1347 (*50 bands*)	433-434, 436-439, 444, 447-449, 552-561, 779-788, 1696-1704, 1722, 1873-1877 (*45 bands*)	99.91	99.89
4	CRIS	502-511, 552-553, 565-566, 569-570, 663-672, 697-698, 705-706, 1041-1050, 1677-1686 (*50 bands*)	626-635, 705-714, 754-763, 1856-1865, 1881-1889, 2015 (*50 bands*)	99.9	99.83
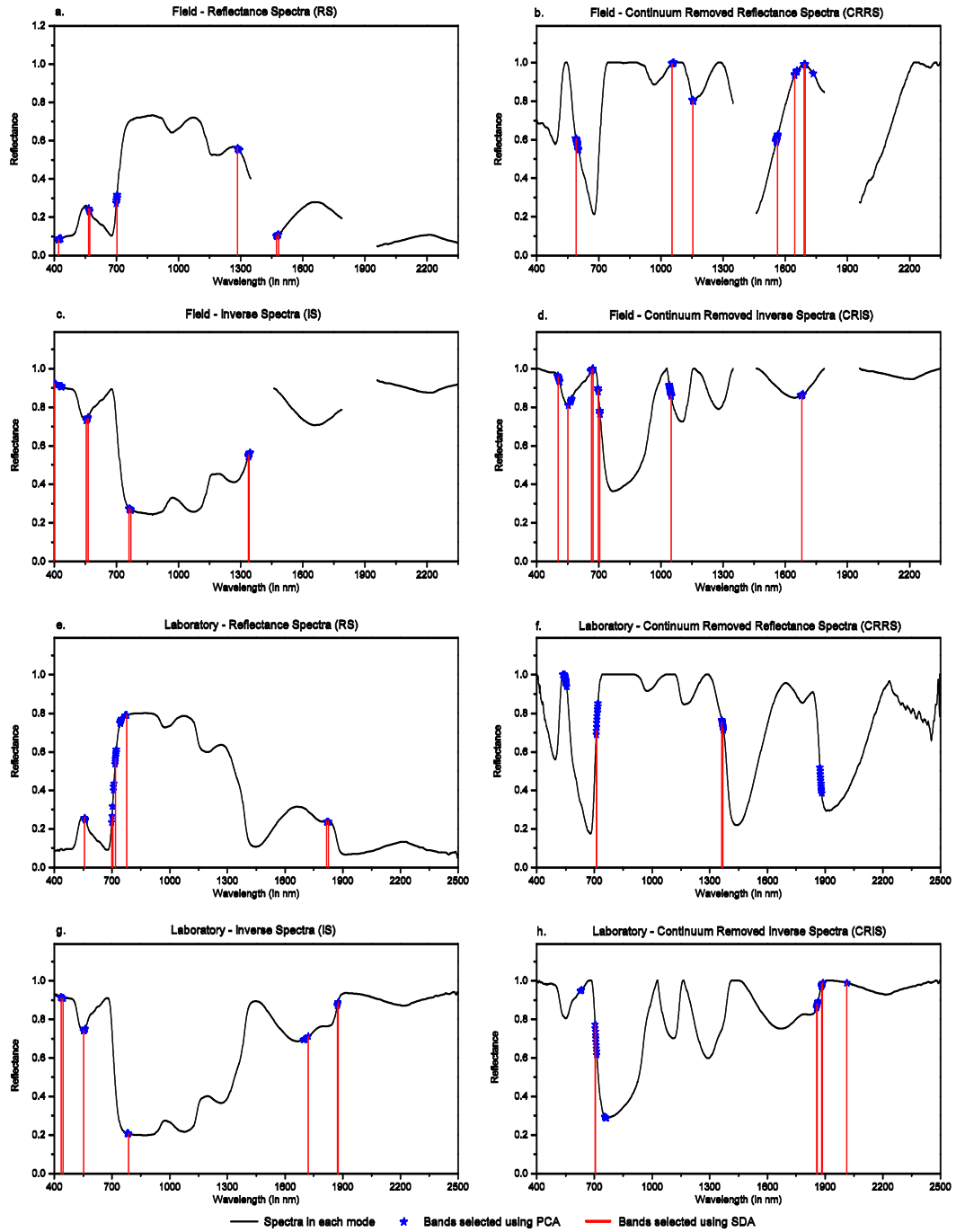
Figure 4.10 Bands selected using feature reduction methods such as PCA (represented by blue star-shaped symbols) and SDA (represented by red lines) in four spectral modes for field and laboratory spectra of eight species of *Rhizophoracaea*. The average spectrum of *R. mucronata* species of each mode is plotted in their respective plot for easy interpretation.

Table 4.5 Optimal wavelengths selected using Stepwise Discriminant Analysis (SDA) in four spectral modes of both field and laboratory spectra for *Rhizophoraceae* mangroves

Sl. no	Spectral Mode	Field - Selected wavelengths (in nm)	Lab - Selected wavelengths (in nm)
1	RS	421, 566, 572, 704, 1285, 1474, 1484 (7 bands)	557, 699, 704, 718, 777, 1818, 1827 (7bands)
2	CRRS	591, 1054, 1155, 1563, 1647, 1692, 1698 (7 bands)	711, 712, 1363, 1369 (4 bands)
3	IS	401, 555, 564, 762, 771, 1337, 1340, 1342 (7 bands)	436, 447, 552, 788, 1722, 1873, 1877 (7 bands)
4	CRIS	504, 552, 665, 672, 698, 706, 1050, 1681 (8 bands)	705, 706, 1857, 1860, 1884, 1889, 2015 (7 bands)

4.3.4. Estimation of spectral separability using J-M distance

Using the optimal bands selected using SDA, JM distance was calculated among each species pair in four spectral modes for field and laboratory spectra and is given in Table 4.6. A threshold value of 1.90 was fixed to determine the separability among the species pair. From the table, in field condition, the spectral distance was found to be consistent in all four spectral modes. In other words, spectral transformation has minimal effect over the spectral discrimination among species. On the other hand in laboratory condition, continuum removal has strong effect over the spectral reflectance rather than inverse spectra. In CRRS, 18 species pairs have JM distance value less than 1.90 in which *Ceriops decandra* and *Ceriops tagal* are found to be less separable from 4 to 6 other species respectively. Contrary to CRRS mode, the continuum removal in CRIS mode has improved the spectral distance among species pairs as only 7 out of 28 species pairs (KC with BP, BS, and RA; RA with BP, and RM; BG vs CT; BS vs CD) have JM distance less than 1.90 (Table 4.6).

Table 4.6 Jeffries-Matusita spectral distance between the species pairs calculated from the optimal wavelengths (bands) selected using Stepwise Discriminant Analysis. The higher value towards 2.00 represents that there is increase in separability between species pairs

Species Pair	Field spectra				Laboratory spectra			
	RS	CRRS	IS	CRIS	RS	CRRS	IS	CRIS
BG vs BP	2.00	2.00	2.00	2.00	2.00	1.86	2.00	2.00
BG vs BS	2.00	2.00	2.00	2.00	2.00	1.61	2.00	1.99
BG vs CD	2.00	2.00	2.00	2.00	2.00	1.93	2.00	2.00
BG vs CT	2.00	2.00	2.00	2.00	1.99	1.98	1.99	1.81
BG vs KC	2.00	2.00	2.00	2.00	2.00	2.00	2.00	2.00
BG vs RA	1.99	2.00	2.00	2.00	1.99	1.90	2.00	1.95
BG vs RM	1.93	2.00	1.99	1.98	2.00	1.92	2.00	1.99
BP vs BS	2.00	2.00	2.00	2.00	1.99	1.68	2.00	1.92
BP vs CD	2.00	2.00	2.00	2.00	2.00	1.97	2.00	2.00
BP vs CT	2.00	2.00	2.00	2.00	1.98	1.83	2.00	1.97
BP vs KC	2.00	2.00	2.00	2.00	2.00	1.91	1.99	1.53
BP vs RA	2.00	2.00	2.00	2.00	2.00	1.89	2.00	1.48
BP vs RM	2.00	2.00	1.95	2.00	2.00	1.66	2.00	1.96
BS vs CD	2.00	2.00	2.00	2.00	1.99	1.29	2.00	1.56
BS vs CT	2.00	2.00	2.00	2.00	1.99	1.65	2.00	2.00
BS vs KC	2.00	2.00	2.00	2.00	1.99	1.89	2.00	1.81
BS vs RA	2.00	2.00	2.00	1.98	1.99	1.22	2.00	1.98
BS vs RM	2.00	2.00	2.00	2.00	2.00	1.71	2.00	1.94
CD vs CT	1.99	2.00	2.00	2.00	1.99	1.86	2.00	2.00
CD vs KC	2.00	2.00	2.00	2.00	1.97	1.98	2.00	2.00
CD vs RA	2.00	2.00	1.99	2.00	2.00	1.84	2.00	2.00
CD vs RM	2.00	2.00	2.00	2.00	2.00	1.35	2.00	2.00
CT vs KC	1.97	2.00	2.00	2.00	1.99	1.58	2.00	2.00
CT vs RA	2.00	2.00	2.00	2.00	2.00	1.80	2.00	2.00
CT vs RM	2.00	2.00	2.00	2.00	2.00	1.81	2.00	1.96
KC vs RA	2.00	2.00	2.00	2.00	2.00	1.98	2.00	1.66
KC vs RM	2.00	2.00	2.00	2.00	2.00	1.77	2.00	2.00
RA vs RM	1.99	2.00	1.94	1.96	2.00	1.90	2.00	1.81

4.4. Extension of the methodology to determine separability among 34 mangrove species

The methodology framed for the separability of closely related *Rhizophoraceae* was further extended to determine the separability among 34 mangrove species (561 species pairs). The details of mangrove species, species code and the number of spectral samples collected in field and laboratory conditions are given in Table 4.7.

4.4.1. Statistical analysis for species discrimination

From the results of spectral separability of *Rhizophoraceae*, it is evident that non-parametric statistical analysis gave better results than parametric statistical analysis. So for the spectral discrimination of 34 species, only non-parametric statistical analysis was carried out.

From non-parametric analysis results, wavelengths (bands) in which the number of separable species pairs more than threshold value (for RS and IS mode threshold was set as 505 and for CRRS and CRIS it was set as 200) were selected for feature reduction analysis (Figure 4.11). The number of such spectrally significant bands obtained for four spectral modes of field and laboratory signatures among 561 mangrove species pairs is given in Table 4.8.

From the Figure 4.11, it is clear that, both RS and IS modes gave same number of separable species pairs in each wavelength for field and laboratory spectra. For *field spectra*, in RS and IS spectral modes, the number of separable species pairs are above threshold in V (400nm to 700nm), S1 (1000nm to 1150nm; 1170nm to 1349nm; 1461nm to 1780nm), and S2 (2000nm to 2300nm) regions (Figure 4.11 a). In CRRS spectral modes, spectral regions such as V (400nm to 550nm), N (800nm to 1000nm), S1 (1150nm to 1349nm; 1461nm to 1789nm), and S2 (1961nm to 2250nm) regions have shown that more number of separable species pairs which are above threshold value. CRIS has given less number of wavelengths than CRRS in which the number of separable species

pairs is above threshold value (Table 4.8). In CRIS, such significant wavelengths are found in V (405nm to 550nm; 680nm to 690nm) and S2 (1789nm; 2000nm to 2320nm) regions.

Table 4.7 The number of field and laboratory spectral samples collected from 34 true and associated mangrove species used for the separability analysis

Sl. No	Species Name	Species Code	Number of Field spectra	Number of Lab spectra
1	*Avicennia alba*	AA	121	150
2	*Acrostichium aureum*	AAU	121	150
3	*Aegiceras corniculatum*	AC	102	150
4	*Amoora cucullata*	ACU	110	150
5	*Acanthus ilicifolius*	AI	109	150
6	*Avicennia marina*	AM	111	150
7	*Avicennia officinalis*	AO	111	150
8	*Aegialitis rotundifolia*	AR	131	150
9	*Bruguiera gymnorrhiza*	BG	89	150
10	*Bruguiera parviflora*	BP	151	150
11	*Bruguiera sexangula*	BS	110	150
12	*Brownlouvia tersa*	BT	120	150
13	*Ceriops decandra*	CD	106	150
14	*Ceriops iripa*	CI	69	150
15	*Cerebra odollam*	CO	129	150
16	*Ceriops tagal*	CT	78	150
17	*Excoecaria agallocha*	EA	111	150
18	*Heritiera fomes*	HF	98	150
19	*Heritiera littoralis*	HL	111	150
20	*Intsia bijuga*	IB	69	150
21	*Kandelia candel*	KC	120	150
22	*Lumnitzera racemosa*	LR	119	150
23	*Merope angulata*	MA	79	150
24	*Phoenix paludosa*	PP	95	150
25	*Rhizophora apiculata*	RA	110	150
26	*Rhizophora mucronata*	RM	136	150
27	*Sonneratia apetala*	SA	120	150
28	*Sonneratia caseolaris*	SC	121	150
29	*Suaeda maritima*	SM	86	150
30	*Salvadoria persica*	SP	139	150
31	*Tamarix troupii*	TT	140	150
32	*Xylocarpus granatum*	XG	111	150
33	*Xylocarpus mekongensis*	XME	110	150
34	*Xylocarpus moluccensis*	XMO	99	150
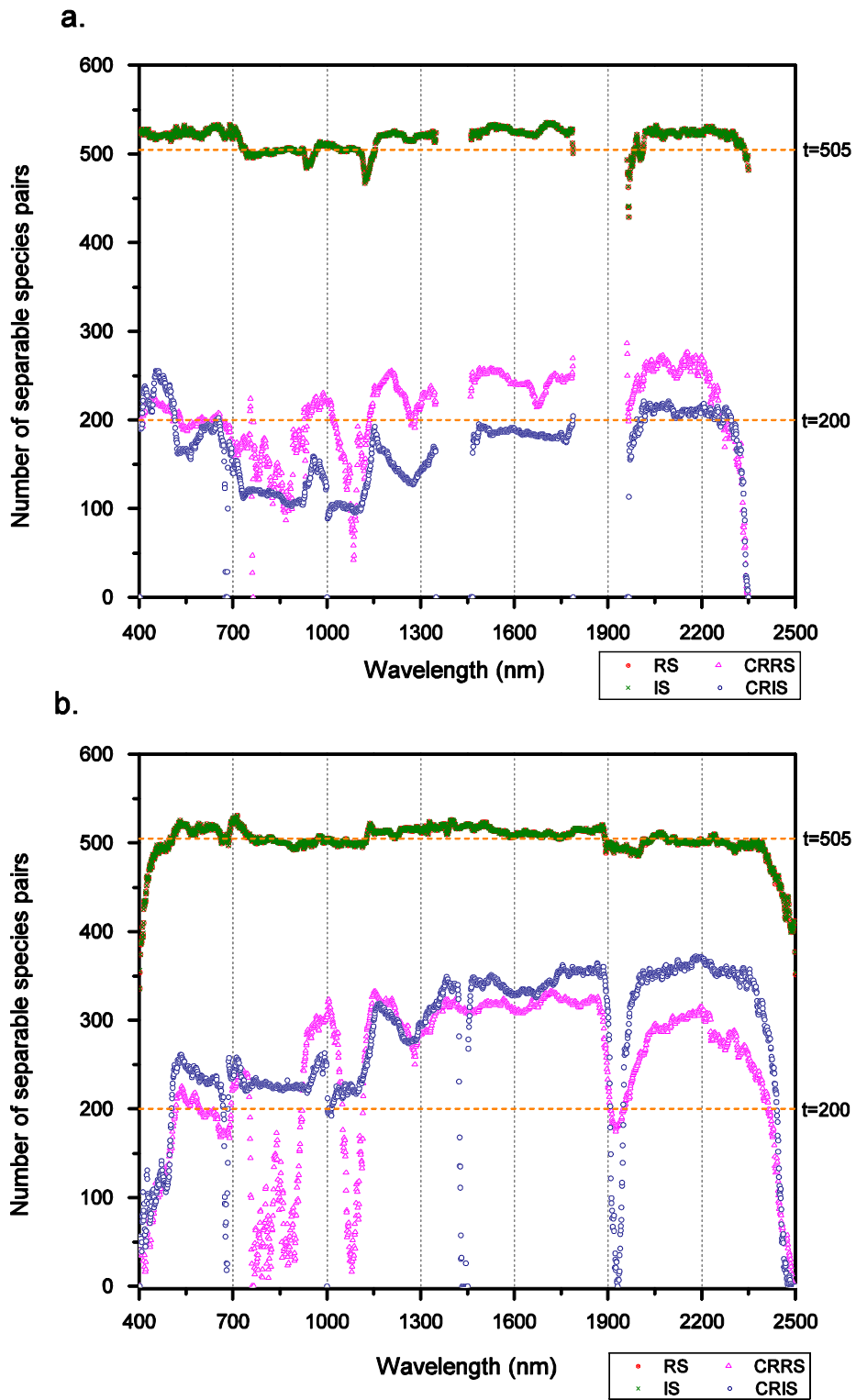
Figure 4.11 Number of significant pairs in each wavelength identified using non–parametric statistical analysis for 34 mangrove species (561 species pairs) in (a) field and (b) laboratory conditions.

Table 4.8 Number of spectrally separable wavelengths (bands) selected using non-parametric Kruskal Wallis test and Mann-Whitney U test for 34 true and associated mangrove species (561 species pairs) using field and laboratory spectra

Spectral data	Spectral Mode	Number of bands selected using non-parametric statistical analysis
Field	RS	1347
	CRRS	1075
	IS	1347
	CRIS	388
Laboratory	RS	1107
	CRRS	1751
	IS	1107
	CRIS	1519

In the case of *laboratory spectra*, similar to field spectra, both RS and IS has same number of wavelengths (1107) which has more number of separable species pairs than the threshold. In these cases, such wavelengths are in V (510nm to 700nm), N (710nm to 820nm; 970nm to 990nm), most of the bands in S1 region between 1128nm to 1830nm, and S2 regions (1831nm to 1890nm; 2042nm to 2083nm; 2229nm to 2245nm) (Figure 4.12 b). In CRRS, V (500nm to 593nm; 695nm to 700nm), N (701nm to 753nm; 923nm to 1051nm), S1 (1117nm to 1830nm) and S2 (1831nm to 1907nm; 1995nm to 2412nm) regions have shown more number of separable species pairs. CRIS has shown more number of wavelengths with higher number of separable species pairs (1751) than CRRS (1519). Wavelengths regions in V (504nm to 670nm), N (701nm to 999nm), S1 (1016nm to 1424nm; 1452nm to 1830nm) and S2 (1831nm to 1907nm; 1949nm to 2439nm) have shown more number of separable species pairs than the threshold in CRIS mode.

4.4.2. Feature reduction for optimal band selection and spectral distance analysis

The selected bands from non-parametric analysis were further reduced using feature reduction methods such as PCA and SDA and measured for J-M distance.

PCA was implemented and principal components were derived. Then first five components were selected and 10 most uncorrelated bands were picked from each of those selected components to further reduce the bands using SDA. The optimal bands selected using PCA and SDA (Table 4.9 and Table 4.10) in four spectral modes are represented by blue stars and red lines respectively in Figure 4.12.

Table 4.9 Wavelengths selected using Principal Component Analysis (PCA) from four spectral modes of field and laboratory spectral signatures of 34 mangrove species

Spectral data	Spectral Mode	PCA selected wavelengths (in nm)	Number of bands selected
Field	RS	636-645; 697-706; 725-730; 732-735; 1461-1462; 1983; 1986; 1988-1994; 2013; 2179-2186	50
	CRRS	516-522; 649-658; 755-757; 929-930; 938-952; 1584-1585; 1594-1601	47
	IS	636-645; 697-706; 725-730; 732-735; 1461-1462; 1983; 1986; 1988-1994; 2013; 2179-2186	50
	CRIS	410-419; 451-460; 511-514; 646-647; 651-654; 1992; 2007-2105; 2102-2111	50
Laboratory	RS	570-579; 703-712; 720-729; 1685-1694; 1884-1891; 2040-2041	50
	CRRS	544-553; 695-704; 753; 1117; 1570; 1575-1583; 2267-2270; 2322-2326; 2404-2412	50
	IS	557-560; 571-580; 704-709; 718-727; 1684-1693; 1884-1891; 2040-2041	50
	CRIS	566-572; 603-605; 617-619;622-625; 649-651; 1040-1043; 1051-1056; 1422-1424; 1696-1705; 1901-1907	50

Table 4.10 Optimal wavelengths selected using Stepwise Discriminant Analysis (SDA) from four spectral modes of field and laboratory spectral signatures of 34 mangrove species (561 species pairs)

Spectral data	Spectral Mode	SDA selected wavelengths (in nm)	Number of bands selected
Field	RS	732, 735	2
	CRRS	522, 649, 658, 755, 756, 938, 952, 1584, 1601	9
	IS	732, 736	2
	CRIS	410, 512, 514, 646, 654, 1992, 2007, 2015, 2102, 2111	10
Laboratory	RS	570, 575, 579, 704, 712, 725, 1687, 1884, 1891, 2041	10
	CRRS	544, 548, 553, 695, 701, 704, 753, 1117, 1570, 1583, 2267, 2270, 2322, 2323, 2326, 2404, 2412	17
	IS	557, 560, 571, 576, 580, 704, 725, 1687, 1884, 1891, 2014	11
	CRIS	566, 569, 572, 603, 605, 618, 622, 625, 649, 650, 1042, 1043, 1051, 1056, 1696, 1901, 1902, 1906, 1907	19

From Figure 4.12, it is observed that, in field as well as in laboratory conditions, the red edge region (680nm to 720nm) is the region prominently selected while analyzed using PCA and SDA feature reduction methods. For *field spectra*, minimum number of bands were selected using SDA in RS and IS spectral modes and they are located in NIR plateau region (732nm, 735nm, and 736nm). In CRRS, apart from visible region optimal bands selected are from NIR and S1 regions (938nm, 952nm, 1584nm, and 1601nm) where as in CRIS these bands are from S2 region (1992nm, 2007nm, 2015nm, 2102nm, and 2111nm). In RS and IS spectral modes of *laboratory spectra* also, almost similar bands were selected using SDA and they are distributed prominently around spectral regions such as green reflectance (550nm), red edge (680nm to 720nm), S1 reflectance peak (1687nm) and water absorption region in S2 region (1884nm, 1891nm and 2041nm). Unlike field condition, both CRRS and CRIS, show similar trend in the selection of bands using SDA and they are distributed in all spectral regions. In CRRS, bands in S2 region (beyond 2200nm) and in CRIS, bands in S1 (around 1050nm) were selected using SDA.
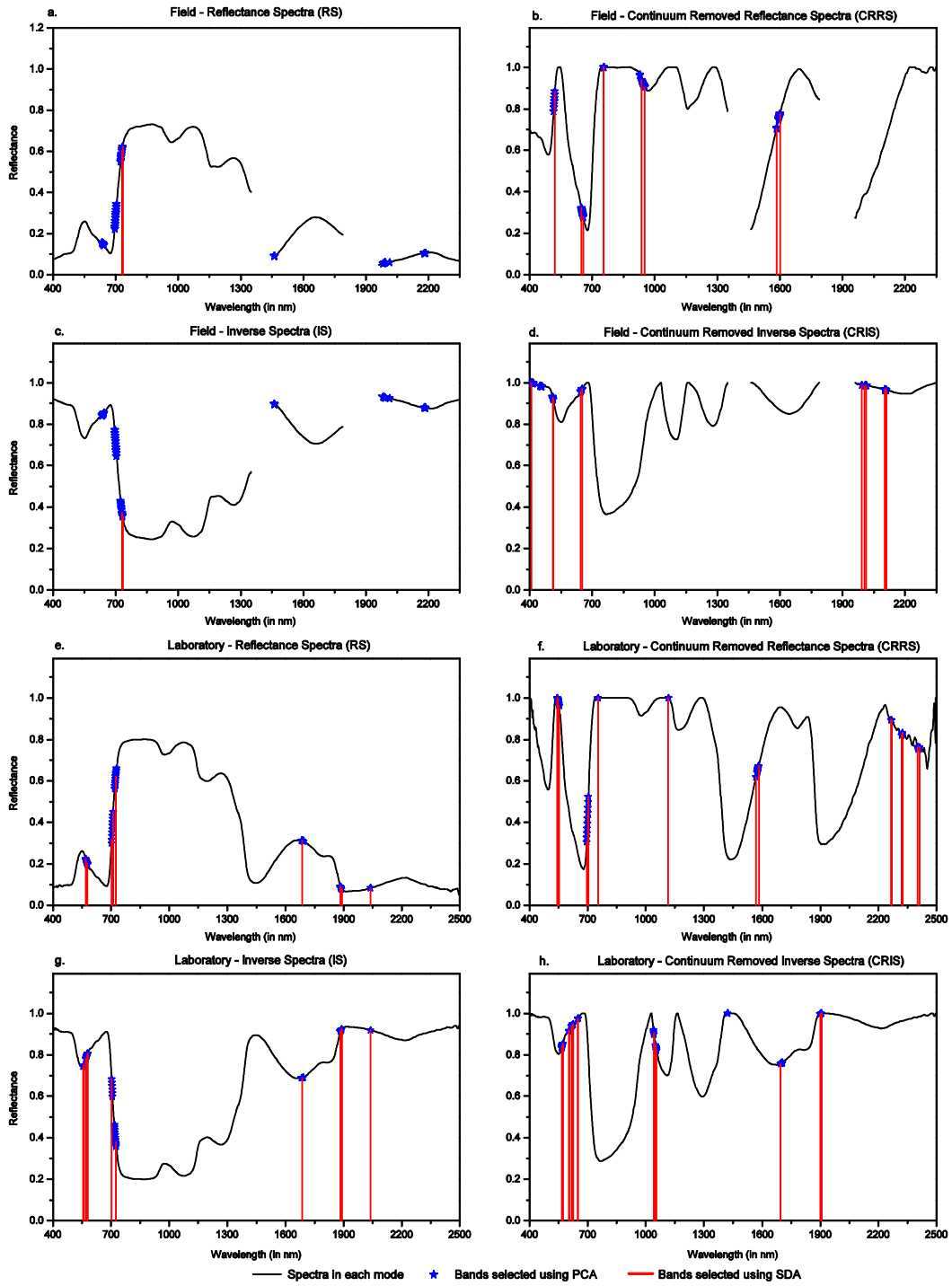
Figure 4.12 Bands selected using feature reduction methods: PCA (represented by blue star-shaped symbols) and SDA (represented by red lines) in four spectral modes of field and laboratory spectra of 34 mangrove species. The average spectrum of *R. mucronata* species of each mode is plotted in their respective plot for easy interpretation.

The optimal bands selected using SDA analysis was then used to quantify the spectral distance by calculating the Jeffries Matusita Distance (JM Distance) among 34 species (561 species pairs). As mentioned earlier, threshold value of 1.90 was fixed to determine the separability among the species pairs. Figure 4.13 represents the number of separable and non-separable species pairs determined using JM distance value in four spectral modes of field and laboratory spectra. In Table 4.11, the species pairs in RS and IS modes of field condition having JM distance less than 1.90 were not given as they are high in number (519 and 447 respectively) with only two input bands from SDA.
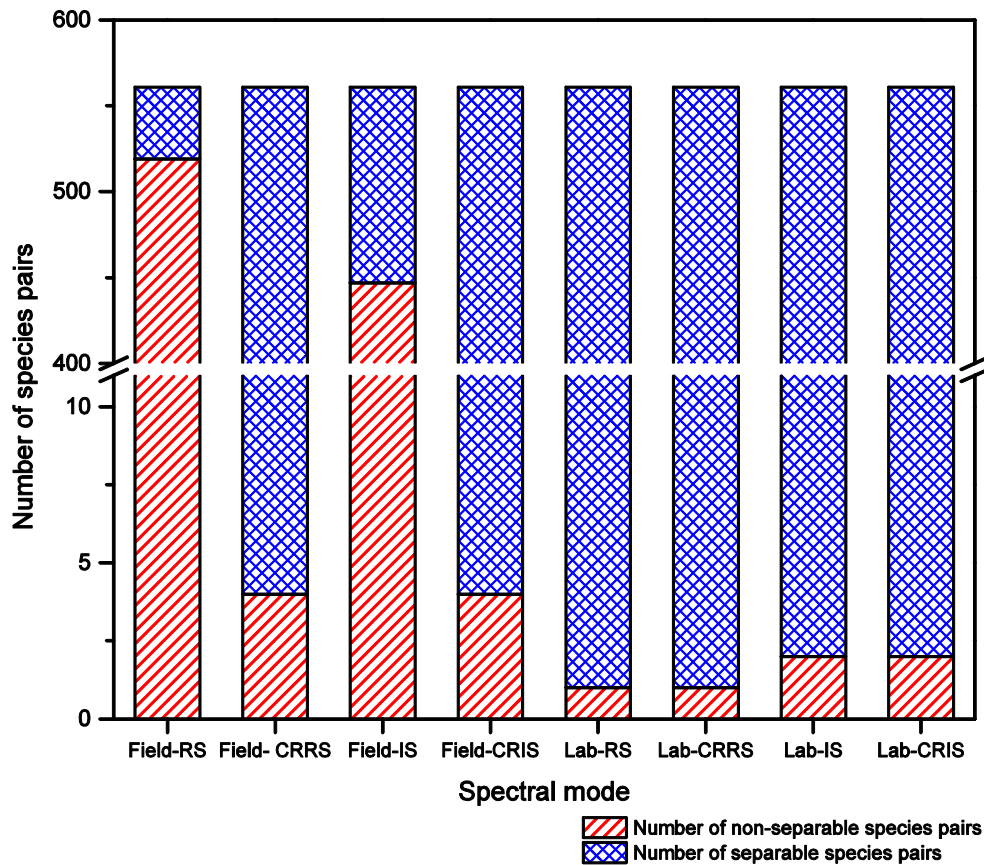
Figure 4.13 Number of separable and non-separable species pairs (out of total 561 species pair combinations) having the JM distance value of greater than and less than 1.90 respectively in each spectral mode of field and laboratory spectra.

In the case of field spectra, the two bands selected using SDA are located in red edge inflection point and most of the species have common value of reflectance in this region. This caused the higher degree of similarity among species. Other than this, only very few species pairs have less separability with other species in other modes. While inferring in species point of view, it is found that all species are found to be separable except, in field condition, the associated species, *Salvadoria persica* has lesser separability whereas in laboratory condition, species such as *Acanthus ilicifolius* and *Heritiera littoralis* have lesser separability.

Table 4.11 Number of non-discriminable species pairs (out of 561 pairs) having Jeffries-Matusita Distance value less than 1.90 (for field only CRRS and CRIS are given)

Spectral mode	Number of non-discriminable species pairs	Non-discriminable species pairs with JM distance value less than 1.90
Field - RS	519	*long list to furnish here*
Field - CRRS	4	ACU vs EA, AI vs RA, AI vs SP, SM vs SP
Field - IS	447	*long list to furnish here*
Field - CRIS	4	AA vs IB, AM vs BT, CT vs LR, RA vs SP
Laboratory - RS	1	AC vs CO
Laboratory - CRRS	1	ACU vs HL
Laboratory - IS	2	AI vs HL, AI vs SP
Laboratory - CRIS	2	ACU vs AI, CI vs HL

4.4.3. Validation of the proposed spectral transformation method using spectra classification

In order to validate the advantage of the proposed spectral transformation method, CRIS and to compare with CRRS transformation method, field and laboratory spectral samples of 34 mangrove species were classified using three supervised classification algorithms: Maximum Likelihood Classification (MLC), Spectral Angle Mapper (SAM), and Support Vector Machines (SVM). The SDA selected wavelengths for CRRS and CRIS spectral modes of field and laboratory spectra were considered for this study. The input training samples were given starting from 5% to 95% of the total spectral samples with an increment of 5% at each step. Testing was done using the remaining samples at each step. There were 10 iterations at each step and at each step random samples were selected for training. Then the final classification accuracy would be the average of accuracies got in ten iterations.

Results show that MLC gave better classification accuracy (more than 95%) than other two classifiers even at 25% of input training samples for both field and laboratory spectra (Figure 4.14 a and b). SAM gave almost same accuracy in each stage of input samples for both field and laboratory (Figure 4.14 c and d) whereas SVM increases the accuracy gradually with more number of training samples. When classified using SVM, for *field spectra*, CRIS showed a significant improvement in accuracy (nearly 40%) when compared with CRRS (Figure 4.14e). On the other hand, for laboratory spectra, CRRS showed an improvement in accuracy (5% to 10%) than CRIS (Figure 4.14f). From the results, we could infer that bands selected in CRIS from SDA (Refer Table 4.10), mainly wavelengths from SWIR 1 and SWIR 2 has enhanced the separability which is the function of biophysical characteristics like Leaf Area Index (LAI), canopy structure and leaf arrangement which are usually well evident in field condition better than laboratory condition where the field conditions were tried to be simulated by arranging leaves randomly. In the *laboratory spectra*, CRRS gave slightly better accuracy than CRIS. This improvement could have been due to the selection of red edge region (690nm to 720nm) in CRRS mode (Table 4.10) which

is more related to the biochemical content of leaves and spectrally discriminant under lab conditions while red edge region is not selected in CRIS mode.
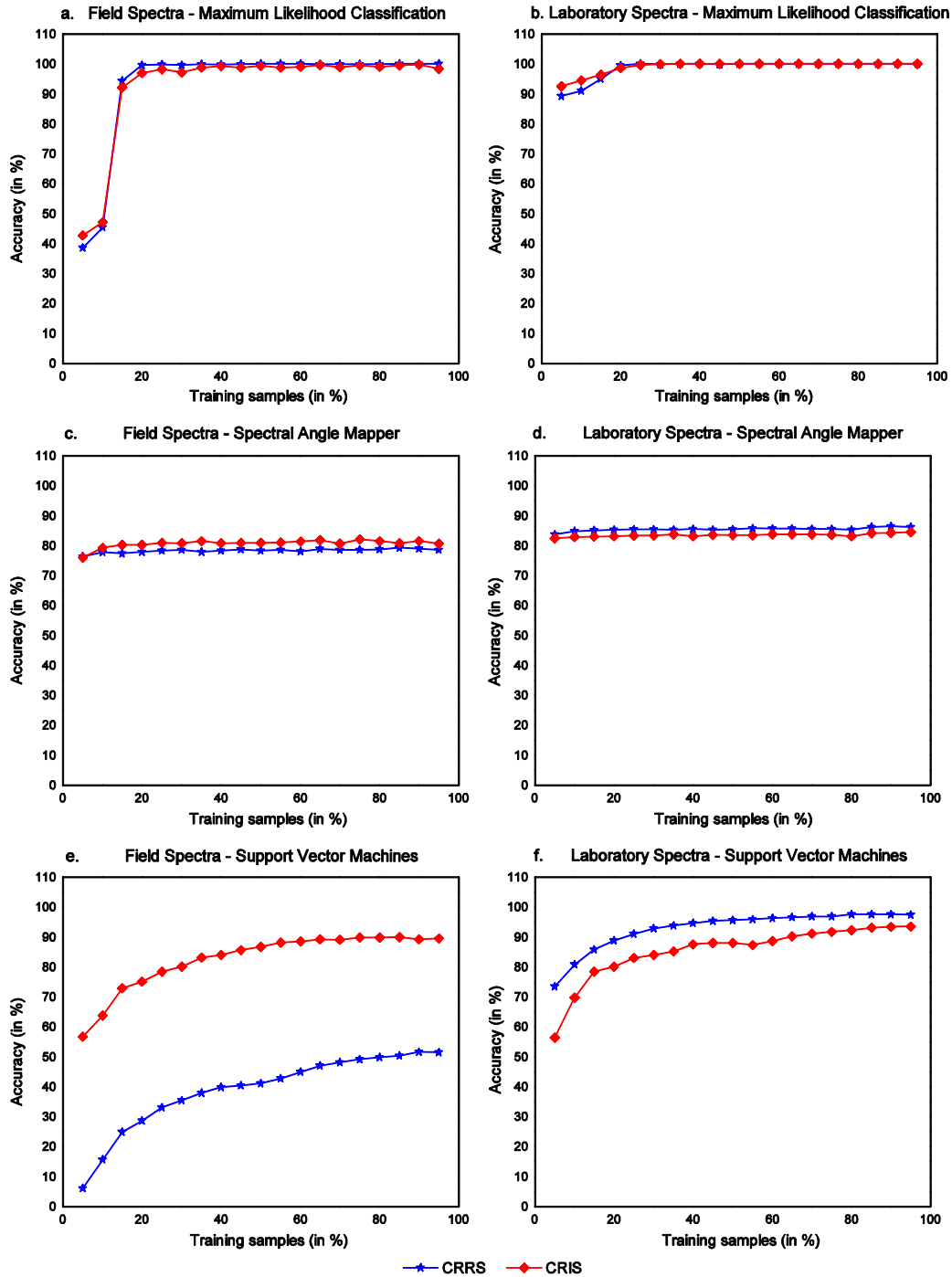
Figure 4.14 Classification accuracy of field and laboratory spectra in CRRS and CRIS modes using three supervised classification algorithms (MLC, SAM, and SVM).

4.5. Discussion

Spectral data in different transformed modes of eight mangrove species of *Rhizophoraceae* have been statistically analyzed using parametric and non-parametric statistical methods for their separability as the first step. The successful transformation and analytical methods are extended for the separability of 34 mangrove species considered in this study.

Even though results of both parametric and non-parametric statistical analysis show that eight species of *Rhizophoraceae* as well as all 34 species considered in this study are spectrally discriminant in many numbers of wavelengths, the results vary among them. This is due to the fact that assumptions made are different in both types of analysis. The non-parametric Mann Whitney U test is found to give relatively better results in most cases when compared to that of parametric one way ANOVA test with Bonferroni post-hoc test. This is because, one way ANOVA test requires homogeneity of variance which is very hard to achieve in the case of vegetation spectra due to high intra-species variation in reflectance and is more susceptible to Type I error which could be controlled by Bonferroni post hoc test by its bound on alpha inflation. But non-parametric statistical analysis is comparatively flexible and it depends on ordinals of values rather than the actual value which makes it easy to analyze. Moreover non-parametric test makes fewer assumptions than parametric test (Manevski et al., 2011).

While laboratory spectra of eight mangrove species of *Rhizophoraceae* are analyzed using derivative spectra, *Ceriops decandra* has higher spectral separability from other species in reflectance and second derivative spectral modes. Red edge region (680nm to 720nm) and water absorption band (around 1150nm and 1400nm) are consistent in discriminating species in reflectance spectra as well its first and second derivative spectra. Non-parametric statistical analysis gave better results than parametric statistical analysis especially in S2 spectral region (1831nm to 2500nm) of second derivative spectra but unable to

discriminate more number of species. This makes the derivative analysis a mediocre method if the separability is expected in SWIR region.

Then, other spectral transformation methods such as continuum removal of reflectance spectra, additive inverse of reflectance spectra (introduced in this study) and continuum removal of inverse spectra are used in this study. The results of parametric and non-parametric statistical analysis of *Rhizophoraceae* species show that bands which are less separable in CRRS are found to be more separable in CRIS and vice versa in spectral region beyond red edge. This is due to the fact that the complementary locations of local maxima in these two modes and subsequent continuum removal, as the original spectra of these two modes (RS and IS) are like mirror image. Also CRIS mode of both field and laboratory spectra increased the number of separable species pairs beyond 2200nm.

While noticing the frequency plots of CRRS and CRIS modes of field and laboratory spectra (Figure 4.8 and Figure 4.9), NIR plateau region is found to lose its potential for spectral discrimination when continuum removed as the local maximum is made to 1. When continuum removed, both parametric and non-parametric statistical analysis of field and laboratory spectra gave separability in visible region (400nm to 700nm). The optimal bands selected using PCA and SDA are highly separable and could be used for species discrimination and the location of such bands varies in each spectral mode. In most cases, wavelengths centered on green reflectance peak (around 550nm) and red edge regions (680nm to 720nm) show high separability. This reveals that there is significant difference in the amount of biochemical contents of leaves such as chlorophyll-b and nitrogen content (Das et al., 2002; Zhang et al., 2014) among *Rhizophoraceae* species as well as other true and associated mangrove species which can lead to another spectro-biochemical study. The other prominent wavelength regions selected after the feature selection are in water absorption region around 1050nm, 1450nm, 1850nm, and 2200nm. The spectral variability in NIR and SWIR regions indicate that the difference in amount of scattering due to multiple refractions and reflections at the boundary between cellular walls and mesophyll cells among

species, presence of nitrogen, protein, lignin and absorption due to water content present in leaves (Tomlinson, 1994; Panigrahy et al., 2012).

Schmidt and Skidmore (2003) has explained that the continuum removal method actually enhances the absorption spectra while normalizing the reflectance peaks thus the outcome of the continuum removal is more correlated with the differences in pigment content rather than that of cell and canopy structure. So in order to understand the correlation between the continuum removal and canopy structure of the vegetation species, in this study continuum removal was applied to the additive inverse spectra for separability analysis (CRIS) and results were found to significantly improve the separability compared to the traditional continuum removal method on reflectance spectra (CRRS). Since the absorption bands in CRRS and CRIS modes are complementary wavelengths, we have the potential advantage of finding out the separability among species pairs in those bands which are less separable in one mode through the other. Thus the effect of continuum removal on canopy structure and cell structure variation could be compensated by continuum removal of additive inverse spectra. The combinations of different spectral modes which give more separability are effectively used in classifying the hyperspectral satellite data which is described in detail in Chapter 5.

In the case of *Rhizophoraceae* mangroves alone, while interpreting the JM distance result, in CRRS, *Ceriops tagal* and *Ceriops decandra* have shown less separability whereas it is significantly improved in CRIS. The reason could be members of *Ceriops* genera possess thicker achlorophyllous tissue when compared with others of *Rhizophoraceae* which could have helped in discriminability through S2 region (Seshavatharam and Srivalli, 1989; Datta et al., 2005; Yuanyue et al., 2009; Manjunath et al., 2013).

On summarizing the outcomes of analysis, we could conclude that non parametric methods result in more separability than parametric methods and the species having maximum separability is found to be *Ceriops decandra* which is separable from five other species in field spectra and from all other seven species in laboratory spectra in RS and IS modes. The methods of statistical separability

analysis followed in this study for CRIS mode could enhance the spectral discrimination among the species of *Rhizophoraceae* in S2 region (particularly beyond 2200nm) compared to earlier methods (Schmidt and Skidmore, 2003). The first part of this study reveals that spectral separability among eight species of *Rhizophoraceae* are evident which was earlier reported as less discriminable in V, N, and S1 regions when six species were analyzed using laboratory spectra (Vaiphasa et al., 2005) and five species were analyzed using field spectra (Manjunath et al., 2013). As already mentioned, CRRS suppresses the separability in NIR and SWIR regions which is actually a function of variability in cell thickness and structure. While CRIS is used, this variability could also be utilized and resulted in better separability. So the proposed method gives an alternative way to enhance the separability by overcoming the homogeneity effect or inseparability in NIR and SWIR regions caused by continuum removal. The PCA and SDA feature selection methods help in identifying the most optimal bands for species discrimination and this methodology could be helpful in identifying the optimal wavelengths in S1 and S2 regions for species discrimination using newly introduced CRIS mode which are normally suppressed when continuum removal was applied over the reflectance spectra.

From the findings of the study on separability among *Rhizophoraceae* mangroves, the methodology developed was extended to find the separability among 34 mangrove species. In the separability analysis of field spectra shows that CRRS mode could discriminate more number of species pairs than CRIS mode in S1 and S2 regions which is reverse in the case of laboratory spectra. Continuum removal generally enhances the absorption bands and so more number of separable species pairs was obtained in absorption troughs. The major outcome of the separability result of 34 mangrove species is that the red edge region (680nm to 720nm) is the most important wavelength region in the spectra for discriminating vegetation agreeing with the results of earlier studies (Schmidt and Skidmore, 2003; Manevski et al., 2011).

The results show that the proposed method has enhanced the separability and helps in identifying significant wavelengths particularly in SWIR 1 and SWIR

2 regions. The validation of the separability result through three supervised classification algorithm also proved that the SWIR region plays a major role in identifying the difference in biophysical properties among mangrove species.

4.6. Conclusion

The results of this study have cleared the uncertainty regarding the lack of spectral discrimination among the *Rhizophoraceae* members and encourage the implementation of the methodology to analyze the spectral separability among vegetation species belonging to the same family. The continuum removal of additive inverse spectra has added the potential advantage of discriminating the species in NIR and SWIR regions based on their variation in cellular and canopy structure which is hard to be achieved in continuum removal of reflectance spectra as it mainly enhances the spectral behavior in visible region resulting due to pigment concentration. The selection of crucial wavelengths which are optimal for species classification of mangrove species could be identified from different spectral modes using PCA and SDA.

In general, green reflectance region (around 550nm), red edge region (680nm to 720nm) and water absorption regions (1470nm and 1850nm) of the spectra play major role in species identification *Rhizophoraceae* species pairs are found to be spectrally separable from the non-parametric analysis and *Ceriops decandra* is found to be the most separable species with other six species of *Rhizophoraceae*. From the separability analysis of 34 species, 557 out of 561 species pairs are found to be separable in field condition and 559 are separable in laboratory condition. In field condition, 4 species pairs, *Salvadoria persica* has lesser separability. On the other hand in laboratory condition, *Acanthus ilicifolius* and *Heritiera littoralis* have lesser separability. The selection of optimal wavelengths from SWIR region has enhanced the separability among species. Therefore, methodology adopted will be helpful in extending the scope of using SWIR regions in species identification of mangroves. Based on the outcome of this chapter, the methodology was implemented for species level classification using hyperspectral satellite data to enhance classification accuracy.

CHAPTER 5

ANALYSIS OF MULTISPECTRAL AND HYPERSPECTRAL IMAGES FOR MANGROVE SPECIES CLASSIFICATION

This study aims at classifying multispectral and hyperspectral images using ten supervised classification algorithms (base classifiers) and multiple classification system for species level classification. Initially, multispectral images (Landsat-8 OLI and IRS-P6 LISS III) were classified using ten base classifiers and its combination, the Multiple Classifier System (MCS) combined using six combination rules (majority voting, maximum, minimum, average, median, and product rules). Results show that, Support Vector Machine (SVM) algorithm gave better accuracy among base classifiers and among MCS combination functions, product rule gave better accuracy. MCS increased the accuracy increased when compared with single best classifier (SVM) in both multispectral images. In case of hyperspectral image (EO-1 Hyperion), the data was transformed into four spectral modes (RS, CRRS, IS, and CRIS) similar to the spectral data transformation adopted in the last chapter. Also, the transformed images in four spectral modes were compiled to utilize the complementary spectral information provided by each of the spectral mode for mangrove species classification. The transformed hyperspectral images in four spectral modes and combined mode were dimensionally reduced using three dimensionality reduction (DR) methods: Principal Component Analysis (PCA), Minimum Noise Fraction (MNF), and Independent Component Analysis (ICA). The dimensionally reduced images in five spectral modes were then classified individually using ten base (single) supervised classifiers. On analyzing the results, MNF-SVM was identified as the best DR-Classifier combination. Then the decisive function values from these ten base classifiers were combined using six combination functions to derive MCS classified image. Results have shown that among MCS, the combined mode gave better accuracy (82.82%) than all the four spectral modes individually.

5.1. Introduction

Remote sensing technology plays a major role in environmental resource monitoring and management activities by providing a plethora of data in regional to micro-level scale for land use/land cover change detection using archived as well as real-time data. The recent developments in spatial, spectral, radiometric, and temporal resolutions have widened the scope of the technology in large-scale applications for continuous monitoring of earth surface dynamics. Melesse et al. (2007) have comprehensively reviewed the potential areas of applications of the technology in environmental resource monitoring and management. As far as the mangroves are concerned, the application of multispectral data for site-specific mangrove zonation mapping is in practice since last thirty years. Generally, medium or coarse resolution multispectral images acquired from Landsat, SPOT, IRS series of satellites were used for regional or community level mapping of mangroves due to its modest spatial as well as spectral resolution. Pixel based classification approach is widely practiced to delineate and quantitatively analyze mangrove cover areas, to demarcate mangroves from other land use/land cover areas and for change detection analysis using multi-temporal images (Jensen et al., 1991; Gao, 1998; Nayak and Bahuguna, 2001; Binh et al., 2005; Giri and Muhlhausen, 2008; Adam et al., 2009; Ajai et al., 2012; Kanniah et al., 2015).

Later, with the development of high spatial resolution sensors and object-based classification approaches, the classification accuracy in mangrove mapping also upgraded to the next level. Satyanarayana et al. (2011) used pan-sharpened multispectral IKONOS image (1m resolution) acquired in 2004 over Galle-Unawatuna sheltered mangroves in Sri Lanka dominated by species such as *Rhizophora apiculata, Excoecaria agallocha, Bruguiera gymnorrhiza,* and *Bruguiera sexangula*. They compared the classification output with 1994 base map and found that there is a dynamic shift in the vegetation of the species *Bruguiera gymnorrhiza* over ten years. True and fringing mangroves of Galapagos Island were distinguished using the hybrid approach of object-based image analysis which combines decision tree classification with SVM algorithm to utilize both spatial and spectral properties of WorldView-2 data. The

110

classification results showed an overall accuracy of 94% (κ = 0.863) to discriminate true mangroves species and other dense coastal vegetation at object level (Heumann, 2011a). Mangroves and non-mangroves were discriminated using Object-Based Image Analysis (OBIA) of high-resolution aerial photographs and WorldView-2 data acquired over Rapid Creek coastal mangrove forest, Darwin, Australia. The highest classification accuracy (89%) was obtained from the pan-sharpened WorldView-2 image when classified using Support Vector Machines (SVM) algorithm to derive species level map (Heenkenda et al., 2014). Kamal et al. (2015) implemented conceptual hierarchical model of multi-scale mangrove features implemented through the rule sets in Geographic Object-Based Image Analysis (GEOBIA) approach for mapping scale-specific, ecologically relevant information on mangroves by classifying Landsat TM, ALOS AVNIR-2, and WorldView-2 data of Moreton Bay (Australia) and Karimunjawa National Park (Indonesia).

Even though multispectral data provides multi-temporal, cost-effective, and high-resolution data, their limited spectral resolution makes it inferior when species level classification becomes our primary objective. Over the last two decades, advancement in areas of research such as sensor optics, data storage and mining, image classification, etc. had made hyperspectral remote sensing an inevitable field in remote sensing technology. The contemporary airborne and spaceborne hyperspectral sensors such as AVIRIS, HyMap, CHRIS Proba, Hyperion, etc. have made the availability of such spectrally rich data for public use which makes the data mining from highly complex hyperspectral data an interesting and challenging field of research. Hyperspectral remote sensing also referred as "imaging spectroscopy" provides user with a huge volume of data inherited with spectrally rich information about various elements of earth surface features which are spectrally similar in multispectral domain (Thenkabail et al., 2012). Hyperspectral remote sensing has potential areas of applications in several fields including environmental monitoring, vegetation and precision agriculture, forestry and ecology management, geology and planetary sciences, food technology, forensic sciences, and military applications. Knipling (1970) discussed the physical and physiological basis of reflectance in visible and near

Infra-red region from leaf and plant canopy and also described the potential application of high spectral resolution data in the field of vegetation science. Hyperspectral data is very sensitive even to a minimum level of spectral reflectance change caused due to variations in biochemical and biophysical properties of vegetation (Asner, 1998). As far as vegetation and forestry is concerned, hyperspectral remote sensing is broadly used in species identification, health monitoring, nutrient intake modeling, biochemical, and biophysical characterization (Okin et al., 2001; Townsend et al., 2003; Govender et al., 2007; Im and Jensen, 2008; Wu et al., 2008; Stagakis et al., 2010; Nidamanuri and Zbell, 2011; Deventer et al., 2015; Roth et al., 2015).

When the applications of hyperspectral data for mangroves are concerned, studies related to species classification are less when compared to other terrestrial forest ecosystems. Hirano et al. (2003) classified airborne AVIRIS data (224 bands; 400 to 2450nm; 20m) using Spectral Angle Mapper (SAM) algorithm to map wetland species of Everglades National Park, Florida (USA) with an overall accuracy of 66%. Jusoff (2006) was able to discriminate nine mangrove species of Port Klang, Malaysia in NIR region (700nm to 900nm) when analyzed using airborne AISA hyperspectral (288 bands; 430nm to 1100nm) and in-situ spectral data collected using hand-held field spectrometer. Yang et al. (2009) performed minimum noise fraction (MNF) and inverse MNF transforms on AISA+ imagery and applied four classification methods such as Minimum Distance (MD), Mahalanobis Distance (MhD), Maximum Likelihood Classification (MLC), and Spectral Angle Mapper (SAM) to map black mangroves in South Texas Gulf Coast, USA. Classification results of MNF reduced image showed that the overall accuracy of MLC was higher (94.7% and 90.7%) when compared with MD (93.3% and 86%), MhD (94% and 89.3%) and SAM (91.3% and 87.3%). Kamal and Phinn (2011) analyzed airborne CASI-2 hyperspectral with 30 bands and spatial resolution of 4m using two pixel-based approaches namely Spectral Angle Mapper (SAM) and Linear Spectral Unmixing (LSU), and an Object-Based Image Analysis (OBIA) using multi-scale segmentation to classify nine land cover classes including three classes of mangroves in Moreton Bay, Australia. The classification results showed that SAM

112

gave better accuracy (overall accuracy 69%, Kappa coefficient 0.57) when compared with LSU (overall accuracy 56%, Kappa coefficient 0.41) in pixel-based approach and OBIA gave the most accurate results (overall accuracy 76%, Kappa coefficient 0.67). They concluded that object-based approach which is a combination of rule-based and nearest-neighbor classification algorithm was the best classifier to map mangrove species. EO-1 Hyperion data was used to classify mangrove species in Talumpuk cape, Thailand. Genetic Algorithm (GA) and Sequential Forward Selection (SFS) were used to select optimal bands and to classify five mangrove species using SAM (Koedsin and Vaiphasa, 2013). In another study, Spectral Information Divergence (SID) was found to be more accurate than Spectral Angle Mapper (SAM) and Spectral Feature Fitting (SFF) while mangrove species of Karachi Coast, Pakistan such as *Avicennia marina* and *Avicennia germinans* was mapped using Hyperion data (Muhammed and Waqar, 2013).

There are many numbers of classification algorithms conceptualized and developed over the years. All those classifiers are unique in their application in which each of the classifiers has some potential advantages in their measure of diversity among classes and also has some shortcomings in the pattern recognition problem. Remote sensing image has inherent noise which misleads the training model to wrong approximations. Also, most of the training models have certain limitations such as the requirement of a large number of training pixels per class, which often could not be achieved in some cases. Such limitations explicitly prove that there is no perfect classifier for a particular class. The diversity in the interpretation of the data by different classifiers and their outputs lead to the development of the concept called "Multiple Classifiers". Multiple Classifier System (MCS) is also referred in different terminologies such as "Ensemble of classifiers", "Composite classifiers", "Divide and conquer classifiers", etc. (Dasarathy and Sheela, 1979; Kuncheva et al., 2001; Prasad and Bruce, 2011). The MCS scheme includes a set of feature reduction methods and a set of classifiers combined using specific combination pattern to enhance the accuracy of the map derived. It is also to be noted that, the classifiers' ability to discriminate classes is based on the information content of the image derived from

different dimensionality reduction methods involved in the MCS architecture (Kanal, 1974).

Studies based on the application of MCS for enhancing the classification accuracy of species level mapping of vegetation and land cover classification is limited in numbers. Two classifiers (Conjugate Gradient Neural Network and Fuzzy Classifier) were combined using the approach called "Decisive Fusion" which uses fuzzy decision rule to fuse the results provided by the algorithms based on the their capabilities to classify urban environment using IKONOS images. Results showed that their approach gave better accuracy than that of individual classifiers (Fauvel et al., 2006). Kalluri et al. (2010) proposed an approach called Multi-Classifier Decision Fusion (MCDF) which implements decision level fusion of spectral reflectance and its derivative spectra for land use land cover classification by overcoming small sample size problem of high dimensional data. They implemented both single (Stepwise Linear Discriminant Analysis dimensionality reduction followed by Maximum Likelihood classification) as well as ensemble classifiers to classify in-situ (ASD Fieldspec Pro hand-held spectroradiometer), airborne (Pro-Spec TIR VNIR), and spaceborne (Hyperion) datasets to test the effectiveness of their proposed approach. The results proved that MCDF outperformed single classifiers especially when training samples per class were limited. Du et al. (2012) have given a detailed review of application of MCS in remote sensing images and done an experiment on implementation of MCS in multi-source remote sensing data such as high spatial resolution multispectral data (Quick Bird), airborne hyperspectral image (OMIS II - Operational Modular Imaging Spectrometer II), and medium resolution multispectral data (Landsat ETM +). Results showed that MCS approaches gave better accuracy than single classifiers and the diversity measure is vital in the selection of classifier combination. In another study, airborne hyperspectral datasets (AISA and HyMap) over three test sites were analyzed to identify optimal classification approach which gives high accuracy in all the three datasets. Three feature reduction (FR) methods (GA - Genetic algorithm, SVMW - Support Vector Machine Wrapper, and PLS - Partial Least Square selection) each combined with two classifiers (SVM - Support Vector

114

Machine and RF - Random Forest) was used to classify two sets of data: full bands and MNF transformed. From the results it is found that MNF transformed image gave better results than full band image when classified and among FR methods used, SVMW gave better results than GA and PLS methods. Important wavelength locations (450nm to 550nm; 650nm to 750nm; 1150nm to 1250nm; 1450nm to 1500nm, and 1950nm to 2050nm) were also identified to discriminate tree species in test sites (Fassnacht et al., 2014). A similar methodology was adopted by Ghosh et al. (2014) to classify two airborne hyperspectral HyMap images of 4m and 8m resolution showed that the optimal spatial resolution for tree species classification is 8m. SVM and RF classification approaches resulted in similar accuracies when used to identify species. When spaceborne hyperspectral EO-1 Hyperion image of 30m resolution was combined with canopy height information derived from LiDAR data and classified using its MNF transformed image, it was found that LiDAR derived height information had no impact on tree species classification in their study.

Five DR methods (ICA – Independent Component Analysis, PCA – Principal Component Analysis, MNF – Minimum Noise Fraction, DWTDR – Discrete Wavelet Transform based Dimensionality Reduction, and OBS – Optimal Band Selection) were incorporated in the MCS scheme which has seven base classifiers (NED – Normalized Euclidean Distance, SAM – Spectral Angle Mapper, SSM – Spectral Similarity Measure, MF – Matched Filtering, ACE – Adaptive Coherence Estimation, OSP – Orthogonal Subspace Projection, and TCIMF – Target Constrained Interference Minimized Filter) and applied to five airborne hyperspectral data. The results were compared with SVM output to study the impact of different dimensionality reduction (DR) methods on different classification results in the MCS architecture. Results show that MCS gave 5% better accuracy than SVM in all images and concluded that different land cover types within the image gave better results in a different combination of DR and classification methods (Damodaran and Nidamanuri, 2014a). Extending their methodology, Damodaran and Nidamanuri (2014b) proposed a new methodology called Dynamic Linear Classification System (DCS), an algorithmic extension of MCS which identifies the optimal combination of classifiers and DR methods to

classify based only on identified combination. Results showed that DCS gave better accuracy than MCS and SVM classification output. Zhang et al. (2015) used ensemble classification method involving three classifiers: k-Nearest Neighborhood (k-NN), SVM, and Random Forest (RF) to classify three multi-source data (aerial photograph of 1m resolution, LiDAR data, and 30m resolution Hyperion data) to map vegetation in Everglades National Park, USA.

With this background, this study aimed to develop a classification framework to improve the number of classes specific to mangrove species and to improve the classification using multiple classifier system (MCS). Though we have analyzed spectra of 34 mangrove species collected in field and laboratory conditions, the spatial resolution of the satellite data and heterogeneous species distribution of the mangrove forest have restricted the identification of all 34 species. Further to that, most of the species are small and grow mostly as understory plants under few dominant species which grow tall. So for the classification of satellite data we chose canopy dominant single species and mixed species. Both multispectral (Landsat-8 OLI and IRS-P6 LISS III) and hyperspectral (Hyperion) satellite data were used in the analysis with the following objectives.

1. To evaluate the performance of ten base classifiers on the classification of different land cover types and mangrove species and to analyze the advantage of using ensemble of these classifiers in mangrove species classification using multispectral data.

2. To study the advantage of using the spectral transformation method (from Chapter 4) to transform Hyperion data to extract complementary spectral information from different modes of the data to improve accuracy.

3. To investigate the effect of different dimensionality reduction methods on different base classifiers to identify best dimensionality reduction-classifier combination.

5.2. Materials used

Classification analysis using different satellite data was carried out to map the mangrove species of Bhitarkanika National Park located in the state of Odisha, India (Please refer Section 3.2.1 and Figure 3.1).

5.2.1. Satellite Data

Two multispectral datasets namely IRS-P6 LISS III image acquired on 24th February 2012 and Landsat-8 OLI image acquired on 23rd January 2014 and one hyperspectral dataset from EO-1 Hyperion sensor acquired on 14th January 2008 were used in the analysis (Figure 5.1 and Table 5.1).

Table 5.1 Spectral specifications of multispectral and hyperspectral data used in the classification

Sensor	Number of bands used	Spectral Bands used	Wavelength (in nm)
IRS-P6 LISS III	4	1	520 to 590
		2	620 to 680
		3	770 to 860
		4	1550 to 1700
Landsat-8 OLI	5	3	530 to 590
		4	640 to 670
		5	850 to 880
		6	1570 to 1650
		7	2110 to 2290
EO-1 Hyperion	155	10 to 57	448 to 926
		81 to 97	953 to 1114
		101 to 119	1155 to 1336
		134 to 164	1488 to 1790
		182 to 221	1972 to 2365

a. IRS-P6 satellite is from India launched on October 17, 2003, which is also known as Resourcesat – 1 has three payloads and operates at an altitude of 817km. One of its sensors, Medium resolution Linear Imaging Self Scanner (LISS III) is used in the analysis. It acquires data at a spatial resolution of

23.5m in four spectral bands with a repeat cycle of 24 days (Chander et al., 2008).

b. Landsat-8 which was launched on February 11, 2013, carries two instruments (OLI – Operational Land Imager and TIRS – Thermal Infra-red Sensor) collects data in 11 spectral bands at a spatial resolution of 30m and temporal resolution of 16 days (Roy et al., 2014).
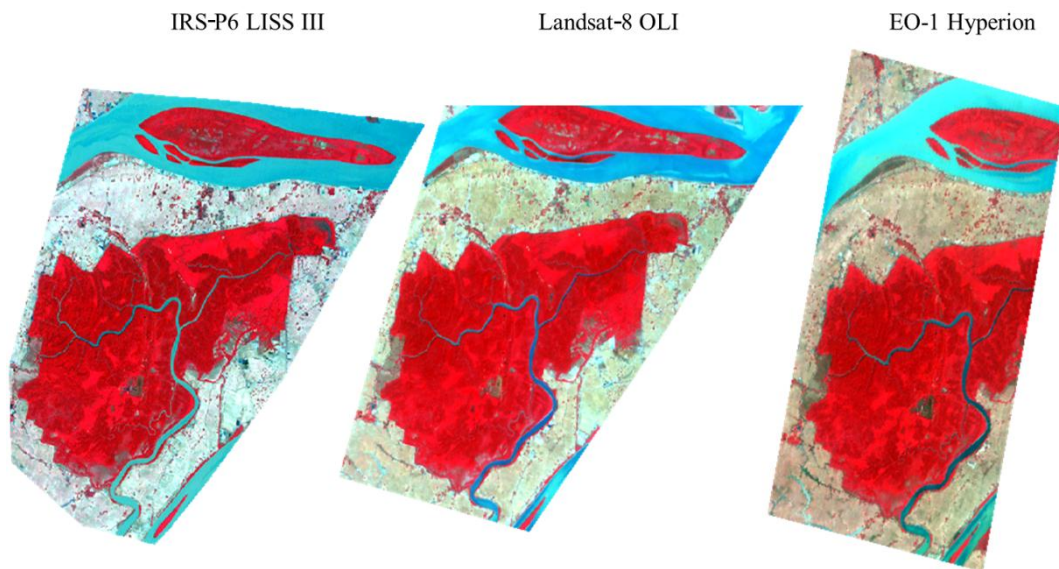
Figure 5.1 False color composites (FCC) images of the study area derived from multispectral (IRS-P6 LISS III and Landsat-8 OLI) and hyperspectral (E0-1 Hyperion) sensors.

Both the multispectral data were preprocessed to convert from Digital Numbers (DN) to reflectance value. In IRS-P6 LISS III data, all the four bands were used for the analysis whereas in Landsat-8 OLI data, only 5 bands (Bands: 3, 4, 5, 6, and 7) were used for the analysis.

c. Hyperion is the first spaceborne hyperspectral instrument aboard NASA's Earth Observation-1 (EO-1) satellite launched on November 21, 2000, in a sun-synchronous orbit at an altitude of 705km. It is a push broom sensor records data in 242 spectral bands (70 bands in VNIR and 172 bands in SWIR) in the spectral range of 400nm to 2500 nm at a spectral resolution of

10nm, spatial resolution of 30m, and swath width of 7.65km. Out of 242 bands, 155 stable bands were selected after removing uncalibrated and atmospheric water vapor absorption bands for further processing (Datt et al., 2003). After that, pre-processing of the image such as removal of noise (smiling effect, streaking, and fixing bad pixels) and atmospheric correction using Fast Line-of-Sight Atmospheric Analysis of Spectral Hypercubes (FLAASH) algorithm of ENVI was done to make the data ready for further processing.

5.2.2. Field data

Species richness and canopy dominant species in stratified random sample locations throughout the study area were identified and recorded with the help of field experts from Forest Department, Government of Odisha who works in Bhitarkanika National Park. During the extensive field data collection during December 2012, April 2013 and April 2014 in the study area, canopy dominant species were recorded from each sample locations as references to select training and testing pixels needed for the classification of images. The geo-coordinates of each sample locations were recorded using Garmin Oregon 550® handheld GPS receiver to collect the locations of training and testing pixels. Apart from the field data collection, the community level mangrove classification map and floristic information and their spatial locations in the study area provided by Space Application Centre, Ahmedabad and M. S. Swaminathan Research Foundation were also taken as secondary data as reference to collect independent training and testing samples for image classification.

5.3. Theoretical background of components of classification framework

In our methodology, we have used the ensemble of classifiers or multiple classifiers system (MCS) for multispectral as well as hyperspectral image analysis. This section of the thesis explains some of the theoretical backgrounds

of MCS, dimensionality reduction methods, and classification algorithms involved in the methodology (Section 5.4) for better understanding.

5.3.1. Developments in Multiple Classifier System

Multiple classifier system (MCS) concept begun in the late 1970's when Kanal (1974) proposed that for a pattern recognition problem, a pool of pattern recognition models will work better than an individual model. MCS attempts to combine decision function values of different classifiers to obtain better accuracy and these component classifiers in MCS are referred as "Base Classifiers". There are three fundamental issues in which single classifiers fails and that could be overcome by the multiple classifier system. They are (i) statistical, (ii) computational and (iii) representational (Dietterich, 2000).

In last two decades, the research on MCS has exponentially increased and widely been used in diverse areas such as target identification, pattern recognition, and image classification. "Bagging", "Boosting", and "Consensus theory" approaches were developed in 1990's for the effective designing of an ensemble of classifiers.

a.   Bagging is the abbreviation of *bootstrap aggregating* which randomly selects different sets of training samples for each of the iteration to design a collection of the classifier and combine their output using vote (Breiman, 1996).

b.   Boosting is the concept introduced by Schapire (1990) which produce very accurate prediction rule by several weak and moderately inaccurate classifiers.

c.   Consensus theory aims at finding consensus among the members of a group of classifiers by assuming that they make a decision based on Bayesian decision theory (Benediktsson and Swain, 1992).

To overcome the shortcomings of previous approaches and to improve the accuracy, Random Forest approach was proposed by Breiman (2001) which is actually an ensemble method uses bagging, or bootstrap aggregating, to form an

ensemble of classification and regression tree (CART) classifier. This classifier model can be implemented as a binary hierarchy to generate a better result for hyperspectral data with limited training samples (Gislason et al., 2006). Ceamanos et al. (2009) introduced SVM-based ensemble which is basically a fusion of multiple classifier system based on SVM and it outperformed other ensemble strategies such as boosting, bagging and random forest in terms of accuracy when large number of training samples are available.

5.3.1.1. Design of MCS

There are three main aspects involved in the successful design of MCS: a) proper selection of diverse classifiers, b) selection of topology for classifier integration, and c) selection of suitable combination function.

In MCS, an ensemble of *diverse* classifiers would be more successful when base classifiers involved disagree with each other when each of the classifiers should predict the class at more than 50% of accuracy and the errors made by each of the classifiers are uncorrelated (Ceamanos et al., 2010; Du et al., 2012).

Next to diversity, the proper choice of *topology* (fusion strategy) improves the performance of the ensemble of classifiers and topology can be categorized into three types: a) cascading, b) parallel and c) hierarchical (Lu, 1996; Ranawana and Palade, 2006).

Combination function is the mathematical function used for the combination of intermediate decision function values of different classifiers involved in the MCS architecture. For example, if $C_1, C_2, ..., C_N$ are set of N classifiers used to approximate a function $f(x)$. To obtain a better approximation result of $f(x)$, MCS combine the outputs $f_{C_1}(x), f_{C_2}(x), ..., f_{C_N}(x)$ from N classifiers using the combination function $f_C(x)$. The combination function of the MSC architecture can be broadly classified into two categories such as trainable and non-trainable combination functions. Non-trainable combination function has no extra parameters that need to be trained once the base classifiers are trained.

Majority voting, maximum, minimum, average, median, and product rules come under this category. On the other hand, in the trainable combination function, combiners are trained to estimate weight of the implementation of the combination function. For example, Behavior Knowledge Space Combiner needs a large independent set of labeled data for training (Roli, 2005).

5.3.2. Dimensionality reduction methods

Hyperspectral data provides the user with lots of spectral information which need to be analyzed effectively for the extraction of only useful information by minimizing the redundant spectral data to avoid misclassification and to increase computational efficiency as well as accuracy (Pal and Foody, 2010). "Hughes phenomenon" refers to the inability of the classifier to classify the hyperspectral data when the number of training pixels per class is lesser than the number of hyperspectral bands (Richards and Jia, 2005). In this study, following three dimensionality reduction methods were used to select uncorrelated bands with useful information for hyperspectral data classification.

5.3.2.1. Principal Component Analysis

Principal component analysis (PCA) is one of the most commonly used dimensionality reduction methods used for hyperspectral data. PCA linearly transforms the correlated features into a set of orthogonal features in a direction of maximum variance in the feature space.

Let x be the individual pixel vector and M be the mean value of the multiband image. First in PCA, the variance-covariance matrix C of the multiband image is calculated.

$$C = \frac{\sum_{j=1}^{n}(x_j - M)(x_j - M)^T}{n-1} \qquad (5.1)$$

where n is the number of pixels. Then the eigenvectors were calculated from the covariance matrix using the equation

$$(C - \lambda_i I)A_i = 0 \qquad (5.2)$$

where $A_i = (a_1, a_2, ..., a_k)^T$ is the eigenvector (direction of the variance) corresponding to the eigenvalue λ_j (variance of the data), k is the total number of feature space dimension and I is the identity matrix. $(C - \lambda I) = 0$ is used to determine all the eigenvalues in the covariance matrix C. Then by using the normalized eigenvectors of the variance-covariance matrix, the new coordinate system is determined where the mapping location f_i of each pixel $x = (x_1, x_2, ..., x_k)$ on the ith principal component can be given as

$$f_i = xA_i = x_1a_1 + x_2a_2 + \cdots + x_ka_k \qquad (5.3)$$

Equation 5.3 represents the rotation of axes of the feature space. The first principal component corresponds to the first eigenvector derived represents the maximum variance of the original data and it decreases subsequently. The number of components extracted from the data depends on the eigenvalue threshold given by the user (Tso and Mather, 2009).

5.3.2.2. Minimum Noise Fraction

Minimum Noise Fraction (MNF) is another popular method used for noise elimination and dimensionality reduction in hyperspectral data analysis. MNF is a linear transformation similar to PCA and essentially it is a "two-cascaded PCA" which performs two consecutive dimensionality reduction steps.

The first transformation estimates the noise covariance matrix which decorrelates and rescales the noise in the data by variance. The resultant data has noise with unit variance and no band to band correlation. In the second transformation, the PCA transformation is performed over the noise whitened data obtained from the first rotation and rescaled by the noise standard deviation in order to reduce the dimensionality of the data. The resultant data after performing the second transformation has a) the noise eliminated coherent MNF eigenimages with larger eigenvalues and b) the noise dominated MNF eigenimages having near unity eigenvalues. Contrary to PCA transform, the resulting axes or components in MNF are not necessarily to be orthogonal but are ordered by decreasing signal-to-noise ratio (Keshava and Mustard, 2002; Harris et al., 2005; Jensen, 2005).

5.3.2.3. Independent Component Analysis

Independent Component Analysis (ICA) is a multivariate data analysis method which assumes that the given data is a linear mixture of statistically independent sources and these components are recovered by calculating an unmixing matrix. Unlike PCA, ICA is based on the concept that maximizes the measure of non-Gaussianity by biorthogonal transformation of the data where axes are not necessarily orthogonal.

Consider a m-dimensional random vector s, and a matrix A of size $m \times n$. The problem is to recover the pair (s, A) from the available n-dimensional vector x and it could be defined as,

$$x = As \qquad\qquad (5.4)$$

This problem is normally referred as "Blind source separation" as there is only a little or no information about mixing matrix A. Also in this problem, for a given x, there is an infinite number of pairs (s, A) that satisfy equation 5.4. In order to get a unique solution, ICA follow some rules such as a) all the components of s have non-Gaussian distribution, b) the number of sources is smaller or equal to the number of observations $(m \leq n)$, and c) only minimum noise is allowed. So the assumption is made that the components of s follow non-Gaussian distribution and are statistically independent. Kurtosis, the fourth order central moment, is used to select non-Gaussian variables. The Fast ICA algorithm is used to obtain the transformation matrix W,

$$y = Wx \Rightarrow y = WAs \qquad\qquad (5.5)$$

The main aim of ICA is to find the matrix $W = A^{-1}$ so that the non-Gaussianity in the projected components y is maximized (Hyvärinen and Oja, 2000).

124

5.3.3. Base Classifiers used in MCS architecture

A few number of hyperspectral image analysis algorithms have been developed mostly from their precursors, multispectral image analysis algorithms. Image classification algorithms deal with the difference in inherent properties of pixels in the dimension of the image and to delineate different regions in the image based on these properties. The decision rule assigned to the allotment of the given pixel to a particular class has to be established in the classification algorithms either by the user or by the algorithm itself which are popularly known as supervised and unsupervised classification algorithms (Varshney and Arora, 2004). In this study, only supervised classification algorithms were used for image classification.

5.3.3.1. Minimum Distance Classification

Minimum Distance Classifier (MD) calculates the mean of the each training class in spectral space and then it measures the spectral distance between each of the pixel in the image to that of the mean of each training class. Euclidean distance is the most common distance measure used in this method. Then, the input pixel will be assigned to the respective spectral class for which the measured distance is minimum. Consider m_i, $i=1,2,…$, M are the means of the M classes in the input data determined from the training data and x is the position of the input pixel to be classified and ω_i is the spectral class. The discriminant function for the MD is defined as,

$$x \epsilon \omega_i, \text{ if } g_i(x) > g_j(x) \text{ for all } j \neq i \tag{5.6}$$

where, $g_i(x) = 2m_i \cdot x - m_i \cdot m_i$

MD is effective when the number of training pixels for each class is limited as it depends only on the mean position of the spectral class and gives better accuracy than maximum likelihood classifier (MLC) in such cases (Joseph, 2005; Richards and Jia, 2005).

5.3.3.2. Maximum Likelihood Classification

The maximum likelihood decision rule is based on the conditional probability of the pixel vector (x) belonging to a particular spectral class (ω_i) is defined as $p(\omega_i|x), i = 1, 2, \ldots, M$ (M - total number of classes). MLC is based on the Bayesian probability formula and the classification rule can be defined as,

$$x \in \omega_i, \quad \text{if} \quad p(x|w_i)\, p(w_i) > p(x|w_j)\, p(w_j) \quad \text{for all } j \neq i \tag{5.7}$$

where $p(\omega_i)$ is the probability of class ω_i occur in the image, $p(x|w_i)$ is estimated from the training data and $p(w_i)$ can also be estimated from expert's knowledge about the image scene (Richards and Jia, 2005; Tso and Mather, 2009).

5.3.3.3. Spectral Angle Mapper

Spectral Angle Mapper (SAM) calculates the similarity of the spectrum of unknown pixel x to the spectrum of the reference pixel r in the vector space of n dimensions. SAM computes the cosine angle between x and t using the formula,

$$SAM_i\,(x) = cos^{-1}\left(\frac{\sum_{i=1}^{N} x_i r_i}{\left(\sum_{i=1}^{N} x_i{}^2\right)^{1/2} \left(\sum_{i=1}^{N} r_i{}^2\right)^{1/2}} \right) \tag{5.8}$$

In SAM, only the angular information of the pixel spectra is considered and so its vector magnitude is ignored. SAM calculates the angle of x with each of the training pixels in N dimensions and assigns the class to which the angle is minimum (Kruse et al., 1993). SAM is also one of the most popular spectral library search methods in hyperspectral image analysis.

5.3.3.4. Spectral Similarity Measure

Spectral similarity measure (SSM) determines the similarity between the unknown pixel and a reference pixel in terms of spectral shape using average spectral brightness and direction. SSM is the hybrid approach which combines normalized Euclidean distance and spectral angle mapper to measure these properties (Granahan and Sweet, 2001). SSM is mathematically expressed as,

$$SSM_i(x) = \left(\frac{1}{N} \sum_{i=1}^{N} (r_i - x_i)^2 + \left(1 - \left[\frac{\frac{1}{N-1} \sum_{i=1}^{N} (r_i - \mu_r)(x_i - \mu_x)}{\sigma_r \sigma_x} \right]^2 \right)^2 \right)^{1/2} \quad (5.9)$$

where N is the total number of bands, r_i and x_i represents reference and unknown pixels respectively. μ_r and μ_x represents mean of r_i and x_i respectively where as σ_r and σ_x represents standard deviation of r_i and x_i respectively. The value of SSM ranges between 0 and $\sqrt{2}$ where $\sqrt{2}$ represents maximum separability among classes.

5.3.3.5. Matched Filter

Matched filter (MF) is one of the covariance based approaches which models the target (*t*) and background (*b*) spectra as random vectors which follow a multivariate normal distribution. The target detection model formulates a binary hypothesis with two components, $H_b : x \sim N(\mu_b, \Sigma_b)$ (target absent) and $H_t : x \sim N(\mu_t, \Sigma_t)$ (target present) with different mean vectors and different covariance matrices (Manolakis et al., 2003). The MF algorithm can be defined as,

$$MF_i(x) = \frac{(r_i - \mu)^T \Sigma^{-1} (x - \mu)}{(r_i - \mu)^T \Sigma^{-1} (r_i - \mu)} \quad , i = 1, 2, \ldots, c \quad (5.10)$$

where, c represents the number of classes, r_i and x represent reference class mean vector and input pixel mean vector. μ and Σ represents background mean vector and covariance matrix respectively. The value of MF becomes 1 when $x = r_i$.

5.3.3.6. Adaptive Coherence Estimation

The Adaptive Coherence Estimation (ACE) method is a commonly used target detection algorithm as it does not require knowledge of all the endmembers. Generalized Likelihood Ratio (GLR) is a statistical distribution model with the assumption that the covariance matrix of the background is same under the two hypotheses (target present and target absent). It is also assumed that, the background has different variance and this variance is directly related to the

percentage of area occupied by the target object in a pixel (Manolakis et al., 2003). This modification in GLR approach is called ACE and is defined as,

$$ACE_i(x) = \frac{\left(r_i^T \Sigma^{-1} x\right)^2}{\left(r_i^T \Sigma^{-1} r_i\right)\left(x^T \Sigma^{-1} x\right)}, i = 1, 2, \ldots, c \qquad (5.11)$$

where c represents the number of classes, r_i and x represent reference class mean vector and input pixel mean vector, and Σ^{-1} represents the covariance matrix of background.

5.3.3.7. Linear Discriminant Classifier

Fisher's Linear Discriminant classifier (LDC) projects high dimensional data onto a low dimensional space to increase separability among classes by maximizing Rayleigh quotient (the ratio of between classes to within class scatter matrices). Assume that there are p classes and n training sample vectors given by $\{r_i\}_{i=1}^n$. Let $C_1, C_2, \ldots, C_p$ be the classes and n_j be the number of samples in j^{th} class, so that total number of training samples can be given as $n = \sum_{i=1}^p n_j$. Let $\mu = \frac{1}{n}\sum_{i=1}^n r_i$ be the mean of entire training sample, and $\mu_j = \frac{1}{n_j}\sum_{r_i \in C_j} r_i$ be the mean of jth class. The within class scatter matrix S_w and between class scatter matrix S_b can be given as

$$S_w = \sum_{r_i \in C_j} \left(r_i - \mu_j\right)\left(r_i - \mu_j\right)^T$$

$$S_b = \sum_{j=1}^p n_j \left(\mu_j - \mu\right)\left(\mu_j - \mu\right)^T$$

In terms of S_w and S_b, Fisher's coefficient can be represented as

$$rq = \frac{W^T S_b W}{W^T S_w W} \qquad (5.12)$$

Here W is the transform matrix of dimension $L \times (p-1)$ which maximizes the Rayleigh quotient (rq) and could be solved by generalized Eigen

value problem $S_b W = \lambda S_w W$ where λ is the generalized Eigen vector by transforming the original L dimensional data into a $(p-1)$ dimensional data to classify p classes (Duda et al., 2001; Du, 2007).

5.3.3.8. Naive Bayes Classifier

Naive Bayes classification (NBC) algorithm is based on Bayes rule, $P(X|Y)$ where X contains n attributes, $X_1, X_2, ..., X_n$ which are conditionally independent of one another given Y and can be expressed as,

$$P(X_1, ..., X_n|Y) = \prod_{i=1}^{n} P(X_i|Y) \tag{5.13}$$

In the case if Y will take on the kth possible value, then the equation 5.13 can be written as,

$$P(Y = y_k|X_1, ..., X_n) = \frac{P(Y=y_k) \prod_i P(X_i|Y=y_k)}{\sum_j P(Y=y_j) \prod_i P(X_i|Y=y_j)} \tag{5.14}$$

This forms the fundamental equation for NBC where $P(Y)$ and $P(X_i|Y)$ can be estimated from training data (Mitchell, 2015). In order to find the most probable value of Y, the NBC rule can be expresses as,

$$Y \leftarrow \underset{yk}{arg\ max}\ P(Y = y_k) \prod_i P(X_i|Y = y_k) \tag{5.15}$$

5.3.3.9. Logistic Regression

Logistic Regression (LR) model is used to predict the probabilities of the classes based on ranking the input features according to their relative importance in the scene. The input pixel x is assigned a class c from the finite set C with the minimum probability of error. LR is also referred as nominal logistic regression (NLR) if there are more than two classes and there is no order between them.

Let p_j, j=1, 2, …., J be the probability that a pixel belongs to class j and J^{th} class is considered as the baseline class. The LR model can be defined as,

$$p_j = \frac{\exp(\beta_{0j} + \beta_{1j}x_1 + \cdots + \beta_{kj}x_k)}{1 + \sum_{l=1}^{J-1}(\beta_{0l} + \beta_{1l}x_1 + \cdots + \beta_{kl}x_k)} \qquad j = 1, ..., J-1$$

$$p_J = \frac{1}{1 + \sum_{l=1}^{J-1}(\beta_{0l} + \beta_{1l}x_1 + \cdots + \beta_{kl}x_k)} \tag{5.16}$$

The parameters $\beta_{ij}, i = 0, \ldots, k$ and $j = 1, \ldots, J - 1$ are parameters need to be optimized and the model is defined in terms of $J - 1$ logit transformation. Then, the sigmoid function is applied over the weighted sum of the input features. To estimate a total of $(J - 1) \cdot (k + 1)$ parameters in 5.16, maximum likelihood method is normally used. For multiclass problem, the logistic regression is implemented by one strategy versus rest strategy (Cheng et al., 2006).

5.3.3.10. Support Vector Machine

Support Vector Machine (SVM) is a non-parametric supervised machine learning classifier frequently used for hyperspectral data classification. SVM employs optimization algorithms to locate optimal boundaries between classes which should be generalized to unseen samples with least errors among all possible boundaries separating classes. In hyperspectral data, the information classes are not linearly separable and often have overlapping training samples and, therefore, slack variable ξ_i , i=1,2,…, n is introduced . The optimal hyperplane can be obtained by solving the optimization problem

$$min\left\{\frac{\|w\|^2}{2} + C\sum_{i=1}^{n}\xi_i\right\}$$

subject to the hyperplanes,

$$y_i(w^T x_i + b) \geq 1 - \xi \; ; \xi_i \geq 0, \; \forall_i = 1,2,\ldots, n \tag{5.17}$$

where x is the point on the hyperplane, w is the normal to the hyperplane, T is the matrix transposition, b represents the bias, C represents the penalty parameter which is purely data dependent. The Lagrangian formulation of optimization problem done using the Lagrangian multiplier $\propto_i$ enforce positivity of the slack variable ξ_i. Then, the decision on the test sample x is determined as,

$$f(x) = sign\left(\sum_i y_i \propto_i x^T x_i + b\right) \tag{5.18}$$

When the training samples are not linearly separable, the samples are mapped using "non-linear SVM". The Kernel function is used to transform the input data to a higher dimensional feature space and the popularly used Kernel function is Gaussian Radial Basis Function (RBF) Kernel (Schölkopf and Smola, 2001; Tso and Mather, 2009).

5.4. Methodology adopted

The methodology adopted in this chapter can be broadly divided into two parts such as (i) multispectral image analysis using MCS and (ii) hyperspectral image analysis using different spectral transformation methods, dimensionality reduction methods and MCS. Following sections 5.4.1 and 5.4.2 describe the procedures of MCS used to classify both multispectral and hyperspectral images. However, for hyperspectral image analysis, additional processing methods such as dimensionality reduction and spectral transformation were carried out at first to derive useful and hidden information from input image and then classified using MCS (Section 5.4.4).

5.4.1. Base Classifiers selection and Classification

The selection of base classifiers is crucial as the ability of classifiers to commit complementary errors is essential to increase diversity in the MCS which eventually enhances the capability of MCS to discriminate classes. We had selected ten base classifiers from different groups of classification algorithms in our methodology for MCS (Section 5.3.3).

a. Three classifiers namely Spectral Angle Mapper (SAM), Spectral Similarity Matching (SSM) and Minimum Distance Classifier (MDC) were based on spectral matching techniques

b. Matched Filtering (MF) and Adaptive Coherence Estimation (ACE) were based on covariance based modeling

c. Linear Discriminant Classifier (LDC), Logistic Regression (LR), Naive Bayes Classification (NBC) and Maximum Likelihood Classification (MLC) were probabilistic methods

d.   A non-parametric supervised classification method, Support Vector Machine (SVM) was also used in MCS. For SVM, RBF (radial basis function) kernel function was used and implemented using LIBSVM toolbox (Chang and Lin, 2011).

The accuracy of classified outputs was assessed using independent testing pixels to derive producer and user accuracy for each class. The classifier which gave higher value of overall accuracy and Kappa coefficient (κ) among the ten base classifiers was labeled as "single best classifier". Then a threshold value was assigned for the maximum overall accuracy for the selection of classifiers by eliminating low performing classifiers for the next step, combination scheme for the MCS. The threshold value for the selection of intermediate classifier outputs was fixed based on many iterations performed to improve overall accuracy.

5.4.2. Combination function for MCS classification

Six non-trainable combination function rules such as (i) majority voting, (ii) maximum, (iii) minimum, (iv) median, (v) average, and (vi) product rules were used to combine intermediate decisive function values (classification outputs) obtained from each classifier in MCS to produce final classification map for each rule. They were then tested for their accuracy using same testing pixels used earlier for the accuracy assessment of base classifiers.

5.4.3. Multispectral Image Analysis using MCS

As the two multispectral datasets used have only limited number of bands (Table 5.1), the dimensionality reduction methods are not necessarily to be implemented and so all bands were given as input in the MCS framework. Based on the primary information collected from the field and the earlier mentioned secondary data, training and testing pixels were collected for 16 spectral classes identified in the image (Table 5.3). The schematic representation of MCS framework followed for the analysis of multispectral images is given in Figure 5.2. The images were classified using ten base classifiers and their accuracy was assessed. A threshold value of 60% was fixed and the intermediate decision values produced by

classifiers which had overall accuracy more than 60% were combined using six non-trainable combination schemes to classify using MCS. And the accuracy was assessed for MCS outputs from six combination functions and the one with highest accuracy was selected as the final classified map.
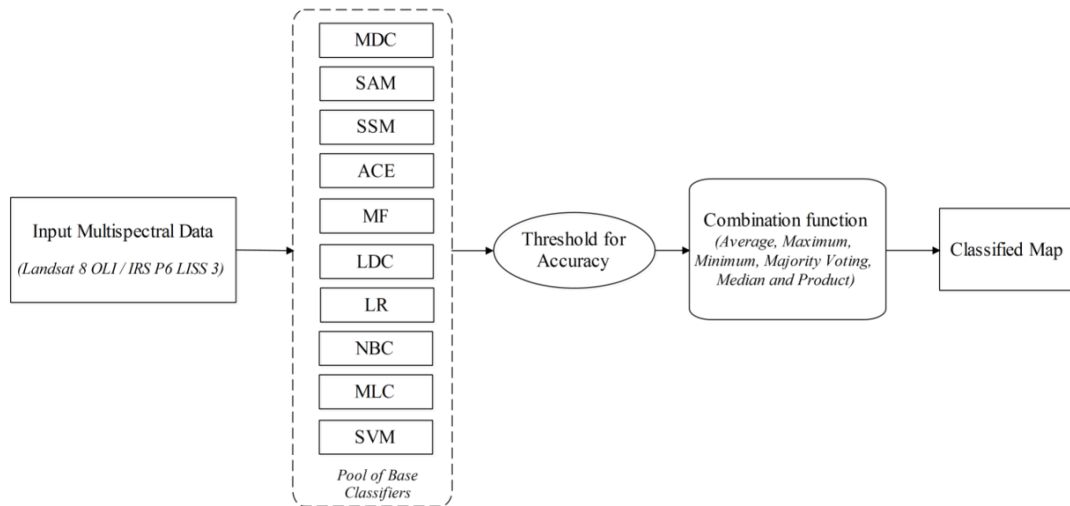
Figure 5.2 Multiple Classifier System (MCS) methodology adopted for the analysis of multispectral (IRS-P6 LISS III and Landsat-8 OLI) image classification.

5.4.4. Hyperspectral Image Analysis using MCS

5.4.4.1. Spectral Transformation of Hyperion Image

Following the atmospheric correction of the Hyperion image, the reflectance image was transformed into images of three other spectral modes such as additive inverse of reflectance spectra (IS), continuum removed reflectance spectra (CRRS) and continuum removal of additive inverse spectra (CRIS) as described in Chapter 4 (Section 4.2.2.2 and 4.2.2.3). For example, the grey scale image of red edge band (690nm) for RS and CRRS spectral modes and SWIR band (1225nm) for IS and CRIS spectral modes of Hyperion image are given in Figure 5.3. The spectral transformation methodology as established in Chapter 4, gives complementary information from additive inverse and continuum removal

techniques which helps in discriminating features which are spectrally similar in reflectance spectra mode (RS).
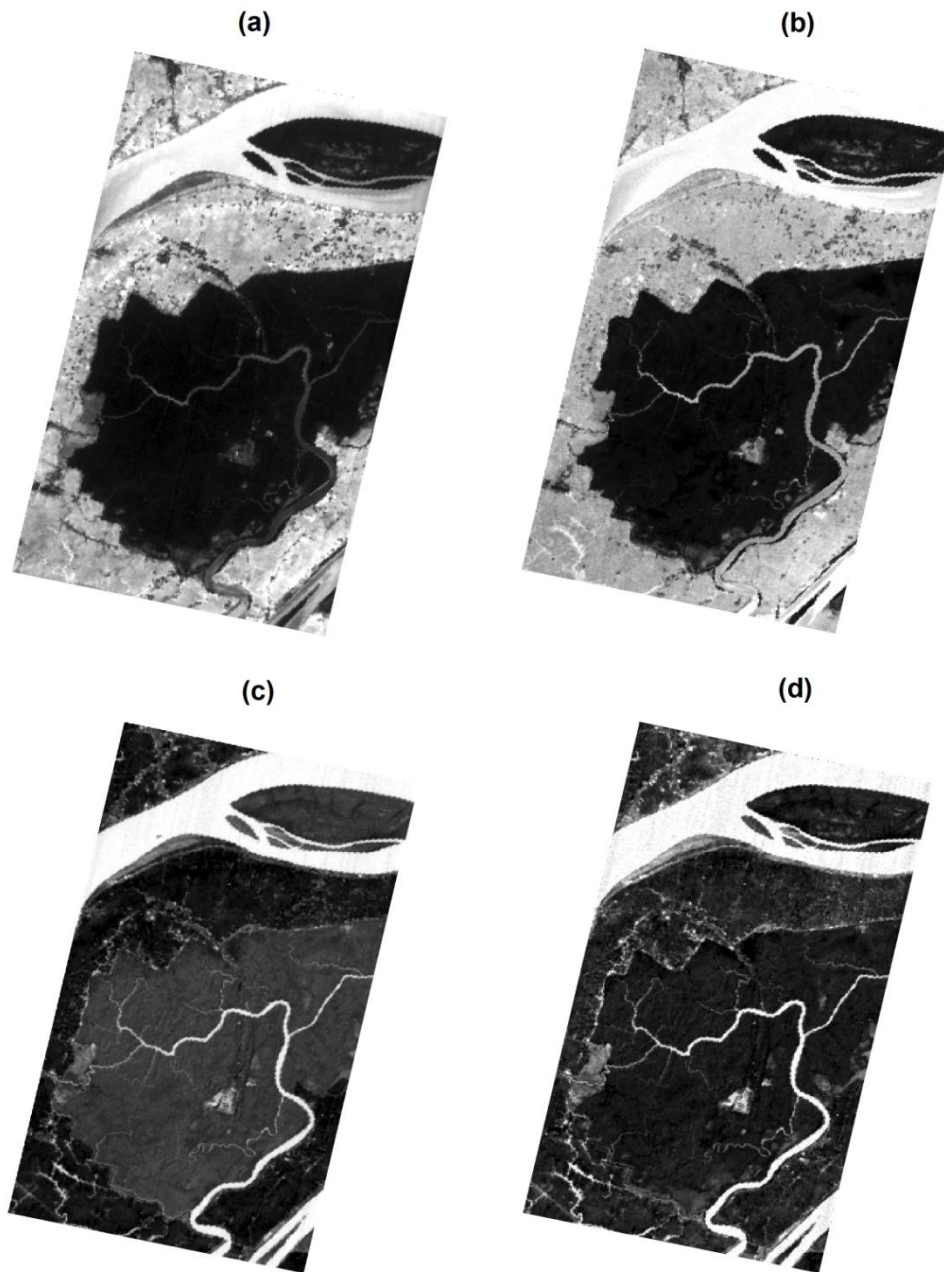
Figure 5.3 Grey scale image of Red edge band (690nm) in (a) RS and (b) CRRS modes and SWIR band (1225nm) in (c) IS and (d) CRIS modes of EO-1 Hyperion image.

5.4.4.2. Dimensionality reduction

In our methodology, three dimensionality reduction (DR) methods such as ICA, PCA and MNF (Section 5.3.2) were implemented in hyperspectral data in four spectral modes separately in order to avoid redundant information and to derive only useful information from the data. First 15 components in each of the DR method output in four spectral modes each were selected for classification. The components selected from each of the DR methods were analyzed for any ambiguities before implementing classification algorithms. The components from all four spectral modes derived from each DR method were compiled together individually. Then all the 15 datasets (5 modes of 3 DR) were classified using MCS.

5.4.4.3. Classification of Hyperion image using MCS

Initially, 19 spectral classes were identified based on the field and secondary datasets. Training and testing pixels were collected for each of these classes. Classification outputs for each of the three DR methods from ten classifiers (3x10 = 30) were obtained for four spectral modes of the hyperspectral image separately. Each of the classification outputs was tested for its accuracy to identify "single best classifier" among the pool of classification output from three dimensionally reduced inputs in each spectral mode. Based on the overall accuracy and Kappa coefficient, a threshold value was fixed to eliminate low performing classifiers out of the combination scheme of the MCS. The threshold value was fixed by giving different iterations of threshold values (65%, 70%, and 75%) to analyze the changes in the overall accuracy of the MCS classification output. The schematic representation of the MCS architecture used for hyperspectral image analysis is represented as Figure 5.4. The Matlab$^{®}$ programme developed for MCS by Damodaran and Nidamanuri (2014a) was adopted with relevant modifications which are essential for the current study such as introduction of spectral transformation techniques, modifications in DR techniques and classifiers.
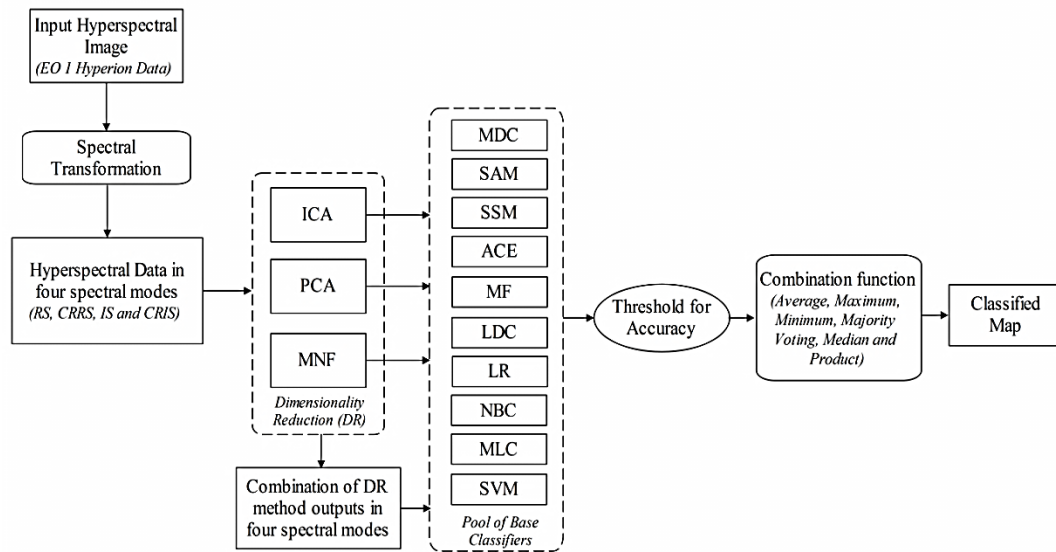
Figure 5.4 Methodology adopted for the classification of hyperspectral (EO-1 Hyperion) image using Multiple Classifier System (MCS).

5.5. Results

In order to achieve our objectives of this chapter, we have conducted two sets of experiments. First, we conducted the classification of multispectral images from Landsat-8 OLI and IRS-P6 LISS III using single classifiers and MCS. Then to identify more number of classes, hyperspectral image from EO-1 Hyperion was used for classification using single classifiers and MCS with additional steps such as spectral transformation and dimensionality reduction methods.

Accuracy assessment was done using test pixels collected separately for IRS-P6 LISS III and Landsat-8 OLI images by calculating user (UA) and producer (PA) accuracies for the 16 classes. Overall accuracy (OA) and Kappa coefficient (κ) were calculated for each of the classification output from ten base classifiers. The OA (in %) and Kappa coefficient (κ) from ten classifiers for IRS-P6 LISS III and Landsat-8 OLI images are given in Table 5.2. From that we could infer that, SVM gave highest accuracy and become "single best classifier" for both of the datasets.

Table 5.2 Overall accuracy (OA) and Kappa coefficient for IRS-P6 LISS III and Landsat-8 OLI multispectral image for ten base classifiers

Data		Base Classifiers in MCS									
		MD	SAM	SSM	ACE	MF	LDC	LR	NBC	MLC	SVM
IRS-P6 LISS III	OA	54.89	55.12	54.98	39.64	2.52	60.90	64.63	68.40	68.15	**75.99**
	Kappa	0.49	0.49	0.49	0.34	0.00	0.53	0.58	0.63	0.63	**0.72**
Landsat-8 OLI	OA	61.94	59.78	60.14	63.47	11.55	65.12	45.68	65.24	69.08	**74.72**
	Kappa	0.58	0.56	0.56	0.60	0.08	0.60	0.36	0.61	0.65	**0.72**

5.5.1. IRS-P6 LISS III multispectral image

From the base classification results of *IRS-P6 LISS III* image, SVM gave the highest accuracy (OA – 75.99% and κ – 0.72) followed by NBC (OA – 68.40% and κ - 0.63) and MLC (OA – 68.15% and κ – 0.63). The least performed classifier in the group was MF, which has the OA of only 2.52% and κ value of 0 (Table 5.2) as it could not classify most of the classes i.e., with "0" output pixels for these classes. Out of 16 classes, the best performing classifier (SVM) resulted the highest PA and UA for river (97.03% and 99.02%) and the lowest (30.91% and 39.08%) for cleared area. Among mangroves, *A. officinalis* (dense) class had the highest PA and UA (75.42% and 74.79%) and the mixed mangroves had the lowest (47.52% and 34.04%) (Appendix 3).

A threshold value of 60% was fixed to select the base classifiers producing higher accuracy. Based on that, five base classifiers namely LDC, LR, NBC, MLC, and SVM were selected for MCS using six combination functions to derive six classification outputs. Comparing the classification results from six combination functions of MCS, the product rule resulted highest accuracy (OA – 76.42% and κ – 0.72) and median rule resulted the lowest (OA – 64.22% and κ – 0.57). On analyzing the PA and UA of the highest performing classification in MCS (product rule) we could observe that, maximum accuracy was obtained for fallow land (98.71% and 100%) while minimum for mixed mangroves (48.51%

137

and 34.03%). Among mangroves, maximum accuracy was obtained for *A. officinalis* (dense) (75.42% and 74.79%) which is similar to the results of single best classifier (SVM) ('Product' in Table 5.3). We could get only marginal increment (i.e., 0.43%) in the overall accuracy of MCS when compared to SVM. The final classified output derived from single best classifier (SVM) and MCS with product rule are given as Figure 5.5.

5.5.2. Landsat-8 OLI multispectral image

As far as the *Landsat- 8 OLI* image is concerned, SVM gave the highest accuracy (OA – 74.72% and κ – 0.72) followed by MLC (OA – 69.08% and κ – 0.65) and NBC (OA – 65.24% and κ – 0.61). Similar to LISS III image, MF has the lowest accuracy (OA – 11.55% and κ – 0.08). The producer and user accuracies of SVM (single best classifier) show that river (100% and 99.37%) and creeks (95.65% and 100%) were classified accurately and the lowest accuracy was observed for wetlands (42.65% and 22.31%). Among mangroves, similar to IRS–P6 LISS III data, *A. officinalis* (dense) was classified with highest PA and UA (94.44% and 99.17%) whereas the lowest (34.58% and 37.76%) was observed for the class *E. agallocha* (dense) (Appendix 4).
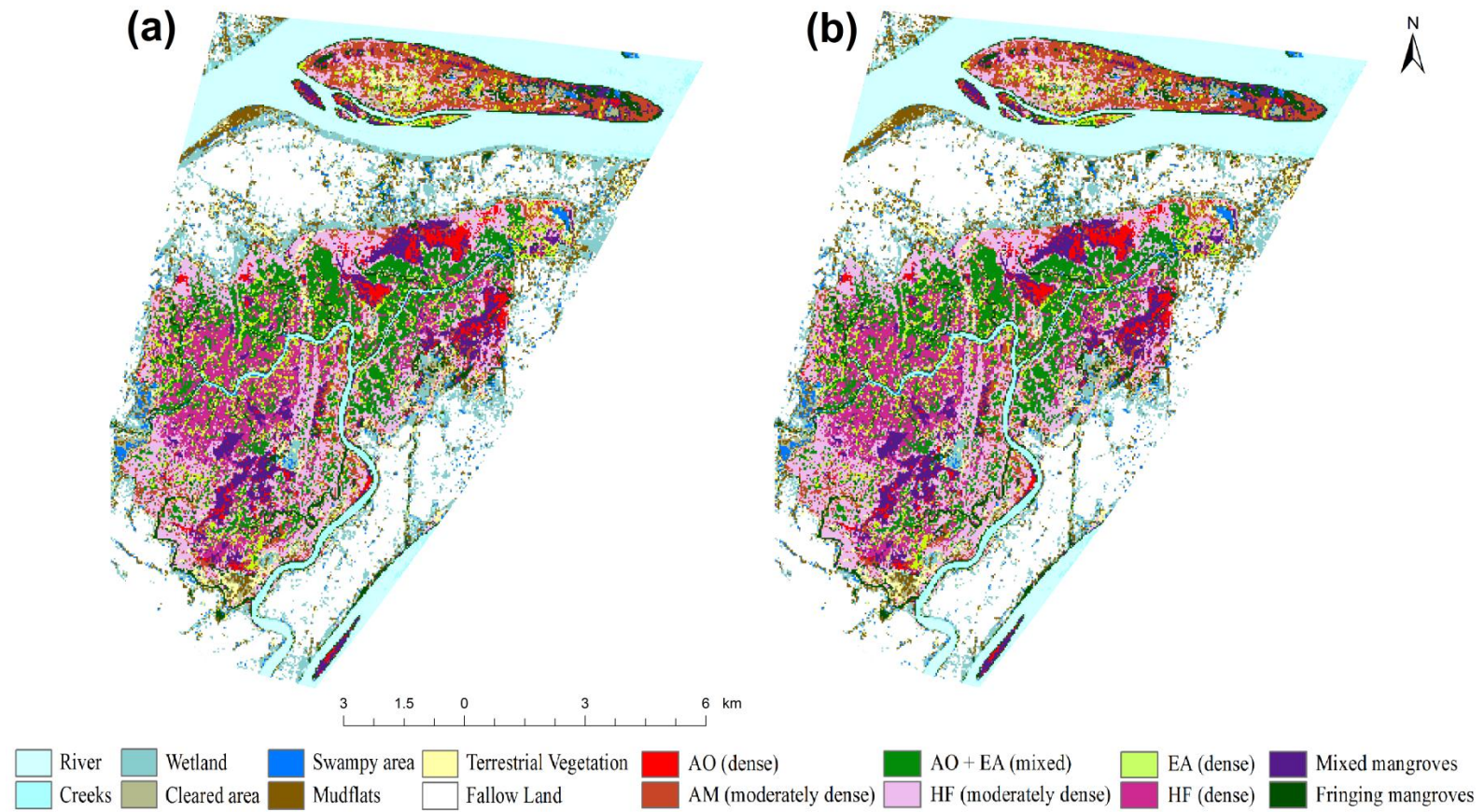
(AO – *Avicennia officinalis*, AM – *Aviccenia marina*, EA – *Excoecaria agallocha*, HF – *Heritiera fomes*)

Figure 5.5 Classification outputs of IRS-P6 LISS III multispectral image obtained from (a) SVM (single best classifier) and (b) MCS (Product rule combination function – MCS output with highest overall accuracy).

Table 5.3 Accuracy assessment of MCS classification of IRS-P6 LISS III for six combination functions

Sl. No	Class	Majority Voting		Maximum		Minimum		Median		Average		Product	
		PA	UA	PA	UA	PA	UA	PA	UA	PA	UA	PA	UA
1	AO (dense)	0.00	0.00	0.85	25.00	75.42	74.79	1.69	18.18	58.47	82.14	75.42	74.79
2	AM (moderately dense)	1.07	15.38	1.60	30.00	33.69	55.75	4.28	17.02	13.90	44.07	33.69	55.26
3	AO + EA (mixed)	77.37	60.57	72.63	61.99	76.64	70.47	81.39	50.45	78.83	62.97	76.28	70.13
4	HF (moderately dense)	64.44	47.74	50.56	48.4	65.28	69.32	67.78	45.27	69.17	50.61	65.56	67.62
5	EA (dense)	30.63	50.75	46.85	40.00	41.44	40.00	0.00	0.00	19.82	46.81	38.74	40.19
6	HF (dense)	22.58	40.38	18.28	41.46	41.94	34.82	0.00	0.00	30.11	34.57	43.01	35.71
7	Mixed mangroves	64.36	22.26	62.38	20.72	47.52	34.04	62.38	22.03	56.44	30.16	48.51	34.03
8	Fringing mangroves	49.52	71.23	68.57	49.32	46.67	73.13	4.76	100.00	23.81	92.59	42.86	72.58
9	River	99.91	93.08	100.00	91.16	97.03	99.02	100.00	85.64	99.91	94.78	97.21	98.93
10	Creeks	58.41	99.21	45.33	100.00	92.99	85.41	10.28	81.48	70.56	97.42	92.52	85.71
11	Wetlands	85.23	60.48	88.64	58.65	65.91	61.70	73.86	50.00	77.27	75.56	68.18	72.29
12	Cleared area	1.82	11.11	8.18	23.08	30.91	39.08	0.00	0.00	16.36	36.73	28.18	38.75
13	Swampy area	50.00	75.56	47.06	68.09	45.59	57.41	32.35	56.41	50.00	50.00	45.59	55.36
14	Mudflats	96.55	57.61	45.52	48.89	70.34	58.62	97.24	43.79	94.48	58.30	75.17	59.56
15	Terrestrial vegetation	56.25	54.55	73.44	33.1	75.00	36.09	0.00	0.00	42.19	46.55	73.44	37.90
16	Fallow land	99.36	100.00	100.00	99.36	94.21	100.00	97.75	100.00	99.68	100.00	98.71	100.00
	OA (%)	71.06		67.95		75.99		64.22		73.87		**76.42**	
	Kappa	0.66		0.62		0.72		0.57		0.69		**0.72**	

(AO – *Avicennia officinalis*, AM – *Aviccenia marina*, EA – *Excoecaria agallocha*, HF – *Heritiera fomes*). Producer accuracy – PA and User Accuracy – UA are given in %.

Seven base classifiers (MDC, SSM, ACE, LDC, NBC, MLC and SVM) having overall accuracy of more than 60% (similar to LISS III image analysis) were selected for MCS. From the accuracy assessment table of MCS classification of Landsat-8 OLI data (Table 5.4), we could infer that, similar to IRS-P6 LISS III classification output, product rule performed well (OA − 75.17% and κ − 0.73) and median rule produced the lowest accuracy (OA − 69.40% and κ − 0.66). Comparing the PA and UA of best performing combination function ('Product' in Table 5.4), creeks and rivers have more than 95% accuracy. The lowest was observed for wetlands (35.29% and 23.08%) which is similar to LISS III data. Among mangrove classes, highest PA and UA were obtained for *A. officinalis* (dense) (94.44% and 99.17%) and lowest for *E. agallocha* (dense) (34.58% and 37.76%) similar to SVM classification. Similar to LISS III classification output, overall accuracy has been improved from SVM to MCS by 0.45%. Figure 5.6 is the final classified output from SVM and MCS with product rule.

Considering mangroves, in Landsat-8 OLI image, the fringing mangroves have been demarcated with some improvement from that of LISS III image. Due to the similar spectral response and difference in canopy closure density from *H. fomes* (dense) and *H. fomes* (moderately dense), some confusion still prevails in the categorization of these two classes as the class *H. fomes* (dense) has lower user accuracy in both the images (35% to 40%). In both the cases, the terrestrial vegetation has been clearly classified which transcends through the middle of the core mangroves and in the middle of the Kalibhanjdhia island found in north of the study area. The terrestrial species includes banyan tree (*Ficus benghalensis*), Beach Hibiscus (*Hibiscus tiliaceus*), and coconut tree (*Cocus nucifera*) are mostly observed in the central part of Dangmal range. Also, there are two classes, mixed mangroves and fringing mangroves in both the images which could not be distinguished further because of the spectral limitations in both the images.
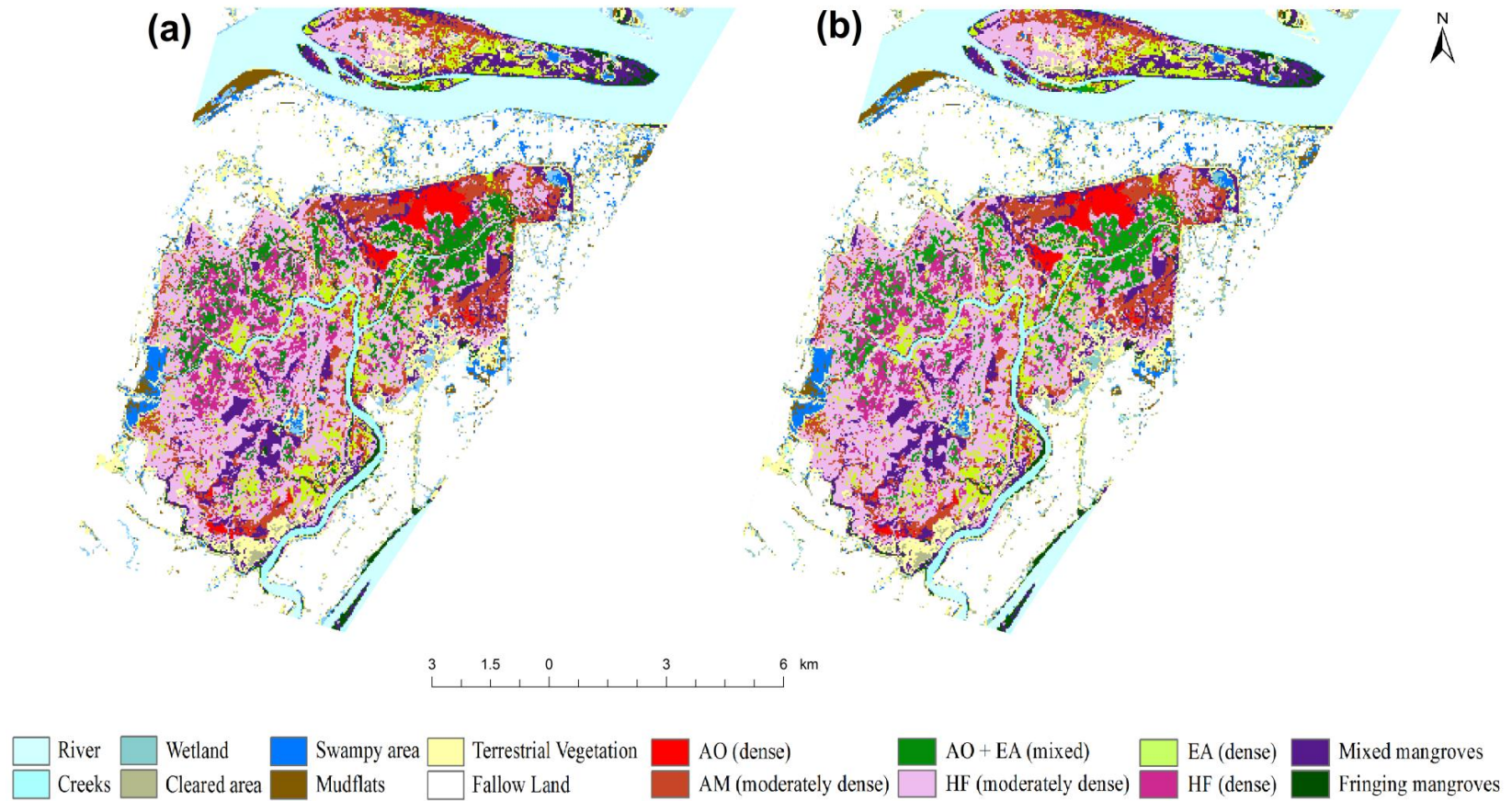
(AO – *Avicennia officinalis*, AM – *Aviccenia marina*, EA – *Excoecaria agallocha*, HF – *Heritiera fomes*)

Figure 5.6 Classification outputs of Landsat-8 OLI multispectral image obtained from (a) SVM (single best classifier) and (b) MCS (Product rule combination function – MCS output with highest overall accuracy).

Table 5.4 Accuracy assessment of MCS classification of Landsat-8 OLI for six combination functions

Sl. No	Class	MCS Combination functions for Landsat-8 OLI image classification											
		Majority Voting		Maximum		Minimum		Median		Average		Product	
		PA	UA	PA	UA	PA	UA	PA	UA	PA	UA	PA	UA
1	AO (dense)	92.86	99.15	92.86	97.50	94.44	99.17	66.67	100.00	92.86	100.00	94.44	99.17
2	AM (moderately dense)	6.79	32.35	14.81	15.58	66.67	54.27	28.4	68.66	40.74	55.46	64.81	55.26
3	AO + EA (mixed)	68.44	45.83	87.11	39.52	87.56	62.74	16.00	94.74	85.33	64.00	87.11	62.42
4	HF (moderately dense)	76.07	55.94	27.61	66.83	58.69	76.74	82.41	47.02	74.64	59.54	62.78	75.99
5	EA (dense)	13.08	33.33	27.10	18.35	34.58	37.76	1.87	28.57	7.48	30.77	33.64	40.91
6	HF (dense)	26.36	46.03	31.82	24.65	48.18	41.09	0.00	0.00	37.27	51.25	47.27	41.94
7	Mixed mangroves	63.78	57.08	63.27	52.54	70.41	70.05	67.35	48.89	64.80	71.35	69.90	72.87
8	Fringing mangroves	28.36	63.33	26.87	50.00	44.78	69.77	73.13	33.11	41.79	93.33	44.78	78.95
9	River	99.84	99.37	99.37	98.12	100.00	99.37	98.41	100.00	99.68	99.37	99.84	99.68
10	Creeks	93.91	99.08	86.96	96.15	95.65	100.00	93.91	93.10	89.57	100.00	95.65	100.00
11	Wetlands	8.82	28.57	5.88	19.05	42.65	22.31	33.82	23.00	14.71	26.32	35.29	23.08
12	Cleared area	71.70	73.08	57.55	50.83	68.87	85.88	65.09	82.14	67.92	87.80	71.70	87.36
13	Swampy area	87.20	64.95	86.85	55.53	51.21	79.57	83.39	67.89	70.24	59.36	52.94	68.61
14	Mudflats	20.99	66.67	15.43	54.35	43.21	41.42	28.40	100.00	35.8	47.93	43.83	42.77
15	Terrestrial vegetation	82.14	58.97	32.14	56.25	85.71	57.83	85.71	52.75	83.93	54.97	84.82	57.23
16	Fallow land	95.41	96.71	90.54	97.10	98.92	96.32	97.03	99.72	98.38	95.29	98.92	96.06
	OA (%)	71.72		63.47		74.72		69.4		74.27		**75.17**	
	Kappa	0.68		0.60		0.72		0.66		0.71		**0.73**	

(AO – *Avicennia officinalis*, AM – *Aviccenia marina*, EA – *Excoecaria agallocha*, HF – *Heritiera fomes*). Producer accuracy – PA and User Accuracy – UA are given in %.

5.5.3. EO-1 Hyperion hyperspectral image

Hyperion data was subjected to additional two processes before classification such as spectral transformation and dimensionality reduction (DR). Hence, the results for Hyperion data analysis are shown with different combinations of DR and transformations then classified using ten base classification algorithms and MCS. Also, each of the DR method outputs from four spectral modes were combined to make use of the complementary information from them and classified using ten base classifiers and named as 'All modes'. The overall accuracy and Kappa coefficient were calculated for all 5 classified outputs (Table 5.5).

When we infer the effect of different DR methods in the classification accuracy of base classifiers, it is found that MNF performed well followed by PCA and ICA. Similar accuracy was obtained for ICA and PCA in all the five modes while classified using MF and LDC. MF was found to produce lowest accuracy for Hyperion data also. With MNF reduced inputs, single best classifier was found to be MLC for RS and IS spectral modes and SVM for other three (CRRS, CRIS and All modes). The classification output of the single best classifier (MNF-SVM combination) of EO-1 Hyperion image is given as Figure 5.7a. In all the five spectral modes MF was the least performing classifier. But when four spectral modes were combined (All modes) and given as input, significant increase in their average overall accuracy (from 13.96% to 62.88%) and Kappa coefficient, κ (from 0.09 to 0.59) was observed (to refer 'MF' column in Table 5.5).

Then the intermediate results from the high performing classifiers have been combined using six non-trainable combination rules for all 5 modes to classify using MCS. Prior to that, the threshold value of 70% of overall accuracy was fixed to select best performing DR-Classifier combinations in each spectral mode. Out of 30 DR-Classifier combination outputs for each spectral mode, 10 from RS mode, 10 from CRRS, 10 from IS, 9 from CRIS and 16 from All Modes having more than 70% overall accuracy were selected for MCS. Classification accuracy was assessed for 19 classes including 11 mangrove classes. In all the

five spectral modes, the 'minimum' rule performed well and gave better overall accuracy and kappa coefficient value followed by 'product' rule (Table 5.6).

In this section, we discuss the results of MCS with 'minimum' rule which gives the highest accuracy among the six rules in all the five spectral modes (Table 5.7). Considering the mangrove classes, *A. officinalis* was classified with highest PA and UA and *R. apiculata + S. apetala* (mixed) with the lowest accuracy in all the five spectral modes. While considering the specific case of *E. agallocha* (dense), the PA and UA in RS mode is 61.90% and 57.78% respectively, which decreases to 36.51% and 45.10% respectively when continuum removed. On the other hand, in IS mode the PA and UA for the same class is 63.49% and 55.94% respectively but when continuum removed on IS (CRIS mode) they are 51.59% and 50.00% and it is better than CRRS which shows that the enhancement of spectral information in Short Wave Infra-red region (SWIR) plays a major role in identifying specific stands of the mangrove species. While considering the same case in "All modes" (combined spectral modes), the PA and UA are 63.49% and 59.26% respectively which is better than all the other four individual spectral modes. The decrease in the class accuracy of *E. agallocha* (dense) while continuum removed is due to the misclassification into the class *E. agallocha + P. pinnata + C. iripa* (mixed) in CRRS and CRIS spectral modes. This effect of continuum removal of RS and IS individually could be solved while the complementary information from all the four spectral modes are combined to get enhanced spectral information from Visible Near Infra-red (VNIR) region from CRRS spectral mode and enhanced spectral information from SWIR region from CRIS spectral mode. Though it is not significant, complementary information from all modes has increased the accuracy than individual spectral modes (Table 5.7 – Column "All modes") (Figure 5.7b).

Considering the performance of spectral modes for individual mangrove classes, CRIS gave better accuracy than CRRS for 8 mangrove classes: *A. officinalis* (dense), *A. marina* (moderately dense), *A. officinalis + E. agallocha* (mixed), *H. fomes* (moderately dense), *E. agallocha* (dense), *H. fomes* (dense), *S. apetala + A. ilicifolius* (mixed), and *C. iripa+ E. agallocha + P. pinnata* (mixed).

145

Both the spectral modes performed equal in two mangrove classes: *R. apiculata +* *S. apetala* (mixed) and *A. officinalis + E. agallocha + H. fomes* (mixed). This could be justified by the results of the methodology we adopted in our last chapter which proved that CRIS enhances the reflectance in SWIR region which is crucial for discriminating species with different canopy structure and leaf physiological properties. Moreover by combining the spectral properties of these classes in four spectral modes gave better classification accuracy (OA – 82.82% and κ – 0.81) and per-class accuracy (PA and UA) for most of the mangrove classes than their individual modes mainly due to the unique complementary information from four spectral modes.

The area covered by each of the land use/land cover categories including mangrove species as classified by single best classifier (MNF-SVM combination) and the best multiple classifier combination (MCS – Minimum rule combination function) is given in Table 5.8. From the result of the best classification output (MCS – Minimum), it is found that the mangrove cover is about 34.85 sq. km in the study area. Of which, the maximum area of 9.92 sq. km is occupied by CI+EA+PP Mixed mangrove class mostly seen in central and western part of the core mangroves followed by EA (dense) and HF (dense). *Avicennia officinalis* (dense mangroves) occupied the least area of 1.02 sq. km which is mostly seen in north-eastern part of the core mangroves (Figure 5.7 b).
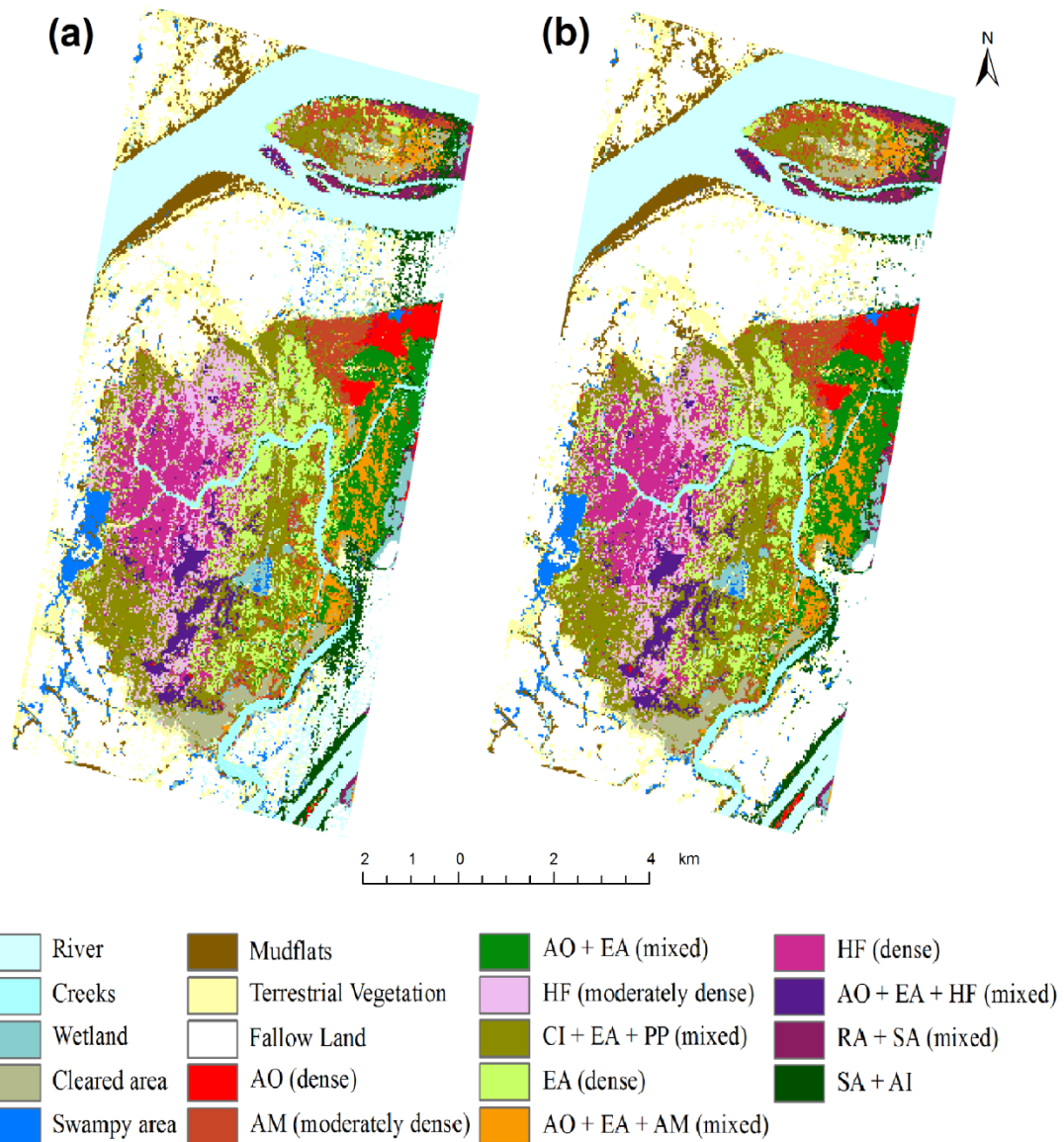
AO – *Avicennia officinalis*, AM – *Aviccenia marina*, EA – *Excoecaria agallocha*, HF – *Heritiera fomes*, CI – *Cyanometra Iripa*, PP – *Pongamia pinnata*, RA – *Rhizophora apiculata*, SA – *Sonneratia apetala*, AI – *Acanthus ilicifolius*

Figure 5.7 Classification outputs of EO-1 Hyperion hyperspectral image in all modes (when four spectral modes are combined) obtained from (a) SVM (single best classifier) and (b) MCS (Product rule).

Table 5.5 Overall accuracy (OA) and Kappa coefficient value for base classifiers of EO-1 Hyperion hyperspectral image classification in four spectral transformation modes (RS, CRRS, IS and CRIS) individually and all spectral modes combined

Spectral Mode	DR Method	Parameter	MDC	SAM	SSM	ACE	MF	LDC	LR	NBC	MLC	SVM
RS	ICA	OA	63.78	62.77	62.83	63.4	11.52	68.55	70.89	52.28	69.22	76.86
		Kappa	0.60	0.59	0.59	0.59	0.06	0.65	0.67	0.45	0.66	0.74
	PCA	OA	68.53	64.03	67.08	63.82	11.52	68.55	65.34	57.37	69.22	77.80
		Kappa	0.65	0.60	0.63	0.60	0.06	0.65	0.61	0.51	0.66	0.75
	MNF	OA	72.48	72.59	72.53	69.5	46.12	71.92	76.65	65.06	**80.97**	80.41
		Kappa	0.69	0.69	0.69	0.66	0.41	0.68	0.74	0.60	**0.79**	0.78
CRRS	ICA	OA	58.69	58.61	58.59	59.51	18.69	60.75	66.72	37.21	55.62	72.12
		Kappa	0.54	0.54	0.54	0.55	0.14	0.56	0.63	0.18	0.51	0.69
	PCA	OA	61.74	61.85	61.63	59.36	18.69	60.75	66.34	58.08	53.96	71.83
		Kappa	0.57	0.57	0.57	0.55	0.14	0.56	0.62	0.52	0.49	0.68
	MNF	OA	71.71	71.58	71.71	70.38	14.95	70.74	75.95	67.12	77.63	**79.00**
		Kappa	0.68	0.68	0.68	0.67	0.09	0.67	0.73	0.63	0.75	**0.76**
IS	ICA	OA	64.75	63.65	64.16	65.17	6.71	67.42	70.27	52.03	69.41	76.58
		Kappa	0.61	0.60	0.60	0.61	0.01	0.63	0.67	0.45	0.66	0.74
	PCA	OA	69.29	66.85	69.29	65.13	6.71	67.42	65.00	60.65	69.39	78.98
		Kappa	0.66	0.63	0.66	0.61	0.01	0.63	0.60	0.55	0.66	0.76
	MNF	OA	72.86	72.78	72.80	69.56	8.96	71.5	76.73	66.49	**80.55**	80.30
		Kappa	0.70	0.70	0.70	0.66	0.04	0.68	0.74	0.62	**0.78**	0.78
CRIS	ICA	OA	64.51	63.55	64.09	63.46	6.18	65.69	69.85	42.13	68.40	74.25
		Kappa	0.61	0.60	0.60	0.60	0.01	0.61	0.66	0.26	0.65	0.71
	PCA	OA	66.89	67.21	66.89	63.48	6.18	65.69	62.64	58.9	68.40	75.09
		Kappa	0.63	0.63	0.63	0.60	0.01	0.61	0.58	0.53	0.65	0.72
	MNF	OA	72.31	72.71	72.42	69.98	11.29	72.31	75.95	67.98	80.03	**81.16**
		Kappa	0.69	0.70	0.69	0.67	0.06	0.69	0.73	0.64	0.78	**0.79**
All modes	ICA	OA	67.42	66.81	67.33	76.31	60.08	76.64	76.86	54.8	67.29	77.99
		Kappa	0.64	0.63	0.64	0.74	0.56	0.74	0.74	0.48	0.63	0.75
	PCA	OA	67.8	67.77	67.82	76.04	60.16	76.64	72.15	59.39	67.48	78.37
		Kappa	0.64	0.64	0.64	0.73	0.56	0.74	0.69	0.54	0.63	0.76
	MNF	OA	72.99	73.18	73.03	78.49	68.40	78.96	81.06	67.31	71.33	**81.58**
		Kappa	0.70	0.70	0.70	0.76	0.65	0.76	0.79	0.63	0.68	**0.80**

Table 5.6 Overall accuracy (OA) and Kappa coefficient value for six combination functions of MCS classification of EO-1 Hyperion hyperspectral image in four spectral transformation modes (RS, CRRS, IS and CRIS) individually and all spectral modes combined

Spectral Mode	Parameter	MCS combination function					
		Majority vote	Average	Maximum	Minimum	Median	Product
RS Mode	OA (%)	79.27	78.79	78.85	**82.66**	72.95	81.77
	Kappa	0.77	0.76	0.76	**0.81**	0.70	0.80
CRRS Mode	OA (%)	75.57	77.65	70.38	**79.86**	71.94	79.42
	Kappa	0.73	0.75	0.67	**0.77**	0.69	0.77
IS Mode	OA (%)	78.98	79.02	78.22	**82.53**	73.20	81.84
	Kappa	0.76	0.76	0.76	**0.80**	0.70	0.80
CRIS Mode	OA (%)	78.22	78.98	78.29	**81.69**	72.25	80.87
	Kappa	0.76	0.76	0.76	**0.79**	0.69	0.79
All Modes	OA (%)	80.93	81.71	78.20	**82.82**	73.74	82.34
	Kappa	0.79	0.79	0.76	**0.81**	0.71	0.80

Table 5.7 Accuracy assessment of Minimum Combination function MCS classification of EO-1 Hyperion hyperspectral image in four spectral transformation modes (RS, CRRS, IS and CRIS) individually and all spectral modes combined

| Sl. No | Class | Accuracy assessment of 19 classes for Minimum rule combination function of MCS | | | | | | | | | |
| | | RS | | CRRS | | IS | | CRIS | | All modes | |
		PA	UA	PA	UA	PA	UA	PA	UA	PA	UA
1	AO (dense)	99.12	93.39	100.00	97.44	99.12	94.96	100.00	93.44	100.00	95.80
2	AM (moderately dense)	58.62	60.28	55.86	64.29	57.93	62.22	53.79	67.83	57.24	66.40
3	AO + EA (mixed)	82.25	81.76	76.92	66.67	79.88	78.95	81.07	80.12	83.43	82.94
4	HF (moderately dense)	46.75	73.47	35.71	73.33	46.10	73.96	38.96	74.07	46.10	75.53
5	CI + EA + PP (mixed)	77.07	51.61	73.87	45.34	77.60	50.96	76.27	49.48	76.80	52.46
6	EA (dense)	61.90	57.78	36.51	45.10	63.49	55.94	51.59	50.00	63.49	59.26
7	AO + EA + AM (mixed)	72.14	83.47	49.29	86.25	66.43	82.30	67.14	83.93	69.29	82.91
8	HF (dense)	89.58	88.36	88.89	84.21	90.97	87.33	91.67	81.48	91.67	83.54
9	AO + EA + HF (mixed)	45.29	73.33	49.41	71.79	44.71	77.55	45.29	71.96	48.24	76.64
10	RA +SA (mixed)	29.25	48.31	28.57	56.76	30.61	48.91	29.25	56.58	29.93	46.81
11	SA + AI	63.03	76.53	61.34	66.36	58.82	75.27	56.30	68.37	63.87	76.00
12	River	98.84	98.91	98.70	98.98	98.84	99.20	99.06	99.35	98.84	98.91
13	Creeks	84.85	86.01	87.54	81.25	83.50	84.07	90.57	85.13	84.51	80.45
14	Wetlands	70.50	82.35	61.87	81.13	70.50	84.48	61.87	76.11	64.75	79.65
15	Cleared area	80.88	86.84	80.88	82.50	85.29	86.57	80.88	84.18	85.29	86.14
16	Swamp	67.16	86.21	57.91	82.20	66.87	83.58	66.57	81.39	67.76	85.02
17	Mudflats	96.80	88.03	93.95	91.35	97.86	87.86	96.09	88.82	96.44	91.86
18	Terrestrial vegetation	84.62	81.35	84.62	77.85	84.95	83.28	81.94	77.78	84.95	83.01
19	Fallow land	99.80	84.40	99.80	79.71	99.21	85.03	100.00	84.56	99.60	83.67
	OA (%)	82.66		79.86		82.53		81.69		**82.82**	
	Kappa	0.81		0.77		0.80		0.79		**0.81**	

(AO – *Avicennia officinalis*, AM – *Aviccenia marina*, EA – *Excoecaria agallocha*, HF – *Heritiera fomes*, CI – *Cyanometra Iripa*, PP – *Pongamia pinnata*, RA – *Rhizophora apiculata*, SA – *Sonneratia apetala*, AI – *Acanthus ilicifolius*). Producer accuracy – PA and User Accuracy – UA are given in %.

Table 5.8 Area covered by different land use / land cover classes including 11 mangrove classes from classified outputs of EO-1 Hyperion image using single best classifier (MNF-SVM) and the best MCS spectral transformation – combination rule function (All modes – Minimum rule)

Sl. No	Class	Area Covered (sq. km)	
		MNF-SVM	MCS-Min
1	AO (dense)	1.00	1.02
2	AM (moderately dense)	2.30	2.16
3	AO + EA (mixed)	2.90	3.09
4	HF (moderately dense)	3.95	3.43
5	CI + EA + PP (mixed)	8.96	9.92
6	EA (dense)	4.41	4.44
7	AO + EA + AM (mixed)	1.92	1.75
8	HF (dense)	4.22	4.33
9	AO + EA + HF (mixed)	1.64	1.67
10	RA +SA (mixed)	2.45	1.87
11	SA + AI	0.93	1.18
12	River	10.57	9.25
13	Creeks	2.59	2.12
14	Wetlands	1.44	1.18
15	Cleared area	1.99	1.91
16	Swamp	1.64	1.40
17	Mudflats	2.45	2.60
18	Terrestrial vegetation	7.16	5.24
19	Fallow land	19.16	23.14
	Total	81.68	81.68

(AO – *Avicennia officinalis*, AM – *Aviccenia marina*, EA – *Excoecaria agallocha*, HF – *Heritiera fomes*, CI – *Cyanometra Iripa*, PP – *Pongamia pinnata*, RA – *Rhizophora apiculata*, SA – *Sonneratia apetala*, AI – *Acanthus ilicifolius*).

5.6. Discussion

The medium resolution multispectral data were earlier used for community level mapping of mangroves in Bhitarkanika using visual interpretation and most commonly used classification algorithms (Jensen et al., 1991; Giri and Muhlhausen, 2008; Kanniah et al., 2015). Multiple Classifier System (MCS) is considered to be the effective method of image classification. In recent times, it is

been used to classify hyperspectral image and LiDAR data for higher order classification such as species discrimination (Du et al., 2012; Damodaran and Nidamanuri, 2014a; Fassnacht et al., 2014; Ghosh et al., 2014). The implementation of MCS by utilizing the advantages of diversity in the component classifiers of MCS architecture using various spectrally transformed data such as IS and CRIS mode is a new attempt in mangrove distribution mapping.

Classification of multispectral data shows that, the average per-class accuracy of eight mangrove classes have above 50% (LISS III: PA – 53.01%, UA – 56.29%; OLI: PA – 63.09%, UA – 65.94%) which is difficult to achieve in species level classification using multispectral data. When comparing the outputs of IRS-P6 LISS III and Landsat-8 OLI, we could observe that in LISS III, *A. marina* (moderately dense) has been misclassified and labeled as mixed mangroves in the northern part of core mangroves. But in Landsat-8 OLI image, the misclassification was comprehensively reduced and resulted in better output with pure *A. marina* stands. This could have been mainly due to the usage of additional SWIR band (Band 7: 2110nm to 2290nm) of Landsat-8 OLI in which the recorded reflectance is purely a function of internal leaf reflectance and canopy structure (Knipling, 1970; Daughtry et al., 2000). The main limitation in multispectral data is the misclassification which is mainly due to the lack of spectral information and that could be observed in the *H. fomes* (dense) and *H. fomes* (moderately dense) where the similar canopy structure and spectral information in broad band lead to this confusion. In both the images, terrestrial vegetation could be demarcated clearly. Since the two images are of two different periods (Landsat-8 OLI – 23rd January 2014; IRS-P6 LISS III – 24th February 2012), the new terrestrial vegetation along the fringes of the forest in 2014 but not observed in 2012 particularly along the southern and eastern boundary of the forest could have been due to the plantation of terrestrial herbs or trees during these two years as a part of the social forestry initiative among the local community. This experimental study of using MCS in multispectral image for species classification was comparatively better when compared with old studies in Bhitarkanika where only community level of classification could be achieved (Nayak and Bahuguna, 2001; Reddy et al., 2007; Ajai et al., 2012).

Since the objective of this study is to map mangroves at species level, hyperspectral image was classified using multiple classifier system (MCS). MCS is mainly used for hyperspectral image classification in order to deal with the inherent challenges in conventional classification algorithms such as data dimensionality, limited training samples, and processing complexities (Kalluri et al., 2010; Richards and Jia, 2005; Bioucas-dias et al., 2013). With the evolution of several dimensionality reduction and classification methods, the hyperspectral image classification become further complex as each of them has its own advantages and disadvantages. So the proper choice of dimensionality reduction and classification algorithms for hyperspectral image classification has become a tougher job. As mentioned earlier, the diversity among the component classifiers is the key for a successful MCS architecture.

In this study, three DR methods and ten base classifiers are used for deriving decisive function values (intermediate classification results) for each input. New spectral transformation approaches (inverse spectra and continuum removal of inverse spectra) are introduced in this study to explore the maximum potential of SWIR region in species discrimination. From the analysis, we could infer that, the three different dimensionality reduction methods have impact on base classifier results in different ways which shows that these feature reduction methods extracts the essence of the image in different ways and resulted in the change in accuracy levels. So the combination of intermediate decisive values of base classifiers for different dimensionality reduction methods also produce varied results due to the difference in inherent quality of the input images. From the results, it is found that MNF performed better than other two DR methods and the optimal DR-classifier combination in most of the spectral modes was found to be MNF-SVM which is similar to the other case studies (Fassnacht et al., 2014; Ghosh et al., 2014). Interestingly, the Matched Filtering (MF) classification algorithm, the poorly performing classifier for individual spectral modes increased the classification accuracy significantly (10% to 60%) when all spectral modes are combined.

A threshold value of 70% for overall accuracy was fixed and those DR-Classifier combinations surpassed that threshold value were used for the second stage, that is MCS combination using six combination function. Among the six combination function, the minimum rule combination function performed better than other combination rules for all the five spectral modes. When comparing the MCS classification output of all spectral modes, "all modes" (combination of four spectral modes) gave better accuracy than individual spectral modes as this has unique complementary information from each of the four spectral modes that helps to improve accuracy.

Using Hyperion data, 19 land use/land cover classes including 11 mangrove classes were identified which is a significant improvement when compared with earlier studies using the same dataset for the same study area (Kumar et al., 2013; Ashokkumar and Shanmugam, 2014). Because of the coarser spatial resolution (30 m) of Hyperion and heterogeneous nature of the mangrove forest, some of the classes are labeled as combination of individual mangrove species that are dominant in canopy level which were identified from sample plots during field data collection. Still, we could achieve better classification accuracy in these classes that is evident in per-class accuracy of these mangrove classes. Considering the spatial distribution of mangroves in the classified output, we could infer that *A. officinalis* in pure stands was classified because of its dominance, unique, broad, and dense canopy structure as well as their thick leaf arrangement when compared with other neighboring species. The lowest classification accuracy was observed for the class, *R. apiculata + S. apetala* (mixed) because they are often identified as mixed pixels with creeks as they occur along the banks of river. From the hyperspectral image classification results, it is observed that among mangrove classes, *C. iripa+ E. agallocha + P. pinnata* (mixed) mangrove class occupies most of the area particularly the central and southwestern part of the forest. This mangrove class could not be distinguished using multispectral image where it was misclassified as *H. fomes* (moderately dense) due to the multispectral characteristics. The stripes of misclassification (caused due to the continuum removal) were found along the eastern part of the study area in single best classifier (SVM) results. Such

misclassification was resolved when MCS combination was used because of the fact that the classifiers deal with these ambiguities in a different way and so the combination of these diverse classifiers helps to improve accuracy (Figure 5.7).

5.7. Conclusion

In this chapter, two multispectral (IRS-P6 LISS III and Landsat-8 OLI) images and a hyperspectral (EO-1 Hyperion) image were classified to achieve species level map of mangroves of Bhitarkanika National Park in Odisha state of India. The results indicate that the combination of classifiers in MCS architecture improved the accuracy of mangroves classes. While using multispectral images, only 8 mangrove classes could be achieved. Of these, two classes are labeled as mixed mangroves and fringing mangroves which are hard to be distinguished in the minimum spectral resolution. In case of hyperspectral image classification, our aim is to analyze the impact of different dimensionality reduction (DR) methods on different base classifier to find the best "DR-Classifier" combination and found that MNF-SVM was the optimal combination for mangrove species classification. The incorporation of different set of DR methods the and base classifiers using the current methodology may be expected to improve the accuracy due to the diversity in the image transformation methods of different DR methods involved and diversity in base classifiers for image classification. This study can also be extended by including Hyperion bands corresponding to the wavelengths which provided maximum discrimination among species in our spectral separability analysis (Chapter 4). Moreover, the spectral transformation techniques such as continuum removal and additive inverse of spectral data adopted in our MCS methodology gave complementary information and its combination increased the classification accuracy though not significant, but marginally. Using Hyperion image, 11 mangrove species classes could be identified and some of the classes are identified as combination of species due to their distribution pattern and the coarser spatial resolution of the satellite data. The species level classification of mangroves can be significantly improved when we adopt the methodology framed in this study to classify hyperspectral data with high spatial resolution.

CHAPTER 6

MANGROVE ABOVE GROUND BIOMASS ESTIMATION USING HIGH RESOLUTION MULTISPECTRAL WORLDVIEW-2 IMAGE

This study attempts to estimate the above ground biomass in mangrove forest of Bhitarkanika National Park, Odisha, India by using very high resolution optical remote sensing data from WorldView-2 sensor. This chapter investigates the potential of WorldView-2 data to estimate biomass of heterogeneous mangrove forest by developing the biomass model that relates the biomass and image derived parameters. Since the destructive sampling for plot biomass estimation was not possible, it was calculated using species specific and common allometric equations which relate biomass with structural properties such as tree height, diameter at breast height (DBH), wood density, etc. developed using destruction methods in earlier studies by many experts. After the pre-processing, image parameters from 8 spectral reflectance bands, 28 simple band ratios, and 12 vegetation indices were derived and their relation with the plot biomass was investigated. Then, the textural parameters using Grey Level Co-occurrence Matrix (GLCM) method were derived from reflectance bands, band ratios, and vegetation indices to investigate the relation with plot biomass using multiple regression modeling. From the results it is found that the textural parameters have an edge over the simple reflectance bands and band ratios where as in the case of vegetation indices there was no such improvement observed. The textural analysis of band ratio has the combined information from band ratio as well as the textural analysis and helps in the improvement of biomass estimation. Further to improve the biomass estimation, the textural parameters of all the three inputs were combined and regressed. Results show that the combination of textural parameters improved the R^2 value (0.46) and the developed model also had minimum RMSE value (169.28 t/ha) when compared with other biomass models developed in this study using different input parameters. This could be explained by the fact that the structural information of vegetation canopy obtained from textural parameters of different input bands has improved the regression model to predict the biomass.

6.1. Introduction

Tropical forests play a critical role in ensuring the stability of the climate change through their efficiency in capturing greenhouse gases (including atmospheric carbon) and sequestrate in their biomass. Thus, they play a major role in understanding global carbon cycle and climate change. The accurate estimation of the above ground biomass and carbon stored in the vegetation is one of the important objectives in the resolutions of the Bali Action Plan (2007) approved by United Nations Framework Convention on Climate Change (UNFCCC) and the Kyoto Protocol (2005). In 2010, the Reducing Emissions from Deforestation and Forest Degradation in Developing Countries (REDD+) strategy was conceived for the conservation, sustainable management of forests, and enhancement of forest carbon stocks in developing countries. The restoration of forest to halt biodiversity loss and to improve global vegetation biomass has been one of the targets of Sustainable Development Goals (SDG's) framed during the Rio+20 Summit held in June 2012 (Eckert, 2012; Mayers, 2014). Conference of the Parties to the UNFCCC (COP21/CMP11) held at Paris in December 2015 also insisted on the two global challenges: tropical deforestation and climate change. COP21 aims at international cooperation for the protection and conservation of tropical forest to sustain global vegetation biomass by reducing the deforestation of tropical forest (Vina and Leon, 2014; UNDP, 2015). One of the most important functions of wetlands including mangroves is that they play a crucial role in trapping atmospheric carbon dioxide, fix in their biomass through photosynthesis, and so often credited as "carbon sinks." Mangrove deforestation generates 10% of carbon emission due to global deforestation per year despite their global tropical forest cover of just 0.7% (Donato et al., 2011). The "Blue Carbon Initiative" project, funded by United Nations Environmental Programme (UNEP), aims to restore and protect mangroves and other vegetated coastal habitats in order to improve carbon sequestration (Nellemann et al., 2009; Ellenbogen, 2012).

The change in biomass is an indicator of the stress in vegetation induced by natural and anthropogenic disturbances and so it needs to be monitored temporally (Klemas, 2013). Since the mangroves live in hostile environment, the

access to the forest through the swampy soil is often not possible. Furthermore, the estimation of biomass using traditional manual survey is time consuming, costly, and regional estimation could not be possible (Ketterings et al., 2001). Remote sensing with its advancements in sensors and data analysis techniques play a major role in estimating biomass and carbon sink in vegetation which is cost effective, time efficient, and provide regional to global coverage. Therefore, the estimation of mangrove biomass by combining field survey and remote sensing is always recommended (Heumann, 2011b). Kale et al. (2002) and Klemas (2013) reviewed the application of remote sensing data for biomass and productivity estimation in different ecosystems. They mentioned that the unique characteristic of plants is displayed by its reflectance in the red and infrared regions of electromagnetic radiation and have a strong relationship with the biophysical parameters of plants. Lu et al. (2014) also made a detailed literature survey on application of different remote sensing techniques in the estimation of above ground biomass in forest ecosystem.

Remote sensing based biomass estimation usually involves field data collection about biophysical properties such as diameter at breast height (DBH), tree height, number of individuals of a particular species, leaf area index (LAI), etc. Using these biophysical parameters, plot biomass are calculated with the help of species specific and common allometric equations which would be then correlated with remote sensing image to develop biomass models (Hirata et al., 2014; Patil et al., 2014). Normalized Difference Vegetation Index (NDVI) values derived were modeled to predict Leaf Area Index (LAI) values ranging between 0.8 and 7.0, with a mean of 3.96 for the mangroves growing on the Caicos Bank, Turks and Caicos Islands (Green et al., 1997). Kovacs et al. (2004) used Simple Ratio (SR) in addition to NDVI derived from IKONOS data to regress with LAI of degraded mangroves forest of the Agua Brava Lagoon System of Nayarit (Mexico) and found that there is a strong correlation of LAI versus NDVI and SR at 8m and 15m plot sizes. Similar methodology was applied on high-spatial resolution QuickBird multispectral imagery and estimated LAI value of 2.71 for areas excluding dead mangroves using NDVI model (Kovacs et al., 2009).

Proisy et al. (2007) assessed the potential of Fourier-based Textural Ordination (FOTO) to estimate mangrove forest biomass of French Guiana from very high resolution IKONOS multispectral images and found that FOTO indices derived from 1m panchromatic channel were able to consistently capture the whole gradient of canopy grain observed from the youngest to decaying stages of mangrove development, without requiring any inter-site image correction. When applied in 4m near-infrared channel, acceptable results with some limitations for characterization of juvenile mangrove types were obtained. ALOS AVNIR-2 multispectral data was utilized to model the biomass and carbon stock of five mangrove species in Karimunjawa Island, Indonesia by integrating image pixel value derived from 13 vegetation indices with the field biomass data collected using empirical modeling (Wicaksono et al., 2016).

Fatoyinbo et al. (2008) used Landsat multispectral data and Shuttle Radar Topography Mission (SRTM) elevation data to determine the spatial distribution of mean tree height and biomass of Mozambique's mangrove forests. Field biomass was calculated using the allometric equations developed from field measurements and common allometric equations to calculate aboveground biomass (AGB). They reported that the total cover of mangrove forests in Mozambique was 2,909 sq. km and total mangrove dry AGB was 23.6 million tons. In another study, high-resolution multispectral QuickBird data of Beilun Estuary, China was used to quantify per-pixel biomass information using sub-pixel analysis. The results obtained from the model were verified using the QuickBird panchromatic data derived from the same acquisition (Ji et al., 2010). Mutanga et al. (2012) stated that the saturation problem associated with use of NDVI for biomass estimation of high canopy density wetland vegetation. They used random forest regression and stepwise multiple linear regression models for predicting the biomass using NDVI derived from WorldView-2 data and found that random forest model performed better in biomass estimation. Zhu et al. (2015) used Back Propagation Artificial Neural Network (BP ANN) model to estimate AGB with and without the consideration of species types using vegetation indices derived from WorldView-2 image and field survey. They concluded that inclusion of species type is an additional informative parameter to

estimate the near real value of AGB. Moreover, they stated that the Red edge band and the associated vegetation indices such as Red edge Normalized Difference Vegetation Index (Re-NDVI), Red edge Simple Ratio Index (Re-SRI), and modified Red edge Simple Ratio Index (mRe-SRI) derived from WorldView-2 images are more efficient than other bands in predicting the biomass of high-density mangrove forests.

Elevation data from Shuttle Radar Topography Mission (SRTM) was extracted to map mangrove tree height in Everglades National Park, USA at 30m resolution. Then field biomass data was used to derive a relationship between mean forest stand height and biomass to map the spatial distribution of standing biomass of mangroves, and estimated that the total mangrove standing biomass in the study site as 5.6×10^6 tons (t) distributed mostly in mangrove stands of intermediate height around 8m (Simard et al., 2006). Mougin et al. (1999) examined the relationship between multi-frequency/multi-polarization AIRSAR microwave data (P, L, and C bands) and mangrove forest parameters (Diameter at Breast Height (DBH), tree height, tree density, basal area, and total above ground biomass) collected from the mangroves of French Guiana. Forest parameters were estimated using multiple stepwise regression analysis of several combinations of frequencies and polarizations which allowed the estimation of total biomass as 240 t/ha. Later, Proisy et al. (2000) further extended the study to provide a physical interpretation of observed polarimetric radar signatures of mangrove forests from AIRSAR data by simulating the response of mangrove canopies at the dominant scattering mechanisms in the radar–forest interactions using polarimetric scattering model and three layers radiative transfer model. Further to that, he evaluated the effects of canopy structure on the polarimetric radar response of mangrove forests and found that the backscattering from the open declining mangrove stand is higher than that of the closed mangrove forest (Proisy et al., 2002).

Kovacs et al. (2006) interpreted the relation between backscattering coefficients from spaceborne RADARSAT-1 C-band and structural parameters collected in a mangrove forest of the Mexican Pacific. They stated that there is a

high coefficient of determination of backscattering with LAI ($r^2 = 0.60$) and mean stem height ($r^2 = 0.72$) when observed using the shallower (~ 40°) and steeper (~ 47°) incident angles respectively but no such significant relationship was found with other parameters such as stem density, basal area, or mean diameter at breast height (DBH). Li et al. (2007) compared Landsat TM and Radarsat images to estimate above ground biomass of mangrove of Guangdong Province in South China. Results concluded that Radarsat gave better correlation than Landsat because the radar data have higher resolution and side-looking features to receive more information about the trunk of mangrove forest. The integration of radar backscatter information with NDVI gave better estimate than NDVI alone but lesser estimate than the backscatter model due to the uncertainties in NDVI. In another study, biomass models of dense and degraded tropical forests in Central Kalimantan, Borneo, Indonesia were developed combining X-band and C-band SAR data of ALOS PALSAR, and TerraSAR-X (Englhart et al., 2011). Similarly, ALOS PALSAR data and above ground biomass (AGB) derived from field observations of mangrove forest of Matang Reserve, Malaysia were used to estimate the AGB in the study area ranged between 298,000 and 3,783,200 ± 339,000 t/ha with an average of 994,000 ± 339,000 t/ha, and a total AGB of about 425 million tons (Hamdan et al., 2014).

Chadwick (2011) combined the digital terrain model (DTM) derived from last-return LiDAR data with IKONOS multispectral imagery to classify red and black mangroves. Then a digital canopy model (DCM) was created by subtracting the digital terrain model from a digital surface model derived from LiDAR first return which is combined with empirical allometric algorithms to estimate stem density and biomass.

This study attempts to analyze the potentiality of the high resolution multispectral WorldView-2 data in estimating the above ground biomass of mangroves of Bhitarkanika National Park, Odisha, India. Image derived parameters such as reflectance bands, band ratios, vegetation indices, and their respective textural parameters derived from Grey Level Co-occurrence Matrix are regressed with the actual plot biomass calculated using allometric equations which

utilizes field inventory biophysical parameters. Statistical multiple regression analyses were used to estimate the plot biomass from various image derived information.

6.2. Materials and Methodology

Above ground biomass models were developed using high spatial resolution image of the study area from the WorldView-2 sensor acquired on 16th January 2011 and biophysical properties of mangroves collected from sample locations in 2012 and 2013. Figure 6.1 represents the methodology framework adopted for biomass modeling. The detailed description of the study area, Bhitarkanika National Park located in Odisha state of India is discussed in Section 3.2.1 with the location map (Figure 3.1).

6.2.1. Satellite Data

WorldView-2 sensor was launched by Digital Globe on 08th October 2009 and it operates at an altitude of 770km. It provides data in eight multispectral bands (Table 6.1) with a high spatial resolution of 0.46m for the panchromatic band and 1.84m for the multispectral band. WorldView-2 is the only new-age commercial and high resolution multispectral sensor to provide data in unique spectral bands such as coastal, yellow, red-edge, and NIR-2 (Tarantino et al., 2012). The red-edge band is more related to the mangrove vegetation health, and also sensitive to biomass at high densities (Zhu et al., 2015).

Table 6.1 Spectral specifications of WorldView-2 multispectral sensor

Band Number	Band Name	Spectral Range (in nm)
1	Coastal	400 to 450
2	Blue	450 to 510
3	Green	510 to 580
4	Yellow	585 to 625
5	Red	630 to 690
6	Red edge	705 to 745
7	Near Infra-red 1 (NIR1)	770 to 895
8	Near Infra-red 2 (NIR2)	860 to 1040
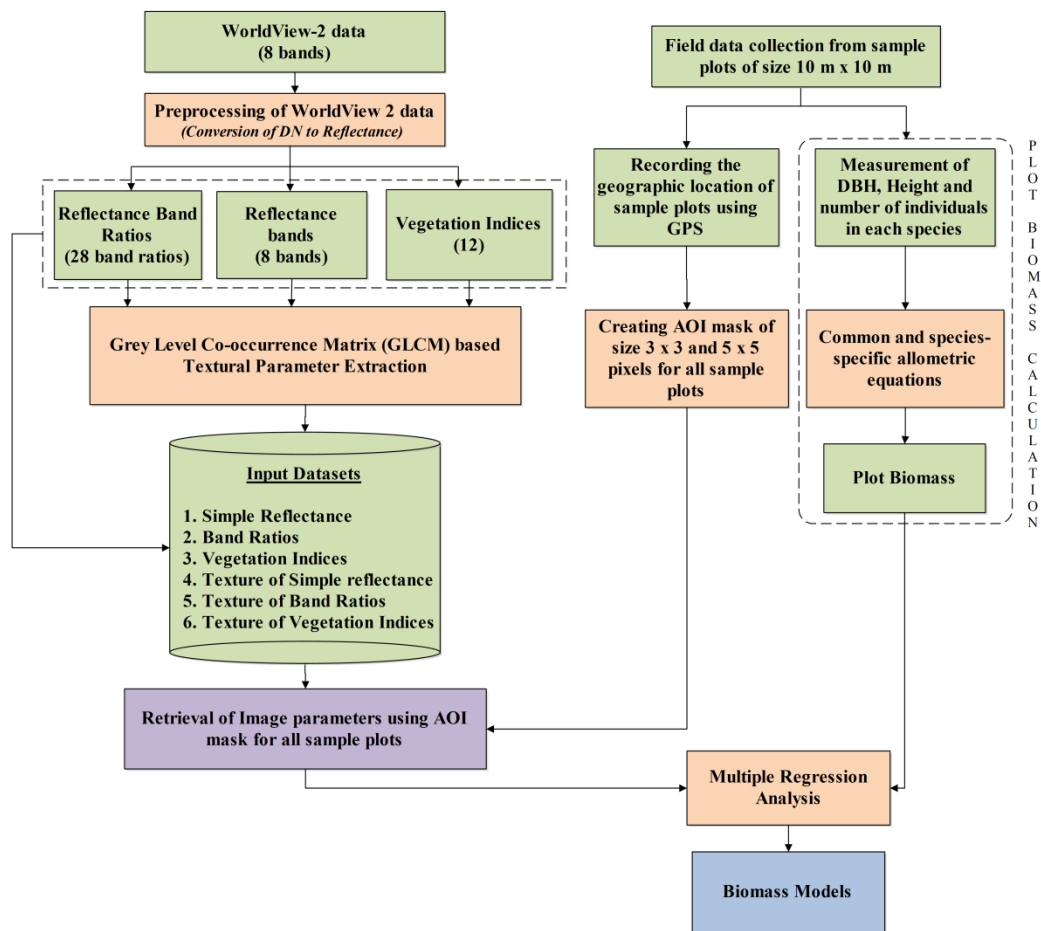
Figure 6.1 Methodology adopted for biomass estimation using WorldView-2 data.

6.2.2. Field data collection and plot biomass calculation using allometric equations

In Bhitarkanika National Park, field biomass variables from sample plots were collected during two time periods: December 2012 and April 2013. Biophysical parameters such as diameter at breast height (DBH), tree height, number of trees in each species, etc. were collected from 40 stratified sample plots (Figure 6.2) selected based on the existing mangrove community map (Space Application Centre, Ahmedabad, India) distributed in the mangrove forest of Bhitarkanika. The sample plots were of size 10m x 10m which is based on the image resolution of WorldView-2. All sample plots were selected carefully based on the criteria

that they are covered with vegetation canopy and without any intervention like roads, creeks, or other features within a buffer of 10m. Tree height was measured using Leica Disto D8 laser distometer, and DBH was recorded at a height of 1.3m from the ground for individual trees. In the case of multi-stemmed mangrove species such as *Rhizophora*, DBH was measured for each stem (Zhu et al., 2015). However, those trees with DBH less than 4cm are not considered in this study but were recorded. Number of trees in each species within the plot and canopy dominant species were recorded with the inputs of field experts from the Forest Department, State Government of Odisha, India.

Being a National Park and Salt Water Crocodile Sanctuary, Bhitarkanika wetlands are highly protected by law. The destructive sampling method by cutting the trees was not permitted by the State Forest Department and so the non-destructive sampling method was adopted. Species specific and common allometric equations from literatures on mangrove species were used for plot biomass estimation (Table 6.2).
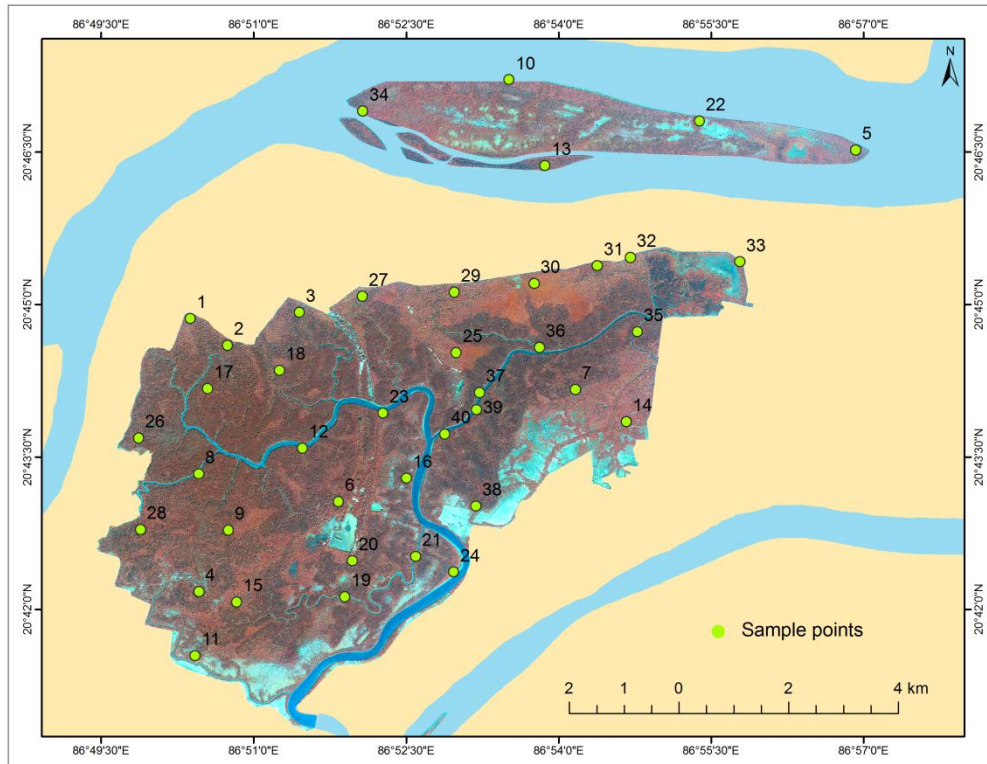
Figure 6.2 False Colour Composite (FCC) image of the study area derived from WorldView-2 sensor showing the locations of sample plots.

Table 6.2 Species-specific allometric equations used for the calculation of plot biomass

Sl. No	Mangrove Species	Species Specific Allometric Equation	Source
1	*Avicennia marina*	$B = 0.308 \times DBH^{2.11}$	(Comley and McGuinness, 2005)
2	*Bruguiera parviflora*	$B = 0.168 \times DBH^{2.42}$	(Clough and Scott, 1989)
3	*Pongamia pinnata*	$B = exp\ \{-2.409 + 0.9522\ ln\ (DBH^2 \times H \times \rho)\}$	(Ahmedin et al., 2013)
4	*Xylocarpus granatum*	$B = 0.0823 \times DBH^{2.59}$	(Clough and Scott, 1989)

H – Tree Height, *DBH* – Diameter at breast height, ρ – wood density.

Since species specific allometric equations were not available for other species, common allometric equation provided by Komiyama et al. (2005) was used and is given below.

$$B = 0.251 \times \rho \times DBH^{2.46} \hspace{2cm} (6.1)$$

Here, ρ represents wood density and Table 6.3 represents the ρ values for a list of species found in sample plots of the study area. Field biophysical variables were collected from 40 stratified sample plots of size 10m x 10m. The total biomass for each sample plot was calculated using the species-specific and common allometric equations and wood density values (Appendix 5).

Table 6.3 Wood Density values of different plant species used for plot biomass calculation using common allometric equation

Sl. No	Species	Wood Density (t/m^3)
1	*Aegialitis rotundifolia*	0.46
2	*Aegiceras corniculatum*	0.51
3	*Amoora cucullata*	0.58
4	*Avicennia alba*	0.56
5	*Avicennia officinalis*	0.59
6	*Bruguiera gymnorrhiza*	0.66
7	*Bruguiera sexangula*	0.74
8	*Ceriops decandra*	0.77
9	*Cynometra iripa*	1.02
10	*Excoecaria agallocha*	0.38
11	*Heritiera fomes*	0.82
12	*Heritiera littoralis*	1.04
13	*Kandelia candel*	0.46
14	*Lumnitzera racemosa*	0.71
15	*Pongamia pinnata*	0.64
16	*Rhizophora mucronata*	0.74
17	*Salvadoria persica*	0.60
18	*Sonneratia apetala*	0.52
19	*Sonneratia caseolaris*	0.39
20	*Tamarix troupii*	0.60
21	*Thespesia populnea*	0.61
22	*Xylocarpus moluccensis*	0.61

Source: Chave et al., 2009; Joshi and Ghose, 2014; Zanne et al., 2009.

6.2.3. Processing of WorldView-2 multispectral data

Initially, the digital number (DN) values of WorldView-2 data were converted to spectral radiance using the calibration step by multiplying the radiometrically corrected image pixels by the appropriate absolute radiometric calibration factor and then dividing by appropriate effective bandwidth. Both absolute radiometric calibration factor and effective bandwidth values were taken from metadata of WorldView-2. Then the spectral radiance image was converted to top of the canopy reflectance image using the FLAASH (Fast Line–of–sight Atmospheric Analysis of the Spectral Hypercubes) atmospheric correction module of ENVI 5.1 using appropriate parameters for tropical coastal wetlands (Immitzer et al., 2012;

Zhu et al., 2015). After the pre-processing, reflectance values of eight spectral reflectance bands (Table 6.1) were obtained. From these 8 reflectance bands, 28 simple band ratios were calculated.

6.2.3.1. Vegetation Indices

Vegetation indices (VI's) are defined as the mathematical transformation of the spectral bands designed to assess the spectral contribution of vegetation to multispectral observation (Elvidge and Chen, 1995). Since VI's are nothing but combination of different spectral bands, it minimizes external effects such as sun angle, sensor angle, shadow, soil background, leaf, and canopy angle, terrain effect etc. (Kasawani et al., 2010). Sarker and Nichol (2011) tested 10 slope based and 11 distance based vegetation indices derived from the AVNIR-2 sensor and compared with other models (texture-based and band ratio-based) for biomass estimation. Eckert (2012) and Zhu et al. (2015) also used vegetation indices derived from WorldView 2 data for mangrove biomass estimation. In the present study, 12 vegetation indices were calculated (Table 6.4) from the WorldView-2 multispectral image to model the biomass using multiple regression analysis.

6.2.3.2. Texture Analysis

Texture is defined as the function of local variance in the image related to the spatial resolution and size of the dominant objects in the scene and it could be used for target detection and object identification (Haralick et al., 1973; Woodcock and Strahler, 1987). Texture analysis in remote sensing is mainly based on the structural and statistical approaches (Haralick, 1979). In the statistical approach, texture is defined as the set of statistical measures based on the spatial distribution of grey levels of an image. In remote sensing, usually the textural parameters are derived from high resolution images as they provide more information than that of reflectance (Ulaby et al., 1986; Podest and Saatchi, 2002).

Table 6.4 Vegetation Indices derived from WorldView-2 used in biomass estimation

Vegetation Indices	Formula	Reference
Difference Vegetation Index (DVI)	NIR1 – Red	(Tucker, 1979)
Enhanced Vegetation Index (EVI)	2.5 * ((NIR1 – Red) / (NIR1 – (6 * Red) – (7.5 * Blue) + 1))	(Huete et al., 1997)
Modified Chlorophyll Absorption Vegetation Index (MCARI)	((Red edge – Red) – 0.2 * (Red edge – Green)) * (Red edge / Red)	(Daughtry et al., 2000)
Modified Soil Adjusted Vegetation Index (MSAVI)	$0.5 * (2 * NIR1 + 1 – ((2 * NIR1 + 1)^2 – 8* (NIR1 – Red))^{1/2})$	(Qi et al., 1994)
Normalized Difference Vegetation Index (NDVI)	(NIR1 – Red) / (NIR1 + Red)	(Tucker, 1979)
Near Infra-Red NDVI (NIRNDVI)	(NIR2 – Red) / (NIR2 + Red)	(Eckert, 2012)
Optimized Soil Adjusted Vegetation Index (OSAVI)	(1 + 0.16) * (NIR1 - Red) / (NIR1 + Red + 0.16)	(Rondeaux et al., 1996)
Renormalized Difference Vegetation Index (RDVI)	$(NIR1 – Red) / (NIR1 + Red)^{1/2}$	(Roujean and Breon, 1995)
Soil and Atmospherically Resistant Vegetation Index (SARVI)	((1+0.5) * (NIR1 – RB)) / (NIR1 + RB +0.5) where, RB = Red – 1 * (Blue – Red)	(Kaufman and Tanre, 1992; Liang, 2005)
Soil Adjusted Vegetation Index (SAVI)	((1+0.5) * (NIR1 – Red)) / (NIR1 + Red +0.5)	(Huete, 1988)
Triangular Vegetation Index (TVI)	0.5 * 120 * (NIR1 – Green) – 200 * (Red – Green))	(Broge and Leblanc, 2000)
Yellow NDVI (YNDVI)	(NIR2 – Yellow) / (NIR2 +Yellow)	(Pu and Landry, 2012)

Some of the important methods and techniques available for texture based statistical models are (a) local statistics, (b) the Grey Level Co-occurrence Matrix (GLCM), (c) texture feature spectrum, (d) Sum and Difference Histograms (SADH), (e) the variogram and (f) the wavelet transform (Kuplich et al., 2005). Of these techniques, the Grey Level Co-occurrence Matrix (GLCM) method is widely used. The selection of moving window size is one important factor to be concerned in GLCM method because the small window size exaggerates the local variance whereas the large window size may not extract textural information because of over-smoothing of the textural variation (Chen et al., 2004; Nichol and Sarker, 2011). So the textural analysis carried out in this study used small to medium moving window sizes of 3x3 to 5x5.

The following eight GLCM textural parameters were derived from three sets of image inputs: (1) 8 reflectance bands, (2) 28 simple band ratios, and (3) 12 Vegetation Indices derived from WorldView-2 image.

1. Mean (ME) $= \sum_{i,j=0}^{N-1} i \, P_{i,j}$

2. Variance (VA) $= \sum_{i,j=0}^{N-1} i \, P_{i,j} \, (i - ME)^2$

3. Homogeneity (HO) $= \sum_{i,j=0}^{N-1} i \, \frac{P_{ij}}{1+(i-j)^2}$

4. Contrast (CO) $= \sum_{i,j=0}^{N-1} i \, P_{i,j} \, (i - j)^2$

5. Dissimilarity (DI) $= \sum_{i,j=0}^{N-1} i \, P_{i,j} \, |i - j|$

6. Entropy (EN) $= \sum_{i,j=0}^{N-1} i \, P_{i,j} \, (-\ln P_{i,j})$

7. Angular Second Moment (ASM) $= \sum_{i,j=0}^{N-1} i \, P_{i,j}{}^2$

8. Correlation (CR) $= \sum_{i,j=0}^{N-1} i \, P_{i,j} \left[\frac{(i-ME)(j-ME)}{\sqrt{VA_i VA_j}} \right]$

where, P (i, j) is the normalized co-occurrence matrix.

6.2.4. Statistical analysis

The relationship between field biomass and information derived from remote sensing data can be established using statistical methods. Several statistical models such as linear regression method with or without log transformation of

plot biomass data (Steininger, 2000; Calvao and Palmeirim, 2004), multiple regression models (Dobson et al., 1995; Hyde et al., 2007; Eckert, 2012), non-linear regression (Santos et al., 2003), Artificial Neural Networks (Foody et al., 2001; Zhu et al., 2015), and semi-empirical models (Castel et al., 2002) were developed in earlier studies. Though none of the above models can perfectly establish the complex relationship between the field biomass and remote sensing derived information, the multiple regression model is still considered best and used in many studies (Hame et al., 1997; Kurvonen et al., 1999; Hyde et al., 2007; Nichol and Sarker, 2011; Sarker and Nichol, 2011) and is used in this study to measure the linear association between the dependent variable and at least two independent variables. Unlike simple linear regression, it selects the optimal set of independent variables that define majority of the variation in dependent variable. Based on the geo-coordinates information recorded by the GPS in the field, sample points were located in the image. Area of Interest (AOI) mask of size 3x3 and 5x5 pixels was created to extract information from the image data. Image parameters from spectral reflectance, band ratio, vegetation indices, and textural parameters from reflectance band, band ratio, and vegetation indices were extracted using 3x3 and 5x5 AOI mask at sample locations. Total biomass of each of the 40 sample plots calculated using allometric equations was used as the dependent variable whereas the parameters extracted using the 3x3 and 5x5 pixel AOI masks from the image derived data were used as independent variables in the multiple regression analysis at a confidence interval of 95%. Prior to the multiple regression analysis, the Pearson's correlation was calculated between independent variables in each of the model and dependent variable and those variables which had high correlation were selected for further analysis.

The multiple regression analysis was done between the dependent variable (total biomass of 40 sample plots) and seven sets of input independent variables, i.e., the image parameters derived from 40 sample locations identified using 3x3 and 5x5 AOI masks for the following datasets and model parameters were derived.

a. 8 spectral reflectance bands,

b. 28 band ratios,

c. 12 vegetation indices,

d. Textural parameters derived from 8 spectral reflectance bands,

e. Textural parameters derived from 28 band ratios,

f. Textural parameters derived from 12 vegetation indices, and

g. Textural parameters from 8 spectral bands, 28 band ratios and 12 vegetation indices combined.

The statistical model parameters such as coefficient of determination (R^2), Root Mean Square Error (RMSE), and significance value of the model (P-value) were calculated to avoid overfitting problem and to find best fit model for biomass estimation. In addition to that, beta coefficient value (B), standard error of B, significance value (p), and Tolerance and Value Inflation Factor (VIF) were also calculated for each independent variable in the model to understand the multicollinearity effect. The tolerance value of less than 0.10 and the VIF value of more than 10 were determined to indicate multicollinearity problem (Belsley, 2006; Nichol and Sarker, 2011).

6.3. Results

The multiple regression statistical analysis was carried out individually for seven input independent variables extracted using 3x3 and 5x5 AOI mask from seven different input image derived datasets at a confidence interval of 95%. Two AOI masks were used to know the influence of mask size in achieving the relation between dependent and independent variables in multiple regression analysis. Following sections give the relationship between biomass and seven sets of image parameters.

6.3.1. Spectral Reflectance and Biomass

From the results of multiple regression, it is observed that the relationship between the reflectance of WorldView-2 spectral bands and the estimated biomass of sample plots is poor. The coefficient of determination (R^2) value for 3x3 mask

is found to be 0.20 which is slightly better than that of 5x5 mask for which the R^2 is 0.17 (Figure 6.3 a and b). Both these models exhibit high RMSE value of 195.67 and 198.98 respectively (Table 6.5) and found to be non-significant models with p-value more than 0.05. However, the multiple regression results in better prediction than that of linear regression results obtained for individual bands. Earlier studies also reported that the relationship between simple reflectance bands and the plot biomass is comparatively poor due to the strong intercorrelation among the reflectance bands and therefore fails in predicting the biomass (Foody et al., 2001; Nichol and Sarker, 2011). The scatter plot representing the relation between observed and predicted biomass obtained from the regression of this model is given as Figure 6.3 a and b.

6.3.2. Band Ratios and Biomass

Considering the results of the multiple regression between the plot biomass and the simple ratio of the reflectance bands, the relation improved from that of the simple reflectance bands. The R^2 value for the 3x3 mask while using simple band ratio is found to be 0.52 and for the 5x5 mask, the R^2 value is 0.46. Meanwhile the RMSE found to be decreased for this model when compared with the earlier model and the values for 3x3 and 5x5 masks are 176.03 t/ha and 181.79 t/ha (Figure 6.3 c and d). Even though, this model is also found to be insignificant, it is comparatively better than the regression with reflectance bands with p-value of 0.17 and 0.23 for 3x3 and 5x5 mask size which validates the fact that for biomass estimation, band ratios perform better than simple reflectance bands. This is because the band ratios generally minimizes the attenuations in simple reflectance bands arises due to solar irradiance, soil background, and topographic effects meanwhile increasing the spectral response from the vegetation (Elvidge and Chen, 1995; Huete et al., 1985).

6.3.3. Vegetation Indices and Biomass

When plot biomass was regressed with 12 vegetation indices, it is found that they performed slightly better than simple reflectance bands but not well enough with band ratios. This could be evident from the R^2 value and RMSE value from the

Table 6.5 and Figure 6.3 (e and f). From the p-value, these models are also found to be insignificant. This is due to the fact that the relation between vegetation indices and the biomass is asymptotic in tropical forest and also the vegetation indices cannot be used together as independent variables in the multiple regression for biomass modeling since they are highly correlated (Foody et al., 2001; Sarker and Nichol, 2011).

Table 6.5 Model fitting parameters derived from the results of biomass estimation using *simple reflectance, band ratios* and *vegetation indices*

Input Data	AOI mask	R^2 value	RMSE (t/ha)	p-value
Spectral Reflectance	3x3	0.20	195.67	0.48
	5x5	0.17	198.98	0.61
Band Ratio	3x3	0.52	176.03	0.17
	5x5	0.46	181.79	0.23
Vegetation Indices	3x3	0.23	194.62	0.45
	5x5	0.31	184.80	0.20

6.3.4. Textural Parameters and Biomass

In addition to the usage of individual bands, band ratios and vegetation indices for biomass modeling, their textural properties were also analyzed and the information derived from the textural parameters were used as inputs for biomass estimation. In earlier studies, it is mentioned that the textural properties actually enhance the prediction of biomass and carbon stocks of different tropical and temperate forest ecosystems when compared with image parameters such as reflectance bands, vegetation indices etc. are modeled individually (Eckert, 2012; Fuchs et al., 2009; Nichol and Sarker, 2011; Zhu et al., 2015).
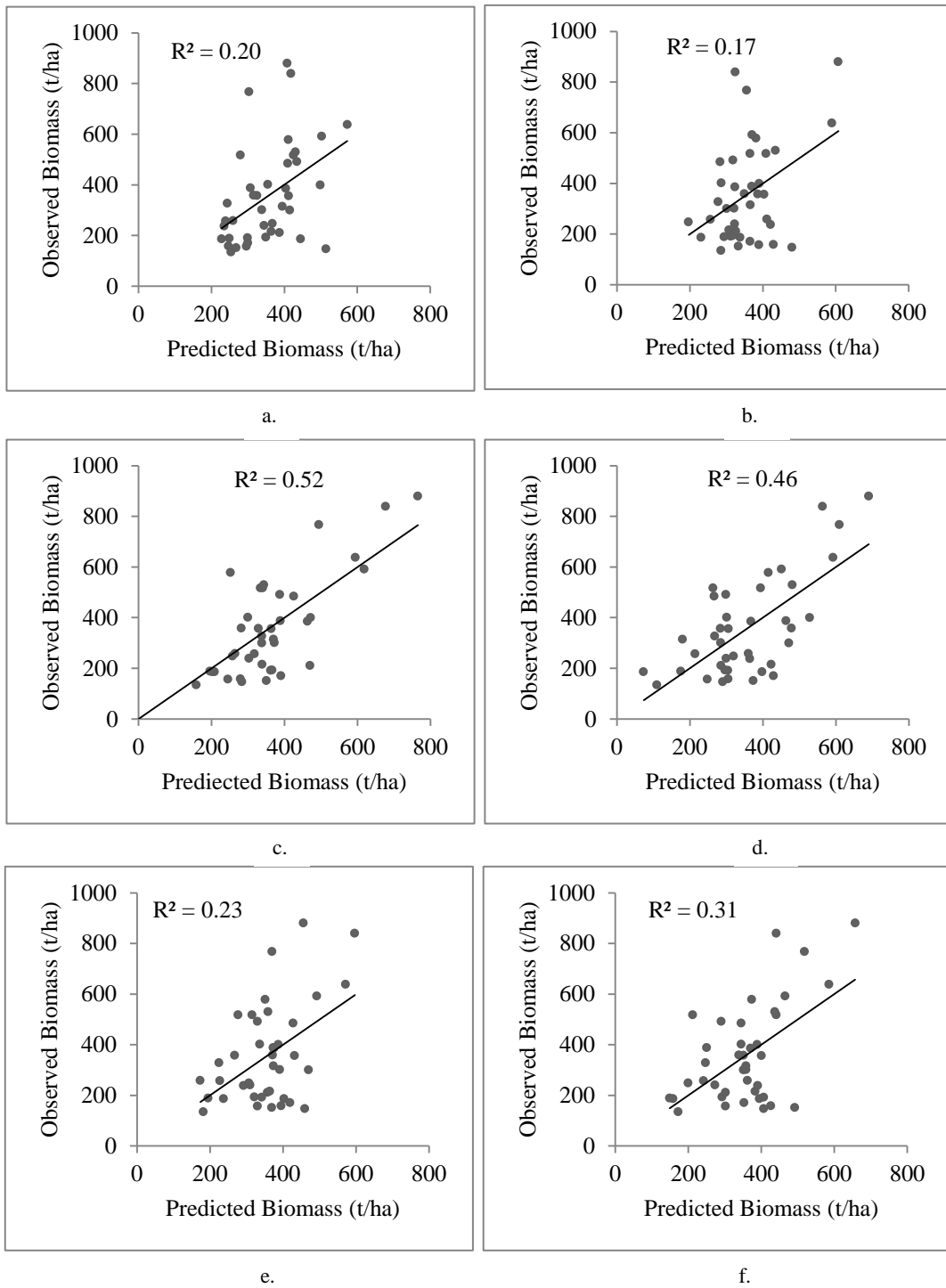
Figure 6.3 Relationship between the field biomass and the model predicted biomass using 8 *spectral reflectance bands* (a and b), 28 *band ratios* (c and d) and 12 *vegetation indices* (e and f) while using 3x3 and 5x5 masks respectively.

As far as the textural parameters of spectral bands are concerned, the model fitting parameters such as R^2 value, RMSE and p-level have shown some improvement. In this particular case, the R^2 value increased from 0.20 to 0.35 (for 3x3 mask) and from 0.17 to 0.30 (for 5x5 mask) when compared with the case where simple reflectance band were used (Figure 6.4 a and b). Also, there is a significant decrease in the RMSE value. Considering the significance of the model, the p-value for the models are 0.07 and 0.23 for 3x3 and 5x5 masks exceeds the upper limit 0.05 to establish the significance (Table 6.6). While considering the case of texture of band ratios, even though the R^2 value decreases from 0.52 to 0.41 (for 3x3 mask) and from 0.46 to 0.35 (for 5x5 mask) (Compare Table 6.5 and 6.6), from the RMSE value and p-value, it could be inferred that textural model is better than simple band ratio model developed earlier (Figure 6.4 c and d). Furthermore, the p-value of 0.07 and 0.12 shows that the significance of the model is improved when textural parameters are used. And, the biomass estimation using textural parameters of vegetation indices found to have no improvement than using vegetation indices (Figure 6.4 e and f). This is also evident from insignificant RMSE value and the p-value (Table 6.6).

Except in the case of vegetation indices, the textural parameters have shown some improvement in biomass estimation when compared with their counterparts while used as it is. As mentioned earlier, the vegetation indices are asymptotically related to the biomass and the higher intercorrelation among the vegetation indices resulted in the textural parameters which also had similar relation with biomass. This could be explained by the fact that the textural properties are sensitive to the shadow effects in the mixed canopy structure and this difference contributes the improvement in the biomass estimation. Similar kind of improvement in biomass estimation while incorporating the textural parameters derived from the optical remote sensing data in the regression model were earlier reported while applied in tropical evergreen forest (Lu, 2005), subtropical mountainous forest (Sarker and Nichol, 2011) and Siberian tundra forest (Fuchs et al., 2009).
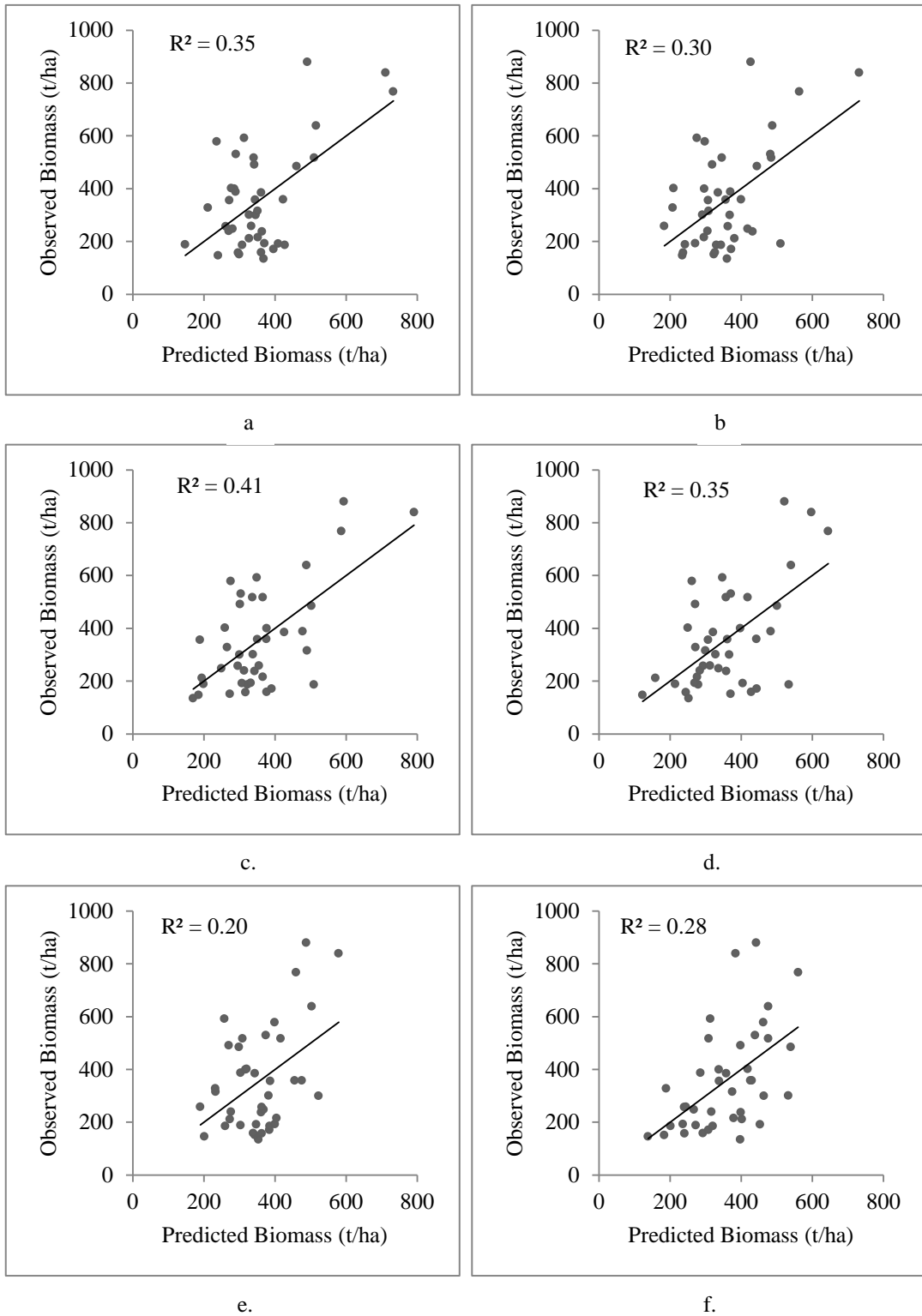
Figure 6.4 Relationship between the field biomass and the model predicted biomass using *textural parameters* derived from 8 *reflectance bands* (a and b), 28 *band ratios* (c and d) and 12 *vegetation indices* (e and f) using 3x3 and 5x5 masks respectively.

Table 6.6 Model fitting parameters derived from the results of biomass estimation using *textural parameters of simple reflectance, band ratios* and *vegetation indices*

Input Data	AOI mask	R^2 value	RMSE (t/ha)	p-value
Texture of Reflectance bands	3x3	0.35	176.42	0.07
	5x5	0.30	186.33	0.23
Texture of Band Ratio	3x3	0.41	173.53	0.07
	5x5	0.35	179.81	0.12
Texture of Vegetation Indices	3x3	0.20	195.09	0.46
	5x5	0.28	187.88	0.26

Table 6.7 Contributing image parameters with minimum p-value in each of the biomass models

Sl. No	Dataset	Contributing Image Parameters	p-value
1	Reflectance bands	Band 7	0.11
		Band 8	0.07
2	Band Ratio	Band ratio 12	0.002
		Band ratio 15	0.01
		Band ratio 24	0.05
		Band ratio 34	0.03
		Band ratio 35	0.05
		Band ratio 48	0.10
3	Vegetation Indices	NIRNDVI	0.03
4	Reflectance bands - Texture	Band 3 - Homogeneity	0.19
		Band 6 - Homogeneity	0.09
5	Band Ratio - Texture	Band ratio 23 - Mean	0.22
		Band ratio 23 - Homogeneity	0.11
		Band ratio 23 - Contrast	0.15
6	Vegetation Indices - Texture	EVI - Mean	0.58
		OSAVI - Mean	0.59

Even though, the textural parameters gave better result, the models developed were not significant statistically as they have p-value more than 0.05. So the alternative method, the combination of textural parameters obtained from all the three individual set of parameters was attempted and their results are discussed in the following section. The image derived parameters with minimum p-value which have more influence on each of the biomass models are listed in Table 6.7.

6.3.5. Combination of all the textural parameters and Biomass

In order to improve the biomass estimation and to obtain the optimal biomass model which is significant, the textural parameters obtained from reflectance bands, band ratios, and vegetation indices were combined together and given as input in multiple regression. From the results, it could be inferred that the combination of the textural parameters has actually improved the R^2 value to 0.46 in the case of 3x3 mask. But in the case of 5x5 mask there is no improvement in the R^2 value (0.34) (Figure 6.5). The RMSE value for the two cases were found to be 169.28 t/ha and 177.63 t/ha which are better than any other models developed in this study.

a.   b.
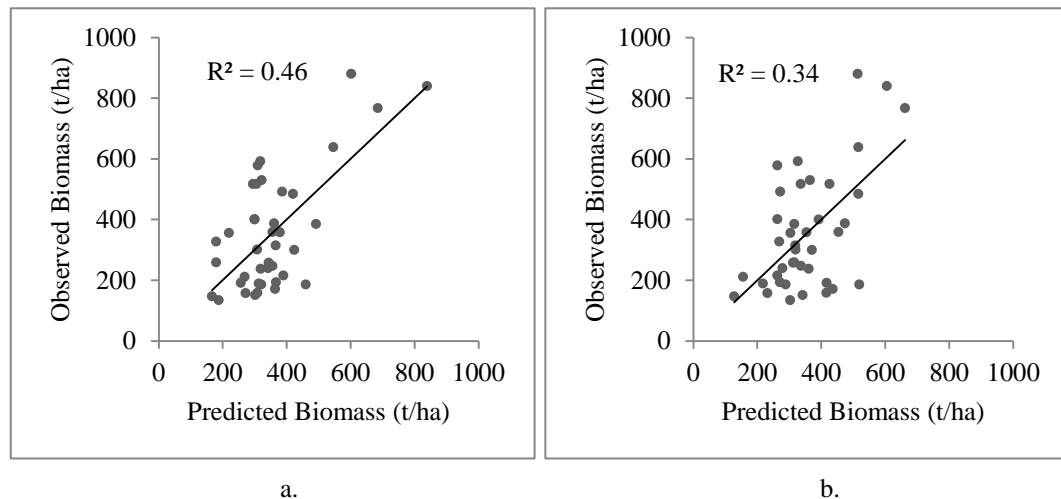
Figure 6.5 Relationship between the field biomass and the model predicted biomass using the *combination of all the textural parameters* derived from *reflectance bands, band ratios* and *vegetation indices* using (a) 3x3 and (b) 5x5 masks respectively.

Moreover, the biomass model developed for 3x3 mask by combining all textural parameters has the significant value of 0.05 and hence this model is comparatively reliable for biomass estimation. On the other hand the biomass model 5x5 mask is less significant with the p-value of 0.08. The fitting parameters for intercept and variables for the significant model (3x3) are given (Table 6.8).

Table 6.8 Model fitting parameters derived from the biomass estimation and their corresponding variables estimated using the *combination of textural parameters of simple reflectance, band ratios* and *vegetation indices*

R value	R² value	Adj R²	RMSE	p-value	Variable names	B	RMSE of B	p-value	Tol	VIF
0.68	0.46	0.25	169.28	0.05	Intercept	-1395.26	760.91	0.08		
					Band 1 - Second Moment	316.94	653.65	0.63	0.24	4.22
					Band 3 – Homogeneity	146.10	296.46	0.63	0.13	7.87
					Band 4 – Homogeneity	-15.26	382.96	0.97	0.09	11.06
					Band 6_Homo	216.22	116.74	0.07	0.45	2.25
					Band ratio 13-Homogeneity	-46.24	103.73	0.66	0.11	9.08
					Band ratio 13-Contrast	-17.35	35.49	0.63	0.09	10.56
					Band ratio 23-Mean	1832.97	876.07	0.05	0.07	15.00
					Band ratio 23- Homogeneity	688.42	288.91	0.02	0.04	23.15
					EVI-Mean	-586.39	872.17	0.51	0.11	9.41
					MSAVI – Mean	333.50	770.51	0.67	0.13	7.74
					RDVI - Mean	-375.36	758.25	0.62	0.13	7.41

From the fitting parameters, in 3x3 mask results, it is evident that the textural variables extracted from the band ratio of second and third spectral bands (Band ratio 23 - Mean and Band ratio 23 - Homogeneity) have higher significance among all the independent variable involved in the model. They also satisfy the conditions of multicollinearity (Tolerance < 0.10 and VIF > 10) among other independent variables involved in the model. This could be explained as the

textual parameter of band ratio contributes more to the significance of the model with the combined information. Apart from that, among reflectance bands, Green, Yellow and Red-edge bands contribute the model whereas among vegetation indices Enhanced Vegetation Index (EVI), Modified Soil Adjusted Vegetation Index (MSAVI) and Renormalized Difference Vegetation Index (RDVI) were selected as fitting variables in the best biomass model.

6.4. Discussion

The objective of this study was to analyze the potential of high resolution WorldView-2 multispectral image to estimate biomass of dense heterogeneous mangrove ecosystem of Bhitarkanika, Odisha, India which is the first of its kind for the study area. From the results there are few points which need to be highlighted and they are,

1. The spectral reflectance bands and vegetation indices gave poor estimation of biomass,
2. The textural analysis has improved the biomass estimation when compared with normal spectral bands and band ratios,
3. The textural parameters of band ratios have given better results when compared with that of reflectance bands and vegetation indices, and
4. The combination of textural parameters has resulted in improvement of biomass estimation.

However, there are some points need to be discussed regarding the moderate results obtained when compared to other studies using WorldView-2 data for improvement of biomass estimation using different image analysis methods (Eckert, 2012; Zhu et al., 2015).

The number of sample location used in this particular study where the biomass variables collected is limited due to the hostile and inaccessible conditions in the swampy mangrove environment. Though the sample points are uniformly distributed over the study area, the sample points were less normally distributed for calculated field biomass.

Since the mangroves in India are highly protected by law and the study area is a National Park (under the privilege of maximum conservation zone), the destructive sampling i.e., the cutting of trees to derive species specific and site specific allometric equations is not possible. Furthermore, the studies related to biomass estimation for Indian mangroves are very limited and there are no many established species specific allometric equations available for Indian mangroves. So the common allometric equations developed by Komiyama et al. (2005) for mangroves were used in which wood density is the key parameter. They recommend using the site-specific wood density value for the equation. For the present study, as the site specific wood density data are not available and measuring the density of mangrove species from Bhitarkanika National Park was not permitted (which is beyond the scope of our study) global wood density database was referred. Hence, the inputs variables such as DBH, tree height were measured in the field except the wood density. These factors might have contributed in the bias occurred in the total biomass calculated in stratified sample plots in the study area. Furthermore, the forest in Bhitarkanika is very dense and highly mixed at canopy level but homogeneous in canopy density in most of the sample locations. So the textural parameters derived from the spectral reflectance bands have little chance to contribute the textural variation to improve the biomass estimation.

In a situation like the canopy is highly heterogeneous, the optical remote sensing model for biomass estimation may lead to errors due to species specific differences in the canopy density to above ground biomass ratio. So the challenge in using optical data for the estimation of biomass still prevails (Lu, 2006). In this chapter, we used the field biomass variables collected from sample plots of size 10 m x 10 m in ground. The spatial resolution of the hyperspectral Hyperion data is 30 m whereas the multispectral Landsat data and IRS data is of 30 m and 23.5 m respectively. So the pixel mask of 3x3 and 5x5 of these data will cover 90 m x 90 m and 150 m x 150 m in ground respectively. The extrapolation of field biomass data collected from 10 m x 10 m to the above mentioned ground size plots in such a heterogeneous and complex mangrove forest in our study would be difficult to justify. So for the biomass estimation we preferred the high spatial

resolution Worldview-2 data for biomass estimation instead of other sensors which we used to study plant diversity. The spectral reflectance data is found to be less sensitive to the biomass change even when the high resolution and specialized spectral bands (Yellow, Red edge) of WorldView-2 were used. This could be the attributed to the thick heterogeneous canopy in the mangrove forest and the multiple canopy layers leading to multiple scattering and reduction of reflectance reaching the sensor (Moran et al., 1994). Sarker and Nichol (2011) have summarized some reasons which argue that vegetation indices are less successful in tropical and sub-tropical forest applications. They pointed out that, unlike temperate or boreal forests, tropical forests are not simple structured and the heterogeneous multi-layered canopy affects the biomass estimation. Moreover, their asymptotic relationship with the high biomass tropical ecosystem, especially mangroves and the higher correlation among each other when given as independent variables for biomass modeling (Foody et al., 2001; Zheng et al., 2004). This is evident from our result as vegetation indices were found to be less sensitive to biomass.

Woodcock and Strahler (1987) stated that in an image of a forested area of heterogeneous stand with high species diversity and when the spatial resolution increases to the size of the dominant tree crown in the pixel, the local variance obviously increases. Especially the differential growth of different stands, uneven canopy arrangement, difference in tree crown size and gaps, tree shadows, and most importantly spatial resolution of the image used improves the local variance in an image. This supports the scope of using the textural parameters in biomass estimation. As mentioned earlier, the textural measurement has given better results which actually consider the spatial aspects of shadow effects and variations in interspecies canopy structure. Since the sample plots considered in this study area is found to be heterogeneous in forest canopy structure, the stronger correlation with the textural parameters is expected. It is stated that when biomass and canopy structure have strong correlation, the spectral reflectance would be a key parameter. On the other hand, in structurally complex ecosystem like mangroves, textural parameter would have strong correlation with biomass (Eckert, 2012). The model based on the textural parameters derived from band

ratios outperformed than that of textural parameters derived from reflectance bands and vegetation indices.

Among the textural parameters derived from different vegetation indices, textural parameters from Enhanced Vegetation Index (EVI), Modified Soil Adjusted Vegetation Index (MSAVI) and Renormalized Difference Vegetation Index (RDVI) were selected as fitting variables in the best biomass model. Among them, EVI outperformed other two with lower Tolerance and higher Value Inflation Factor (VIF) as this index was developed with the aim of increasing the sensitivity of high biomass region. This result is similar to the case studies of Huete et al. (2002) where they used MODIS data and Eckert (2012) in which WorldView-2 was used for vegetation biophysical characteristics assessment using different vegetation indices.

The combination of textural parameters derived from reflectance bands, band ratio and vegetation indices gave better biomass estimation result than other models. This is because of the combination of complementary information from different image derivatives which had improved the prediction of biomass.

6.5. Conclusion

The potential of high resolution WorldView-2 multispectral image with a spectral resolution of 8 bands and spatial resolution of 1.84m was tested for predicting the above ground biomass of highly complex mangrove ecosystem. Even though, the spectral reflectance bands and vegetation indices were not performing well, the band ratio gave acceptable result. But these models were found to be statistically insignificant. Textural analysis has given promising results since the study area is heterogeneous in forest structure and having mixed canopy structure. The textural parameter derived information from band ratio has taken the advantage of information from both band ratio and texture analysis and gave better results. Finally the combination of all the textural parameters resulted in best fitting model with R^2 value of 0.46 and RMSE value of 169.28 t/ha. Though, this biomass estimate is not highly significant with similar kind of studies conducted in other mangrove ecosystem using WorldView-2 data (Eckert, 2012; Zhu et al., 2015),

this is regarded as the primary attempt to characterize biophysical properties of mangrove ecosystem of Bhitarkanika National Park. The reason may be due to the lack of site specific wood density and species specific allometric equations since the drilling or cutting of trees in the forest is prohibited. So we used Global Wood Density Index and allometric equations from earlier studies for available species. For other species, we used common allometric equation derived by Komiyama et al. (2005). The current methodology would be extended and further investigated by taking more number of well distributed sample points and validating the site specific wood density and to derive species specific allometric equations to improve biomass estimation. The potential of using the European Space Agency's (ESA) newly launched Sentinel-2 multispectral data and Sentinel-1 SAR microwave data to improve the biomass prediction is planned for the future work.

CHAPTER 7

CONCLUSIONS AND FUTURE DIRECTIONS

7.1. Conclusions

In this thesis, we investigated some of the important issues that prevailed in the spectral characterization of mangrove species with the help of field spectrometry and hyperspectral data. In addition, high resolution multispectral data was also analyzed to investigate its potential to estimate mangrove biomass.

The important contributions of this thesis are as follows.

- Developed a spectral database of 34 true and associated mangrove species present in India using field spectroscopy techniques.
- Conducted empirical analysis on multiple statistical procedures, combined with feature reduction methods and spectral transformation methods, to identify optimal wavelengths which would spectrally discriminate mangrove species.
- Explored the potential of ensemble classification algorithms to improve accuracy and number of separable classes using multispectral data.
- Investigated the potential of spectrally transformed images to improve the classification accuracy for the species level classification using medium resolution hyperspectral satellite data.
- Explored the impact of dimensionality reduction (DR) methods on base classifiers as well as to identify the best combination of DR – classification algorithm and multiple classifier system to improve the classification accuracy.
- Investigated the potential of textural parameters extracted using the spectral reflectance, band ratios, and vegetation indices of WorldView-2 high resolution multispectral data for biomass estimation.

Mangroves are ecologically and economically important coastal habitat and are in high priority for conservation and management. Literature showed that global coverage of mangroves has declined from 187,940 sq. km to 157,050 sq. km during the period of 1980 to 2000. Remote sensing data acquired using optical, hyperspectral, and microwave remote sensing sensors are being used for such assessments and monitoring activities. More intricacies of mangroves can be explored using remote sensing techniques for the betterment of mangrove management. With this background, the objectives of the study were framed to explore the potential of hyperspectral data to assess species diversity.

As a first outcome of this study, the spectral library of 34 mangrove species was developed using well defined sampling methodology and post-processing techniques. The developed mangrove spectral library is first of its kind for Indian mangroves and covers most of the important species found in India. The techniques to remove ambiguities in collected spectra such as correction of thermo-electric induced spectral drifts, elimination of corrupted wavelengths, and smoothing of spectra to remove minor ambiguities in spectra were systematically discussed.

Following the spectral library development, the study established the spectral separability among 34 mangrove species. Parametric and non-parametric statistical analyses were performed on derivative spectra, continuum removed spectra, additive inverse, and continuum removed additive inverse spectra followed by feature reduction algorithms in order to find the optimal wavelengths for species separability. At first, closely associated eight species from *Rhizophoraceae* were tested using the proposed methodological framework and later extended to 34 species. The major outcome of the separability analysis is that the red edge region (680nm to 720nm) is the most important wavelength region for species discrimination. Green reflectance region (around 550nm) and water absorption regions (1470nm and 1850nm) also played major role in species identification. Results showed that inherent variation in cellular arrangement and canopy structure among the species are spectrally discriminable in Near Infra-red and Short Wave Infra-red regions. The proposed Continuum Removed Inverse

Spectra (CRIS) transformation method was able to enhance such spectral regions in better way than the commonly used Continuum Removed Reflectance Spectra (CRRS) transformation method. Results from spectral separability analysis and classification of species spectra also confirmed the potential advantages of CRIS in species discrimination. Among *Rhizophoraceae* species, *Ceriops decandra* was found to be the most separable species with other six species of *Rhizophoraceae*. From the separability analysis of 34 species, 557 out of 561 species pairs were found to be separable in field condition and 559 were separable in laboratory condition.

The next major outcome of the thesis was higher order mangrove mapping. As a forerunner, multispectral data were classified using ten base classifiers and Multiple Classifier System (MCS) for species mapping. The experimental study using MCS identified 8 mangrove classes which was comparatively better than the old studies conducted for Bhitarkanika where only community level classification was achieved. The analysis of hyperspectral data compensated misclassification seen in the multispectral image analysis. In case of hyperspectral image analysis, Minimum Noise Fraction-Support Vector Machine (SVM) combination was identified as the optimal DR-Classifier for species level classification. Moreover, spectral transformation techniques such as continuum removal and additive inverse of spectral data adopted in the MCS methodology provided complementary information and the combination increased classification accuracy. Using Hyperion image, 11 mangrove species classes were identified. Some of them could be identified as combination of two or three species due to their heterogeneous distribution pattern and the coarser spatial resolution of the satellite data. Hence, the methodology developed in this study for hyperspectral image classification is expected to classify pure stands of species when airborne image data with high spatial and spectral resolution is used for species identification.

The potential of high spatial resolution multispectral data, WorldView-2 for the estimation of above ground biomass of mangrove forest in Bhitarkanika National Park was also attempted in this research. For biomass estimation, plot

biomass was calculated using non-destructive method (allometric equations which use field collected biophysical parameters) for sample plots and regressed with image parameters derived from the multispectral data. Textural parameters derived from image parameters such as reflectance bands, band ratios, and vegetation indices were found to give more promising results than individual parameters. This trend was observed due to the heterogeneous nature of vegetation types and mixed canopy structure of the study area. Textural parameters derived from band ratio took the advantage of information from both band ratio as well as texture analysis and showed better results. Furthermore, the combination of all textural parameters was attempted and resulted in the best fitting model with R^2 value of 0.46 and Root Mean Square Error (RMSE) of 169.28 t/ha. This biomass estimate, which was not highly significant to similar kind of studies conducted in other mangrove ecosystem using WorldView-2 data, can be regarded as the primary attempt to characterize biophysical properties of mangrove ecosystem of Bhitarkanika National Park.

7.2. Scope for Future Research

Following are some of the future directions to further enhance the studies presented in this thesis.

- Mangrove species such as *Acanthus volubilis, Cynometra ramiflora, Dalichondrone spathaceae, Excoecaria indica, Heritiera kanikensis, Rhizophora stylosa, Scyphiphora hydrophyllaceae,* and *Sonneratia griffithii* are very rare in the study area and could not be identified for spectral data collection. Spectral signatures of these species are also to be collected to develop a complete collection of spectral signatures when Indian mangroves are concerned.

- Seasonal variability of pigment concentration and its effect over the separability among closely associated mangrove species has a wide scope for further investigation. Therefore, studying the possibilities of phenological variations by acquiring temporal spectral data and its

implications on mangrove species discrimination can be another interesting topic of research.

- The potential of spatio-temporal transferability of the generated spectral library for studying other critical mangrove ecosystems in the country can also be investigated in our future work to address the utility of the library.

- Different dimensionality reduction methods and classification algorithms can be incorporated in the current multiple classifier system framework to improve diversity in input data and investigate the relation between them. The potential of trainable combination function for the integration of decisive function values of high performing classification algorithms can also be investigated to improve the classification accuracy.

- The extension of the MCS framework by including identified bands of Hyperion from our spectral separability analysis for improved species mapping is also aimed.

- The extension of the classification methodology for high resolution airborne hyperspectral images covering different vegetation types can also be aimed to test the efficacy of the proposed framework.

- The methodology that was followed for biomass estimation using WorldView-2 data can be extended using more number of normally distributed sample points and also with validated site specific wood density. This can be useful to derive species specific allometric equations for further improvement of the biomass estimation using satellite data.

- The species information derived from the classification result of Worldview-2 data can be used as the complimentary information to apply species specific allometric equation to improve biomass estimation.

- The potential of Sentinel-2 multispectral data and Sentinel-1 Synthetic Aperture Radar microwave data to improve the estimation of mangrove biomass is planned for the future work.

Mangroves are critical habitat mostly seen in tropical coastal zone, which need effective conservation and management practices for the sustainable development. The efficiency of such management practices can be significantly enhanced by

adopting appropriate remote sensing based technologies and developing integrated geospatial tools using contemporary methods.

REFERENCES

1. Abdi, H. (2007). The Bonferonni and Šidák corrections for multiple comparisons. In N. Salkind (Ed.), *Encyclopedia of measurement and statistics* (pp. 103–107). Thousand Oaks (CA): Sage.

2. Adam, E., and Mutanga, O. (2009). Spectral discrimination of papyrus vegetation (*Cyperus papyrus* L.) in swamp wetlands using field spectrometry. *ISPRS Journal of Photogrammetry and Remote Sensing*, *64*(6): 612–620.

3. Adam, E., Mutanga, O., and Rugege, D. (2009). Multispectral and hyperspectral remote sensing for identification and mapping of wetland vegetation: A Review. *Wetlands Ecology and Management*, *18*(3): 281–296.

4. Ahmedin, A. M., Bam, S., Siraj, K. T., and Raju, A. J. S. (2013). Assessment of biomass and carbon sequestration potentials of standing *Pongamia pinnata* in Andhra University , Visakhapatnam , India. *Bioscience Discovery*, *4*(2): 143–148.

5. Ajai, Bahuguna, A., Chauhan, H. B., Sen Sarma, K., Bhattacharya, S., Ashutosh, S., Pandey, C. N., Thangaradjou ,T., Gnanappazham L., Selvam V. and Nayak, S. R. (2012). Mangrove Inventory of India at Community Level. *National Academy Science Letters*, 36(1): 67–77.

6. Aksornkoae, S. (1993). *Ecology and management of mangroves. IUCN*. Bangkok, Thailand: IUCN.

7. Alongi, D. M. (2002). Present state and future of the world's mangrove forests. *Environmental Conservation*, 29(3): 331–349.

8. Alongi, D. M. (2008). Mangrove forests: Resilience, protection from tsunamis, and responses to global climate change. *Estuarine, Coastal and Shelf Science*, 76(1): 1–13.

9. Alongi, D. M. (2014). Carbon cycling and storage in mangrove forests. *Annual Review of Marine Science*, 6: 195–219.

10. Alongi, D. M., Murdiyarso, D., Fourqurean, J. W., Kauffman, J. B., Hutahaean, A., Crooks, S., Lovelock, C. E., Howard, J., Herr, D., Fortes, M., Pidgeon, E., Wagey, T. (2015). Indonesia's blue carbon: a globally significant and vulnerable sink for seagrass and mangrove carbon. *Wetlands Ecology and Management*, 24(1): 3-13.

11. Ambastha, K. R., Hussain, S. A., Badola, R., and Roy, P. S. (2010). Spatial analysis of anthropogenic disturbances in mangrove forests of Bhitarkanika Conservation Area, India. *Journal of the Indian Society of Remote Sensing*, 38(1): 67–83.

12. Andrew, M. E., and Ustin, S. L. (2006). Spectral and physiological uniqueness of perennial pepperweed (*Lepidium latifolium*). *Weed Science*, 54(6): 1051–1062.

13. Aschbacher, J., Ofren, R., Delsol, J. P., Suselo, T. B., Vibulsresth, S., and Charrupat, T. (1995). An integrated comparative approach to mangrove vegetation mapping using advanced remote sensing and GIS technologies: preliminary results. *Hydrobiologia*, 295(1-3): 285–294.

14. ASD. (2008). *ViewSpec Pro ^{TM} User Manual*. ASD Document 600555 Rev. A.

15. ASD. (2001). *Field spectrometry: Techniques and instrumentation*. ASD.

16. Ashokkumar, L., and Shanmugam, S. (2014). Hyperspectral band selection and classification of Hyperion image of Bhitarkanika mangrove ecosystem, eastern India. In C. M. U. Neale & A. Maltese (Eds.), *Proceeding of SPIE: Remote Sensing for Agriculture, Ecosystems, and Hydrology XVI*, 9239, pp. 923914–1 – 923914–9.

17. Asner, G. P. (1998). Biophysical and biochemical sources of variability in canopy reflectance. *Remote Sensing of Environment*, *64*(3): 234–253.

18. Azariah, J., Azariah, H., Gunasekaran, S., and Selvam, V. (1992). Structure and species distribution in Coringa mangrove forest, Godavari Delta, Andhra Pradesh, India. *Hydrobiologia*, 80(247): 11–16.

19. Badola, R., and Hussain, S. A. (2005). Valuing ecosystem functions: An empirical study on the storm protection function of Bhitarkanika mangrove ecosystem, India. *Environmental Conservation*, 32(1): 85–92.

20. Baldridge, A. M., Hook, S. J., Grove, C. I., and Rivera, G. (2009). The ASTER spectral library version 2.0. *Remote Sensing of Environment*, 113(4): 711–715.

21. Barik, J., and Chowdhury, S. (2014). True Mangrove Species of Sundarbans Delta, West Bengal , Eastern India. *Journal of Species Lists and Distribution*, 10(2): 329–334.

22. Beal, D., and Eamon, M. (1996). *Preliminary Results of Testing and a Proposal for Radiometric Error Correction Using Dynamic, Parabolic Linear Transformations of "Stepped" Data*. Analytical Spectral Devices Inc., Boulder, CO, pp. 1–5.

23. Becker, B. L., Lusch, D. P., and Qi, J. (2005). Identifying optimal spectral bands from in situ measurements of Great Lakes coastal wetlands using second-derivative analysis. *Remote Sensing of Environment*, *97*(2): 238–248.

24. Belluco, E., Camuffo, M., Ferrari, S., Modenese, L., Silvestri, S., Marani, A, and Marani, M. (2006). Mapping salt-marsh vegetation by multispectral and hyperspectral remote sensing. *Remote Sensing of Environment*, *105*(1): 54–67.

25. Belsley, D. A. (2006). Conditioning diagnostics. In *Encyclopedia of Statistical Sciences*. John Wiley & Sons, Inc.

26. Benediktsson, J. A., and Swain, P. H. (1992). Consensus Theoretic Classification Methods. *IEEE Transactions on Systems, Man and Cybernetics*, *22*(4): 688–704.

27. Benfield, S. L., Guzman, H. M., and Mair, J. M. (2005). Temporal mangrove dynamics in relation to coastal development in Pacific Panama. *Journal of Environmental Management*, 76(3): 263–276.

28. Binh, T. N. K. D., Vromant, N., Hung, N. T., Hens, L., and Boon, E. K. (2005). Land cover changes between 1968 and 2003 in Cai Nuoc, Ca Mau Peninsula, Vietnam. *Environment, Development and Sustainability*, 7(4): 519–536.

29. Bioucas-dias, J. M., Plaza, A., Camps-valls, G., Scheunders, P., Nasrabadi, N. M., and Chanussot, J. (2013). Hyperspectral Remote Sensing Data Analysis and Future Challenges. *IEEE Geoscience and Remote Sensing Magazine*, (June): 6–36.

30. Bongiovi, R. P., Hackwell, J. A., and Hayburst, T. L. (1996). Airborne LWIR hyperspectral measurements of military vehicles. *1996 IEEE Aerospace Applications Conference Proceedings*, pp. 121-135.

31. Borengasser, M., Hungate, W. S., and Watkins, R. (2008). *Hyperspectral Remote Sensing: principles and Applications*. CRC Press, Boka Raton.

32. Bosire, J. O., Dahdouh-Guebas, F., Walton, M., Crona, B. I., Lewis, R. R., Field, C., Kairo, J. G. and Koedam, N. (2008). Functionality of restored mangroves: A Review. *Aquatic Botany*, 89(2): 251–259.

33. Bouillon, S., Borges, A. V., Castañeda-Moya, E., Diele, K., Dittmar, T., Duke, N. C., Kristensen, E., Lee, S. Y., Marchand, C., Middelburg, J. J., Rivera-Monroy., V. H., Smith, T. J., and Twilley, R. R. (2008). Mangrove production and carbon sinks: A revision of global budget estimates. *Global Biogeochemical Cycles*, 22(2): 1–12.

34. Breiman, L. (1996). Bagging Predictors. *Machine Learning*, *24*: 123–140.

35. Breiman, L. (2001). Random forests. *Machine Learning*, *45*(1): 5–32.

36. Broge, N. H., and Leblanc, E. (2000). Comparing prediction power and stability of broadband and hyperspectral vegetation indices for estimation of green leaf area index and canopy chlorophyll density. *Remote Sensing of Environment*, *76*(2): 156–172.

37. Brown, A., Walter, M., and Cudahy, T. (2005). Hyperspectral imaging spectroscopy of a Mars analogue environment at the North Pole Dome, Pilbara Craton, Western Australia. *Australian Journal of Earth Sciences*, 52(3): 353–364.

38. Calvao, T., and Palmeirim, J. M. (2004). Mapping Mediterranean scrub with satellite imagery: biomass estimation and spectral behaviour. *International Journal of Remote Sensing*, *25*(16): 3113–3126.

39. Campbell, N. A., and Atchley, W. R. (1981). The geometry of cacnonical variate analysis. *Systematic Zoology*, *30*(3): 268–280.

40. Casal, G., Kutser, T., Domínguez-Gómez, J. A., Sánchez-Carnero, N., and Freire, J. (2013). Assessment of the hyperspectral sensor CASI-2 for macroalgal discrimination on the ría de vigo coast (NW Spain) using field spectroscopy and modelled spectral libraries. *Continental Shelf Research*. 55: 129–140.

41. Castel, T., Guerra, F., Caraglio, Y., and Houllier, F. (2002). Retrieval biomass of a large Venezuelan pine plantation using JERS-1 SAR data. Analysis of forest structure impact on radar signature. *Remote Sensing of Environment*, *79*(1): 30–41.

42. Ceamanos, X., Waske, B., Benediktsson, J. A., Chanussot, J., Fauvel, M., and Sveinsson, J. R. (2010). A classifier ensemble based on fusion of support vector machines for classifying hyperspectral data. *International Journal of Image and Data Fusion*, *1*(4): 293–307.

43. Ceamanos, X., Waske, B., Benediktsson, J. A., Chanussot, J., and Sveinsson, J. R. (2009). Ensemble strategies for classifying hyperspectral remote sensing data. *Lecture Notes in Computer Science (Including Subseries Lecture Notes in Artificial Intelligence and Lecture Notes in Bioinformatics)*, *5519 LNCS:* 62–71.

44. Cebrian, J. (2002). Variability and control of carbon consumption, export, and accumulation in marine communities. *Limnology and Oceanography*, 47(1): 11–22.

45. Chadwick, J. (2011). Integrated LiDAR and IKONOS multispectral imagery for mapping mangrove distribution and physical properties. *International Journal of Remote Sensing*, 32(21): 6765–6781.

46. Chakravortty, S., and Sinha, D. (2015). Analysis of Multiple Scattering of Radiation amongst End Members in a Mixed Pixel of Hyperspectral Data for Identification of Mangrove Species in a Mixed Stand. *Journal of the Indian Society of Remote Sensing*, 43(3): 559–569.

47. Chander, G., Coan, M. J., and Scaramuzza, P. L. (2008). Evaluation and comparison of the IRS-P6 and the landsat sensors. *IEEE Transactions on Geoscience and Remote Sensing*, *46*(1): 209–221.

48. Chang, C. C., and Lin, C. J. (2011). LIBSVM: A Library for Support Vector Machines. *ACM Transactions on Intelligent Systems and Technology*, *2*(3): 1–27.

49. Chave, J., Coomes, D., Jansen, S., Lewis, S. L., Swenson, N. G., and Zanne, A. E. (2009). Towards a worldwide wood economics spectrum. *Ecology Letters*, *12*(4): 351–366.

50. Chaves, A. B., and Lakshumanan, C. (2008). Remote Sensing and GIS-Based Integrated Study and Analysis for Mangrove-Wetland Restoration in Ennore Creek, Chennai, South India. *Proceeding of Taal 2007: The 12th World Lake Conference*, pp. 685–690.

51. Chen, D., Stow, D. A., and Gong, P. (2004). Examining the effect of spatial resolution and texture window size on classification accuracy: an urban environment case. *International Journal of Remote Sensing*, *25*(11): 2177–2192.

52. Cheng, Q., Varshney, P. K., and Arora, M. K. (2006). Logistic Regression for Feature Selection and Soft Classification of Remote Sensing Data. *IEEE Geoscience and Remote Sensing Letters*, *3*(4): 491–494.

53. Cho, M. A., Debba, P., Mathieu, R., Naidoo, L., Van Aardt, J., and Asner, G. P. (2010). Improving discrimination of savanna tree species through a multiple-endmember spectral angle mapper approach: Canopy-level analysis. *IEEE Transactions on Geoscience and Remote Sensing*, *48*(11): 4133–4142.

54. Choe, E., van der Meer, F., van Ruitenbeek, F., van der Werff, H., de Smeth, B., and Kim, K. W. (2008). Mapping of heavy metal pollution in stream sediments using combined geochemistry, field spectroscopy, and hyperspectral remote sensing: A case study of the Rodalquilar mining area, SE Spain. *Remote Sensing of Environment*, 112(7): 3222–3233.

55. Christensen, P. R., Bandfield, J. L., Hamilton, V. E., Howard, D. A., Lane, M. D., Piatek, J. L., Ruff S. W., and Stefanov, W. L. (2000). A thermal emission spectral library of rock-forming minerals. *Journal of Geophysical Research*, 105(E4): 9735–9739.

56. Clark, C. D., Ripley, H. T., Green, E. P., Edwards, A. J., and Mumby, P. J. (1997). Cover Mapping and measurement of tropical coastal environments with hyperspectral and high spatial resolution data. *International Journal of Remote Sensing*, 18(2): 237–242.

57. Clark, M., Roberts, D., and Clark, D. (2005). Hyperspectral discrimination of tropical rain forest tree species at leaf to crown scales. *Remote Sensing of Environment*, *96*(3-4): 375–398.

58. Clark, R., Swayze, G., Wise, R., Livo, K., Hoefman, T., and Kokaly RF. (2007). USGS digital spectral library splib06a. *U.S. Geological Survey*, (Digital Data Series 231): 1–23. Retrieved from http://speclab.cr.usgs.gov/spectral.lib06/ds231/.

59. Clough, B. F., and Scott, K. (1989). Allometric relationships for estimating above-ground biomass in six mangrove species. *Forest Ecology and Management*, *27*(2): 117–127.

60. Cochrane, M. (2000). Using vegetation reflectance variability for species level classification of hyperspectral data. *International Journal of Remote Sensing*, 21(10): 2075–2087.

61. Comley, B. W. T., and McGuinness, K. A. (2005). Above and below-ground biomass, and allometry, of four common northern Australian mangroves. *Australian Journal of Botany*, *53*(5): 431–436.

62. Curran, P. J. (1994). Imaging spectrometry. *Progress in Physical Geography*, 18(2): 247–266.

63. Curran, P. J. (1989). Remote sensing of foliar chemistry. *Remote Sensing of Environment*, *278*: 271–278.

64. Curtiss, B., and Goetz, A. F. H. (2012). Collection and quality control of spectral signatures in the field. In S. S. Shen & P. E. Lewis (Eds.), *SPIE Conference on Algorithms and Technologies for Multispectral, Hyperspectral, and Ultraspectral Imagery XVIII Volume 8390*, pp. 839011–839011–9.

65. Dahdouh-Guebas, F., Zetterström, T., Rönnbäck, P., Troell, M., Wickramasinghe, A., and Koedam, N. (2002). Recent Changes in Land-Use in the Pambala–Chilaw Lagoon Complex (Sri Lanka) Investigated Using Remote Sensing and GIS: Conservation of Mangroves vs. Development of Shrimp Farming. *Environment, Development and Sustainability*, 4(2): 185–200.

66. Dale, P. E. R., Knight, J., Ritchie, S. A., and Kay, B. H. (2005). A practical tool to identify water bodies with potential for mosquito habitat under mangrove canopy: Large-scale airborne scanning in the thermal band 8-13 μm. *Wetlands Ecology and Management*, 13: 389–394.

67. Damodaran, B. B., and Nidamanuri, R. R. (2014a). Assessment of the impact of dimensionality reduction methods on information classes and classifiers for hyperspectral image classification by multiple classifier system. *Advances in Space Research*, *53*(12): 1720–1734.

68. Damodaran, B. B., and Nidamanuri, R. R. (2014b). Dynamic Linear Classifier System for Hyperspectral Image Classification for Land Cover Mapping. *IEEE Journal of Selected Topics in Applied Earth Observations and Remote Sensing*, *7*(6): 2080–2093.

69. Danielsen, F., Sørensen, M. K., Olwig, M. F., Selvam, V., Parish, F., Burgess, N. D., Hiraishi, T., Karunagaran, V. M., Rasmussen, M. S., Hansen, L. B., Quarto, A., and Suryadiputra, N. (2005). The Asian tsunami: a protective role for coastal vegetation. *Science*, 310(5748): 643.

70. Das, A. B., Parida, A., Basak, U. C., and Das, P. (2002). Studies on pigments, proteins and photosynthetic rates in some mangroves and mangrove associates from Bhitarkanika, Orissa. *Marine Biology*, *141*(3): 415–422.

71. Dasarathy, B. V., and Sheela, B. V. (1979). Composite Classifier System Design: Concepts and Methodology. *Proc IEEE*, *67*: 708–713.

72. Datt, B., Mcvicar, T. R., Niel, T. G. Van, Jupp, D. L. B., and Pearlman, J. S. (2003). Preprocessing EO-1 Hyperion Hyperspectral Data to Support the Application of Agricultural Indexes. *IEEE Transactions on Geoscience and Remote Sensing*, 41(6): 1246–1259.

73. Datta, P. N., Das, S., and Ghose, M. (2005). Relation of leaf micromorphology with photosynthesis and water efflux in some Indian mangroves. *Acta Botanica Croatica*, *64*(2): 331–340.

74. Daughtry, C. S. T., Walthall, C. L., Kim, M. S., Colstoun, E. B. de, and McMurtrey, J. E. (2000). Estimating Corn Leaf Chlorophyll Concentration from Leaf and Canopy Reflectance. *Remote Sensing of Environment*, *74*(2): 229–239.

75. Daughtry, C. S. T., and Walthall, C. L. (1998). Spectral Discrimination of *Cannabis sativa L.* Leaves and Canopies. *Remote Sensing of Environment*, *64*(October 1996): 192–201.

76. Dehaan, R., and Taylor, G. (2003). Image-derived spectral endmembers as indicators of salinisation. *International Journal of Remote Sensing*, 24(4): 775–794.

77. Demuro, M., and Chisholm, L. (2003). Assessment of Hyperion for characterizing mangrove communities. *Proceedings of the International Conference on AVIRIS 2003 Workshop*, pp. 18–23.

78. Deventer, H. Van, Cho, M. A., Mutanga, O., Naidoo, L., and Dudeni-tlhone, N. (2015). Reducing Leaf-Level Hyperspectral Data to 22 Components of Biochemical and Biophysical Bands Optimizes Tree Species Discrimination. *IEEE Journal of Selected Topics in Applied Earth Observations and Remote Sensing*: 1–11.

79. Díaz, R., Cervera, L., Fenollosa, S., Ávila, C., and Belenguer, J. (2011). Hyperspectral system for the detection of foreign bodies in meat products. *Procedia Engineering*, 25: 313–316.

80. Dietterich, T. G. (2000). Ensemble methods in machine learning. *Multiple Classifier Systems*, *1857*: 1–15.

81. Dobson, C. M., Ulaby, F. T., Pierce, L. E., Sharik, T. L., Bergen, K. M., Kellndorfer, J., Kendra, J. R., Li, E., Lin, Y. C., Nashashibi, A., Sarabandi, K., and Siqueira, P. (1995). Estimation of forest biophysical characteristics in northern Michigan with SIR-C/X-SAR. *IEEE Transactions on Geoscience and Remote Sensing*, *33*(4): 877–895.

82. Donato, D., Kauffman, J. B., Murdiyarso, D., Kurnianto, S., Stidham, M., and Kanninen, M. (2011). Mangroves among the most carbon-rich forests in the tropics. *Nature Geoscience*. 4(5): 293-297.

83. Du, P., Xia, J., Zhang, W., Tan, K., Liu, Y., and Liu, S. (2012). Multiple classifier system for remote sensing image classification: A Review. *Sensors*, *12*(4): 4764–4792.

84. Du, Q. (2007). Modified Fisher's Linear Discriminant Analysis for Hyperspectral Imagery. *IEEE Geoscience and Remote Sensing Letters*, *4*(4): 503–507.

85. Duda, R. O., Hart, P. E., and Stork, D. G. (2001). *Pattern Classification. John Wiley & Sons Inc.* (Second Edi). New York, USA: John Wiley & Sons Inc.

86. Duke, N. C. (1992). Mangrove floristics and biogeography. In A. I. Robertson & D. M. Alongi (Eds.), *Tropical mangrove ecosystems*. American Geophysical Union, Washington, D. C., pp. 63 – 100.

87. Duke, N. C., Ball, M. C., and Ellison, J. C. (1998). Factors influencing biodiversity and distributional gradients in mangroves. *Global Ecology and Biogeography Letters*, 7(1): 27–47.

88. Duke, N., Meynecke, J., and Dittmann, S. (2007). A world without mangroves? *Science*, 317(July): 41–43.

89. Dwivedi, R. S., Rao, B. R. M., and Bhattacharya, S. (1999). Mapping wetlands of the Sundaban Delta and it's environs using ERS-1 SAR data. *International Journal of Remote Sensing*, 20(11): 2235–2247.

90. Eckert, S. (2012). Improved Forest Biomass and Carbon Estimations Using Texture Measures from WorldView-2 Satellite Data. *Remote Sensing*, *4*(12): 810–829.

91. Edelman, G. J., Gaston, E., van Leeuwen, T. G., Cullen, P. J., and Aalders, M. C. G. (2012). Hyperspectral imaging for non-contact analysis of forensic traces. *Forensic Science International*, 223(1-3): 28–39.

92. Ellenbogen, K. (2012). Coastal Ecosystems: Why sound management of these key natural carbon sinks matter for greenhouse gas emissions and climate change? *The Blue Carbon Initiative*, pp. 1-15.

93. Elvidge, C. D., and Chen, Z. K. (1995). Comparison of Broad-Band and Narrow-Band Red and near-Infrared Vegetation Indexes. *Remote Sensing of Environment*, *54*(1): 38–48.

94. Englhart, S., Keuck, V., and Siegert, F. (2011). Aboveground biomass retrieval in tropical forests - The potential of combined X- and L-band SAR data use. *Remote Sensing of Environment*, 115(5): 1260–1271.

95. Everitt, J., Escobar, D., and Judd, F. (1991). Evaluation of Airborne Video Imagery for Distuinguishing Black Mangrove (*Avicennia germinans*) on the Lower Texas Gulf Coast. *Journal of Coastal Research*, 7(4): 1169–1173.

96. Everitt, J. H., Judd, F. W., Escobar, D. E., and Davis, M. R. (1996). Integration of Remote Sensing and Spatial Information Technologies for Mapping Black Mangrove on the Texas Gulf Coast. *Journal of Coastal Research*, 12(1): 64–69.

97. Everitt, J., and Judd, F. (1989). Using remote sensing techniques to distinguish and monitor black mangrove (*Avicennia germinans*). *Journal of Coastal Research*, 5(4): 737–745.

98. FAO. (2007). The world's mangroves 1980-2005. *FAO Forestry Paper 153*: 89.

99. Fassnacht, F. E., Neumann, C., Forster, M., Buddenbaum, H., Ghosh, A., Clasen, A., Joshi, P. K., and Koch, B. (2014). Comparison of feature reduction algorithms for classifying tree species with hyperspectral data on three central European test sites. *IEEE Journal of Selected Topics in Applies Earth Observations and Remote Sensing*, *7*(6): 1–15.

100. Fatoyinbo, T. E., and Armstrong, A. H. (2010). Remote Characterization of Biomass Measurements : Case Study of Mangrove Forests. In M. N. B. Momba & F. Bux (Eds.), *Biomass*: 65–78.

101. Fatoyinbo, T. E., Simard, M., Washington-Allen, R. A., and Shugart, H. H. (2008). Landscape-scale extent, height, biomass, and carbon estimation of Mozambique's mangrove forests with Landsat ETM+ and Shuttle Radar Topography Mission elevation data. *Journal of Geophysical Research*, *113*(G2): 1–13.

102. Fauvel, M., Chanussot, J., and Benediktsson, J. A. (2006). Decision Fusion for the Classification of Urban Remote Sensing Images. *IEEE Transactions on Geoscience and Remote Sensing*, *44*(10): 2828–2838.

103. Ferrier, G. (1999). Application of imaging spectrometer data in identifying environmental pollution caused by mining at Rodaquilar, Spain. *Remote Sensing of Environment*, 68(2): 125–137.

104. Foody, G. M., Cutler, M. E., Mcmorrow, J., Pelz, D., Tangki, H., Boyd, D. S., and Douglas, I. (2001). Mapping the biomass of Bornean tropical rain forest from remotely sensed data. *Global Ecology and Biogeography*, *10*: 379–387.

105. Forzieri, G., Moser, G., and Catani, F. (2012). Assessment of hyperspectral MIVIS sensor capability for heterogeneous landscape classification. *ISPRS Journal of Photogrammetry and Remote Sensing*, *74*: 175–184.

106. Fromard, F., Vega, C., and Proisy, C. (2004). Half a century of dynamic coastal change affecting mangrove shorelines of French Guiana. A case study based on remote sensing data analyses and field surveys. *Marine Geology*, 208(2-4): 265–280.

107. FSI. (2015a). Forest Cover in India: India State of Forest Report 2015 by Forest Survey of India. Dehradun, India.

108. FSI. (2015b). *Mangrove Cover in India: India State of Forest Report 2015*. Forest Survey of India: 62–67.

109. Fuchs, H., Magdon, P., Kleinn, C., and Flessa, H. (2009). Estimating aboveground carbon in a catchment of the Siberian forest tundra: Combining satellite imagery and field inventory. *Remote Sensing of Environment*, *113*(3): 518–531.

110. Gao, B. C., and Goetz, A. F. H. (1991). Cloud area determination from AVIRIS data using water vapor channels near 1 micron. *Journal of Geophysical Research*, 96(90): 2857–2864.

111. Gao, J. (1998). A hybrid method toward accurate mapping of mangroves in a marginal habitat from SPOT multispectral data. *International Journal of Remote Sensing*, 19(10): 1887–1899.

112. Ghosh, A., Fassnacht, F. E., Joshi, P. K., and Kochb, B. (2014). A framework for mapping tree species combining hyperspectral and LiDAR data: Role of selected classifiers and sensor across three spatial scales. *International Journal of Applied Earth Observation and Geoinformation*, 26(1): 49–63.

113. Gilman, E. L., Ellison, J., Duke, N. C., and Field, C. (2008). Threats to mangroves from climate change and adaptation options: A Review. *Aquatic Botany*, 89(2): 237–250.

114. Giri, C., Long, J., and Tieszen, L. (2011). Mapping and Monitoring Louisiana's Mangroves in the Aftermath of the 2010 Gulf of Mexico Oil Spill. *Journal of Coastal Research*, 277(6): 1059–1064.

115. Giri, C., and Muhlhausen, J. (2008). Mangrove forest distributions and dynamics in Madagascar (1975-2005). *Sensors*, 8(4): 2104–2117.

116. Giri, C., Ochieng, E., Tieszen, L. L., Zhu, Z., Singh, A., Loveland, T., Masek, J., and Duke, N. (2011). Status and distribution of mangrove forests of the world using earth observation satellite data. *Global Ecology and Biogeography*, 20(1): 154–159.

117. Giri, C. P., and Delsol, J. P. (1993). Mangrove forest cover mapping in Phangnga Bay, Thailand, Using SPOT HRV and JERS-1 data in conjunction with GIS. In *Proceedings of International Seminar on Remote Sensing for Coastal Zone and Coral Reef Applications,* ATF, Bangkok, Thailand (25 October - 1 November 1993). Bangkok, Thailand, pp. 1-16.

118. Giri, C., Pengra, B., Zhu, Z., Singh, A., and Tieszen, L. L. (2007). Monitoring mangrove forest dynamics of the Sundarbans in Bangladesh and India using multi-temporal satellite data from 1973 to 2000. *Estuarine, Coastal and Shelf Science*, 73(1-2): 91–100.

119. Gislason, P. O., Benediktsson, J. A., and Sveinsson, J. R. (2006). Random forests for land cover classification. *Pattern Recognition Letters*, 27(4): 294–300.

120. Gnanappazham, L., and Selvam, V. (2011). The dynamics in the distribution of mangrove forests in Pichavaram, South India – perception by user community and remote sensing. *Geocarto International*, 26(6): 475–490.

121. Gong, P., Pu, R., and Yu, B. (1997). Conifer species recognition: An exploratory analysis of in situ hyperspectral data. *Remote Sensing of Environment*, *62*: 189–200.

122. Govender, M., Chetty, K., and Bulcock, H. (2007). A review of hyperspectral remote sensing and its application in vegetation and water resource studies. *WaterSA*, 33(2): 145–152.

123. Gowen, A. A., O'Donnell, C. P., Cullen, P. J., Downey, G., and Frias, J. M. (2007). Hyperspectral imaging - an emerging process analytical tool for food quality and safety control. *Trends in Food Science and Technology*, 18(12): 590–598.

124. Granahan, J. C., and Sweet, J. N. (2001). An evaluation of atmospheric correction techniques using the spectral similarity scale. *IGARSS 2001. Scanning the Present and Resolving the Future. Proceedings. IEEE 2001 International Geoscience and Remote Sensing Symposium (Cat. No.01CH37217)*, 5(C): 7031–7033.

125. Green, E. P., Clark, C. D., Mumby, P. J., Edwards, A. J., and Ellis, A. C. (1998). Remote sensing techniques for mangrove mapping. *International Journal of Remote Sensing*, 19(5): 935–956.

126. Green, E. P., Mumby, P. J., Edwards, A. J., Clark, C. D., and Ellis, A. C. (1997). Estimating leaf area index of mangroves from satellite data. *Aquatic Botany*, 58(1): 11–19.

127. Green, E. P., Mumby, P. J., Edwards, A. J., and Clark, C. D. (1996). A review of remote sensing for the assessment and management of tropical coastal resources. *Coastal Management*, 24(1): 1–40.

128. Gupta, R. K., Vijayan, D., and Prasad, T. S. (2006). The relationship of hyper-spectral vegetation indices with leaf area index (LAI) over the growth cycle of wheat and chickpea at 3nm spectral resolution. *Advances in Space Research*, 38(10): 2212–2217.

129. Gurram, P., and Kwon, H. (2010). A full diagonal bandwidth Gaussian kernel SVM based ensemble learning for hyperspectral chemical plume detection. *Proceedings of IEEE International Geoscience and Remote Sensing Symposium (IGARSS 2010)*, pp. 2804–2807.

130. Hackwell, J. A, Warren, D. W., Bongiovi, R. P., Hansel, S. J., Hayhurst, T. L., Mabry, D. J., Sivjee, M. G., and Skinner, J. W. (1996). LWIR/MWIR Imaging Hyperspectral Sensor for Airborne and Ground-Based Remote Sensing. *In Proceedings of SPIE : Imaging Spectrometry II*, Vol. 2819, pp. 102–107.

131. Hamdan, O., Khali Aziz, H., and Mohd Hasmadi, I. (2014). L-band ALOS PALSAR for biomass estimation of Matang Mangroves, Malaysia. *Remote Sensing of Environment*, 155: 69–78.

132. Hame, T., Salli, A., Andersson, K., and Lohi, A. (1997). A new methodology for the estimation of biomass of conifer-dominated boreal forest using NOAA AVHRR data. *International Journal of Remote Sensing*, *18*(15): 3211–3243.

133. Hamilton, S. J., and Lodder, R. A. (2002). Hyperspectral imaging technology for pharmaceutical analysis. *Proceedings of SPIE 4626, Biomedical Nanotechnology Architectures and Applications*, pp. 136–147.

134. Haralick, R. M. (1979). Statistical and structural approach to texture. *Proceeding of the IEEE*, *67*(5): 786–804.

135. Haralick, R., Shanmugam, K., and Dinstein, I. (1973). Textural Features for Image Classification. *IEEE Transactions on Systems, Man and Cybernetics*, *SMC-3*(6): 610–621.

136. Harris, J. R., Rogge, D., Hitchcock, R., Ijewliw, O., and Wright, D. (2005). Mapping lithology in Canada's Arctic : Application of hyperspectral data using the minimum noise fraction transformation and matched filtering. *Canadian Journal for Earth Science*, *42*: 2173–2193.

137. Heenkenda, M. K., Joyce, K. E., Maier, S. W., and Bartolo, R. (2014). Mangrove species identification: Comparing WorldView-2 with aerial photographs. *Remote Sensing*, *6*(7): 6064–6088.

138. Held, A., Ticehurst, C., Lymburner, L., and Williams, N. (2003). High resolution mapping of tropical mangrove ecosystems using hyperspectral and radar remote sensing. *International Journal of Remote Sensing*, 24(13): 2739–2759.

139. Herold, M., Roberts, D. A, Gardner, M. E., and Dennison, P. E. (2004). Spectrometry for urban area remote sensing - Development and analysis of a spectral library from 350 to 2400 nm. *Remote Sensing of Environment*, 91(3-4): 304–319.

140. Heumann, B. W. (2011a). An object-based classification of mangroves using a hybrid decision tree-support vector machine approach. *Remote Sensing*, *3*(11): 2440–2460.

141. Heumann, B. W. (2011b). Satellite remote sensing of mangrove forests: Recent advances and future opportunities. *Progress in Physical Geography*, *35*(1): 87–108.

142. Hirano, A., Madden, M., and Welch, R. (2003). Hyperspectral image data for mapping wetland vegetation. *Wetlands*, *23*(2): 436–448.

143. Hirata, Y., Tabuchi, R., Patanaponpaiboon, P., Poungparn, S., Yoneda, R., and Fujioka, Y. (2014). Estimation of aboveground biomass in mangrove forests using high-resolution satellite data. *Journal of Forest Research*, *19*(1): 34–41.

144. Hirsch, E., and Agassi, E. (2010). Detection of gaseous plumes in IR hyperspectral images-performance analysis. *IEEE Sensors Journal*, 10(3): 732–736.

145. Hogarth, P. J. (2007). *The Biology of Mangroves and Seagrasses*. Oxford University Press Inc., New York.

146. Huete, A., Didan, K., Miura, T., Rodriguez, E. P., Gao, X., and Ferreira, L. G. (2002). Overview of the radiometric and biophysical performance of the MODIS vegetation indices. *Remote Sensing of Environment*, *83*(1-2): 195–213.

147. Huete, A. R. (1988). A soil-adjusted vegetation index (SAVI). *Remote Sensing of Environment*, *25*: 295–309.

148. Huete, A. R., Jackson, R. D., and Post, D. F. (1985). Spectral response of a plant canopy with different soil backgrounds. *Remote Sensing of Environment*, *17*(1): 37–53.

149. Huete, A. R., Liu, H. Q., Batchily, K., and Van Leeuwen, W. (1997). A comparison of vegetation indices over a global set of TM images for EOS-MODIS. *Remote Sensing of Environment*, *59*(3): 440–451.

150. Huitric, M., Folke, C., and Kautsky, N. (2002). Development and government policies of the shrimp farming industry in Thailand in relation to mangrove ecosystems. *Ecological Economics*, 40(3): 441–455.

151. Hyde, P., Nelson, R., Kimes, D., and Levine, E. (2007). Exploring LiDAR-RaDAR synergy-predicting aboveground biomass in a southwestern ponderosa pine forest using LiDAR, SAR and InSAR. *Remote Sensing of Environment*, *106*(1): 28–38.

152. Hyvärinen, A., and Oja, E. (2000). Independent component analysis: Algorithms and applications. *Neural Networks*, *13*(4-5): 411–430.

153. Im, J., and Jensen, J. R. (2008). Hyperspectral remote sensing of vegetation. *Geography Compass*, *2*(6): 1943–1961.

154. Immitzer, M., Atzberger, C., and Koukal, T. (2012). Tree species classification with Random forest using very high spatial resolution 8-band WorldView-2 satellite data. *Remote Sensing*, *4*(9): 2661–2693.

155. Jackson, R. D., Pinter, P. J., Reginato, R. J., and Idso, S. B. (1980). *Hand-held radiometry*. In Agricultural Reviews and Manuals ARM - W - 19/October 1980. U.S. Department of Agriculture Report, pp. 66.

156. Jensen, J. R., Lin, H., Yang, X., Ramsey, E., Davis, B. A., and Thoemke, C. W. (1991). The measurement of mangrove characteristics in Southwest Florida using SPOT multispectral data. *Geocarto International*, 6(2): 13–21.

157. Jensen, J. R. (2005). *Introductory Digital Image Processing: A Remote Sensing Perspective*. (Third Edition). New Jersey, USA. Pearson Eductaion Inc.

158. Jensen, R., Mausel, P., Dias, N., Gonser, R., Yang, C., Everitt, J., and Fletcher, R. (2007). Spectral analysis of coastal vegetation and land cover using AISA+ hyperspectral data. *Geocarto International*, 22(1): 17–28.

159. Ji, M., Hu, J., and Feng, J. (2010). Measuring mangrove biomass via remote sensing subpixel analysis. *In Proceedings of SPIE Remote Sensing and Modeling of Ecosystems for Sustainability VII*. Vol. 7809, pp. 780907–1–780907–6.

160. Jiménez, M., and Díaz-Delgado, R. (2015). Towards a Standard Plant Species Spectral Library Protocol for Vegetation Mapping: A Case Study in the Shrubland of Doñana National Park. *ISPRS International Journal of Geo-Information*, 4(4): 2472–2495.

161. Joo Kim, S., Deng, F., and Brown, M. S. (2011). Visual enhancement of old documents with hyperspectral imaging. *Pattern Recognition*, 44(7): 1461–1469.

162. Joseph, G. (2005). *Fundamentals of remote sensing*. (Second Edition). Universities Press (India) Private Limited, Hyderbad, India.

163. Joshi, H. G., and Ghose, M. (2014). Community structure, species diversity, and aboveground biomass of the Sundarbans mangrove swamps. *Tropical Ecology*, *55*(3): 283–303.

164. Jusoff, K. (2006). Individual mangrove species identification and mapping in Port Klang using Airborne Hyperspectral Imaging. *Journal of Sustainability Science and Management*, *1*(2): 27–36.

165. Kairo, J. G., Dahdouh-Guebas, F., Bosire, J., and Koedam, N. (2001). Restoration and management of mangrove systems - a lesson for and from the East African region. *South African Journal of Botany*, 67: 383-389.

166. Kairo, J. G., Kivyatu, B., and Koedam, N. (2002). Application of remote sensing and GIS in the management of mangrove forests within and adjacent to Kiuga marine protected area, Lamu, Kenya. *Environment, Development and Sustainability*, 4(2): 153–166.

167. Kale, M. P., Singh, S., and Roy, P. S. (2002). Biomass and productivity estimation using aerospace data and geographic information system. *Tropical Ecology*, 43(1): 123–136.

168. Kalluri, H. R., Prasad, S., and Bruce, L. M. (2010). Decision-level fusion of spectral reflectance and derivative information for Robust hyperspectral land cover classification. *IEEE Transactions on Geoscience and Remote Sensing*, *48*(11): 4047–4058.

169. Kamal, M., Phinn, S., and Johansen, K. (2015). Object-Based Approach for Multi-Scale Mangrove Composition Mapping Using Multi-Resolution Image Datasets. *Remote Sensing*, 7(4): 4753–4783.

170. Kamal, M., and Phinn, S. (2011). Hyperspectral Data for Mangrove Species Mapping: A Comparison of Pixel-Based and Object-Based Approach. *Remote Sensing*, *3*(10): 2222–2242.

171. Kamaruzaman, J., and Kasawani, I. (2007a). Spectral signatures of some mangrove species in Malaysia. *In 5th WSEAS International Conference on Environment, Ecosystems and Development*, pp. 440–449.

172. Kamaruzaman, J., and Kasawani, I. (2007b). Imaging spectrometry on mangrove species identification and mapping in Malaysia. *WSEAS Transactions on Biology and Biomedicine*, 4(8): 118–126.

173. Kanal, L. (1974). Patterns in Pattern Recognition: 1968-1974. *IEEE Transactions on Information Theory*, *IT-20*(6): 697–717.

174. Kanniah, K., Sheikhi, A., Cracknell, A., Goh, H., Tan, K., Ho, C., and Rasli, F. (2015). Satellite Images for Monitoring Mangrove Cover Changes in a Fast Growing Economic Region in Southern Peninsular Malaysia. *Remote Sensing*, 7(11): 14360–14385.

175. Kar, C. S., and Satapathy, G. R. (2012). Mangrove ecosystem and its biodiversity in Orissa coast with respect to Bhitarkanika. In B. C. Guru, B. K. Senapati, N. Behera, & P. C. Mishra (Eds.), *Advances in Ecology and Environmental Sciences* (pp. 419–438). APH Publishing Corporation, New Delhi.

176. Kasawani, I., Norsaliza, U., and Hasmadi, I. M. (2010). Analysis of Spectral Vegetation Indices Related to Soil-Line for Mapping Mangrove Forest Using Satellite magery. *Applied Remote Sensing Journal*, *1*(1): 25–31.

177. Kathiresan, K., and Bingham, B. L. (2001). Biology of Mangroves and Mangrove Ecosystems. *Advances in Marine Biology*, 40: 81–251.

178. Kathiresan, K., and Rajendran, N. (2002). Fishery resources and economic gain in three mangrove areas on the. *Fisheries Management and Ecology*, 9(5): 277–283.

179. Kathiresan, K., and Rajendran, N. (2005). Coastal mangrove forests mitigated tsunami. *Estuarine, Coastal and Shelf Science*, 65(3): 601–606.

180. Kaufman, Y. J., and Tanre, D. (1992). Atmospherically Resistant Vegetation Index (ARVI) for EOS-MODIS. *IEEE Transactions on Geoscience and Remote Sensing*, *30*(2): 261–270.

181. Keshava, N., and Mustard, J. F. (2002). Spectral Unmixing. *IEEE Signal Processing Magazine*, (January): 44–57.

182. Ketterings, Q. M., Coe, R., van Noordwijk, M., Ambagau, Y., and Palm, C. A. (2001). Reducing uncertainty in the use of allometric biomass equations for predicting above-ground tree biomass in mixed secondary forests. *Forest Ecology and Management*, *146*(1-3): 199–209.

183. Klemas, V. (2013). Remote Sensing of Coastal Wetland Biomass: An Overview. *Journal of Coastal Research*, 290(5): 1016–1028.

184. Knight, J. M., Dale, P. E. R., Spencer, J., and Griffin, L. (2009). Exploring LiDAR data for mapping the micro-topography and tidal hydro-dynamics of mangrove systems: An example from southeast Queensland, Australia. *Estuarine, Coastal and Shelf Science*, 85(4): 593–600.

185. Knipling, E. B. (1970). Physical and physiological basis for the reflectance of visible and near-infrared radiation from vegetation. *Remote Sensing of Environment*, *1*(3): 155–159.

186. Koch, B. (2010). Status and future of laser scanning, synthetic aperture radar and hyperspectral remote sensing data for forest biomass assessment. *ISPRS Journal of Photogrammetry and Remote Sensing*, 65(6): 581–590.

187. Koedsin, W., and Vaiphasa, C. (2013). Discrimination of tropical mangroves at the species level with EO-1 Hyperion data. *Remote Sensing*, 5(7): 3562–3582.

188. Kokaly, R., Despain, D., Clark, R., and Livo, K. (2003). Mapping vegetation in Yellowstone National Park using spectral feature analysis of AVIRIS data. *Remote Sensing of Environment*, *84*: 437–456.

189. Komiyama, A., Poungparn, S., and Kato, S. (2005). Common allometric equations for estimating the tree weight of mangroves. *Journal of Tropical Ecology*, *21*(04): 471–477.

190. Kovacs, J. M., King, J. M. L., Flores de Santiago, F., and Flores-Verdugo, F. (2009). Evaluating the condition of a mangrove forest of the Mexican Pacific based on an estimated leaf area index mapping approach. *Environmental Monitoring and Assessment*, *157*(1-4): 137–149.

191. Kovacs, J. M., Flores-Verdugo, F., Wang, J., and Aspden, L. P. (2004). Estimating leaf area index of a degraded mangrove forest using high spatial resolution satellite data. *Aquatic Botany*, 80(1): 13–22.

192. Kovacs, J. M., Vandenberg, C. V., and Flores-Verdugo, F. (2006). Assessing fine beam RADARSAT-1 backscatter from a white mangrove (*Laguncularia racemosa* (Gaertner)) canopy. *Wetlands Ecology and Management*, 14(5): 401–408.

193. Kovacs, J. M., Wang, J., and Blanco-Correa, M. (2001). Mapping disturbances in a mangrove forest using multi-date Landsat TM imagery. *Environmental Management*, 27(5): 763–776.

194. Kristensen, E., Bouillon, S., Dittmar, T., and Marchand, C. (2008). Organic carbon dynamics in mangrove ecosystems: A Review. *Aquatic Botany*, 89(2): 201–219.

195. Kruse, F. A., Lefkoff, A. B., Boardman, J. W., Heidebrecht, K. B., Shapiro, A. T., Barloon, P. J., and Goetz, A. F. H. (1993). The spectral image processing system (SIPS) - interactive visualization and analysis of imaging spectrometer data. *Remote Sensing of Environment*, *44*(2-3): 145–163.

196. Kuenzer, C., Bluemel, A., Gebhardt, S., Quoc, T. V., and Dech, S. (2011). Remote Sensing of Mangrove Ecosystems: A Review. *Remote Sensing*, *3*(5): 878–928.

197. Kumar, T., Panigrahy, S., Kumar, P., and Parihar, J. S. (2013). Classification of floristic composition of mangrove forests using hyperspectral data: Case study of Bhitarkanika National Park, India. *Journal of Coastal Conservation Planning and Management*, 17(1): 121–132.

198. Kumar, T., and Patnaik, C. (2013). Discrimination of mangrove forests and characterization of adjoining land cover classes using temporal C-band Synthetic Aperture Radar data: A case study of Sundarbans. *International Journal of Applied Earth Observation and Geoinformation*, 23(1): 119–131.

199. Kuncheva, L. I., Bezdek, J. C., and Duin, R. P. W. (2001). Decision Templates for Multiple Classifier Fusion : An Experimental Comparison. *Pattern Recognition*, *34*(2): 299–314.

200. Kuplich, T. M., Curran, P. J., and Atkinson, P. M. (2005). Relating SAR image texture to the biomass of regenerating tropical forests. *International Journal of Remote Sensing*, *26*(21): 4829–4854.

201. Kurvonen, L., Pulliainen, J., and Hallikainen, M. (1999). Retrieval of biomass in boreal forests from multitempotal ERS-1 and JERS-1 SAR images. *IEEE Transactions on Geoscience and Remote Sensing*, *37*(1): 198–205.

202. Kutser, T., Miller, I., and Jupp, D. L. B. (2006). Mapping coral reef benthic substrates using hyperspectral space-borne images and spectral libraries. *Estuarine, Coastal and Shelf Science*, 70(3): 449–460.

203. Lee, T.-M., and Yeh, H.-C. (2009). Applying remote sensing techniques to monitor shifting wetland vegetation: A case study of Danshui River estuary mangrove communities, Taiwan. *Ecological Engineering*, 35(4): 487–496.

204. Lewicki, P., and Hill, T. (2005). *Statistics : Methods and Applications. Statsoft Inc.* (Vol. 1st). Tulsa, OK: Statsoft Inc.

205. Li, X., Gar-On Yeh, A., Wang, S., Liu, K., Liu, X., Qian, J., and Chen, X. (2007). Regression and analytical models for estimating mangrove wetland biomass in South China using Radarsat images. *International Journal of Remote Sensing*, 28(24): 5567–5582.

206. Liang, H. (2012). Advances in multispectral and hyperspectral imaging for archaeology and art conservation. *Applied Physics A: Materials Science and Processing*, 106(2): 309–323.

207. Liang, S. (2005). *Quantitative remote sensing of land surfaces*. John Wiley & Sons Inc.

208. Long, B. G., and Skewes, T. D. (1996). A Technique for Mapping Mangroves with Landsat TM Satellite Data and Geographic Information System. *Estuarine, Coastal and Shelf Science*, 43: 373–381.

209. Long, J., Napton, D., Giri, C., and Graesser, J. (2014). A Mapping and Monitoring Assessment of the Philippines' Mangrove Forests from 1990 to 2010. *Journal of Coastal Research*, 30(2): 260–271.

210. Lu, Y. (1996). Knowledge integration in a multiple classifier system. *Applied Intelligence*, *6*(2): 75–86.

211. Lu, D. (2005). Aboveground biomass estimation using Landsat TM data in the Brazilian Amazon. *International Journal of Remote Sensing*, *26*(12): 2509–2525.

212. Lu, D. (2006). The potential and challenge of remote sensing based biomass estimation. *International Journal of Remote Sensing*, *27*(7): 1297–1328.

213. Lu, D., Chen, Q., Wang, G., Liu, L., Li, G., and Moran, E. (2014). A survey of remote sensing-based aboveground biomass estimation methods in forest ecosystems. *International Journal of Digital Earth*, (February 2015): 1–43.

214. Lucas, R., Lee, A., Armston, J., Breyer, J., Bunting, P., and Carreiras, J. (2008). Advances in forest characterisation, mapping and monitoring through integration of LiDAR and other remote sensing datasets. *In SilviLaser2008* Edinburgh, UK. *Sept. 17-19, 2008*, pp. 2–12.

215. Lucas, R. M., Ellison, J. C., Mitchell, A., Donnelly, B., Finlayson, M., and Milne, A. K. (2002). Use of stereo aerial photography for quantifying changes in the extent and height of mangroves in tropical Australia. *Wetlands Ecology and Management*, 10: 161–175.

216. Lugo, A. E., and Snedaker, S. C. (1974). The Ecology of Mangroves. *Annual Review of Ecology and Systematics*, 5: 39–64.

217. MacKay, H., Finlayson, C. M., Fernández-Prieto, D., Davidson, N., Pritchard, D., and Rebelo, L. M. (2009). The role of Earth Observation (EO) technologies in supporting implementation of the Ramsar Convention on Wetlands. *Journal of Environmental Management*, 90(7): 2234–2242.

218. Maimaitiyiming, M., Miller, A. J., and Ghulam, A. (2016). Discriminating Spectral Signatures Among and Within Two Closely Related Grapevine Species. *Photogrammetric Engineering & Remote Sensing*, *82*(1): 51–62.

219. Manakos, I., Manevski, K., and Petropoulos, G. P. (2010). Development of a spectral library for mediterranean land cover types. *Proc. 30th EARSeL Symp.: Remote Sensing for Science, Education and Natural and Cultural Heritage*, pp. 663–668.

220. Manevski, K., Manakos, I., Petropoulos, G. P., and Kalaitzidis, C. (2011). Discrimination of common Mediterranean plant species using field spectroradiometry. *International Journal of Applied Earth Observation and Geoinformation*, 13(6): 922–933.

221. Manjunath, K., Kumar, T., Kundu, N., and Panigrahy, S. (2013). Discrimination of mangrove species and mudflat classes using in situ hyperspectral data: A case study of Indian Sundarbans. *GIScience & Remote Sensing*, 50(4): 400–417.

222. Manolakis, D., Golowich, S., and Dipietro, R. S. (2014). Long-wave infrared hyperspectral remote sensing of chemical clouds: A focus on signal processing approaches. *IEEE Signal Processing Magazine*, 31(4): 120–141.

223. Manolakis, D., Marden, D., and Shaw, G. A. (2003). Hyperspectral Image Processing for Automatic Target Detection Applications. *Lincoln Laboratory Journal*, 14(1): 79–116.

224. Manson, F. J., Loneragan, N. R., McLeod, I. M., and Kenyon, R. A. (2001). Assessing techniques for estimating the extent of mangroves: Topographic maps, aerial photographs and Landsat TM images. *Marine and Freshwater Research*, 52(5): 787–792.

225. Manson, F. J., Loneragan, N. R., and Phinn, S. R. (2003). Spatial and temporal variation in distribution of mangroves in Moreton Bay, subtropical Australia: A comparison of pattern metrics and change detection analyses based on aerial photographs. *Estuarine, Coastal and Shelf Science*, 57(4): 653–666.

226. Mayers, J. (2014). Forests in the sustainable development goals. *Biores*, *8*(3).

227. Melesse, A. M., Weng, Q., Thenkabail, P. S., and Senay, G. B. (2007). Remote Sensing Sensors and Applications in Environmental Resources Mapping and Modelling. *Sensors*, *7*: 3209–3241.

228. Mitchell, T. M. (2015). Generative and Discriminative Classifiers: Naive Bayes and Logistic Regression. In *Machine Learning*: 1–17.

229. MoEF. (2002). *Biological Diversity Act 2002. New Delhi: Ministry of Environment and Forests, Government of India.*

230. Moorthy, P., and Kathiresan, K. (1997). Photosynthetic Pigments in Tropical Mangroves: Impacts of Seasonal Flux of UV-B Radiation and Other Environmental Attributes. *Botanica Marina*, 40(1-6): 341–349.

231. Moran, E. F., Brondizio, E., Mausel, P., and Wu, Y. (1994). Integrating Amazonian Vegetation, Land-Use, and Satellite Data. *BioScience*, *44*(5): 329–338.

232. Mougin, E., Proisy, C., Marty, G., Fromard, F., Puig, H., Betoulle, J. L., and Rudant, J. P. (1999). Multifrequency and multipolarization radar backscattering from mangrove forests. *IEEE Transactions on Geoscience and Remote Sensing*, 37(1): 94–102.

233. Muhammed, S., and Waqar, M. M. (2013). Hyperspectral Mapping Methods for Differentiating Mangrove Species along Karachi Coast. *International Journal of Environmental, Ecological, Geomatics, Earth Science and Engineering*, *7*(12): 931–933.

234. Murdiyarso, D., Purbopuspito, J., Kauffman, J. B., Warren, M. W., Sasmito, S. D., Donato, D. C., Manuri, S., Krisnawati, H., Taberima, S., and Kurnianto, S. (2015). The potential of Indonesian mangrove forests for global climate change mitigation. *Nature Climate Change*, (July): 8–11.

235. Mutanga, O., Adam, E., and Cho, M. A. (2012). High density biomass estimation for wetland vegetation using WorldView-2 imagery and random forest regression algorithm. *International Journal of Applied Earth Observation and Geoinformation*, *18*(1): 399–406.

236. Mutanga, O., and Skidmore, A. (2007). Red edge shift and biochemical content in grass canopies. *ISPRS Journal of Photogrammetry and Remote Sensing*, *62*(1): 34–42.

237. Mutanga, O., Skidmore, A. K., and Prins, H. H. T. (2004). Predicting in situ pasture quality in the Kruger National Park, South Africa, using continuum-removed absorption features. *Remote Sensing of Environment*, 89(3): 393–408.

238. Muttitanon, W., and Tripathi, N. K. (2005). Land use/land cover changes in the coastal zone of Ban Don Bay, Thailand using Landsat 5 TM data. *International Journal of Remote Sensing*, 26(11): 2311–2323.

239. Nascimento, J. M. P., and Bioucas-Dias, J. M. (2009). Nonlinear mixture model for hyperspectral unmixing. *In Proceedings of SPIE Conference on Image and Signal Processing for Remote Sensing XV* (Vol. 7477), pp. 74770I–1–74770I–8.

240. Nayak, S., and Bahuguna, A. (2001). Application of remote sensing data to monitor mangroves and other coastal vegetation of India. *Indian Journal of Marine Sciences*, 30 (December): 195–213.

241. Nayak, A. K. (2004). *Pictorial Guide to Mangrove Flora of Bhitarkanika*.

242. Nellemann, C., Corcoran, E., Duarte, C. M., Valdés, L., De Young, C., Fonseca, L., and Grimsditch, G. (2009). *Blue carbon: A Rapid Response Assessment*. United Nations Environmental Programme, GRID-Arendal, www.grida.no.

243. Nichol, J. E., and Sarker, M. L. R. (2011). Improved Biomass Estimation Using the Texture Parameters of Two High-Resolution Optical Sensors. *IEEE Transactions on Geoscience and Remote Sensing*, *49*(3): 930–948.

244. Nidamanuri, R. R., and Zbell, B. (2011). Use of field reflectance data for crop mapping using airborne hyperspectral image. *ISPRS Journal of Photogrammetry and Remote Sensing*, 66(5): 683–691.

245. Nidamanuri, R. R., and Zbell, B. (2012). Understanding the Unique Spectral Signature of Winter Rape. *Journal of the Indian Society of Remote Sensing*, 41(1): 57–70.

246. Okin, G. S., Roberts, D. A., Murray, B., and Okin, W. J. (2001). Practical limits on hyperspectral vegetation discrimination in arid and semiarid environments. *Remote Sensing of Environment*, 77(2): 212–225.

247. Ong, C., Cudahy, T., Caccetta, M., Hick, P., and Piggott, M. (2001). Quantifying dust loading on mangroves using hyperspectral techniques. *IGARSS 2001. Scanning the Present and Resolving the Future. Proceedings. IEEE 2001 International Geoscience and Remote Sensing Symposium*, pp. 296–298.

248. Padma, S., and Sanjeevi, S. (2014). Jeffries Matusita based mixed-measure for improved spectral matching in hyperspectral image analysis. *International Journal of Applied Earth Observation and Geoinformation*, 32: 138–151.

249. Pal, M., and Foody, G. M. (2010). Feature selection for classification of hyperspectral data by SVM. *IEEE Transactions on Geoscience and Remote Sensing*, 48(5): 2297–2307.

250. Pandya, M. R., Shah, D. B., Trivedi, H. J., Lunagaria, M. M., Pandey, V., Panigrahy, S., and Parihar, J. S. (2013). Field Measurements of Plant Emissivity Spectra: An Experimental Study on Remote Sensing of Vegetation in the Thermal Infrared Region. *Journal of the Indian Society of Remote Sensing*, 41(4): 787–796.

251. Panigrahy, S., Kumar, T., and Manjunath, K. R. (2012). Hyperspectral leaf signature as an added dimension for species discrimination: case study of four tropical mangroves. *Wetlands Ecology and Management*, 20(2): 101–110.

252. Pasqualini, V., Iltis, J., Dessay, N., Lointier, M., Guelorget, O., and Polidori, L. (1999). Mangrove mapping in North-Western Madagascar using SPOT-XS and SIR-C radar data. *Hydrobiologia*, 413: 127–133.

253. Patil, V., Singh, A., Naik, N., and Unnikrishnan, S. (2014). Estimation of carbon stocks in avicennia marina stand using allometry, CHN analysis, and GIS methods. *Wetlands*, 34(2): 379–391.

254. Patnaik, S. K., Kar, C. S., and Kar, S. K. (2000). Chapter XIV - Biodiversity in tidal swamps with special reference to Bhitarkanika. In N. K. Mahalik (Ed.), *Mahanadi delta* (pp. 139–153). AIT Alumni Association, New Delhi.

255. Podest, E., and Saatchi, S. (2002). Application of multiscale texture in classifying JERS-1 radar data over tropical vegetation. *International Journal of Remote Sensing*, 23(7): 1487–1506.

256. Prasad, S., and Bruce, L. M. (2011). A Divide-and-Conquer Paradigm for Hyperspectral Classification and Target Recognition. In S. Prasad, L. M. Bruce, & J. Chanussot (Eds.), *Optical Remote Sensing* (pp. 99–121). Springer-Verlag Berlin Heidelberg.

257. Prasad, P. R. C., Reddy, C. S., Rajan, K. S., Raza, S. H., and Dutt, C. B. S. (2009). Assessment of tsunami and anthropogenic impacts on the forest of the North Andaman Islands, India. *International Journal of Remote Sensing*, 30(5): 1235–1249.

258. Price, J. C. (1994). How unique are spectral signatures? *Remote Sensing of Environment*, 49(3): 181–186.

259. Proisy, C., Couteron, P., and Fromard, F. (2007). Predicting and mapping mangrove biomass from canopy grain analysis using Fourier-based textural ordination of IKONOS images. *Remote Sensing of Environment*, 109(3): 379–392.

260. Proisy, C., Mougin, E., Fromard, F., and Karam, M. A. (2000). Interpretation of polarimetric radar signatures of mangrove forests. *Remote Sensing of Environment*, *71*(1): 56–66.

261. Proisy, C., Mougin, E., Fromard, F., Trichon, V., and Karam, M. A. (2002). On the influence of canopy structure on the radar backscattering of mangrove forests. *International Journal of Remote Sensing*, 23(20): 4197–4210.

262. Pu, R. (2009). Broadleaf species recognition with in situ hyperspectral data. *International Journal of Remote Sensing*, *30*(11): 2759–2779.

263. Pu, R., and Landry, S. (2012). A comparative analysis of high spatial resolution IKONOS and WorldView-2 imagery for mapping urban tree species. *Remote Sensing of Environment*, *124*: 516–533.

264. Qi, J., Chehbouni, A., Huete, A. R., Kerr, Y. H., and Sorooshian, S. (1994). A modified soil adjusted vegetation index. *Remote Sensing of Environment*, *48*(2): 119–126.

265. Ramasubramanian, R., Gnanappazham, L., Ravishankar, T., and Navamuniyammal, M. (2006). Mangroves of Godavari – Analysis Through Remote Sensing Approach. *Wetlands Ecology and Management*, 14(1): 29–37.

266. Ranawana, R., and Palade, V. (2006). Multi-Classifier Systems: Review and a roadmap for developers. *International Journal of Hybrid Intelligent Systems*, *3*(1): 35–61.

267. Rao, B. R. M., Dwivedi, R. S., Kushwaha, S. P. S., Bhattacharya, S. N., Anand, J. B., and Dasgupta, S. (1999). Monitoring the spatial extent of coastal wetlands using ERS-1 SAR data. *International Journal of Remote Sensing*, 20(13): 2509–2517.

268. Rao, N. R., Garg, P. K., and Ghosh, S. K. (2007). Development of an agricultural crops spectral library and classification of crops at cultivator level using hyperspectral data. *Precision Agriculture*, 8: 173–185.

269. Rapantzikos, K., and Balas, C. (2005). Hyperspectral Imaging : Potential in Non-Destructive Analysis of Palimpsets. *In IEEE International Conference on Image Processing, 2005 (ICIP 2005)* Vol (2), 11-14 Sept. 2005, pp. 618–621.

270. Ravishankar, T., Gnanappazham, L., Ramasubramanian, R., Sridhar, D., Navamuniyammal, M., and Selvam, V. (2004a). *Atlas of Mangrove Wetlands of India: Part 2 - Andhra Pradesh*. M. S. Swaminathan Research Foundation, Chennai, India.

271. Ravishankar, T., Navamuniyammal, M., Gnanappazham, L., Nayak, S. S., Mahapatra, G. C., and Selvam, V. (2004b). *Atlas of Mangrove Wetlands of India: Part 3 - Orissa*. M. S. Swaminathan Research Foundation, Chennai, India.

272. Reddy, C. S., Pattanaik, C., and Murthy, M. S. R. (2007). Assessment and monitoring of mangroves of Bhitarkanika Wildlife Sanctuary, Orissa, India using remote sensing and GIS. *Current Science*, 92(10): 1409–1415.

273. Research Systems Inc., R. (2004). *ENVI User's Guide*. Boulder, Colorado, USA.

274. Richards, J. A., and Jia, X. (2005). *Remote Sensing Digital Image Analysis: An Introduction* (Fourth Edition). Springer-Verlag, Berlin.

275. Ricklefs, R. E., and Latham, R. E. (1993). *Global Patterns of Diversity in Mangrove Floras*. In R. E. Ricklefs & D. Schluter (Eds.), Species Diversity in Ecological Communities: Historical and Geographical Perspectives. University of Chicago Press. pp. 215–229.

276. Rocha, F., Pereira, D. S., and Kampel, M. (2012). Mapping of mangrove forests on the southern coast of São Paulo , Brazil , using synthetic aperture radar data from ALOS / PALSAR. *Remote Sensing Letters*, 3(7): 567–576.

277. Roli, F. (2005). Semi-supervised Multiple Classifier Systems: Background and Research Directions. In N. C. Oza, R. Polikar, J. Kittler, & F. Roli (Eds.), *Multiple Classifier Systems, Lecture Notes in Computer Science* (pp. 3541:1–11). Springer Berlin Heidelberg.

278. Rondeaux, G., Steven, M., and Baret, F. (1996). Optimization of soil-adjusted vegetation indices. *Remote Sensing of Environment*, *55*(2): 95–107.

279. Rosso, P. H., Ustin, S. L., and Hastings, A. (2005). Mapping marshland vegetation of San Francisco Bay, California, using hyperspectral data. *International Journal of Remote Sensing*, *26*(23): 5169–5191.

280. Roth, K. L., Roberts, D. A., Dennison, P. E., Alonzo, M., Peterson, S. H., and Beland, M. (2015). Differentiating plant species within and across diverse ecosystems with imaging spectroscopy. *Remote Sensing of Environment*. (In Press).

281. Roujean, J. L., and Breon, F. M. (1995). Estimating PAR absorbed by vegetation from bidirectional reflectance measurements. *Remote Sensing of Environment*, *51*(3): 375–384.

282. Roy, D. P., Wulder, M. A., Loveland, T. R., C.E., W., Allen, R. G., Anderson, M. C., Helder, D., Irons, J. R., Johnson, D. M., Kennedy, R., Scambos, D. A., Schaaf, C. B., Schott, J. R., Sheng, Y., Vermote, E. F., Belward, A. S., Bindschadler, R., Cohen, W. B., Gao, F., Hipple, J. D., Hostert, P., Huntington, J., Justice, C. O., Kilic, A., Kovalsky, V., Lee, Z. P., Lymburner, L., Masek, J. G., McCorkel, J., Shuai, Y., Trezza, R., Vogelmann, J., Wynne, R. H., and Zhu, Z. (2014). Landsat-8: Science and product vision for terrestrial global change research. *Remote Sensing of Environment*, *145*: 154–172.

283. Ruiz-Luna, A., and Berlanga-Robles, C. A. (1999). Modifications in Coverage Patterns and Land Use around the Huizache-Caimanero Lagoon System, Sinaloa, Mexico: A Multi-temporal Analysis using Landsat Images. *Estuarine, Coastal and Shelf Science*, 49: 37–44.

284. Saito, H., Bellan, M. F., Al-Habshi, A., Aizpuru, M., and Blasco, F. (2003). Mangrove research and coastal ecosystem studies with SPOT-4 HRVIR and TERRA ASTER in the Arabian Gulf. *International Journal of Remote Sensing*, 24(21): 4073–4092.

285. Salerno, E., Tonazzini, A., and Bedini, L. (2007). Digital image analysis to enhance underwritten text in the Archimedes palimpsest. *International Journal on Document Analysis and Recognition*, 9: 79–87.

286. Santos, J. R., Freitas, C. C., Araujo, L. S., Dutra, L. V., Mura, J. C., Gama, F. F., Soler, L. S., and Sant'Anna, S. J. S. (2003). Airborne P-band SAR applied to the aboveground biomass studies in the Brazilian tropical rainforest. *Remote Sensing of Environment*, *87*(4): 482–493.

287. Sarker, L. R., and Nichol, J. E. (2011). Improved forest biomass estimates using ALOS AVNIR-2 texture indices. *Remote Sensing of Environment*, *115*(4): 968–977.

288. Satyanarayana, B., Koedam, N., De Smet, K., Di Nitto, D., Bauwens, M., Jayatissa, L., Cannicci, S., and Dahdouh-Guebas, F. (2011). Long-term mangrove forest development in Sri Lanka: early predictions evaluated against outcomes using VHR remote sensing and VHR ground-truth data. *Marine Ecology Progress Series*, *443*: 51–63.

289. Savitzky, A., and Golay, M. (1964). Smoothing and differentiation of data by simplified least squares procedures. *Analytical Chemistry*, 36(8): 1627–1639.

290. Schapire, R. E. (1990). The Strength of Weak Learnability. *Machine Learning*, *5*(2): 197–227.

291. Schlerf, M., Atzberger, C., and Hill, J. (2005). Remote sensing of forest biophysical variables using HyMap imaging spectrometer data. *Remote Sensing of Environment*, *95*(2): 177–194.

292. Schmid, T., Koch, M., Gumuzzio, J., and Mather, P. M. (2004). A spectral library for a semi-arid wetland and its application to studies of wetland degradation using hyperspectral and multispectral data. *International Journal of Remote Sensing*, 25(13): 2485–2496.

293. Schmidt, K. S., and Skidmore, A. K. (2001). Exploring spectral discrimination of grass species in African rangelands. *International Journal of Remote Sensing*, 22(17): 3421–3434

294. Schmidt, K.S., and Skidmore, A. K. (2003). Spectral discrimination of vegetation types in a coastal wetland. *Remote Sensing of Environment*, 85(1): 92–108.

295. Schölkopf, B., and Smola, A. J. (2001). *Learning with kernel: Support Vector Machines, Regularization, Optimization and Beyond*. The MIT Press. Cambridge, Massachusetts, London, England.

296. Selvam, V., Ravichandran, K. K., Gnanappazham, L., and Navamuniyammal, M. (2003). Assessment of community-based restoration of Pichavaram mangrove wetland using remote sensing data. *Current Science*, 85(6): 794–798.

297. Seshavatharam, V., and Srivalli, M. (1989). Systematic leaf anatomy of some Indian mangroves. *Proceedings of Indian Academy of Science (Plant Sciences)*, *99*(6): 557–565.

298. Shanmugam, P., Manjunath, A. S., Ahn, Y. H., Sanjeevi, S., and Ryu, J. H. (2005). Application of multisensor fusion techniques in remote sensing of coastal mangrove wetlands. *International Journal of Geoinformatics*, 1(3): 1–17.

299. Shepherd, K. D., and Walsh, M. G. (2002). Development of Reflectance Spectral Libraries for Characterization of Soil Properties. *Soil Science Society of America Journal*, 66(3): 988–998.

300. Sheskin, D. J. (2004). *Handbook of Parametric and Nonparametric Statistical Procedures. The American Statistician* (Vol. 51). CRC Press, Boka Raton.

301. Shi, R. (2006). Simulated Hyperspectral Data Analysis using Continuum Removal : Case Study on Leaf Chlorophyll Prediction. In *IEEE 8th International Conference on Signal Processing (ICSP 2006)* (pp. 16–20).

302. Simard, M., Grandi, G. De, Saatchi, S., and Mayaux, P. (2002). Mapping tropical coastal vegetation using JERS-1 and ERS-1 radar data with a decision tree classifier. *International Journal of Remote Sensing*, 23(7): 1461–1474.

303. Simard, M., Zhang, K., Rivera-monroy, V. H., Ross, M. S., Ruiz, P. L., Castañeda-Moya, E., Twilley, R. R., and Rodriguez, E. (2006). Mapping Height and Biomass of Mangrove Forests in Everglades National Park with SRTM Elevation Data. *Photogrammetric Engineering Remote Sensing*, *72*(3): 299–311.

304. Singh, I. J., Singh, S. K., Kushwaha, S. P. S., Ashutosh, S., and Singh, R. K. (2004). Assessment and monitoring of estuarine mangrove forests of Goa using satellite remote sensing. *Journal of the Indian Society of Remote Sensing*, 32(2): 167–174.

305. Smith, K. L., Steven, M. D., and Colls, J. J. (2004). Use of hyperspectral derivative ratios in the red-edge region to identify plant stress responses to gas leaks. *Remote Sensing of Environment*, *92*(2): 207–217.

306. SmithIII, T. J. (1992). Forest structure. In A. I. Robertson & D. M. Alongi (Eds.), *Tropical Mangrove Ecosystems* (Vol. 41, pp. 101–136). Washington, D. C: American Geophysical Union, Washington, D. C.

307. Song, S., Gong, W., Zhu, B., and Huang, X. (2011). Wavelength selection and spectral discrimination for paddy rice, with laboratory measurements of hyperspectral leaf reflectance. *ISPRS Journal of Photogrammetry and Remote Sensing*, *66*(5): 672–682.

308. Spadling, M., Kainuma, M., and Collins, Lord. (2010). *World Atlas of Mangroves.* A collaborative project of ITTO, ISME, FAO, UNEP-WCMC, UNESCO-MAB, UNU-INWEH and TNC. Earthscan Publications, Abingdon, Oxon OX144RN, UK.

309. Stagakis, S., Markos, N., Sykioti, O., and Kyparissis, A. (2010). Monitoring canopy biophysical and biochemical parameters in ecosystem scale using satellite hyperspectral imagery: An application on a *Phlomis fruticosa* Mediterranean ecosystem using multiangular CHRIS/PROBA observations. *Remote Sensing of Environment*, 114(5): 977–994.

310. Steininger, M. K. (2000). Satellite estimation of tropical secondary forest above-ground biomass: Data from Brazil and Bolivia. *International Journal of Remote Sensing*, *21*(6-7): 1139–1157.

311. Sulong, I., Mohd-Lokman, H., Mohd-Tarmizi, K., and Ismail, A. (2002). Mangrove Mapping Using Landsat Imagery and Aerial Photographs : Kemaman District, Terengganu, Malaysia. *Environment, Development and Sustainability*, 4: 135–152.

312. Sun, Y., Liu, X., Wu, Y., and Liao, C. (2008). Identifying hyperspectral characters of wetland species using in situ data. *The International Archives of the Photogrammetry, Remote Sensing and Spatial Information Sciences*, *37*(Part B7): 459–466.

313. Tarantino, C., Adamo, M., Pasquariello, G., Lovergine, F., Blonda, P., and Tomaselli, V. (2012). *8-Band Image Data Processing of the WorldView-2 Satellite in a Wide Area of Applications*. (R. B. Rustamov & S. E. Salahova, Eds.) *Earth Observation*.

314. Thenkabail, P. S., Mariotto, I., Gumma, M. K., Middleton, E. M., Landis, D. R., and Huemmrich, K. F. (2013). Selection of hyperspectral narrowbands (HNBs) and composition of hyperspectral twoband vegetation indices (HVIs) for biophysical characterization and discrimination of crop types using field reflectance and Hyperion/EO-1 data. *IEEE Journal of Selected Topics in Applied Earth Observations and Remote Sensing*, 6(2): 427–439.

315. Thenkabail, P. S., Lyon, J. G., and Huete, A. (2012). *Hyperspectral Remote Sensing of Vegetation*. (P. S. Thenkabail, J. G. Lyon, & A. Huete, Eds.). CRC Press.

316. Thenkabail, P. S., Smith, R. B., and De Pauw, E. (2000). Hyperspectral vegetation indices and their relationships with agricultural crop characteristics. *Remote Sensing of Environment*, 71(2): 158–182.

317. Thomas, V., Treitz, P., Jelinski, D., Miller, J., Lafleur, P., and McCaughey, J. H. (2002). Image classificaiton of a northern peatland complex using spectral and plant community data. *Remote Sensing of Environment*, *84*: 83–99.

318. Ting-ting, Z. (2012). Application of Hyperspectral Remote Sensing in Mineral Identification and Mapping. *In 2nd International Conference on Computer Science and Network Technology (ICCSNT)*. Changchun, pp. 103–106.

319. Tomlinson, P. B. (1994). *The Botany of Mangroves*. Cambridge, UK: Cambridge University Press.

320. Townsend, P. A., Foster, J. R., Chastian Jr, R. A., and Currie, W. S. (2003). Canopy nitrogen in the forests of the Central Appalachian Mountains using Hyperion and AVIRIS. *IEEE Transactions on Geoscience and Remote Sensing*, *41*(6): 1347–1354.

321. Tsai, F., and Philpot, W. (1998). Derivative Analysis of Hyperspectral Data. *Remote Sensing of Environment*, *66*(1): 41–51.

322. Tso, B., and Mather, P. M. (2009). *Classification Methods for Remotely Sensed Data* (Second Edition). Boca Raton: CRC Press, Boka Raton.

323. Tucker, C. J. (1979). Red and photographic Infrared linear combinations for monitoring vegetation. *Remote Sensing of Environment*, *8*(2): 127–150.

324. Ulaby, F. T., Kouyate, F., Brisco, B., and Williams, T. H. L. (1986). Textural Infornation in SAR Images. *IEEE Transactions on Geoscience and Remote Sensing*, *GE-24*(2): 235–245.

325. Ullah, S., Schlerf, M., Skidmore, A. K., and Hecker, C. (2012). Identifying plant species using Mid-wave Infrared (2.5–6μm) and Thermal Infrared (8–14μm) emissivity spectra. *Remote Sensing of Environment*, *118*: 95–102.

326. Underwood, E. (2003). Mapping nonnative plants using hyperspectral imagery. *Remote Sensing of Environment*, 86(2): 150–161.

327. UNDP. (2015). *Sustainable Development Goals. United Nations Development Programme*.

328. Upadhyay, V. P., and Mishra, P. K. (2008). Population status of mangrove species in estuarine regions of Orissa coast, India. *Tropical Ecology*, 49(2): 183–188.

329. Vaiphasa, C. (2006). Consideration of smoothing techniques for hyperspectral remote sensing. *ISPRS Journal of Photogrammetry and Remote Sensing*, 60(2): 91–99.

330. Vaiphasa, C., Ongsomwang, S., Vaiphasa, T., and Skidmore, A. K. (2005). Tropical mangrove species discrimination using hyperspectral data: A laboratory study. *Estuarine, Coastal and Shelf Science*, 65: 371–379.

331. Valiela, I., Bowen, J. L., and York, J. K. (2001). Mangrove Forests : One of the World's Threatened Major Tropical Environments. *BioScience*, 51(10): 807–815.

332. van der Meer, F. D., van der Werff, H. M. A, van Ruitenbeek, F. J. A, Hecker, C. A., Bakker, W. H., Noomen, M. F., van der Meijde, M., Carranza, E. J. M., de Smeth, J. B., and Woldai, T. (2012). Multi- and hyperspectral geologic remote sensing: A Review. *International Journal of Applied Earth Observation and Geoinformation*, 14(1): 112–128.

333. Varshney, P. K., and Arora, M. K. (2004). *Advanced Image Processing Techniques for Remotely Sensed Hyperspectral Data*. Springer-Verlag Berlin, Heidelberg.

334. Verheyden, A., Dahdouh-Guebas, F., Thomaes, K., De Genst, W., Hettiarachchi, S., and Koedam, N. (2002). High-resolution vegetation data for mangrove research as obtained from aerial photography. *Environment, Development and Sustainability*, 4(2): 113–133.

335. Vina, A. G. M. La, and Leon, A. de. (2014). *Two Global Challenges, One Solution: International Cooperation to Combat Climate Change and Tropical Deforestation. Centre for Global Development Climate and Forest Paper Series 14* (Vol. 15).

336. Viscarra Rossel, R. A., Jeon, Y. S., Odeh, I. O. A., and McBratney, A. B. (2008). Using a legacy soil sample to develop a mid-IR spectral library. *Australian Journal of Soil Research*, 46(1): 1–16.

337. Vo, Q. T., Oppelt, N., Leinenkugel, P., and Kuenzer, C. (2013). Remote sensing in mapping mangrove ecosystems - an object-based approach. *Remote Sensing*, 5(1), 183–201.

338. Wang, L., and Sousa, W. P. (2009). Distinguishing mangrove species with laboratory measurements of hyperspectral leaf reflectance. *International Journal of Remote Sensing*, 30(5): 1267–1281.

339. Wang, Y., and Imhoff, M. L. (1993). Simulated and observed L-HH radar backscatter from tropical mangrove forests. *International Journal of Remote Sensing*, 14(15): 2819–2828.

340. Wells, S. (2006). *In the front line: Shoreline protection and other ecosystem services from mangroves and coral reefs*. *UNEP World Conservation Monitoring Centre*. Cambridge. Retrieved from www.unep-wcmc.org

341. Wicaksono, P., Danoedoro, P., Hartono, and Nehren, U. (2016). Mangrove biomass carbon stock mapping of the Karimunjawa Islands using multispectral remote sensing. *International Journal of Remote Sensing*, 37(1): 26–52.

342. Wong, F. K. K., and Fung, T. (2014). Combining EO-1 Hyperion and Envisat ASAR data for mangrove species classification in Mai Po Ramsar Site, Hong Kong. *International Journal of Remote Sensing*, 35(23): 7828–7856.

343. Woodcock, C. E., and Strahler, A. H. (1987). The Factor of Scale in Remote Sensing. *Remote Sensing of Environment*, *21*: 311–332.

344. Woodroffe, C. (1992). Mangrove Sediments and Geomorphology. In A. I. Robertson & D. M. Alongi (Eds.), *Tropical Mangrove Ecosystems* (Vol. 41). Washington, D. C: American Geophysical Union, Washington, D. C.

345. Wu, C., Niu, Z., Tang, Q., and Huang, W. (2008). Estimating chlorophyll content from hyperspectral vegetation indices: Modeling and validation. *Agricultural and Forest Meteorology*, *148*(8-9): 1230–1241.

346. Yang, C., Everitt, J. H., Fletcher, R. S., James, R. R., and Mausel, P. W. (2009). Evaluating AISA+ hyperspectral imagery for mapping black mangrove along the South Texas Gulf Coast. *Photogrammetric Engineering & Remote Sensing*, 75(4): 425–435.

347. Yuanyue, L., Zhongbao, L., and Peng, L. (2009). The Study on the Leaf Anatomy of Some Mangrove Species of China. *2009 International Conference on Environmental Science and Information Application Technology* (pp. 47–51).

348. Zanne, A. E., Lopez-Gonzalez, G., Coomes, D. A., Ilic, J., Jansen, S., Lewis, S. L., Miller, R. B., Swenson, N. G., Wiemann, M. C., and Chave, J. (2009). *Global Wood Density Database: Towards a worldwide wood economics spectrum. Dryad Digital Repository*.

349. Zhang, B., Wu, D., Zhang, L., Jiao, Q., and Li, Q. (2012). Application of hyperspectral remote sensing for environment monitoring in mining areas. *Environmental Earth Sciences*, 65(3): 649–658.

350. Zhang, C., Kovacs, J. M., Liu, Y., Flores-verdugo, F., and Flores-de-santiago, F. (2014). Separating Mangrove Species and Conditions Using Laboratory Hyperspectral Data: A Case Study of a Degraded Mangrove Forest of the Mexican Pacific. *Remote Sensing*, 6(12): 11673–11688.

351. Zhang, C., Selch, D., and Cooper, H. (2015). A Framework to Combine Three Remotely Sensed Data Sources for Vegetation Mapping in the Central Florida Everglades. *Wetlands*: 1–13. (Published online on 29 December 2015).

352. Zhang, J., Rivard, B., Sánchez-Azofeifa, A., and Castro-Esau, K. (2006). Intra- and inter-class spectral variability of tropical tree species at La Selva, Costa Rica: Implications for species identification using HYDICE imagery. *Remote Sensing of Environment*, *105*(2): 129–141.

353. Zheng, D., Rademacher, J., Chen, J., Crow, T., Bresee, M., Le Moine, J., and Ryu, S.-R. (2004). Estimating aboveground biomass using Landsat 7 ETM+ data across a managed landscape in northern Wisconsin, USA. *Remote Sensing of Environment*, *93*(3): 402–411.

354. Zhu, Y., Liu, K., Liu, L., Wang, S., and Liu, H. (2015). Retrieval of Mangrove Aboveground Biomass at the Individual Species Level with WorldView-2 Images. *Remote Sensing*, 7: 12192–12214.

355. Zomer, R., Trabucco, A., and Ustin, S. (2009). Building spectral libraries for wetlands land cover classification and hyperspectral remote sensing. *Journal of Environmental Management*, 90(7): 2170–2177.

356. Zomer, R., and Ustin, S. (1999). Ground-Truth Data Collection Protocol For Hyperspectral Remote Sensing. *Unpublished*, pp. 1–26.

APPENDIX 1

MANGROVE SPECIES CONSIDERED IN THE STUDY

Following are the photographs of 34 mangrove (25 true and 9 associated) species considered for the development of spectral library and spectral separability analysis.

Acanthus ilicifolius

Aegialitis rotundifolia

Aegiceras corniculatum

Amoora cucullata

Avicennia alba

Avicennia marina

Avicennia officinalis

Bruguiera gymnorrhiza

Bruguiera parviflora

Bruguiera sexangula

Ceriops decandra

Ceriops tagal

Cyanometra iripa

Excoecaria agallocha

Heritiera fomes

Heritiera littoralis

Kandelia candel

Lumnitzera racemosa

Rhizophora apiculata

Rhizophora mucronata

Sonneratia apetala

Sonneratia caseolaris

Xylocarpus granatum

Xylocarpus mekongensis

Xylocarpus moluccensis

Acrostichium aureum

Brownlowia tersa

Cerebra odollam

Intsia bijuga

Merope angulata

Phoenix paludosa

Salvadoria persica

Suaeda maritime
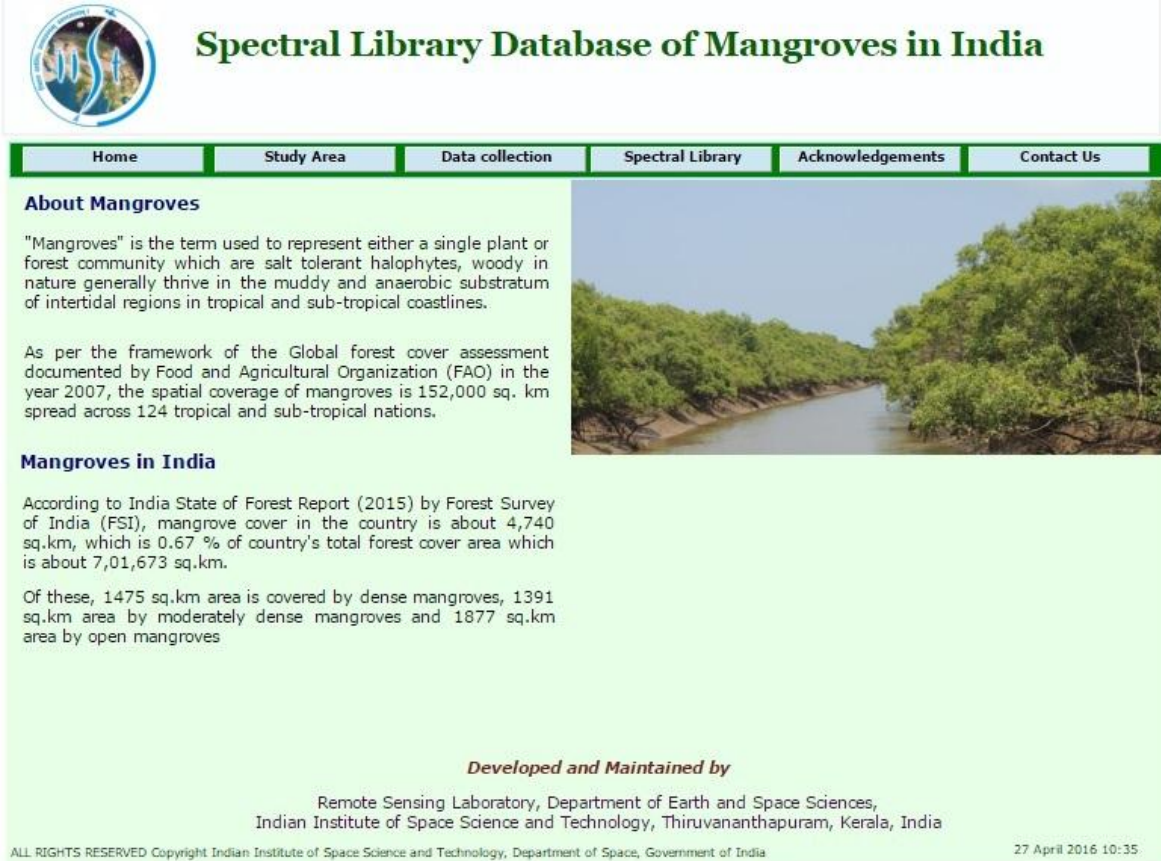
Tamarix troupii

APPENDIX 2

Spectral Library of Mangroves in India – Web portal in Intranet

The spectral library of 34 mangrove species developed in this study will be soon published online with necessary permission. The screenshots of the webpage developed for the online portal is given in this section.

Spectral Library Database of Mangroves in India

| Home | Study Area | Spectral Library | Download | Acknowledgements | Contact Us |

Species: Acanthus ilicifolius

Family: Acanthaceae

Common Name (English): Holy Mangroves
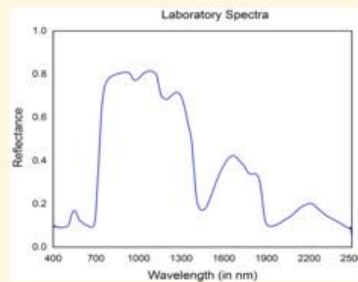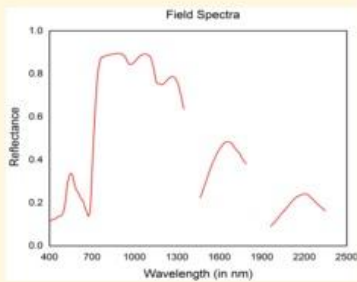
Field Spectra

Laboratory Spectra

Download Spectra

27 April 2016 10:33

From this portal, registered users can download field and laboratory spectral signatures of 34 mangrove species.

The copyright of the webpage belongs to the Indian Institute of Space Science and Technology, Thiruvananthapuram, Kerala, India.

APPENDIX 3

Accuracy Assessment of classification results of IRS-P6 LISS III multispectral image using ten base classifiers

Sl. No	Class	MDC		SAM		SSM		ACE		MF	
		PA	UA	PA	UA	PA	UA	PA	UA	PA	UA
1	AO (dense)	87.29	57.22	94.92	71.79	87.29	57.87	56.78	38.07	0.00	0.00
2	AM (moderately dense)	5.35	13.70	3.21	10.34	5.35	13.70	4.28	13.79	0.00	0.00
3	AO+EA (mixed)	64.96	53.29	62.41	56.07	64.96	53.13	61.31	47.19	0.00	0.00
4	HF (moderately dense)	32.22	59.18	15.00	28.57	32.22	59.18	11.11	40.82	0.00	0.00
5	EA (dense)	59.46	25.58	45.95	36.17	59.46	25.58	52.25	21.89	0.00	0.00
6	HF (dense)	17.20	14.41	19.35	6.02	17.20	14.41	11.83	4.98	0.00	0.00
7	Mixed mangroves	40.59	31.78	26.73	25.71	40.59	31.30	43.56	34.38	0.00	0.00
8	Fringing mangroves	8.57	64.29	24.76	68.42	8.57	64.29	17.14	58.06	0.00	0.00
9	River	67.25	100.00	67.86	100.00	67.25	100.00	34.41	93.81	0.00	0.00
10	Creeks	100.00	34.41	99.53	36.22	99.53	34.75	87.38	19.87	0.00	0.00
11	Wetlands	11.36	20.00	43.18	44.71	11.36	20.41	4.55	14.81	100.00	2.60
12	Cleared area	9.09	10.00	15.45	10.06	9.09	10.00	41.82	47.92	0.00	0.00
13	Swampy area	61.76	21.99	83.82	67.06	66.18	22.50	0.00	0.00	0.00	0.00
14	Mudflats	1.38	2.70	8.28	16.00	1.38	2.74	3.45	14.71	0.00	0.00
15	Terrestrial vegetation	51.56	37.08	62.50	34.19	51.56	37.08	50.00	15.24	0.00	0.00
16	Fallow land	95.82	98.35	98.71	100.00	96.14	98.36	97.43	96.81	0.00	0.00
	OA (%)	54.89		55.12		54.98		39.64		2.52	
	Kappa	0.49		0.49		0.49		0.34		0.00	

Sl. No	Class	LDC		LR		NBC		MLC		SVM	
		PA	UA	PA	UA	PA	UA	PA	UA	PA	UA
1	AO (dense)	3.39	30.77	0.00	0.00	9.32	100.00	4.24	55.56	75.42	74.79
2	AM (moderately dense)	0.00	0.00	4.28	16.33	2.67	19.23	2.14	33.33	33.69	55.75
3	AO+EA (mixed)	71.53	44.95	81.39	45.05	78.83	63.16	64.23	75.54	76.64	70.47
4	HF (moderately dense)	67.50	37.67	67.78	47.01	63.06	42.75	49.17	47.71	65.28	69.32
5	EA (dense)	0.00	0.00	0.00	0.00	1.80	50.00	56.76	37.95	41.44	40.00
6	HF (dense)	9.68	25.71	0.00	0.00	36.56	34.69	11.83	37.93	41.94	34.82
7	Mixed mangroves	60.40	22.18	62.38	21.88	61.39	22.88	62.38	20.72	47.52	34.04
8	Fringing mangroves	0.00	0.00	0.00	0.00	26.67	41.18	74.29	46.43	46.67	73.13
9	River	99.91	80.06	100.00	86.16	99.91	92.93	93.10	99.35	97.03	99.02
10	Creeks	5.61	70.59	14.02	68.18	57.01	99.19	92.52	71.48	92.99	85.41
11	Wetlands	42.05	38.95	85.23	68.81	46.59	93.18	89.77	54.48	65.91	61.70
12	Cleared area	1.82	40.00	0.00	0.00	0.00	0.00	8.18	23.08	30.91	39.08
13	Swampy area	1.47	3.45	26.47	85.71	79.41	43.55	47.06	68.09	45.59	57.41
14	Mudflats	84.83	59.71	97.24	44.90	86.21	45.62	45.52	48.53	70.34	58.62
15	Terrestrial vegetation	1.56	100.00	0.00	0.00	29.69	52.78	81.25	28.42	75.00	36.09
16	Fallow land	94.86	95.78	100.00	100.00	96.46	96.46	97.11	100.00	94.21	100.00
	OA (%)	60.90		64.63		68.40		68.15		**75.99**	
	Kappa	0.52		0.57		0.62		0.63		**0.72**	

(AO – *Avicennia officinalis*, AM – *Aviccenia marina*, EA – *Excoecaria agallocha*, HF – *Heritiera fomes*)

Producer accuracy – PA and User Accuracy – UA are given in %.

APPENDIX 4

Accuracy Assessment of classification results of Landsat-8 OLI multispectral image using ten base classifiers

Sl. No	Class	MDC		SAM		SSM		ACE		MF	
		PA	UA	PA	UA	PA	UA	PA	UA	PA	UA
1	AO (dense)	100.00	56.50	100.00	56.76	99.21	61.27	92.86	97.50	0.00	0.00
2	AM (moderately dense)	17.90	20.57	11.73	13.01	18.52	21.13	14.81	15.58	0.00	0.00
3	AO+EA (mixed)	84.44	44.39	86.22	45.43	88.44	47.72	87.11	39.52	96.00	32.53
4	HF (moderately dense)	19.63	71.11	23.72	72.96	25.15	73.21	27.61	66.83	0.00	0.00
5	EA (dense)	42.06	18.37	19.63	14.79	41.12	19.64	27.10	18.35	0.00	0.00
6	HF (dense)	30.91	31.19	22.73	17.86	31.82	31.25	31.82	24.65	0.00	0.00
7	Mixed mangroves	14.80	16.86	15.31	20.00	23.47	29.11	63.27	52.54	0.00	0.00
8	Fringing mangroves	20.90	45.16	53.73	43.90	53.73	54.55	26.87	50.00	0.00	0.00
9	River	99.05	100.00	95.56	100.00	98.73	100.00	99.37	98.12	0.00	0.00
10	Creeks	100.00	92.74	97.39	80.58	98.26	91.13	86.96	96.15	0.00	0.00
11	Wetlands	48.53	16.02	35.29	14.91	33.82	13.22	5.88	19.05	17.65	0.82
12	Cleared area	87.74	46.73	70.75	52.82	70.75	62.50	57.55	50.83	0.00	0.00
13	Swampy area	75.43	93.16	62.98	72.80	40.83	62.43	86.85	55.53	0.00	0.00
14	Mudflats	7.41	60.00	4.94	9.09	5.56	6.38	15.43	54.35	96.91	13.03
15	Terrestrial vegetation	42.86	61.54	58.93	54.10	37.50	42.86	32.14	56.25	0.00	0.00
16	Fallow land	97.03	98.36	96.49	98.62	98.65	97.33	90.54	97.10	0.00	0.00
	OA (%)	61.94		59.78		60.14		63.47		11.55	
	Kappa	0.58		0.56		0.56		0.60		0.08	

Sl. No	Class	LDC		LR		NBC		MLC		SVM	
		PA	UA	PA	UA	PA	UA	PA	UA	PA	UA
1	AO (dense)	83.33	100.00	0.00	0.00	77.78	100.00	66.67	100.00	94.44	99.17
2	AM (moderately dense)	0.00	0.00	0.00	0.00	0.00	0.00	28.40	68.66	66.67	54.27
3	AO+EA (mixed)	70.22	45.01	0.00	0.00	43.56	70.00	16.00	94.74	87.56	62.74
4	HF (moderately dense)	87.12	41.85	100.00	27.49	85.48	40.19	82.41	47.02	58.69	76.74
5	EA (dense)	0.00	0.00	0.00	0.00	0.00	0.00	1.87	28.57	34.58	37.76
6	HF (dense)	0.00	0.00	0.00	0.00	40.91	34.09	0.00	0.00	48.18	41.09
7	Mixed mangroves	51.53	56.42	0.00	0.00	4.08	22.86	67.35	48.89	70.41	70.05
8	Fringing mangroves	0.00	0.00	0.00	0.00	10.45	63.64	68.66	31.08	44.78	69.77
9	River	99.84	94.30	100.00	82.46	98.89	100.00	98.41	100.00	100.00	99.37
10	Creeks	73.91	98.84	0.00	0.00	93.91	95.58	92.17	92.98	95.65	100.00
11	Wetlands	1.47	14.29	0.00	0.00	0.00	0.00	35.29	22.22	42.65	22.31
12	Cleared area	54.72	63.74	0.00	0.00	64.15	68.69	65.09	84.15	68.87	85.88
13	Swampy area	80.62	66.57	0.00	0.00	77.16	81.68	83.04	67.80	51.21	79.57
14	Mudflats	11.73	27.14	20.99	57.63	17.90	50.88	28.40	100.00	43.21	41.42
15	Terrestrial vegetation	9.82	47.83	0.00	0.00	75.00	25.23	87.50	52.41	85.71	57.83
16	Fallow land	93.24	89.15	100.00	50.55	98.92	97.86	94.86	99.72	98.92	96.32
	OA (%)	65.12		45.68		65.24		69.08		**74.72**	
	Kappa	0.60		0.36		0.61		0.65		**0.72**	

(AO – *Avicennia officinalis*, AM – *Aviccenia marina*, EA – *Excoecaria agallocha*, HF – *Heritiera fomes*)

Producer accuracy – PA and User Accuracy – UA are given in %.

APPENDIX 5

BIOMASS CALCULATED FOR 40 SAMPLE PLOTS

As the part of the biomass study, biomass for 40 sample plots were calculated using allometric equations with inputs from field collected biophysical parameters. This section gives the brief details of the biophysical inputs used for plot biomass estimation.

Plot ID	Species	DBH range (cm)	Height range (m)	Total Biomass (t/ha)
1	S apetala	26 to 41	15.5 to 17	300.60
2	E agallocha	4 to 24	4.5 to 12	839.35
	H fomes	6 to 62	3.5 to 8.5	
	P pinnata	13 to 32	7.5 to 8.2	
3	H fomes	5 to 22	7 to 8.2	150.80
	E agallocha	8 to 20	5.5 to 6	
4	S persica	21 to 52	2.7 to 3.6	516.94
	P pinnata	7 to 30	4.9 to 6.2	
5	A alba	6 to 8	5 to 7	638.04
	S apetala	68 to 70	12 to 14	
	E agallocha	4	2.5	
	A rotundifolia	4 to 5	2.8 to 6	
	B parviflora	10 to 14	10.3 to 13.6	
6	E agallocha	4 to 23	3.6 to 4.8	185.81
	L racemosa	9 to 12	3.4 to 4.4	
7	H fomes	8 to 20	7.7 to 8.7	399.42
	E agallocha	6 to 29	6.9 to 7.2	
	C iripa	17 t0 22	3.8	

Plot ID	Species	DBH range (cm)	Height range (m)	Total Biomass (t/ha)
8	A cucullata	4 to 24	10 to 13.8	170.59
	H fomes	5 to 6	10.5 to 12.3	
9	A officinalis	70 to 72	10 to 12	767.22
	H fomes	14	3.8	
	E agallocha	5 to 10	2.2 to 5.2	
10	R mucronata	18 to 35	3.9 to 4.8	516.94
	X granatum	12 to 16	4.3 to 6.9	
	A marina	20 to 38	6.2 to 7.3	
	P pinnata	9 to 17	4.2 to 5.3	
11	H fomes	7 to 30	2.5 to 7	314.90
	E aggalocha	6 to 25	4.2 to 5.6	
	S persica	7	3.2	
12	H fomes	5 to 11	7.3 to 11.7	157.06
	A cucullata	8 to 10	7 to 9	
	S apetala	31	10.2	
13	S apetala	12 to 32	7.3 to 9.1	299.58
	A marina	9 to 11	6.9 to 8.7	
14	T troupii	5 to 32	4.7 to 5.7	247.42
	T populnea	4 to 7	1.9 to 2.9	
	E agallocha	4 to 15	3.2 to 3.4	
15	A officinalis	13 to 30	3.9 to 4.2	239.47
	E agallocha	5 to 11	3.6 to 4.2	
16	E agallocha	7 to 17	4.7 to 6.3	357.50
	S persica	52	3.5	
	C decandra	5 to 8	3.2 to 4.6	
17	A officinalis	27 to 33	7.1 to 8.9	211.03
	E agallocha	5 to 11	2.8 to 4.7	
	C decandra	5	3.4	
18	A officinalis	12 to 22	6.8 8.9	237.26
	E agallocha	4 to 30	1.2 to 3.2	
19	H fomes	8 to 35	7.3 to 7.6	401.15
	C iripa	12	3.7	

Plot ID	Species	DBH range (cm)	Height range (m)	Total Biomass (t/ha)
20	*H fomes*	10 to 42	4 to 12.26	591.74
	E aggalocha	8	2.4	
21	*E agallocha*	6 to 15	8.3 to 8.8	133.91
	H fomes	10	9.2	
22	*R mucronata*	15 to 23	5.5 to 7.4	491.17
23	*C decandra*	23	7.48	188.54
	E aggalocha	8 to 23	5.5 to 7.4	
24	*A alba*	5 to 26	4.2 to 6.3	191.77
25	*A officinalis*	8 to 37	7.5 to 8	355.97
26	*K candel*	8	4.9	192.77
	A officinalis	16 to 18	6.5 to 7.2	
	R mucronata	24 to 30	5.8 to 6.2	
27	*C iripa*	17 to 22	6.2 to 9.8	185.76
	A rotundifolia	4 to 5	2.8 to 3.9	
	P pinnata	15 to 36	10 to 10.8	
28	*A officinalis*	35	9.3	879.80
	E agallocha	5 to 10	7 to 7.8	
	R mucronata	19 to 64	6.8 to 7.1	
29	*A officinalis*	56 to 64	12 to 14	484.74
30	*C decandra*	4 to 9	3.3 to 5.8	327.30
	A corniculatum	21	7	
	E agallocha	20 to 53	12 to 13.5	
31	*A officinalis*	32 to 38	16.1 to 16.5	358.24
	B sexangula	30 to 34	7.5 to 7.8	
	C decandra	5	3.5	
32	*A officinalis*	11 to 29	7.2 to 10.7	387.44
	E agallocha	5 to 26	4.9 to5.6	
	C decandra	12	4.8	
33	*A offcinalis*	5 to 27	7.9 to 8.7	258.19
	E agallocha	5 to 10	6.9 to 9.2	
34	*C iripa*	6 to 27	4.5 to 5.1	146.35
	P pinnata	8 to 10	6 to 7.5	

Plot ID	Species	DBH range (cm)	Height range (m)	Total Biomass (t/ha)
35	*H fomes*	11 to 21	9.8 to 11.3	529.85
	E agallocha	11 to 15	7.6 to 8.5	
	C iripa	46	6.9	
36	*H fomes*	10 to 20	4.5 to 12.3	215.29
	E agallocha	6 to 19	4.7 to 10.3	
37	*H fomes*	7 to 25	8.1 to 9.2	385.13
	E agallocha	6 to 15	8.8 to 9.5	
	C iripa	5	4.8	
38	*H fomes*	9 to 32	7.5 to 8.3	578.34
	E agallocha	15 to 31	6.9 to 8.5	
39	*C iripa*	6 to 10	3.7 to 5.3	158.15
	H fomes	19 to 21	4.2 to 4.9	
	S persica	25 to 27	3.6 to 3.9	
	P pinnata	22	4.8	
40	*E agallocha*	6 to 16	12.3 to 13	257.22
	H fomes	7 to 11	14 to 14.4	
	B sexangula	13 to 30	11.2 to 12.1	

LIST OF PUBLICATIONS BASED ON THE THESIS

Papers in Peer Reviewed Journals

1. Prasad, K. A., and Gnanappazham, L. (2015). Multiple statistical approaches for the discrimination of mangrove species of *Rhizophoraceae* using transformed field and laboratory hyperspectral data. *Geocarto International*, *6049*(November): 1–22. http://doi.org/10.1080/10106049.2015.1094521

2. Prasad, K. A., Gnanappazham, L., Selvam, V., Ramasubramanian, R., and Kar, C. S. (2015). Developing a spectral library of mangrove species of Indian East Coast using field spectroscopy. *Geocarto International*, *30*(5): 580–599. Retrieved from http://www.tandfonline.com/doi/abs/10.1080/10106049.2014.985743

3. Prasad, K. A., Damodaran, B. B., Gnanappazham, L., and Nidamanuri, R. Multiple classifier system for improved species classification of mangrove forest in Bhitarkanika National Park, Odisha, India using EO-1 Hyperion hyperspectral image. (To be Communicated)

4. Prasad, K. A., and Gnanappazham, L. Spectral separability analysis and classification of spectral signatures of 34 mangrove species in India using different spectral transformation methods. (To be Communicated)

5. Prasad, K. A., and Gnanappazham, L. Estimation of above ground biomass of mangrove ecosystem in Bhitarkanika National Park using high resolution WorldView-2 data. (To be Communicated)

Papers in Conference Proceedings

1. Prasad, K. A., Damodaran, B. B., Gnanappazham, L., Nidamanuri, R., Ramasubramanian, R., and Selvam, V. (2016). Multiple classification system for classification of mangrove at species level using multispectral image data. *ECSA 56 Conference on Coastal systems in transition: From a 'natural' to an 'anthropogenically-modified' state*, Bremen, Germany (Oral Presentation).

2. K. Arun Prasad and L. Gnanappazham. (2014). "Species Discrimination of mangroves using Derivative Spectral Analysis" Proceedings of ISPRS 2014: *ISPRS Annals of the Photogrammetry, Remote Sensing and Spatial Information Sciences*, Volume II-8, 2014. ISPRS Technical Commission VIII Symposium, Hyderabad, India. doi: 10.5194/isprsannals-II-8-45-2014 (Oral Presentation)

3. K. Arun Prasad and L. Gnanappazham. (2014). "Discrimination of mangrove species of *Rhizophoraceae* using laboratory spectral signatures" P*roceedings of IGARSS 2014: International Geoscience and Remote Sensing Symposium (IGARSS 2014)*, Quebec, Canada. doi:10.1109/IGARSS.2014.6947084 (Poster Presentation)

4. K. Arun Prasad and L. Gnanappazham. (2013). "Spectral distance as an approach for species level discrimination of mangroves", *Proceedings of AGSE 2013: International Conference on Geospatial Momentum for Society and Environment*, Ahmedabad, India. (Oral Presentation)

5. K. Arun Prasad and L. Gnanappazham. (2013). "Spectral separability among mangrove species of *Rhizophoraceae* family using field spectroscopy", *IEEE Conference Proceedings of Symposium on Ocean Electronics (SYMPOL 2013)*, Kochi, India. doi:10.1109/SYMPOL.2013.6701933. (Oral Presentation)